Springer Series in Materials Science 178

Mitsuteru Inoue
Miguel Levy
Alexander V. Baryshev *Editors*

Magnetophotonics

From Theory to Applications

Springer

Springer Series in Materials Science

Volume 178

For further volumes:
www.springer.com/series/856

The Springer Series in Materials Science covers the complete spectrum of materials physics, including fundamental principles, physical properties, materials theory and design. Recognizing the increasing importance of materials science in future device technologies, the book titles in this series reflect the state-of-the-art in understanding and controlling the structure and properties of all important classes of materials.

Mitsuteru Inoue • Miguel Levy •
Alexander V. Baryshev
Editors

Magnetophotonics

From Theory to Applications

Springer

Editors
Mitsuteru Inoue
Dept. of Electric and Electronic Eng.
Toyohashi University of Technology
Toyohashi, Aichi, Japan

Miguel Levy
Physics Department
Michigan Technological University
Houghton, MI, USA

Alexander V. Baryshev
Electronics-Inspired Interdisciplinary
Research Institute
Toyohashi University of Technology
Toyohashi, Aichi, Japan

ISSN 0933-033X
ISSN 2196-2812 (electronic)
Springer Series in Materials Science
ISBN 978-3-642-35508-0
ISBN 978-3-642-35509-7 (eBook)
DOI 10.1007/978-3-642-35509-7
Springer Heidelberg New York Dordrecht London

Library of Congress Control Number: 2013934548

Printed on acid-free paper

Springer is part of Springer Science+Business Media (www.springer.com)

Preface

The advances in experimental and applied photonics are connected with the rising potential of modern fabrication techniques, allowing the creation of tiny artificial structures with characteristic lengths (periodicity) comparable to or even smaller than the wavelength of light. Theoretical developments in this field have advanced apace and consisted to a considerable degree of the translation or mapping of wave phenomena from the quantum theory of solids into electrodynamics. This mapping has led to the appearance of theories of photonic crystals, light diffusion, backscattering and Anderson localization of light. Among the representatives of photonic crystals is their remarkable extension to magneto-optic systems, the subject of the current volume, magnetophotonic crystals. Pioneering studies on magnetophotonic crystals were motivated by fundamental and practical interests to enhance or take advantage of the magneto-optical response in existing magneto-optical materials and the possibility of controlling the flow of light by external magnetic fields.

When the constitutive elements of periodic media are magnetic, the resultant magnetophotonic crystals demonstrate unique optical and magneto-optical properties. For such magnetic, nonreciprocal media, there exists an additional degree of freedom to operate the photonic band structure, diffraction patterns, and the state of polarization of light—all these characteristics can be controlled by external magnetic fields. We believe that this volume will be a timely contribution to the development of this field by delivering results of many efforts devoted to experimental and theoretical studies of the magnetophotonic crystals and their applications.

We thank all the authors for their valuable contribution to this book.

Aichi, Japan — Mitsuteru Inoue
Houghton, MI, USA — Miguel Levy
Aichi, Japan — Alexander Baryshev

Contents

Contributors

Oleg A. Aktsipetrov Faculty of Physics, M.V. Lomonosov Moscow State University, Moscow, Russia

Seugmin M. Baek Department of Electrical and Electronic Information Engineering, Toyohashi University of Technology, Toyohashi, Aichi, Japan

Alexander V. Baryshev Electronics-Inspired Interdisciplinary Research Institute, Toyohashi University of Technology, Toyohashi, Aichi, Japan; Ioffe Physical-Technical Institute, St. Petersburg, Russia

Vladimir I. Belotelov Prokhorov General Physics Institute, Russian Academy of Sciences, Moscow, Russia; Lomonosov Moscow State University, Moscow, Russia

David J. Bergman School of Physics and Astronomy, Tel Aviv University, Tel Aviv, Israel

Ashim Chakravarty Physics Department, Michigan Technological University, Houghton, MI, USA

Alexander V. Dorofeenko Institute for Theoretical and Applied Electromagnetics RAS (ITAE RAS), Moscow, Russia; Moscow Institute of Physics and Technology, Dolgoprudniy, Moscow Reg., Russia

Andrey A. Fedyanin Faculty of Physics, M.V. Lomonosov Moscow State University, Moscow, Russia

Alex Figotin University of California, Irvine, CA, USA

Elena A. Gan'shina Faculty of Physics, M.V. Lomonosov Moscow State University, Moscow, Russia

Taichi Goto Department of Electrical and Electronic Information Engineering, Toyohashi University of Technology, Toyohashi, Aichi, Japan

Alexander B. Granovsky Faculty of Physics, M.V. Lomonosov Moscow State University, Moscow, Russia

Xiaoyue Huang Physics Department, Michigan Technological University, Houghton, MI, USA

Mitsuteru Inoue Department of Electrical and Electronic Information Engineering, Toyohashi University of Technology, Toyohashi, Aichi, Japan

Andrey N. Kalish Prokhorov General Physics Institute, Russian Academy of Sciences, Moscow, Russia; Lomonosov Moscow State University, Moscow, Russia

Pradeep Kumar Physics Department, Michigan Technological University, Houghton, MI, USA

Akhlesh Lakhtakia Nanoengineered Metamaterials Group, Department of Engineering Science and Mechanics, Pennsylvania State University, University Park, PA, USA

Miguel Levy Physics Department, Michigan Technological University, Houghton, MI, USA

Pang Boey Lim Department of Electrical and Electronic Information Engineering, Toyohashi University of Technology, Toyohashi, Aichi, Japan

Alexander A. Lisyansky Physics Department, Queens College of the City University of New York, Flushing, NY, USA

Alexander M. Merzlikin Institute for Theoretical and Applied Electromagnetics RAS (ITAE RAS), Moscow, Russia

Shinichiro Mito Department of Electrical and Electronic Information Engineering, Toyohashi University of Technology, Toyohashi, Aichi, Japan

Tatyana V. Murzina Faculty of Physics, M.V. Lomonosov Moscow State University, Moscow, Russia

Yakov M. Strelniker Department of Physics, Bar-Ilan University, Ramat-Gan, Israel

Yurii P. Sukhorukov Institute of Metal Physics, Russian Academy of Sciences, Yekaterinburg, Russia

Hiroyuki Takagi Department of Electrical and Electronic Information Engineering, Toyohashi University of Technology, Toyohashi, Aichi, Japan

Andrey V. Telegin Institute of Metal Physics, Russian Academy of Sciences, Yekaterinburg, Russia

Alexey P. Vinogradov Institute for Theoretical and Applied Electromagnetics RAS (ITAE RAS), Moscow, Russia; Moscow Institute of Physics and Technology, Dolgoprudniy, Moscow Reg., Russia

Ilya Vitebskiy Air Force Research Laboratory, Sensors Directorate, Wright Patterson AFB, OH, USA

Fei Wang Research and Development, Micron Technology, Inc., Boise, ID, USA

Anatoly K. Zvezdin Lebedev Physical Institute, Russian Academy of Sciences, Moscow, Russia; Moscow Institute of Physics and Technology (State University), Dolgoprudny, Russia

Chapter 1
Enhancement of the Faraday and Other Magneto-Optical Effects in Magnetophotonic Crystals

A.P. Vinogradov, A.V. Dorofeenko, A.M. Merzlikin, Y.M. Strelniker, A.A. Lisyansky, A.B. Granovsky, and D.J. Bergman

Abstract It is shown that for existent natural materials the Faraday rotation is far below the theoretical limit [Steel et al. in J. Lightwave Technol. 18:1297, 2000]. Under this condition the value of the Faraday rotation is primarily determined by the Q-factor, while the low group velocity value, multipass traveling and energy concentration in magneto-optical material play a secondary role. A comparative analysis of the efficiency of different schemes employing defect modes, Tamm surface states, the Borrmann effect and plasmon resonance is presented.

1.1 Introduction

Magneto-optical (MO) effects have been known since 1846 when Faraday discovered a rotation of the polarization of a linearly polarized electromagnetic wave traveling through a slab of a gyrotropic substance placed in a static magnetic field. It is also known that Faraday and other MO effects can be essentially enhanced

A.P. Vinogradov (✉) · A.V. Dorofeenko · A.M. Merzlikin
Institute for Theoretical and Applied Electromagnetics RAS (ITAE RAS), Moscow 125412, Russia
e-mail: A-Vinogr@yandex.ru

A.P. Vinogradov · A.V. Dorofeenko
Moscow Institute of Physics and Technology, Dolgoprudniy, Moscow Reg. 141700, Russia

Y.M. Strelniker
Department of Physics, Bar-Ilan University, Ramat-Gan, Israel

A.A. Lisyansky
Physics Department, Queens College of the City University of New York, Flushing, NY 11367, USA

A.B. Granovsky
Faculty of Physics, M.V. Lomonosov Moscow State University, Moscow 119991, Russia

D.J. Bergman
School of Physics and Astronomy, Tel Aviv University, Tel Aviv 69978, Israel

M. Inoue et al. (eds.), *Magnetophotonics*, Springer Series in Materials Science 178,
DOI 10.1007/978-3-642-35509-7_1,

in the presence of a resonance. One such resonance, which is currently under intensive study, is the surface plasmon resonance [1]. It is commonly believed that this or similar resonances are responsible for the Extraordinary Light Transmission (ELT) through a metal film, perforated by a periodic array of sub-wavelength holes [2, 3], as well for other new phenomena recently found in photonic crystals with bandgaps [4–6]. Application of a static magnetic field to such systems induces strong optical and transport anisotropy, leads to appearance of additional off-diagonal tensor components in the effective permittivity tensor $\hat{\varepsilon}$ and changes the surface plasmon frequency [7–13]. Therefore, the application of a static magnetic field to conducting systems with dielectric islands or to dielectric systems with metallic islands, as well the introduction of gyrotropic inclusions into photonic crystals [4, 14–17] should lead to the appearance of strong MO effects [18–23] and to possibilities for manipulation of light propagation [7–13, 24–33].

Enhancements of the Faraday and Kerr effects was demonstrated in one-dimensional MO quasicrystals [34], in systems with a random distribution of MO layers [35], in magnetophotonic crystals (MPC's) [6], in MPC's with one or two defects [36–40], and in a system of two adjoined PC's including MO layers and having an optical Tamm state [4, 5, 16]. At the present time, microscopic mechanisms of MO phenomena are well studied [41]. They are caused by the spin-orbit interaction at inter- and intraband optical transitions. Although, MO phenomena are weak, like all relativistic effects, they can be substantially enhanced by using MPCs. Below we discuss the physical phenomena underlying such an enhancement.

While the very fact of enhancement of MO effects in multilayer structures has been known for a long time [42, 43], the mechanism which leads to this enhancement is still under discussion. In some papers [36, 44, 45], the origin of the enhancement is attributed to the fact that the light localized near a defect has an increased optical path length, which results in the increase of the Faraday rotation, similar to the classical Faraday experiment. The authors of Refs. [46, 47] consider the low group velocity, which increases the time of interaction of light with matter, as the cause of the enhancement.

Considerable understanding was achieved in Ref. [36], where the role of the phase change in the vicinity of a resonance was shown, the decrease of the transmission with the growth of the Faraday rotation was explained and a two-defect scheme, providing high transmission at large Faraday rotation, was suggested.

In the present chapter, we theoretically predict the phase shift of π, provided naturally by the resonance, causes a giant increase of the Faraday angle from the small bulk value, determined by the MO constant, to a large value close to $\pi/2$. If the splitting of the resonance for the right and left circular polarizations is small, the Faraday effect is shown to be proportional to the Q-factor of the resonance and to the field confinement factor. If the splitting is not small, the signal amplitude inevitably decreases with the increase of the Faraday angle. To avoid this shortcoming, a structure using resonances of different orders is suggested, in principle providing the maximum Faraday rotation of $\pi/2$ at the transmission equal to unity.

1.2 Voigt Configuration

MO effects in metamaterial and magnetophotonic crystals should be calculated using proper formulas written in general form without making any assumptions and simplifications which could be correct for natural materials but not valid for artificial metamaterials. As was shown in Refs. [7–12], an application of a static magnetic field to metamaterials (see Fig. 1.1) can lead to magneto-induced anisotropy and to the appearance of additional off-diagonal terms in the electric permittivity and magnetic permeability tensors. Here we only briefly outline their derivation, referring the reader to Refs. [48–56] for more details.

We are looking for a solution to Maxwell's equations in the form of a monochromatic plane wave with the frequency ω propagating along the y-axis, with electric and magnetic fields $E = E_0 \exp(-i\omega t + i\mathbf{k}\cdot\mathbf{r})$ and $H = H_0 \exp(-i\omega t + i\mathbf{k}\cdot\mathbf{r})$, respectively. Here $\mathbf{E}_0$ and $\mathbf{H}_0$ are constant amplitudes and $\mathbf{k} \equiv (0, k, 0)$ is the wavevector in the y-direction. Substituting this into Maxwell's equations we obtain

$$k^2\mathbf{E}_0 - \mathbf{k}(\mathbf{E}_0\cdot\mathbf{k}) = \left(\frac{c}{\omega}\right)^2 \hat{\varepsilon}\mathbf{E}_0, \tag{1.1}$$

where $\hat{\varepsilon}$ is the electric permittivity tensor of the considered metamaterial and $\mathbf{k}$ is a complex wavevector.

For the vector directions shown in Fig. 1.1, (1.1) takes the form

$$\begin{aligned}
&\left[\left(\frac{c}{\omega}\right)^2 k^2 - \varepsilon_{xx} + \frac{\varepsilon_{xy}\varepsilon_{yx}}{\varepsilon_{yy}}\right]E_x - \left(\varepsilon_{xz} - \frac{\varepsilon_{xy}\varepsilon_{yz}}{\varepsilon_{yy}}\right)E_z = 0,\\
&-\left(\varepsilon_{zx} - \frac{\varepsilon_{zy}\varepsilon_{yx}}{\varepsilon_{yy}}\right)E_x + \left[\left(\frac{c}{\omega}\right)^2 k^2 - \varepsilon_{zz} + \frac{\varepsilon_{zy}\varepsilon_{yz}}{\varepsilon_{yy}}\right]E_z = 0.
\end{aligned} \tag{1.2}$$

These equations have a solution only if their determinant vanishes. This gives the following values for the wavevectors $k_\pm$:

$$\begin{aligned}
N_\pm^2 &\equiv \left(\frac{c}{\omega}\right)^2 k_\pm^2\\
&= \frac{1}{2}\left(\varepsilon_{xx} + \varepsilon_{zz} - \frac{\varepsilon_{zy}\varepsilon_{yz}}{\varepsilon_{yy}} - \frac{\varepsilon_{xy}\varepsilon_{yx}}{\varepsilon_{yy}}\right)\\
&\quad \pm \left[\frac{1}{4}\left(\varepsilon_{xx} + \varepsilon_{zz} - \frac{\varepsilon_{zy}\varepsilon_{yz}}{\varepsilon_{yy}} - \frac{\varepsilon_{xy}\varepsilon_{yx}}{\varepsilon_{yy}}\right)^2 - \left(\varepsilon_{xx} - \frac{\varepsilon_{xy}\varepsilon_{yx}}{\varepsilon_{yy}}\right)\left(\varepsilon_{zz} - \frac{\varepsilon_{zy}\varepsilon_{yz}}{\varepsilon_{yy}}\right)\right.\\
&\quad \left. + \left(\varepsilon_{xz} - \frac{\varepsilon_{xy}\varepsilon_{yx}}{\varepsilon_{yy}}\right)\left(\varepsilon_{zx} - \frac{\varepsilon_{zy}\varepsilon_{yx}}{\varepsilon_{yy}}\right)\right]^{1/2}.
\end{aligned} \tag{1.3}$$

Thus, there are four solutions to (1.1): two of them represent forward propagating waves with $k_\pm = \sqrt{N_\pm^2}\omega/c$ while the other two represent backward propagating waves with $k_\pm = -\sqrt{N_\pm^2}\omega/c$. Therefore, a plane-polarized wave normally incident

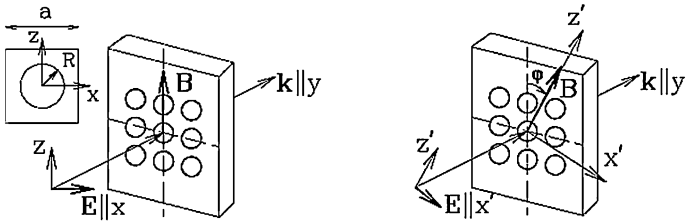

Fig. 1.1 (**a**) Schematic drawing of a metal film with a periodic array of holes. The coordinate axes x, y, and z are always directed along the principal axes of the simple square lattice, and the applied static magnetic field **B** always lies in the film plane. The incident light beam is normal to the film surface, i.e., the *ac* electric field **E** is parallel to the film plane, while the wavevector is normal to the film plane (i.e., $\boldsymbol{k} \parallel y$). Note that the *ac* magnetic field **H** of the light wave (**H**⊥**E**) is not important in our considerations and we omit it everywhere. Inset shows an $a \times a$ unit cell of the periodic composite film with a cylindrical hole of radius R at its center. (**b**) The same as in (**a**) but both **B** and the incident field **E** are rotated *together* in the film plane. Here we show the case of the transverse polarization $\mathbf{E} \parallel x' \perp \mathbf{B} \parallel z'$, denoted in the text as ⊥. The longitudinal polarization $\mathbf{E} \parallel \mathbf{B} \parallel z'$ is denoted in the text as ∥. After Ref. [10]

at the sample surface evolves into a refracted wave and a reflected wave. If $\varepsilon_{zy} = \varepsilon_{yz} = 0$, we have

$$N_{\pm}^2 \equiv \left(\frac{c}{\omega}\right)^2 k_{\pm}^2 = \frac{\varepsilon_{xx} + \varepsilon_{yy}}{2} \pm \sqrt{(\frac{\varepsilon_{xx} - \varepsilon_{yy}}{2})^2 \pm \varepsilon_{xy}\varepsilon_{yx}}. \tag{1.4}$$

The refracted beam becomes elliptically polarized with the major axis rotated by the (Faraday) angle [48–56] ϑ_F:

$$\vartheta_F \equiv \frac{1}{2}\left(\frac{\omega l}{c}\right) \mathrm{Re}(N_+ - N_-). \tag{1.5}$$

The expression for the *ellipticity* (the ratio of minor to major axis) e_F can be found in Refs. [48–56]. The reflected beam is also elliptically polarized with ellipticity e_K and the major axis rotated by an angle ϑ_K, similar to the refracted wave (see Refs. [48–56]).

When $\varepsilon_{xx} = \varepsilon_{yy}$ and $\varepsilon_{yx} = -\varepsilon_{xy}$, (1.1) and (1.4) are simplified to the form of right-handed and left-handed elliptically polarized waves $k^2 E_{0\pm} = (\omega/c)^2 \varepsilon_{\pm} E_{0\pm}$, and $N_{\pm}^2 = \varepsilon_{xx} \pm i\varepsilon_{xy}$, respectively. Here $E_{0\pm} = E_{0x} \pm i E_{0y}$, and $\varepsilon_{\pm} = \varepsilon_{xx} \pm i\varepsilon_{xy}$. Equation (1.5) then takes the form $\vartheta_F = \nu B l$, where B is the external applied magnetic field (in Tesla) in the direction of propagation, l is the length of the path (in meters) over which the light and the magnetic field interact, ν is the Verdet constant of the material.

In addition to the longitudinal or Faraday configuration, in which the wave propagates through the sample along the applied magnetic field **B**, there is also the so-called Voigt configuration, in which **B** is perpendicular to the direction of the wave propagation, $k \parallel y$ and $B \parallel z$. The latter case is convenient for demonstrating how important additional off-diagonal terms of the permittivity tensor can be in the case

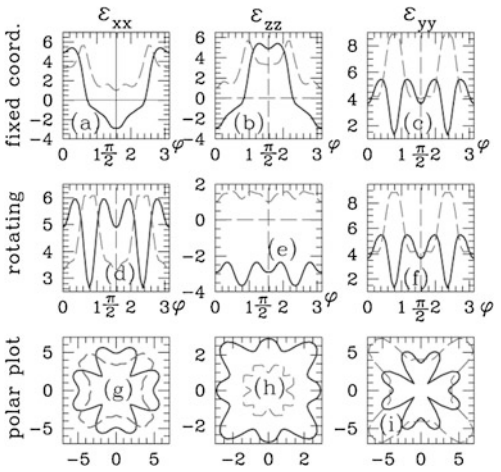

Fig. 1.2 Real (*solid lines*) and imaginary (*dashed lines*) parts of the diagonal components ε_{xx}, ε_{zz}, and ε_{yy} [in the fixed non-rotating (**a**)–(**c**) and rotating (**d**)–(**f**) coordinate systems] of the macroscopic permittivity tensor $\hat{\varepsilon}$ of the metamaterial, made of a simple-square array (with the lattice constant a) of cylindrical circular holes (of radius $R = 0.3a$) in the metallic film. (**a**)–(**c**) ε_{xx}, ε_{zz},and ε_{yy}, plotted vs. the rotation angle ϕ of Fig. 1.1(b), but where these components are taken along the *fixed* coordinates x, y, z of Figs. 1.1(a) and (b). (**d**)–(**f**) Similar to panels (**a**)–(**c**), but now the components of $\hat{\varepsilon}$ are taken along the *rotating* coordinates x', y, z' of Fig. 1.1(b). (**g**)–(**i**) polar plots of (**d**)–(**f**). The permittivity tensor is taken in the quasi-static approximation $\hat{\varepsilon} = \hat{\varepsilon}_0 + i4\pi\hat{\sigma}/\omega$, where $\hat{\sigma}$ is the conductivity tensor of the metal taken in the Drude form with the plasma frequency ω_p and the electron relaxation time τ is such that $\omega_p\tau = 20$. The light frequency is $\omega = 0.4\omega_p$

of metamaterials and why the formulas for MO effects should be expressed in a general form.

If **B** has an arbitrary direction with respect to the lattice axes of the metamaterial, all components of the permittivity tensor can be nonzero [7–12]. When both **B** and **E** are rotated in the film plane, the angular profiles of $\hat{\varepsilon}$ and the optical transmission coefficients $T_\perp$ and $T_\parallel$ are anisotropic (see Ref. [10]). The angular profiles of the diagonal components ε_{xx}, ε_{yy}, ε_{zz}, and the off-diagonal tensor components ε_{xy}, ε_{xz}, ε_{yx}, ε_{yz}, ε_{zx}, and ε_{zy} in non-rotating and rotating coordinate systems are shown in Figs. 1.2 and 1.3. The general expressions for the Faraday rotation and Voigt effect are cumbersome [57]. However, when $\mathbf{B} \parallel z$ is directed along the main lattice axes, some of the permittivity tensor components vanish ($\varepsilon_{xz} = \varepsilon_{yz} = \varepsilon_{zx} = \varepsilon_{zy} = 0$) and general formulas simplify. Equation (1.3) then takes the form

$$N_\perp^2 \equiv \left(\frac{\omega}{c}\right)^2 k_\perp^2 = \varepsilon_{xx} - \frac{\varepsilon_{xy}\varepsilon_{yx}}{\varepsilon_{yy}}, \quad \text{for } E \perp B,$$
$$N_\parallel^2 \equiv \left(\frac{\omega}{c}\right)^2 k_\parallel^2 = \varepsilon_{zz}, \quad \text{for } E \parallel B. \tag{1.6}$$

The Voigt effect, which is also known as the Cotton–Mouton effect, is magnetic birefringence. It is caused by the difference between the transverse, $n_\perp$, and longi-

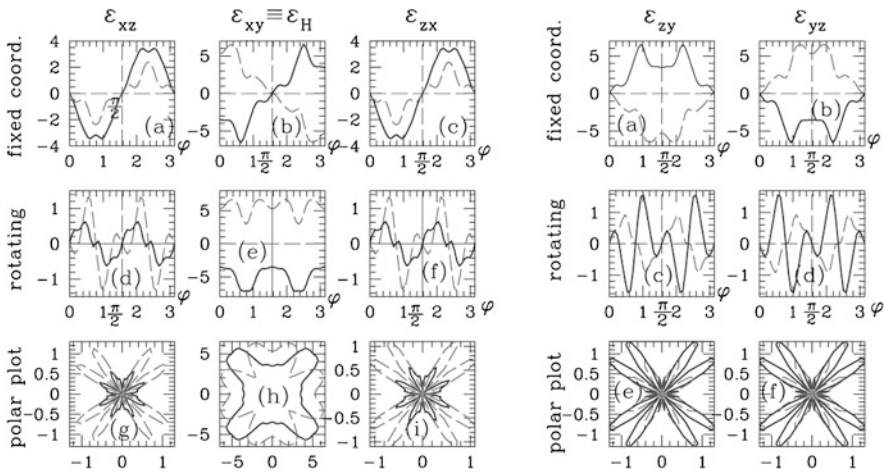

Fig. 1.3 The *left part* is similar to Fig. 1.2, with the off-diagonal components, ε_{xz}, $\varepsilon_{xy}\equiv\varepsilon_H$, and ε_{zx}, taken in fixed non-rotating (**a**)–(**c**) and rotating (**d**)–(**f**) coordinate systems. The component $\varepsilon_{xy}\equiv\varepsilon_H$ of the permittivity tensor is the Hall component. In the polar plots (**g**)–(**i**), the absolute values of the above quantities are shown. The *right part* is similar to the left part, but for the off-diagonal components, ε_{zy}, and ε_{yz}

tudinal, $n_\parallel$, components of $N_{\perp,\parallel}=n_{\perp,\parallel}+i\kappa_{\perp,\parallel}$, where κ is the *absorption index*. The Voigt phase shift δ is given by

$$\delta=\frac{\omega l}{c}(n_\parallel-n_\perp), \tag{1.7}$$

where l is the length of the path.

Assuming that $\omega l/c\sim 1$ and using (1.7) and values of the permittivity tensor $\hat{\varepsilon}$ components shown in Figs. 1.2 and 1.3, we can estimate and compare the values of δ in the (001)- and (011)-directions when $\varepsilon_{xz}=\varepsilon_{yz}=\varepsilon_{zx}=\varepsilon_{zy}=0$. For arbitrary directions, (1.7) would have a much more complicated form. For the values of $\hat{\varepsilon}$ shown in Figs. 1.2 and 1.3, $\delta\sim-0.03$ in the (001)-direction, while in the (011)-direction, $\delta\sim 0.02$. Thus, it is possible to observe the magneto-induced angular anisotropy of δ in periodic metamaterials. The angular anisotropy of other MO effects can be considered similarly.

1.3 Longitudinal Configuration: Enhancement of Magneto-Optical Effects in Gyrotropic Photonic Metamaterials

In order to be consistent with our previous publications [4, 58–61], for the further consideration we denote diagonal and off-diagonal components of the permittivity tensor as ε and g, respectively. For the longitudinal configuration, when the wave

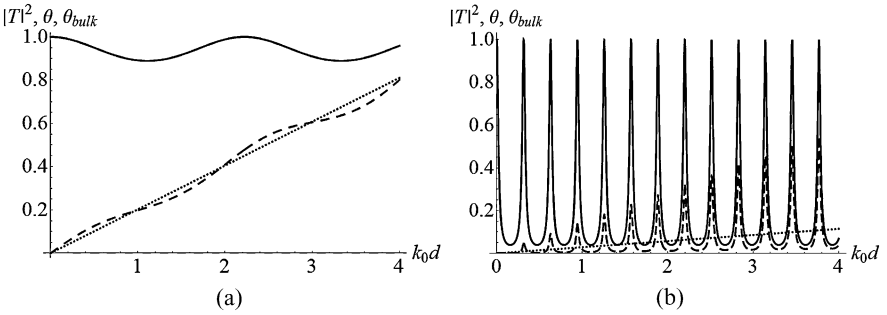

Fig. 1.4 The transmission (*solid lines*), the angle of rotation of the polarization plane ϑ by a slab (*dashed lines*), and the bulk angle of rotation ϑ_{bulk} (*dotted lines*) as a function of frequency k_0 normalized by the thickness of layer d for the parameters (**a**) $\varepsilon = 2$, $g = 0.01$ and (**b**) $\varepsilon = 100$, $g = 0.07$. The external medium is vacuum

travels along the direction of the static magnetic field, (1.5) and (1.6) for the angle of rotation due to smallness of g may be expressed as (see for review [41, 62] and references therein)

$$\vartheta_{\text{bulk}} = \frac{1}{2}\frac{\omega}{c} d(\sqrt{\varepsilon + g} - \sqrt{\varepsilon - g}) \approx \frac{1}{2}\frac{\omega}{c} d\sqrt{\varepsilon}\frac{g}{\varepsilon} = \frac{g}{2\varepsilon} k_{\text{MO}} d_{\text{MO}}, \tag{1.8}$$

where d_{MO} is the light path, $k_{\text{MO}} = k_0\sqrt{\varepsilon}$, and $k_0 = \omega/c$ is the free space wavenumber.

Let us continue with the consideration of the Faraday effect observed in a single homogeneous layer. This example clearly shows the difference between Faraday effects in bulk and bounded systems.

If the magnetized slab has permittivity of the order of unity, the reflected wave is weak, and the Faraday effect is close to its bulk value (see Fig. 1.4(a)). In the case of high permittivity, multiple reflections inside the slab cause sharp Fabry–Pérot resonances in the transmission at the frequencies $\omega_n/c = \pi n/d\sqrt{\varepsilon}$ (where n is an integer). The reflections also modify the Faraday rotation, which is enhanced in the vicinity of resonances and suppressed far from them (see Fig. 1.4(b)).

When the slab is magnetized, the waves with left and right circular polarizations have slightly different wavenumbers. As a result, the transmission maxima are observed at different frequencies

$$\frac{\omega_r^{\pm}}{c} = \frac{\pi n}{d\sqrt{\varepsilon \pm g}}, \tag{1.9}$$

where "+" and "−" indicate right and left polarizations, respectively. A splitting of the circular polarizations similar to (1.9) appears in the case of normal incidence for any multilayered structure, containing MO layers and producing a resonance (see the next section). The enhancement of the Faraday effect is due to general properties of the resonance; therefore, below a general case is considered.

The frequency dependences of phase $\phi(k_0)$ and transmittance $T(k_0)$ near a MO-split resonance for the right and left polarizations are shown in Fig. 1.5 by the dashed

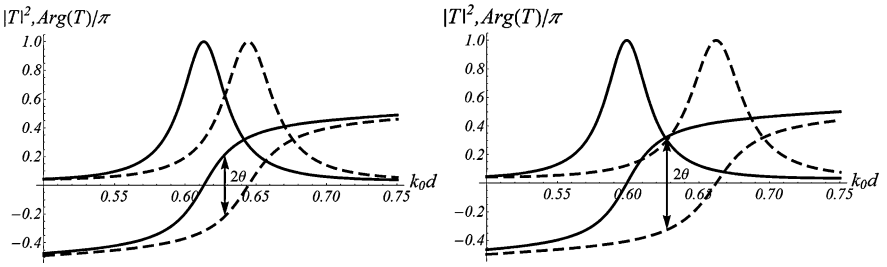

Fig. 1.5 The amplitude and the argument of the transmission coefficient for the case of nonzero magnetization. (**a**) $\varepsilon = 100$, $g = 5$, and (**b**) $\varepsilon = 100$, $g = 10$. The value of g is taken large enough to make the splitting visible

and solid lines, respectively. Disregarding the deformation of curves, one can express these dependences for the left and right circular polarizations as

$$\begin{aligned} &\varphi^+(\omega) = \varphi(\omega + 0.5\Delta\omega_r) \quad \text{and} \quad \varphi^-(\omega) = \varphi(\omega - 0.5\Delta\omega_r), \\ &\left|T^+(\omega)\right|^2 = \left|T(\omega + 0.5\Delta\omega_r)\right|^2 \quad \text{and} \quad \left|T^-(\omega)\right|^2 = \left|T(\omega - 0.5\Delta\omega_r)\right|^2, \end{aligned} \tag{1.10}$$

where $\varphi(\omega)$, $|T(\omega)|^2$ are the dependences at zero magnetization, $\Delta\omega_r = \omega_r^+ - \omega_r^-$. The angle of the Faraday rotation is equal to [41]

$$\vartheta = 0.5\big(\varphi^+(\omega) - \varphi^-(\omega)\big). \tag{1.11}$$

It is obvious from Fig. 1.5 that the enhancement is due to the fast growth of the phase, which changes by π on the scale of the resonant line width. Note that instead of the small bulk value (1.8) one can obtain the Faraday angle of the order of $\pi/2$, which follows from the fact that the phase changes by π in the vicinity of any resonance and from the formula (1.11).

The transmitted wave is linearly polarized at the frequency ω^*, defined by the condition

$$\left|T^+\big(\omega^*\big)\right|^2 = \left|T^-\big(\omega^*\big)\right|^2 \tag{1.12}$$

(we imply that the incident wave is linearly polarized). Taking into account a single resonance only, the value of ω^* is evaluated as

$$\omega^* = 0.5\big(\omega_r^- + \omega_r^+\big) = \omega_r, \tag{1.13}$$

i.e., ω^* is equal to the resonant frequency of non-magnetized system.

It is essential that the enhancement of the Faraday rotation is observed when the condition (1.13) is fulfilled, or, at least, the frequency lies between the split resonance frequencies. Suppose that the Q-factors of "+" and "−" resonances significantly differ (Fig. 1.6). There exist two points satisfying the condition (1.12). The number of paths the light makes traveling through the system is the same but the Faraday rotation is different. Comparison of Figs. 1.5 and 1.6 shows that it is important that $\omega_r^+ < \omega^* < \omega_r^-$.

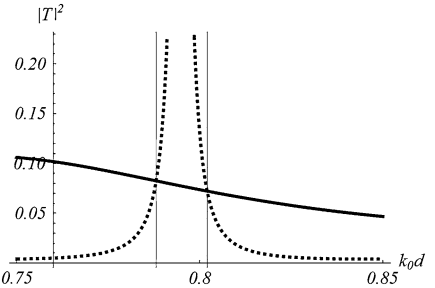

Fig. 1.6 Two resonances for different Q-factors

The smaller the MO splitting the higher transmittance (1.12) and smaller the Faraday rotation (Figs. 1.5(a) and (b)). It can be shown (see [36] and Appendix A) that

$$T = T_0 \cos^2 \vartheta \tag{1.14}$$

where T_0 is a transmittance at zero magnetization. When ϑ increases, the rotation angle saturates at the value of $\pi/2$. At the same time, the amplitude of the transmitted wave tends to zero.

Usually, the splitting $\Delta\omega_r$ is much smaller than the resonance width. Then the Faraday rotation angle, according to (1.10) and (1.11), can be estimated as

$$\begin{aligned}\vartheta(\omega_r) &= \frac{1}{2}\left[\varphi\left(\omega_r^- + \Delta\omega_r/2\right) - \varphi\left(\omega_r^+ - \Delta\omega_r/2\right)\right] \approx \frac{1}{2}\left.\frac{d\varphi(\omega)}{d\omega}\right|_{\omega=\omega_r} \Delta\omega_r \\ &= \left.\frac{d\varphi(\omega)}{d\omega}\right|_{\omega=\omega_r} \frac{\partial\omega_r}{\partial\varepsilon} g. \end{aligned} \tag{1.15}$$

According to (1.15), $\vartheta(\omega_r)$ is determined by three factors. The first one, $d\varphi(\omega)/d\omega|_{\omega=\omega_r}$, is equal to the inverse width of the resonance $1/\Gamma$ (see Appendix B). The second factor, $\partial\omega_r/\partial\varepsilon$, is the sensitivity of the resonance position to the value of the dielectric constant of the MO layers. Note that this parameter is not related to MO properties of the slab. If the structure is a uniform MO slab of the width d, one has

$$\omega_r = \frac{\pi n}{d\sqrt{\varepsilon}} \quad \text{and} \quad \frac{\partial\omega_r}{\partial\varepsilon} = -\omega_r \frac{1}{2\varepsilon},$$

from which we obtain

$$\vartheta \approx -\frac{1}{\Gamma}\omega_r \frac{g}{2\varepsilon} = -Q\frac{g}{\varepsilon} \tag{1.16}$$

where $\omega_r/2\Gamma = Q$ is the Q-factor of the resonance. In the general case of arbitrary multilayer structure, (1.16) can be rewritten as

$$\vartheta \approx \frac{1}{\Gamma}\omega_r \frac{g}{\varepsilon}\frac{\partial \ln\omega_r}{\partial \ln\varepsilon} = Q\frac{g}{\varepsilon}2\frac{\partial \ln\omega_r}{\partial \ln\varepsilon}, \tag{1.17}$$

where the derivative corresponds to the shift of the resonance frequency with the change of the permittivity of the MO layers. One can show that

$$-\frac{1}{2} \le \frac{\partial \ln\omega_r}{\partial \ln\varepsilon} \le 0.$$

For closed resonators (with infinite Q-factor) the shift of the resonance frequency with the change of permittivity is determined by the expression [63]:

$$\frac{\partial \ln \omega_r}{\partial \ln \varepsilon} \approx -\frac{1}{2} \frac{\int_{\mathrm{MO}} \varepsilon |E|^2 \, dz}{\int_{\mathrm{res}} \varepsilon |E|^2 \, dz} \tag{1.18}$$

where the integrals in the numerator and the denominator are calculated over the MO layers (their permittivity changes) and over the whole resonance structure, respectively. The latter expression can approximately be applied to a high-Q cavity, such as a finite PC with defect. According to (1.18), the value of $-2\frac{\partial \ln \omega_r}{\partial \ln \varepsilon}$ is approximately equal to the fraction of the energy of the electric field localized in the MO layers. The numerical calculations for the optical Tamm state give $\frac{\partial \ln \omega_r}{\partial \ln \varepsilon} = -0.1786$, which is close to the value given by (1.18)

$$-\frac{1}{2} \frac{\int_{\mathrm{MO}} \varepsilon |E|^2 \, dz}{\int_{\mathrm{res}} \varepsilon |E|^2 \, dz} = -0.1793.$$

Thus, we obtain a simple expression for the resonantly enhanced Faraday rotation:

$$\vartheta \approx -Q W \frac{g}{\varepsilon}, \tag{1.19}$$

where

$$W = \frac{\int_{\mathrm{MO}} \varepsilon |E|^2 \, dz}{\int_{\mathrm{res}} \varepsilon |E|^2 \, dz}$$

is the confinement factor [64] and Q is the quality factor of the resonance. It follows from (1.19) that the rotation angle depends not only on the relative concentration of the electric field in MO layers, but also on the total quality factor of the resonance structure. In particular, some decrease in $|\frac{\partial \ln \omega_r}{\partial \ln \varepsilon}|$ can be justified by significant increase in Q. This is the case when multilayered structures are used instead of a single homogeneous MO layer.

1.4 Employing Magnetophotonic Crystals to Enhance the Faraday Effect

Enhancement of the Faraday effect requires a high Q-factor. In the case of a single homogeneous MO layer, in order to achieve a high Q-factor, it is necessary to have an exceedingly large permittivity value. Therefore, more complicated structures should be used, e.g., photonic crystals with defects [35, 65], coupled photonic crystals with optical Tamm states [5, 6, 16], random systems [44], etc.

The simplest structure is a MO layer (defect) placed inside of a bounded PC sample. The working frequency is placed inside the PC's bandgap. If considering two pieces of PC sandwiching the MO-defect as dielectric mirrors, the structure looks like a common Fabry–Pérot resonator, where the resonant frequency is equal to the frequency of the defect mode [66] localized at the defect.

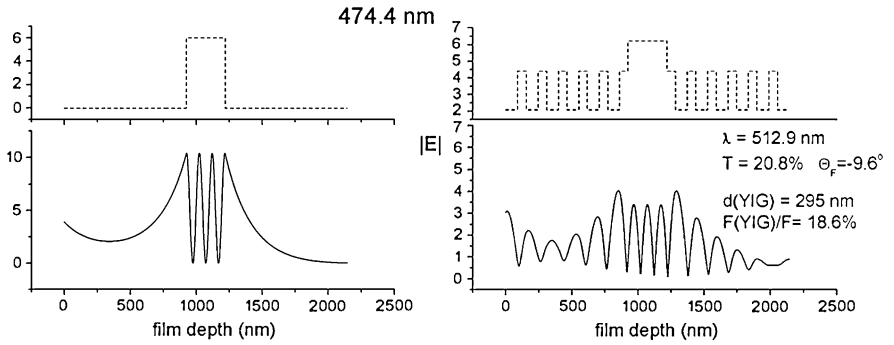

Fig. 1.7 Permittivity (*top figures*) and field distribution (*bottom figures*) in a cavity with (**a**) homogeneous (low-permittivity) mirrors and (**b**) layered mirrors (a PC with bandgap)

The benefits of employing a MPC instead of metallic mirrors originate from possibility of increasing the Q-factor by the redistribution of the light energy from materials with losses into low loss materials [6]. Due to the complicated structure of the Bloch wave, an exponential decay in the bandgap happens only on average. Locally, the field may achieve high values (Fig. 1.7). Thus, a significant part of the energy may be concentrated in low-loss dielectric mirrors instead of lossy defect. This leads to increase of the Q-factor.

Instead of the defect mode one can use the surface Tamm state appearing in between two PCs. In this case, there is no cavity, and the field is located inside the PC-mirrors, incorporating MO layers.

The Faraday rotation can be enhanced by employing the Borrmann effect [64]. This effect is related to the fact that for a frequency of band edge, the Bloch wave is a standing wave whose maxima lie either in the higher- or in the lower-permittivity layers [67]. In such a way, the energy of the electric field can be concentrated in the MO layers, thereby increasing the confinement factor W.

Using a single resonance, one can obtain any value of the Faraday rotation angle up to 90°. However, it is accompanied by inevitable decrease in the signal amplitude (see (1.14) and [36]). Using two resonances [36], one can have the 90° Faraday rotation at $T = 1$, overcoming the limit, expressed by (1.14). So, let us now consider the case when the splitting of the resonance Δk_r is equal to the distance between neighboring resonances. This can be achieved either by using a structure with two defects [36, 37], or by choosing a defect-free MPC with sufficiently large number of layers. In this case, the resonances of different orders, $T_n^+(k_0)$ and $T_{n-1}^-(k_0)$, overlap, as shown in Fig. 1.8(a). Since each resonance causes a change of the phase by π, the phase difference between two polarizations is also π (see Fig. 1.8(b) and 7 at $k_0 L = 11.58$). Thus, the angle of the Faraday rotation is equal to $\pi/2$, whereas the coincidence of resonances for both polarizations leads to transmission equal to unity (Fig. 1.9).

For a practical realization of this situation with existing MO materials, different resonances must be close to each other. This can be achieved by increasing the number of layers in a PC and using a wavenumber that is close to a bandedge. The

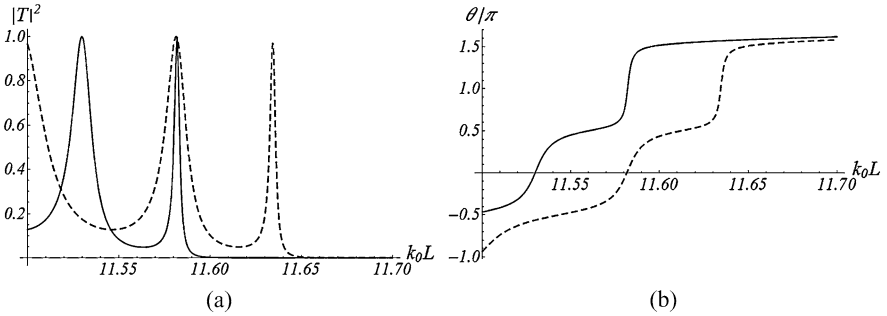

Fig. 1.8 The transmission coefficient (**a**) and the phase shift (**b**) in the case when resonances of different order coincide. *Solid* and *dashed lines* correspond to the right and left polarizations, respectively. The elementary cell of the PC consists of two layers with parameters $\varepsilon_1 = 1$, $d_1 = 0.1$ μm, $\varepsilon_2 = 2$, $g = 0.01$, and $d_2 = 0.1$ μm. The total number of layers is 58

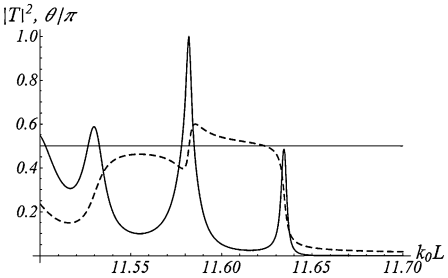

Fig. 1.9 The transmission (*solid line*) and the angle of rotation of the polarization plane (*dashed line*) for a sample with parameters described in Fig. 1.8

density of the resonances is proportional to the density of states (inversely proportional to the group velocity) that has a maximum at the bandedge. An increase in the number of layers allows one to make the density of states arbitrarily large. This makes the transmission resonances dense enough.

To conclude it is worth mentioning some systems, employing plasmon resonance for enhancement of the Faraday effect. In these systems, the property of surface plasmon to have given (*TM*) polarization is used [68, 69]. The obliquely incident *TE*-polarized wave in the frustrated total internal reflection geometry (Fig. 1.10(a)) does not excite a surface plasmon at the metal/dielectric interface, if the magnetization is zero. However, in the presence of magnetization, there arises an interaction between the *TE* and *TM* polarizations, and the generation of *TM*-polarized surface plasmon enhances the cross-polarization. Thus, the scheme in Fig. 1.10(a) transforms a *TE*-polarized wave into *TM*-polarized wave producing an effective rotation of the polarization plane by $\pi/2$. At the same time, the intensity of the transmitted wave is low. The effectiveness of the plasmonic scheme can be compared to the one of the usual schemes, discussed above, by calculating the cross-polarization intensity in the usual schemes. It is easy to see from (1.12) that in the usual scheme the cross-polarization intensity, which is proportional to the square of ϑ, grows with the quality factor as Q^2. In the plasmonic scheme, it depends on Q logarithmically, which in fact reduces the enhancement to nothing. The reason for such dependence

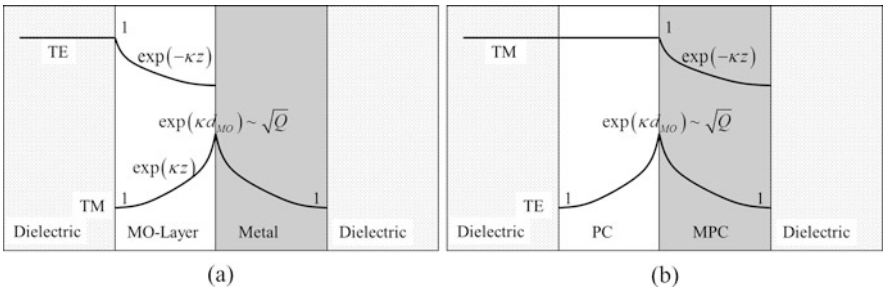

Fig. 1.10 Plasmonic enhancement of the Faraday rotation. (**a**) The original scheme [68], providing the logarithmic in Q-factor enhancement of the cross-polarization intensity. (**b**) Modified scheme providing the linear in Q-factor enhancement of the cross-polarization intensity (the Bloch wave envelope is shown)

is the weak interaction between the incident wave and the one having the perpendicular polarization. This interaction is proportional to the overlap of the *TE*- and *TM*-polarized fields in the MO layer (Fig. 1.10(a)).

The overlap can be increased, if the surface wave at the PC/MPC interface (Fig. 1.10(b)) is used instead of the surface plasmon at the interface of the homogeneous medium. In this case, the wave of *TM* polarization should reach the PC/MPC interface without decay, and only in the MPC it should become evanescent due to the bandgap. MO layers create the cross-(*TE*) polarization, which decays in both the PC and MPC due to the bandgap. The conditions for existence of the *TE*-polarized surface wave at the PC/MPC interface should be satisfied, which results in the cross-polarization enhancement. It turns out that all these conditions are easily satisfied if: (1) the angle of incidence ensures the Brewster condition for the layers of the PC; (2) all the layers are quarter-wavelength ones at the given angle. The overlap of the fields in the MO layers (Fig. 1.10(b)) is now increased, leading to the cross-polarization intensity being proportional to the Q-factor. However, even this scheme is not as good as the usual one, working at normal incidence. The reason is that the resonance in the usual schemes amplifies not only the cross-polarization, but also the incident one. Since the cross-polarization is created by the incident wave, it undergoes quadratic in Q amplification. The schemes amplifying only the cross-polarization cannot give more than a linear dependence.

1.5 Conclusions

In this chapter, we develop a general approach for considering structures used for the Faraday effect enhancement. These structures can be considered as open resonators in which bulk MO properties remove the degeneracy with respect to the polarization and split the resonance frequencies. At the frequency in-between the frequencies of the split resonance, a large rotation of the polarization plane can be observed. This rotation is due to the rapid change of the phase of the transmitted wave by a value

of π when the frequency of the incident wave crosses the resonance. Indeed, at these frequencies, the phase of the red shifted wave gains a value of the order of π, while the phase of the blue shifted wave hardly changes. When the splitting is much smaller than the resonance width, the Faraday rotation is shown to be a product of the resonance Q-factor, confinement factor and the MO factor.

Appendix A: Relationship Between the Transmission Coefficient and the Faraday Rotation Angle

We assume that the distance between a given resonance and other ones is much larger than the resonance width. In principle, if the resonance has a large Q-factor, a small magnetization is sufficient for obtaining the required value of splitting of resonances. But, irrespective of the Q-factor, one obtains the same dependence of the transmission coefficient $|T|^2$ on the Faraday rotation angle ϑ (Fig. 1.11). This is due to the fact that the frequency range in the vicinity of the resonance, at which the amplitude, $|T|^2$, and the phase, $\arg T$, change significantly, is the same for both these quantities. More precisely, for $T(k_0) = \frac{\alpha}{k_0 - \tilde{k}_0}$ with a real frequency, k_0, and complex values of residue, α, and the pole position, $\tilde{k}_0 = k_r - i\Gamma$, one can obtain the expression $|T|^2 = T_0^2 \cos^2 \vartheta$ (T_0^2 is the resonant transmission), which is independent of the Q-factor. Indeed, designating a deviation of the frequency from the resonant one as $\delta k_0 = k_0 - k_r$, one has $T(\delta k_0) = \frac{\alpha}{\delta k_0 + i\Gamma}$ and

$$\left|T(\delta k_0)\right|^2 = \frac{|\alpha|^2}{\delta k_0^2 + \Gamma^2}. \tag{1.20}$$

Presuming that the presence of the magnetization shifts the peak without changing its form, one obtains $\vartheta = (\arg T(\delta k_0) - \arg T(-\delta k_0))/2$, from which it follows that

$$\tan \vartheta = -\frac{\delta k_0}{\Gamma}. \tag{1.21}$$

Eliminating δk_0 from expressions (1.20) and (1.21), one obtains $|T|^2 = \frac{|\alpha|^2}{\Gamma^2} \cos^2 \vartheta$. After denoting the transmission at the resonance as $T_0^2 = \frac{|\alpha|^2}{\Gamma^2}$, the required result arises:

$$|T|^2 = T_0^2 \cos^2 \vartheta. \tag{1.22}$$

The comparison between the one-resonance model system meeting condition (1.22) and results obtained from calculations of the Tamm state (Fig. 1.11) shows that a difference appears when the frequency moves away from the resonance, to the region in which the resonances next to the Tamm state become visible.

From this analysis one can conclude that for any lossless system with separated resonances, a large rotation angle is possible only for a small transmission, and their mutual dependence is the same for any Q-factor. A large Q-factor is needed only for obtaining the desirable value of splitting of peaks which is equal to $2\delta k_0$.

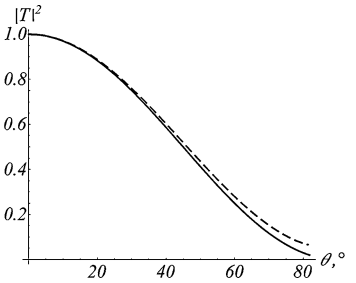

Fig. 1.11 Universal dependence of the transmission coefficient on the Faraday rotation angle for a single pole (*solid line*) and the same dependence for the optical Tamm state resonance (*dashed line*). The deviation is caused by resonances neighboring to the Tamm state

Appendix B: Rate of the Phase Change at the Resonance Frequency

In this appendix we show that at the resonance, the absolute value of the quantity $d\varphi/d\omega|_{\omega=\omega_r}$ in (1.15), is equal to the inverse width of the resonance. Near the resonance, the transfer function can be approximated as

$$T(\omega) = \frac{\alpha}{\omega - \omega_r - i\Gamma},$$

where ω_r and Γ are the frequency and the half-width of the resonance, respectively. By differentiating the relation $T(\omega) = |T(\omega)| \exp(i\varphi(\omega))$, one obtains

$$\frac{\partial\varphi}{\partial\omega} = \frac{i}{|T|}\frac{\partial|T|}{\partial\omega} - \frac{i}{T}\frac{\partial T}{\partial\omega}.$$

Calculating derivatives

$$\frac{\partial|T|}{\partial\omega} = \frac{\partial}{\partial k}\frac{|\alpha|}{\sqrt{(\omega-\omega_r)^2+\Gamma^2}} = -|T|\frac{\omega-\omega_r}{(\omega-\omega_r)^2+\Gamma^2}$$

and

$$\frac{\partial T}{\partial\omega} = -\frac{T}{\omega-\omega_r-i\Gamma},$$

we find

$$\frac{\partial\varphi}{\partial\omega} = -\frac{\Gamma}{(\omega-\omega_r)^2+\Gamma^2}.$$

It immediately follows that at the resonance

$$\frac{d\varphi(\omega)}{d\omega} = -\frac{1}{\Gamma}.$$

References

1. H. Raether, *Surface Plasmons on Smooth and Rough Surfaces and on Gratings* (Springer, Berlin, 1988)

2. T.W. Ebbesen, H.J. Lezec, H.F. Ghaemi, T. Thio, P.A. Wolff, Nature **391**, 667–669 (1998)
3. C. Genet, T.W. Ebbesen, Nature **445**, 39–46 (2007)
4. T. Goto, A.V. Dorofeenko, A.M. Merzlikin, A.V. Baryshev, A.P. Vinogradov, M. Inoue, A.A. Lisyansky, A.B. Granovsky, Phys. Rev. Lett. **101**, 113902 (2008)
5. A.P. Vinogradov, A.V. Dorofeenko, S.G. Erokhin, M. Inoue, A.A. Lisyansky, A.M. Merzlikin, A.B. Granovsky, Phys. Rev. B **74**, 045128 (2006)
6. A.P. Vinogradov, S.G. Erokhin, A. Granovsky, M. Inoue, J. Commun. Technol. Electron. **49**, 88 (2004)
7. D.J. Bergman, Y.M. Strelniker, Phys. Rev. Lett. **80**, 857–860 (1998)
8. Y. Fleger, M. Rosenbluh, Y.M. Strelniker, D.J. Bergman, A.N. Lagarkov, Eur. Phys. J. B **81**, 85–93 (2011)
9. Y.M. Strelniker, Phys. Rev. B **76**, 085409 (2007)
10. Y.M. Strelniker, D.J. Bergman, Phys. Rev. B **59**, R12763–R12766 (1999)
11. Y.M. Strelniker, D.J. Bergman, Phys. Rev. B **77**, 205113 (2008)
12. Y.M. Strelniker, D. Stroud, A.O. Voznesenskaya, Eur. Phys. J. B **52**, 1–7 (2006)
13. N. Ou, J.H. Shyu, J.C. Wu, T.H. Wu, IEEE Trans. Magn. **45**, 4027–4029 (2009)
14. S. Erokhin, L. Deych, A. Lisyansky, A. Granovsky, Tech. Phys. Lett. **35**, 785–788 (2009)
15. A. Merzlikin, A. Vinogradov, M. Inoue, A. Granovsky, Phys. Solid State **50**, 873–877 (2008)
16. A.M. Merzlikin, A.P. Vinogradov, A.V. Dorofeenko, M. Inoue, M. Levy, A.B. Granovsky, Physica B, Condens. Matter **394**, 277–280 (2007)
17. A.M. Merzlikin, A.P. Vinogradov, M. Inoue, A.B. Khanikaev, A.B. Granovsky, J. Magn. Magn. Mater. **300**, 108–111 (2006)
18. V. Belotelov, D. Bykov, L. Doskolovich, A. Kalish, A. Zvezdin, Phys. Solid State **51**, 1656–1662 (2009)
19. V.I. Belotelov, L.L. Doskolovich, V.A. Kotov, E.A. Bezus, D.A. Bykov, A.K. Zvezdin, Opt. Commun. **278**, 104–109 (2007)
20. A.B. Khanikaev, A.V. Baryshev, A.A. Fedyanin, A.B. Granovsky, M. Inoue, Opt. Express **15**, 6612–6622 (2007)
21. V.G. Kravets, A.S. Lapchuk, Appl. Opt. **49**, 5013–5019 (2010)
22. A. García-Martín, G. Armelles, S. Pereira, Phys. Rev. B **71**, 205116 (2005)
23. B. Sepúlveda, L.M. Lechuga, G. Armelles, J. Lightwave Technol. **24**, 945 (2006)
24. L.E. Helseth, Phys. Rev. B **72**, 033409 (2005)
25. A. Battula, S. Chen, Y. Lu, R.J. Knize, K. Reinhardt, Opt. Lett. **32**, 2692–2694 (2007)
26. G.A. Wurtz, W. Hendren, R. Pollard, R. Atkinson, L.L. Guyader, A. Kirilyuk, R. Th, I.I. Smolyaninov, A.V. Zayats, New J. Phys. **10**, 105012 (2008)
27. G. Armelles, J.B. González-Díaz, A. García-Martín, J.M. García-Martín, A. Cebollada, M.U. González, S. Acimovic, J. Cesario, R. Quidant, G. Badenes, Opt. Express **16**, 16104–16112 (2008)
28. J. Han, A. Lakhtakia, Z. Tian, X. Lu, W. Zhang, Opt. Lett. **34**, 1465–1467 (2009)
29. R. Zhou, H. Li, B. Zhou, L. Wu, X. Liu, Y. Gao, Solid State Commun. **149**, 657–661 (2009)
30. J.H. Kang, Q.H. Park, D.S. Kim, J. Korean Phys. Soc. **55**, 1295 (2009)
31. B. Hu, B.-Y. Gu, Y. Zhang, M. Liu, Appl. Phys. Lett. **95**, 121103 (2009)
32. C. Clavero, K. Yang, J.R. Skuza, R.A. Lukaszew, Opt. Express **18**, 7743–7752 (2010)
33. D.M. Newman, M.L. Wears, R.J. Matelon, Europhys. Lett. **68**, 692 (2004)
34. M. Kohmoto, B. Sutherland, K. Iguchi, Phys. Rev. Lett. **58**, 2436–2438 (1987)
35. M. Inoue, T. Fujii, J. Appl. Phys. **81**, 5659–5661 (1997)
36. M.J. Steel, M. Levy, R.M. Osgood, J. Lightwave Technol. **18**, 1297 (2000)
37. S. Sakaguchi, N. Sugimoto, J. Lightwave Technol. **17**, 1087–1092 (1999)
38. H. Shimizu, M. Miyamura, M. Tanaka, Appl. Phys. Lett. **78**, 1523–1525 (2001)
39. H. Kato, T. Matsushita, A. Takayama, M. Egawa, K. Nishimura, M. Inoue, J. Appl. Phys. **93**, 3906–3911 (2003)
40. M. Inoue, K. Arai, T. Fujii, M. Abe, J. Appl. Phys. **85**, 5768–5770 (1999)
41. A.K. Zvezdin, V.A. Kotov, *Modern Magnetooptics and Magnetooptical Materials* (IOP, Bristol, 1997)

42. S. Visnovsky, V. Prosser, R. Krishnan, J. Appl. Phys. **49**, 403–408 (1978)
43. G.S. Krinchik, O.B. Esikova, A.A. Kostyurin, Opt. Spectrosc. **44**, 471–472 (1978)
44. M. Inoue, K. Arai, T. Fujii, M. Abe, J. Appl. Phys. **83**, 6768–6770 (1998)
45. E. Takeda, N. Todoroki, Y. Kitamoto, M. Abe, M. Inoue, T. Fujii, K. Arai, J. Appl. Phys. **87**, 6782–6784 (2000)
46. A.K. Zvezdin, V.I. Belotelov, Eur. Phys. J. B **37**, 479–487 (2004)
47. V.I. Belotelov, L.L. Doskolovich, A.K. Zvezdin, Phys. Rev. Lett. **98**, 077401 (2007)
48. S.D. Smith, in *Light and Matter, Ia, Encyclopedia of Physics*, ed. by L. Genzel (Springer, Berlin, 1967)
49. P.N. Argyres, Phys. Rev. **97**, 334–345 (1955)
50. R. Stevenson, Can. J. Phys. **38**, 941–944 (1960)
51. J.G. Mavroides, in *Properties of Solids*, ed. by F. Abeles (North-Holland, Amsterdam, 1972)
52. F. Abeles, in *Properties of Solids*, ed. by F. Abeles (North-Holland, Amsterdam, 1972)
53. W.J. Tabor, F.S. Chen, J. Appl. Phys. **40**, 2760–2765 (1969)
54. N. Saleh, S. Zukotynski, Phys. Status Solidi (b) **37**, 879–888 (1970)
55. S. Zukotynski, N. Saleh, Phys. Status Solidi (b) **36**, 593–599 (1969)
56. A.V. Sokolov, *Optical Properties of Metals* (Elsevier, New York, 1967)
57. Y.M. Strelniker, D.J. Bergman, A.P. Vinogradov, Physica B (2013, accepted for publication)
58. A.V. Dorofeenko, A.P. Vinogradov, A.M. Merzlikin, A.B. Granovsky, A.A. Lisyansky, Y.E. Lozovik, in *Proceedings of NMMM–21*, Moscow, June 28–July 4 (2009), pp. 206–208
59. S. Erokhin, A. Lisyansky, A. Merzlikin, A. Vinogradov, A. Granovsky, Phys. Solid State **52**, 65–69 (2010)
60. S.G. Erokhin, A.A. Lisyansky, A.M. Merzlikin, A.P. Vinogradov, A.B. Granovsky, Phys. Rev. B **77**, 233102 (2008)
61. T. Goto, A.V. Baryshev, M. Inoue, A.V. Dorofeenko, A.M. Merzlikin, A.P. Vinogradov, A.A. Lisyansky, A.B. Granovsky, Phys. Rev. B **79**, 125103 (2009)
62. J. Stöhr, H.C. Siegmann, *Magnetism: From Fundamentals to Nanoscale Dynamics* (Springer, Berlin, 2006)
63. L.D. Landau, E.M. Lifshitz, L.P. Pitaevskii, in *Electrodynamics of Continuous Media*, (Butterworth-Heinemann, Oxford, 1995)
64. A.P. Vinogradov, Y.E. Lozovik, A.M. Merzlikin, A.V. Dorofeenko, I. Vitebskiy, A. Figotin, A.B. Granovsky, A.A. Lisyansky, Phys. Rev. B **80**, 235106 (2009)
65. M. Inoue, R. Fujikawa, A. Baryshev, A. Khanikaev, P.B. Lim, H. Uchida, O. Aktsipetrov, A. Fedyanin, T. Murzina, A. Granovsky, J. Phys. D, Appl. Phys. **39**, R151 (2006)
66. A. Figotin, V. Gorentsveig, Phys. Rev. B **58**, 180–188 (1998)
67. J.D. Joannopoulos, S.G. Johnson, J.N. Winn, R.D. Meade, *Photonic Crystals: Molding the Flow of Light* (Princeton University Press, Princeton, 2008)
68. V.I. Safarov, V.A. Kosobukin, C. Hermann, G. Lampel, J. Peretti, C. Marlière, Phys. Rev. Lett. **73**, 3584–3587 (1994)
69. N. Richard, A. Dereux, E. Bourillot, T. David, J.P. Goudonnet, F. Scheurer, E. Beaurepaire, J. Appl. Phys. **88**, 2541–2547 (2000)

Chapter 2
Multifaceted Tunability of One-Dimensional Helicoidal Magnetophotonic Crystals

Fei Wang and Akhlesh Lakhtakia

Abstract The photonic bandgaps (PBGs) of a 1D photonic crystal can be tailored in a variety of ways, depending on the types of mechanism incorporated in the design of that photonic crystal. These mechanisms can be structural, that is, frozen into the photonic crystal during fabrication, or dynamic, that is, they can be varied post-fabrication by manipulating, say, a low-frequency magnetic field. Interleaving magnetophotonic garnet layers with layers of a structurally chiral material (SCM) leads to a 1D helicoidal magnetophotonic crystal (HMPC), the interaction of whose overall period and the helicoidal period of the SCM layers leads to intra-Brillouin-zone PBGs which depend on the structural handedness of the SCM layers and whose gapwidths are tunable in a multifaceted fashion. Even as the overall period grows very large, one PBG remains unaffected as it is due to the helicoidal period. The gapwidths can be magnetically tuned by an externally impressed dc magnetic field.

2.1 Introduction

Structurally periodic materials appear in nature [1, 2] and can also be synthesized—as photonic crystals [3], cholesteric liquid crystals [4], and sculptured thin films [5]. The most optically notable attribute of structurally periodic materials is the presence of photonic bandgaps (PBGs) in Brillouin diagrams [3]. The PBGs underpin the use of structurally periodic materials for optical filtering [6–8], optical sensing [9, 10], lasing [11, 12], and waveguiding [13, 14]. Furthermore, these applications can be dramatically enhanced by introducing defects into the structurally periodic materials for exciting defect modes either within a PBG or at the band edges [15–18], enabling nanophotonic devices such as multi-channel nanofilters [19, 20] and ultra-low-threshold nanolasers [21, 22].

F. Wang
Research and Development, Micron Technology, Inc., Boise, ID 83707-0006, USA

A. Lakhtakia (✉)
Nanoengineered Metamaterials Group, Department of Engineering Science and Mechanics, Pennsylvania State University, University Park, PA 16802-6812, USA
e-mail: akhlesh@psu.edu

M. Inoue et al. (eds.), *Magnetophotonics*, Springer Series in Materials Science 178,
DOI 10.1007/978-3-642-35509-7_2,

Parametric control of optical properties of structurally periodic materials is highly desirable—for instance, to realize dynamically tunable PBGs. Focusing on unit cells with two constituent layers of dissimilar materials, we note that PBGs are structurally tunable, as demonstrated decades ago with the Šolc folded filters (ŠFFs) [23], wherein the optic axes of the two constituent materials are misaligned by a certain angle. Hence, ŠFFs are 1D photonic crystals which exhibit PBGs within the Brillouin zones, the bandgap widths depending on the magnitude of the misalignment angle [24]. Tunability via electrically controlled crystalline misalignment also occurs when ferroelectric (smectic) liquid crystalline layers are used [25, 26]. Another example of dynamic tunability has been recently provided by 1D magnetophotonic crystals (MPCs), wherein at least one of the two constituent materials is made of a ferrimagnetic garnet that displays optical gyrotropy under the influence of an externally impressed magnetic field [27–30]. In the 1D MPCs, the PBGs occur also inside the Brillouin zones and are magnetically tunable [31, 32]. Other factors such as misalignment between the optic axes of two consecutive layers in the unit cell of a 1D MPC can either aid or impede magnetic tunability [34].

The incorporation of helicoidal periodicity in a photonic crystal is yet another mechanism to produce and affect tunable PBGs. Significantly, helicoidal periodicity is additional to the overall periodicity which comes from a repetition of unit cells; such 1D photonic crystals can be considered to *doubly periodic*. Incorporation of the helicoidal morphology in photonic crystals is practically feasible and straightforward, e.g., in a 1D helicoidal photonic crystal (HPC) [17, 33] containing a structurally chiral material (SCM) [4, 5] in the unit cell. Because the helicoidal morphology of an SCM amounts to a continuous rotation of the optic axes and it is easily adjustable especially in nonrigid materials, an HPC will affect the tunability of PBGs by its helicoidal periodicity through an effect similar to (i.e., conceivably as a continuous version of) but yet notably different from the crystalline misalignment manifested in ŠFFs. Also, as the helicoidal and the overall periodicities interact [33], the optical response characteristics of an SCM—exemplified by the circular Bragg phenomenon [5] and the saturated defect-mode resonance [15, 34]—affect the PBGs of HPCs.

Multiple structural periodicities are desirable for 1D MPCs to operate in multiple frequency bands, each band being magnetically tunable. One way to accomplish that is to interleave homogeneous layers of a ferrimagnetic garnet with SCM layers. Having thus proposed this 1D helicoidal MPC (HMPC) with two periodicities, our main task in this chapter is to examine how the two periodicities interact with optical gyrotropy of the ferrimagnetic garnet to generate tunable PBGs that are distinct from those displayed by traditional 1D photonic crystals.

2.2 Theory

2.2.1 Constitutive Description of a 1D HMPC

Let us consider a 1D photonic crystal made of two alternating dielectric materials with the overall period $\Lambda = t^{(a)} + t^{(b)}$ along the thickness direction, i.e., the z axis,

where $t^{(a)}$ and $t^{(b)}$ are the thicknesses of the layers of dissimilar materials in the unit cell. The two materials are labeled as a and b, with the former denoting a magnetophotonic garnet layer and the latter a nonmagnetophotonic SCM layer. We fix their relative permittivity 3×3 matrices as

$$\underline{\underline{\epsilon}}^{(a)} = \underline{\underline{\epsilon}}_g + \text{Diag}\left[\epsilon^{(a)} + \Delta^{(a)}, \epsilon^{(a)} - \Delta^{(a)}, \epsilon_{zz}^{(a)}\right] \tag{2.1}$$

and

$$\underline{\underline{\epsilon}}^{(b)} = \underline{\underline{S}}\left(\xi + h\frac{\pi z}{\Omega}\right) \cdot \text{Diag}\left[\epsilon^{(b)} + \Delta^{(b)}, \epsilon^{(b)} - \Delta^{(b)}, \epsilon_{zz}^{(b)}\right] \cdot \underline{\underline{S}}^{-1}\left(\xi + h\frac{\pi z}{\Omega}\right). \tag{2.2}$$

The diagonal matrices (with components $\epsilon^{(a,b)} \pm \Delta^{(a,b)}$ and $\epsilon_{zz}^{(a,b)}$) are unaffected by any externally applied low-frequency magnetic field, but the gyrotropy matrix

$$\underline{\underline{\epsilon}}_g = i\epsilon_g \begin{bmatrix} 0 & 1 & 0 \\ -1 & 0 & 0 \\ 0 & 0 & 0 \end{bmatrix} \tag{2.3}$$

contains a nonzero scalar ϵ_g when an external low-frequency magnetic field is applied parallel to the z axis. Finally, the 3×3 matrix

$$\underline{\underline{S}}(\zeta) = \begin{bmatrix} \cos\zeta & -\sin\zeta & 0 \\ \sin\zeta & \cos\zeta & 0 \\ 0 & 0 & 1 \end{bmatrix}, \tag{2.4}$$

with $\zeta = \xi + h\pi z/\Omega$, is used to delineate two structural mechanisms. First, ξ is the misalignment angle that is introduced across the interface between layers a and b; second, the helicoidal periodicity of the SCM layer is expressed through Ω and $h = \pm 1$ which, respectively, denote the helicoidal period and the structural handedness. While (2.2) describes a relatively general form for the SCM layer, a special case ($h = 0$ and $\xi \notin \{0, \pi\}$) representing the crystalline misalignment alone (as in an ŠFF) can be meaningfully incorporated into the constituent layers of MPCs. Combinations are thus possible, e.g.,

(i) the 1D bicrystalline magnetophotonic crystal (BMPC) [32] for which $h = 0$ but both optical gyrotropy and crystalline misalignment are present, and
(ii) the 1D HMPC that combines optical gyrotropy and helicoidal periodicity [33] but does not have crystalline misalignment ($\xi = 0$).

Figure 2.1 shows the schematic evolution from a 1D PC to a 1D HMPC with structural and material mechanisms described thus far. For simplicity, we let both materials in the unit cell be nondispersive, nondissipative, and nonmagnetic. The two materials can be dielectrically similar ($\epsilon^{(a)} = \epsilon^{(b)}$ and $\Delta^{(a)} = \Delta^{(b)}$) or not, and we note that both $\epsilon_{zz}^{(a)}$ and $\epsilon_{zz}^{(b)}$ do not affect propagation along the z axis. Let us also characterize the optical gyrotropy through the magnetophotonic angle $\alpha = \tan^{-1}[\epsilon_g/\Delta^{(a)}]$, and denote angular frequency by ω, the speed of light by c, the intrinsic impedance of free space by η_0, and the free-space wavenumber by k_0. We also assume that the SCM layer is sufficiently thick so as to exhibit a fully developed circular Bragg phenomenon [5, Chap. 9].

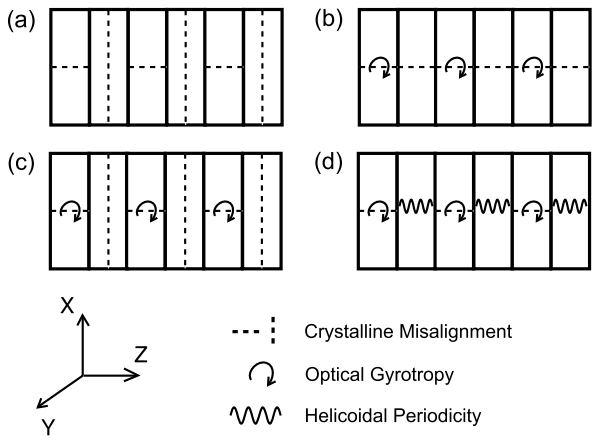

Fig. 2.1 Schematics of 1D photonic crystals evolving from nonmagnetophotonic to magnetophotonic materials described in (2.1)–(2.4). (**a**) an ŠFF, (**b**) a 1D MPC, (**c**) a 1D BMPC, and (**d**) a 1D HMPC, the unit cells of which, respectively, contain (**a**) two misaligned nonmagnetophotonic homogeneous material layers, (**b**) a magnetophotonic garnet layer and an aligned nonmagnetophotonic layer, (**c**) a magnetophotonic garnet layer and a misaligned nonmagnetophotonic layer, and (**d**) a magnetophotonic garnet layer and a SCM layer. Light propagation occurs along the z axis

2.2.2 Axial Wave Propagation

Wave propagation along the z axis can be formulated using standard techniques based on the Floquet–Bloch theorem for Bloch states and the emergence of PBGs in the Brillouin diagrams. In the context of axial wave propagation, the electric field phasors in the two constituent layers of the unit cell of the 1D HMPC only contain components in the xy plane and can be described using the column 4-vector

$$\underline{F}(z) = \begin{bmatrix} E_x(z) \\ E_y(z) \\ -\eta_0 H_y(z) \\ \eta_0 H_x(z) \end{bmatrix}. \tag{2.5}$$

In the magnetophotonic layers,

$$\begin{bmatrix} E_x(z) \\ E_y(z) \end{bmatrix} = \sum_{j=1}^{4} a_{n_j} \exp\left[i\sigma_j k_0 (z - n\Lambda)\right] \underline{p}_j, \quad z \in \left[n\Lambda, n\Lambda + t^{(a)}\right], \tag{2.6}$$

where the eigenmodes indexed by $j \in [1, 4]$ involve the column 2-vectors

$$\underline{p}_1 = \underline{p}_2 = \begin{bmatrix} \sin(\alpha/2) \\ -i\cos(\alpha/2) \end{bmatrix}, \qquad \underline{p}_3 = \underline{p}_4 = \begin{bmatrix} \sin(\alpha/2) \\ i\cos(\alpha/2) \end{bmatrix} \tag{2.7}$$

representing the eigenpolarization states; $k_0\sigma_j$ are the eigenmodal wavenumbers with

$$\sigma_1 = -\sigma_2 = \sqrt{\epsilon^{(a)} + \sqrt{\Delta^{(a)2} + \epsilon_g^2}}, \qquad \sigma_3 = -\sigma_4 = \sqrt{\epsilon^{(a)} - \sqrt{\Delta^{(a)2} + \epsilon_g^2}}; \tag{2.8}$$

and a_{n_j} are the eigenmodal amplitudes for the magnetophotonic layer in the nth unit cell, i.e., $z \in [n\Lambda, n\Lambda + t^{(a)}]$. The boundary values of $\underline{F}(z)$ on the magnetophotonic sides of the interfaces $z = n\Lambda + t^{(a)}$ and $z = (n+1)\Lambda$ are given by

$$\underline{F}\big[n\Lambda + t^{(a)}\big] = \underline{\underline{D}} \cdot \underline{\underline{P}}^{(a)} \cdot \underline{A}^{(n)} \tag{2.9}$$

and

$$\underline{F}\big[(n+1)\Lambda\big] = \underline{\underline{D}} \cdot \underline{\underline{P}}^{(a)} \cdot \underline{A}^{(n+1)}, \tag{2.10}$$

where the 4×4 matrices

$$\underline{\underline{D}} = \begin{bmatrix} \sin(\alpha/2) & \sin(\alpha/2) & \sin(\alpha/2) & \sin(\alpha/2) \\ -i\cos(\alpha/2) & -i\cos(\alpha/2) & i\cos(\alpha/2) & i\cos(\alpha/2) \\ \sigma_1\sin(\alpha/2) & \sigma_2\sin(\alpha/2) & \sigma_3\sin(\alpha/2) & \sigma_4\sin(\alpha/2) \\ -i\sigma_1\cos(\alpha/2) & -i\sigma_2\cos(\alpha/2) & i\sigma_3\cos(\alpha/2) & i\sigma_4\cos(\alpha/2) \end{bmatrix}, \tag{2.11}$$

and

$$\underline{\underline{P}}^{(a)} = \exp\big\{i\sigma_j k_0 t^{(a)}\,\mathrm{Diag}[\sigma_1, \sigma_2, \sigma_3, \sigma_4]\big\}, \tag{2.12}$$

and the column 4-vectors

$$\underline{A}^{(n)} = \begin{bmatrix} a_{n_1} \\ a_{n_2} \\ a_{n_3} \\ a_{n_4} \end{bmatrix}. \tag{2.13}$$

In each SCM layer, the propagating wave can be decomposed into forward-propagating and backward-propagating components. Each of those components has left-handed and right-handed components. Therefore, in any SCM layer we can write

$$\underline{F}(z) = \underline{\underline{Y}} \cdot \underline{f}(z), \tag{2.14}$$

where the 4×4 matrix

$$\underline{\underline{Y}} = \begin{bmatrix} \underline{\underline{U}} & \underline{\underline{U}} \\ \underline{\underline{U}} \cdot \underline{\underline{Z}} & -\underline{\underline{U}} \cdot \underline{\underline{Z}} \end{bmatrix}, \tag{2.15}$$

involves the 2×2 matrices

$$\underline{\underline{U}} = \frac{1}{\sqrt{2}} \begin{bmatrix} 1 & 1 \\ i & -i \end{bmatrix} \tag{2.16}$$

and

$$\underline{\underline{Z}} = \begin{bmatrix} n^{(b)} & -\Delta n^{(b)} \\ -\Delta n^{(b)} & n^{(b)} \end{bmatrix} \tag{2.17}$$

with $n^{(b)} = \sqrt{\epsilon^{(b)}}$ and $\Delta n^{(b)} = \Delta^{(b)}/2n^{(b)}$. A matrizant $\underline{\underline{W}}(z)$ can be prescribed such that

$$\underline{f}(z) = \underline{\underline{W}}\big(z - z'\big) \cdot \underline{f}\big(z'\big) \tag{2.18}$$

for both z and z' inside the same SCM layer. Exact calculation of $\underline{\underline{W}}(z)$ is possible [35]; however, coupled-mode theory [34] provides an approximate closed-form expression of the matrizant as follows:

$$\underline{\underline{W}}(z) = \begin{bmatrix} P_-(z) & 0 & 0 & Q_-(z) \\ 0 & P_+(z) & Q_+(z) & 0 \\ 0 & Q_+^*(z) & P_+^*(z) & 0 \\ Q_-^*(z) & 0 & 0 & P_-^*(z) \end{bmatrix}, \tag{2.19}$$

where

$$P_\pm(z) = e^{\pm ih\pi z/\Omega}\left[\cosh(\Delta_\mp z) + \frac{i(k_0 n^{(b)} \mp h\pi/\Omega)}{\Delta_\mp}\sinh(\Delta_\mp z)\right], \tag{2.20}$$

$$Q_\pm(z) = e^{\pm ih\pi z/\Omega}\left[\frac{ik_\Delta}{\Delta_\mp}\sinh(\Delta_\mp z)\right], \tag{2.21}$$

$\Delta_\pm = \sqrt{k_\Delta^2 - (k_0 n^{(b)} \pm h\pi/\Omega)^2}$, $k_\Delta = k_0 \Delta n^{(b)}$, and the asterisk denotes the transpose. Equation (2.19) holds only if dissipation in the SCM layer is small enough to be ignored, but the formulation for a dissipative SCM layer can be done similarly yielding modifications to (2.19)–(2.21) [36].

The tangential components of the electromagnetic field must be continuous across all interfaces of the two constituent layers. Enforcing these boundary conditions as well as the periodicity condition $\underline{A}^{(n+1)} = \exp(iK\Lambda)\underline{A}^{(n)}$, by virtue of the Floquet–Bloch theorem with K as the Bloch wavenumber, we obtain an eigenvalue problem that governs the emergence of Bloch states in the Brillouin diagram; thus,

$$\underline{\underline{D}}^{-1} \cdot \underline{\underline{Y}} \cdot \underline{\underline{W}}(b) \cdot \underline{\underline{Y}}^{-1} \cdot \underline{\underline{D}} \cdot \underline{\underline{P}}^{(a)} \cdot \underline{A}_n = \exp(iK\Lambda)\underline{A}^{(n)}, \tag{2.22}$$

where $\underline{\underline{W}}(b) \equiv \underline{\underline{W}}(t^{(b)})$. Solution of (1.16) yields the relationship between K and the angular frequency ω. As propagating Bloch states are indicated by real-values K, and evanescent Bloch states by complex-valued K, PBGs can be identified in Brillouin diagrams.

2.3 Numerical Results and Discussions

2.3.1 1D BMPC

Let us begin by setting $h = 0$. The crystalline misalignment between the two constitutive layers in the 1D BMPC in Fig. 2.1(b), represents a vestigial form of the continuous rotation of the relative permittivity matrix of SCM layers in the 1D HMPC in Fig. 2.1(c). The 1D BMPC thus provides a starting point to look at the magnetophotonic features that could be common in both types of structured MPC (i.e., BMPC and HMPC).

Interest lies in identifying the effects of (a) crystalline misalignment and (b) optical gyrotropy in the Brillouin diagram of the 1D BMPC. The intra-Brillouin-zone PBGs for the two factors separately turn out to be drastically different from each other [32]. Figure 2.2 presents the fifth branch in the Brillouin diagram for a 1D BMPC with a dielectrically similar configuration ($\epsilon^{(a)} = \epsilon^{(b)}$ and $\Delta^{(a)} = \Delta^{(b)}$), for six different sets $\{\xi, \alpha\}$. In conformity with Refs. [28, 31, 38, 39], the aligned 1D BMPC (i.e., $\xi = 0$) exhibits magnetically tunable intra-Brillouin-zone PBGs in Fig. 2.2(a), wherein the gapwidths $\Delta\omega$ increase with the optical gyrotropy ϵ_g of the magnetophotonic layer in the unit cell. The Brillouin diagram for complete misalignment (i.e., $\xi = \pi/2$) in Fig. 2.2(b) is very different. The gapwidths (i) are significant larger than for $\xi = 0$ and (ii) are not significantly affected by the optical gyrotropy of the magnetophotonic layer. For both $\xi = 0$ and $\xi = \pi/2$ in Fig. 2.2, the PBGs shift away from the boundaries of Brillouin zones as α is increased, but are closer to the boundaries for the larger value of ξ.

Coupling of the influences of the crystalline misalignment and the optical gyrotropy on the PBGs of the dielectrically similar BMPCs can be identified in Fig. 2.3. This figure indicates a strong dependence of the gapwidth on ξ when α is relatively small, but this dependence significantly weakens as α increases. Similarly, the gapwidth is closely tied to the value of α for small values of ξ, but loses its α-dependences when ξ is close to $\pi/2$. Therefore, the individual effects of crystalline misalignment and optical gyrotropy can be offset simply by choosing significantly large values of α and ξ, respectively. In particular, a high degree of crystalline misalignment ($\xi \approx \pi/2$) in a dielectrically similar configuration should stabilize the gapwidth with respect to the externally applied low-frequency magnetic field. We conclude that crystalline misalignment trumps optical gyrotropy.

The gapwidths of PBGs have very different characteristics for 1D BMPCs with dielectrically dissimilar configurations. As an example, setting $\bar{\epsilon}^{(a)} = \bar{\epsilon}^{(b)}$ but varying the ratio $\gamma = \Delta^{(b)}/\Delta^{(a)}$, we found that if γ is substantially either larger or smaller than unity, the magnetic tunability of gapwidths is significantly affected. This becomes evident from Fig. 2.4 wherein the gapwidth in the fifth branch has been plotted against α for both dielectrically similar ($\gamma = 1$) and dielectrically dissimilar BMPCs ($\gamma = 0.2$ or 10). The gapwidth for α in the neighborhood of $\pi/2$ is greatly enhanced for $\gamma \gg 1$ but reduced for $\gamma \ll 1$. Thus, the effect of the externally applied low-frequency magnetic field on the gapwidth can be either enhanced or reduced by an appropriate selection of the materials of the two constituent layers

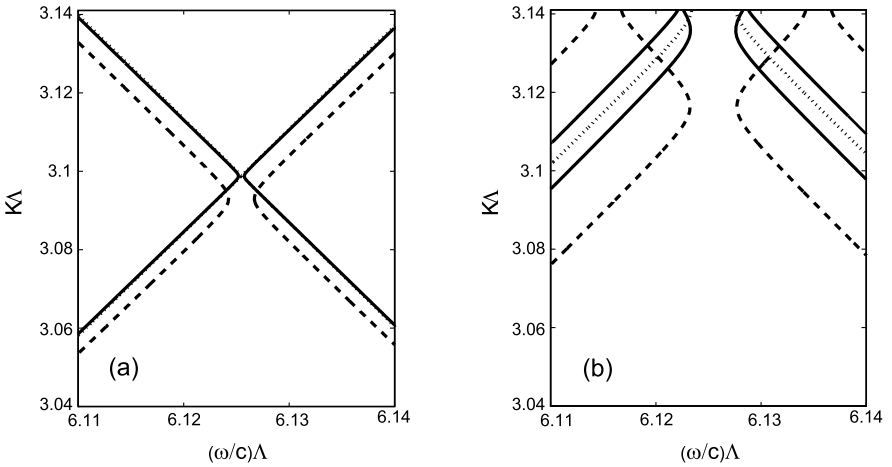

Fig. 2.2 The fifth branch in the Brillouin diagram for a 1D BMPC with (**a**) $\xi = 0$ and (**b**) $\xi = \pi/2$. The two constituent layers in the unit cell are dielectrically similar: $\bar{\epsilon}^{(a)} = \bar{\epsilon}^{(b)} = 6.6$ and $\Delta^{(a)} = \Delta^{(b)} = 0.05$, which are typical of the constitutive properties of bismuth iron garnet in the infrared regime [37]. *Dotted lines* are for the limiting case $\alpha = 0$ (no optical gyrotropy), *solid lines* for $\alpha = \pi/12$, and *dashed lines* for $\alpha = 5\pi/18$. Similar features can be observed for other branches in the Brillouin diagram. The Bloch states for $\alpha = 0$ in (**b**) are degenerate, despite both layers in the unit cell being anisotropic

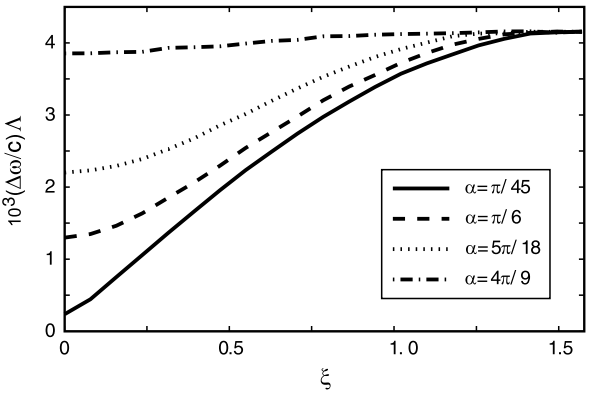

Fig. 2.3 Calculated ξ-dependence of the gapwidth $\Delta\omega$ in the fifth branch in the Brillouin diagram, for different values of α. The 1D BMPC has the same constitutive properties as in Fig. 2.2

of the unit cell. Furthermore, whereas the enhancement with $\gamma \gg 1$ appears to be huge and nonlinear with respect to α, the reduction with $\gamma \ll 1$ is moderate and quasilinear.

Figure 2.4 also shows that dielectric dissimilarity can trump crystalline misalignment. The gapwidths for $\xi \in \{0, \pi/2\}$ are quite comparable for $\gamma \neq 1$. As a consequence, although crystalline misalignment plays a significant role for dielectrically similar BMPCs by trumping optical gyrotropy, it tends to lose its importance for magnetic control of the PBGs displayed by dielectrically dissimilar BMPCs.

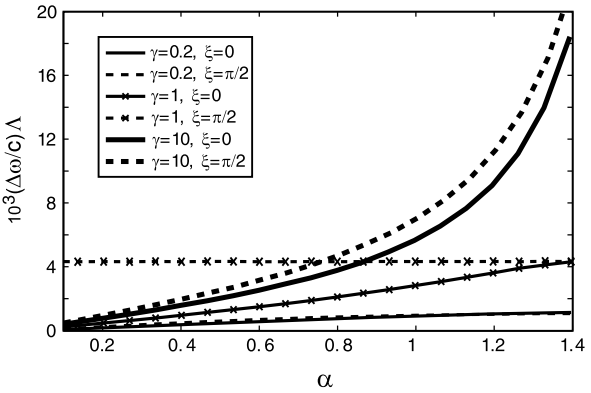

Fig. 2.4 Calculated α-dependence of the gapwidth $\Delta\omega$ in the fifth branch in the Brillouin diagram for different values of $\gamma = \Delta^{(b)}/\Delta^{(a)}$ and ξ. These calculations were made for a 1D BMPC with dielectrically dissimilar configuration: $\bar{\epsilon}^{(a)} = \bar{\epsilon}^{(b)} = 6.6$ and $\Delta^{(a)} = \Delta^{(b)}/\gamma = 0.05$

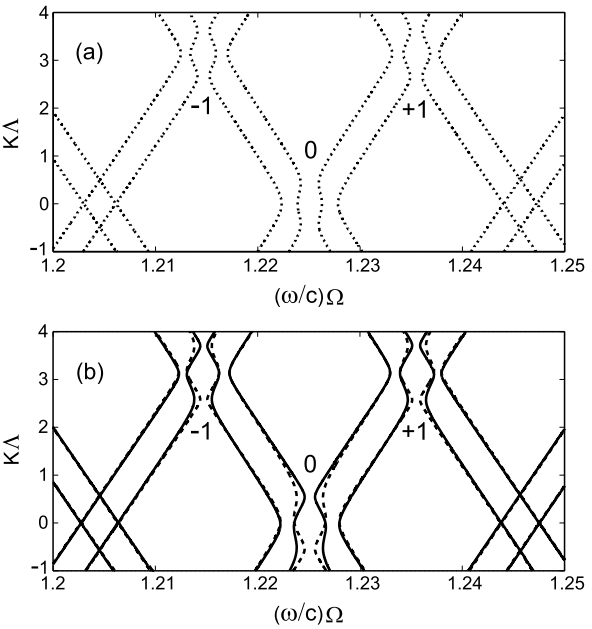

Fig. 2.5 Brillouin diagrams for 1D HMPC with (**a**) $\alpha = 0$ and (**b**) $\alpha = \pi/6$. Both constituent layers of the unit cell are dielectrically similar ($\bar{\epsilon}^{(a)} = \bar{\epsilon}^{(b)} = 6.6$ and $\Delta^{(a)} = \Delta^{(b)} = 0.05$) and their thicknesses are equal ($t^{(a)} = t^{(b)} = 60\Omega$). The *dotted lines* in (**a**) are for the HMPC of either handedness, the *solid* and *dashed lines* in (**b**) are for the left-handed ($h = -1$) and right-handed ($h = +1$) HMPC, respectively. Intra-Brillouin-zone PBGs in the diagrams are labeled by 0 and ± 1

2.3.2 1D HMPC

Let us now move on to $h = \pm 1$ so that the second constituent layer of the unit cell is a nonmagnetophotonic SCM layer. Figure 2.5 shows the Brillouin diagrams for a 1D HMPC made of dielectrically similar materials ($\bar{\epsilon}^{(a)} = \bar{\epsilon}^{(b)}$ and $\Delta^{(a)} = \Delta^{(b)}$), when the externally applied low-frequency magnetic field is either absent ($\alpha = 0$) or present ($\alpha = \pi/6$). Several PBGs are present inside the Brillouin zone, near the zone boundaries $K\Lambda = 0$ and π. The band profiles around these intra-Brillouin-zone PBGs are dependent on the structural handedness for $\alpha > 0$ but not for $\alpha = 0$; however, the gapwidths are independent of handedness, regardless of α.

The PBGs have been classified elsewhere [33] into groups $\mathcal{A}$ and $\mathcal{B}$ when they are in close proximity of the zone boundaries $K\Lambda = 0$ and π, respectively; furthermore, PBGs in group $\mathcal{A}$ are labeled $\{0, \pm 2, \pm 4, \ldots\}$, while those in group $\mathcal{B}$ are labeled $\{\pm 1, \pm 3, \pm 5, \ldots\}$. In Fig. 2.5, group $\mathcal{A}$ is represented only by the PBG labeled 0, whereas group $\mathcal{B}$ is fully populated, as can be seen by extending the horizontal axis beyond the limits shown in the figure.

PBGs not labeled 0 reflect the interaction of the overall period Λ with the electromagnetic field. These PBGs are found when Ω is finite (HMPCs) and even in the limit $\Omega \to \infty$ (non-helicoidal MPCs). But the PBG labeled 0 is located at $\omega = (\pi/n^{(b)})(c/\Omega)$, which is the center frequency of the Bragg regime of the SCM layer [16, 17], and therefore exists only for HMPCs (finite Ω).

In an isolated SCM layer with a sufficient number $N^{(b)} = t^{(b)}/\Omega$ of periods, a PBG is known to occur when a central phase defect is introduced in the form of either a twist defect [15, 32], or a spacer layer [36, 40, 41], or some combination thereof [16, 41]. A resonance, which is localized spatially at the defect site and spectrally at the center of the Bragg regime, can be excited by either left- or right-circularly polarized light, depending on the thickness of the isolated SCM layer. When the handedness of the incident circularly polarized light is the same as the structural handedness of the isolated SCM layer, the resonance develops and vanishes as $N^{(b)}$ is increased from a small value. When the two handednesses differ, the resonance develops and saturates as $N^{(b)}$ is increased from a large value [15, 32], because the localized energy density increases drastically with $N^{(b)}$ until attaining a saturation level—this phenomenon is manifested in the Brillouin diagram as a PBG that blocks arbitrarily polarized light from propagating through the isolated SCM layer containing a central phase defect.

As PBGs exist in isolated SCM layers with central phase defects, and as the PBG labeled 0 does not exist when $t^{(a)} = 0$ in the 1D HMPC, we conclude that this PBG is solely due to each magnetophotonic garnet layer acting as a phase defect inserted between two identical SCM layers with sufficiently large numbers of periods. Numerical studies [33] have shown that this PBG is weakly affected by $N^{(b)}$.

The PBGs labeled ± 1 in Fig. 2.5(b) exhibit notable dependences on the ratio Λ/Ω. For a fixed helicoidal period, the center frequencies and the gapwidths of these two PBGs from group $\mathcal{B}$ appear to vary inversely as the overall period Λ. This tendency—which is generally observed for PBGs in single-period, non-helicoidal PCs [42]—affirms that the PBGs of group $\mathcal{B}$ are intimately connected to the overall periodicity of the 1D HMPC. But, because it is retained even in the limit $\Lambda \to \infty$, the helicoidal periodicity also affects these PBGs significantly. For fixed Ω, as Λ increases, (i) their center frequencies approach the center frequency of the PBG labeled 0, and (ii) their gapwidths remain finite [33]. If $h = 0$, the center frequencies and gapwidths of all PBGs go to zero as $\Lambda \to \infty$.

The interplay between the two different structural periodicities—i.e., the helicoidal periodicity and the overall periodicity—can be further appreciated with the 1D HMPC. Figure 2.6 shows that the gapwidths of the PBGs of a 1D HMPC are strongly dependent on the spatial variation of the properties in the unit cell, as expressed by the angle $\chi = \tan^{-1}(t^{(b)}/t^{(a)}) \in (0, \pi/2)$. The gapwidth of every PBG

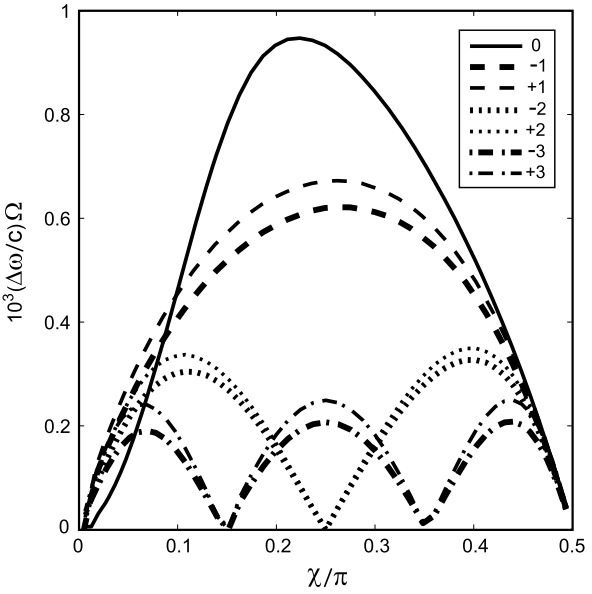

Fig. 2.6 Dependence of the gapwidth $\Delta\omega$ on $\chi = \tan^{-1}(t^{(b)}/t^{(a)})$ for the 1D HMPC. The constitutive properties of materials of the two constituent layers of the unit cell are the same as for Fig. 2.5, except that $\alpha = \pi/9$, $\Lambda/\Omega = 50$, and $N^{(b)} = t^{(b)}/\Omega \in \{1, 2, \ldots, 49\}$. The PBG labels for all curves are identified in the *inset*

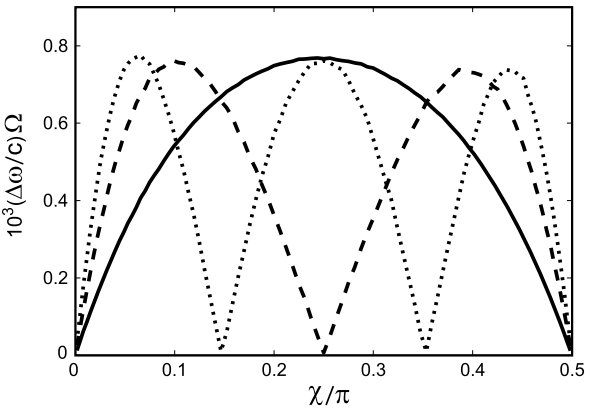

Fig. 2.7 Dependence of the gapwidth $\Delta\omega$ on χ for a 1D MPC with $\alpha = \pi/9$. *Solid*, *dashed*, and *dotted lines* are for the PBGs in the first, second, and third branches, respectively, in the Brillouin diagram. See Fig. 2.2 for other parameters

displays an oscillatory pattern with respect to χ: it varies from low to high and back to low in one cycling period on the χ axis. The oscillation of gapwidth with χ has to be an intrinsic feature of PBGs in any 1D PC because of the overall periodicity, which conclusion emerges on noting that the gapwidths of PBGs of all three non-helicoidal 1D PCs shown in Figs. 2.1(a)–(c) oscillate with χ in a similar manner.

However, there are distinctions in the oscillatory χ-dependences of gapwidths between the 1D HMPC and the non-helicoidal 1D PCs, which are attributable to the influence of helicoidal periodicity on the PBGs. The main distinction is that the gapwidth of a higher-frequency PBG of a non-helicoidal 1D PC will cycle through more periods than that of a lower-frequency PBG in the range $\chi \in (0, \pi/2)$, see Fig. 2.7 for the example of a 1D MPC; while the number of cycling periods of

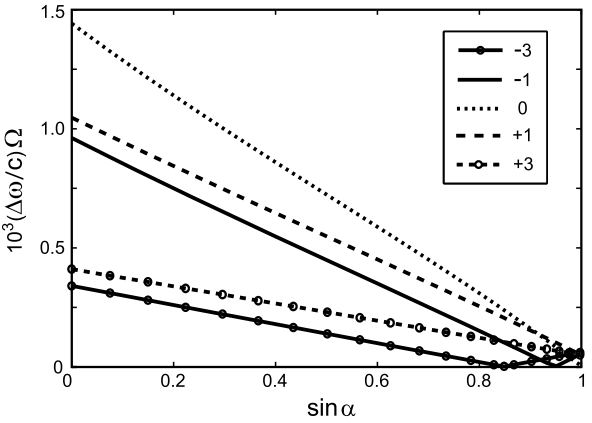

Fig. 2.8 Dependences of the gapwidths $\Delta\omega$ of PBGs of different labels, identified in the *inset*, on α. All parameters are the same as for Fig. 2.5 except $\Lambda = 20\Omega$

the gapwidth of a 1D HMPC over $\chi \in (0, \pi/2)$ increases as the PBG distances, in either of the frequency directions, away from the PBG centered in the Bragg regime of the SCM layer of the unit cell. Because the PBG at the center of Bragg regime, labeled 0, occurs mainly due to the helicoidal periodicity while all the other PBGs, labeled $n \in \{\pm 1, \pm 2, \ldots\}$, are mainly a result of overall periodicity [33], the interplay between the two periodicities in a 1D HMPC can be seen vividly as follows: the PBGs labeled 0 and ± 1 for the 1D HMPC exhibit identically a single cycling period of gapwidth over $\chi \in (0, \pi/2)$, while the gapwidths of any two PBGs of a non-helicoidal 1D PC will have different numbers of cycling periods across the χ axis.

The PBGs of the 1D HMPC in both groups $\mathcal{A}$ and $\mathcal{B}$ depend on α, as illustrated in Fig. 2.8. The gapwidths of the higher-frequency PBGs (with labels $\in \{0, 1, 3, 5, \ldots\}$) decline linearly with increase of $\sin\alpha$, but the gapwidths of the lower-frequency PBGs (with labels $\in \{-1, -3, -5, \ldots\}$) first decrease to zero and then increase as $\sin\alpha$ increases. For each of the lower-frequency PBGs, we can designate a value α_c of α when the PBG vanishes and so does the gapwidth. The farther that a negatively labeled PBG is from the PBG labeled 0 on the ω axis, the lower is the value of the former's α_c.

The magnetic tunablity of gapwidths of HMPCs differs from that of non-helicoidal MPCs in a significant manner. The gapwidths in non-helicoidal MPCs increase with α [31, 34]. In contrast, the gapwidths in Fig. 2.8 for HMPCs decrease as α increases for the higher-frequency PBGs, and similarly for $\alpha < \alpha_c$ for the lower-frequency PBGs. The role of the helicoidal periodicity diminishes in the lower-frequency regime, because the SCM layer of the HMPC tends to become effectively homogeneous as $(\omega/c)\Omega \to 0$. In other words, the optical role of helicoidal periodicity can be trumped by a sufficiently large $\alpha > \alpha_c$) magnetically induced optical gyrotropy at sufficiently low frequencies.

Both groups $\mathcal{A}$ and $\mathcal{B}$ of PBGs are also exhibited by a 1D HMPC made of dielectrically dissimilar materials [33]. As shown in Fig. 2.9, the amplitudes of the $\Delta^{(a)}$ and $\Delta^{(b)}$ affect the center frequencies and the gapwidths of PBGs. Increases in these parameters tend to amplify the gapwidths, as may be seen by comparing the

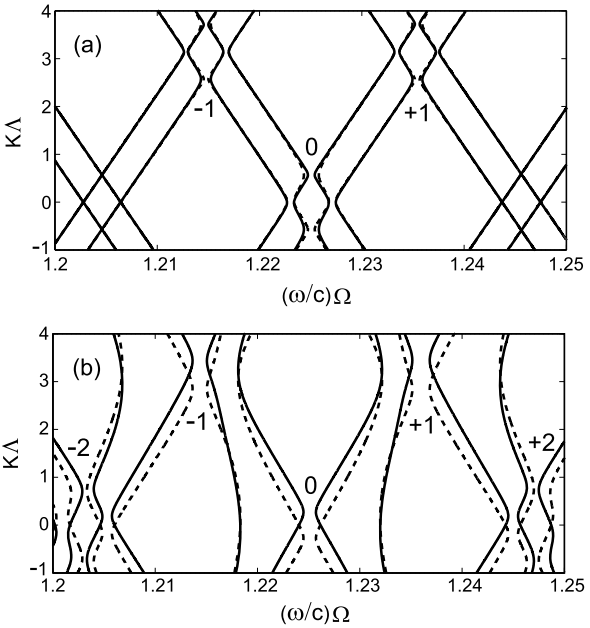

Fig. 2.9 Brillouin diagrams for 1D HMPC made of dielectrically dissimilar materials such as (**a**) $\Delta^{(b)} = 0.5\Delta^{(a)}$ and (**b**) $\Delta^{(b)} = 5\Delta^{(a)}$. Other parameters are as same as for Fig. 2.5 with $\Delta^{(a)} = 0.05$ fixed. The *solid lines* are for the left-handed HMPC, and the *dashed lines* are for the right-handed HMPC

gapwidths in Fig. 2.9(a) for lower $\Delta^{(b)}$ with those in Fig. 2.9(b) for higher $\Delta^{(b)}$. Furthermore, the density of PBGs on the ω-axis increases as well, for which Fig. 2.9(b) contains evidence. Finally, the effect of structural handedness gets amplified, as may be seen by comparing the two parts in Fig. 2.9.

2.3.3 Multifaceted Tunability of PBGs

Figure 2.10 shows the dependence of the gapwidth of an intra-Brillouin-zone PBG of an ŠFF on ξ and similar dependences on α of the remaining three 1D PCs illustrated in Fig. 2.1. The gapwidth increases with either ξ or α for the non-helicoidal 1D PCs; therefore, crystalline misalignment and optical gyrotropy, in essence, function similarly to tune PBGs. However, whereas crystal misalignment is to be chosen before making the PC, optical gyrotropy can be dynamically altered after fabrication by the application of an external low-frequency magnetic field. Magnetic tunability of PBGs is also evinced by a PC which can be tuned by a combination of mechanisms. Among them is the 1D BMPC in which the gap widths of PBGs vary with α in general, but can also become unaffected by the amplitude of optical gyrotropy when the misalignment angle $\xi = \pi/2$, as shown in Fig. 2.10. A 1D HMPC demonstrates bimodal magnetic tunability of PBGs: first the bandgap width decreases to almost the vanishing point and then increases, as the magnetophotonic angle α increases.

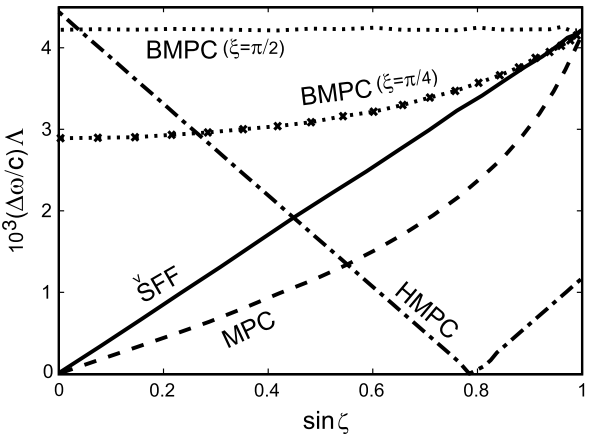

Fig. 2.10 Dependence of gapwidth $\Delta\omega$ on the angle ζ for 1D PCs illustrated in Fig. 2.1; $\zeta = \xi$ for the ŠFF, but $\zeta = \alpha$ for the other PCs. Other parameters are as follows: (i) ŠFF: $\alpha = 0$, $h = 0$; (ii) MPC: $\xi = 0$, $h = 0$; (iii) BMPC: $\xi \in \{\pi/4, \pi/2\}$, $h = 0$; and (iv) HMPC: $\xi = 0$, $h = \pm 1$, $\Lambda/\Omega = 24$. The two base layers have equal thickness and are made of dielectrically similar materials ($\bar{\epsilon}^{(a)} = \bar{\epsilon}^{(b)} = 6.6$ and $\Delta^{(a)} = \Delta^{(b)} = 0.05$). The PBGs for 1D non-helicoidal ($h = 0$) PCs occur at the fifth branch in the Brillouin diagram, while the PBG for the 1D HMPC ($h = \pm 1$) is in the third lower-frequency PBG labeled -3 [43]

Thus, in PCs with either one or two tunability mechanisms, we find that (i) different types of tuning trend are possible and (ii) the tunability with more than one physical mechanism is multifaceted.

2.4 Concluding Remarks

In conclusion, we have delineated the characteristic features and the multifaceted tunability of intra-Brillouin-zone PBGs that are displayed by the 1D HMPC because the effects of its overall period Λ are significantly modified by the helicoidal period 2Ω of the SCM layer contained in its unit cell. One of the PBGs (labeled 0) can be attributed entirely to a saturated wave resonance that occurs because each magnetophotonic garnet layer acts as a phase defect inserted between two identical SCM layers with sufficiently large numbers of periods [40]. The helicoidal period is responsible for other qualitative differences with respect to non-helicoidal 1D MPCs. For example, the center frequencies of all PBGs approach a non-diminishing value even as $\Lambda \to \infty$, and the gapwidths of the PBGs can be magnetically tuned down and up by turning up the magnitude of the externally impressed dc magnetic field. These magnetically controllable PBGs are also affected by the structural left-handedness or right-handedness of the HMPC.

One-dimensional HMPCs can be conceived to display even more remarkable magnetophotonic features. For instance, all three tunability mechanisms—i.e., crystalline misalignment, optical gyrotropy, and helicoidal periodicity—can be simulta-

neously hosted in the 1D HMPC so that the tunability of PBGs is multifaceted. The crystalline misalignment may be introduced by twisting all the magnetophotonic garnet layers by a certain angle about the z axis [34], which would introduce new features same as the 1D BMPC has exhibited. Another possibility is to use ferroelectric crystals for the magnetophotonic layers, which would introduce additional control by an externally impressed dc electric field. Yet another possibility is that the magnetophotonic layers also have a helicoidal morphology; then, the additional helicoidal periodicity would introduce new features.

Acknowledgements F.W. is grateful to Prof. Thomas W. Lester (University of Kentucky, College of Engineering) for encouraging this research effort. A.L. thanks the Charles Godfrey Binder Endowment at Penn State for partial support of his research efforts. The continuing support from the families of both authors is much appreciated.

References

1. R.M. Graham, D.W. Lee, K. Nortsog, Am. J. Bot. **80**, 198 (1993)
2. K.S. Gould, D.W. Lee, Am. J. Bot. **83**, 45 (1996)
3. J.D. Joannopoulos, S.G. Johnson, J.N. Winn, R.D. Meade, *Photonic Crystals: Molding the Flow of Light*, 2nd edn. (Princeton University Press, Princeton, 2008)
4. S. Chandrasekhar, *Liquid Crystals*, 2nd edn. (Cambridge University Press, Cambridge, 1992)
5. A. Lakhtakia, R. Messier, *Sculptured Thin Films: Nanoengineered Morphology and Optics* (SPIE, Bellingham, 2005)
6. H.A. Macleod, *Thin-Film Optical Filters*, 3rd edn. (IOP, Bristol, 2001)
7. I.J. Hodgkinson, Q.h. Wu, Adv. Mater. **13**, 889 (2001)
8. J. Lub, P. Whitte, C. Doornkamp, J.P. Vogels, R.T. Wegh, Adv. Mater. **15**, 1420 (2003)
9. A. Lakhtakia, M.W. McCall, J.A. Sherwin, Q.H. Wu, I.J. Hodgkinson, Opt. Commun. **194**, 33 (2001)
10. Y.J. Liu, J. Shi, F. Zhang, H. Liang, J. Xu, A. Lakhtakia, S.J. Fonash, T.J. Huang, Sens. Actuators B, Chem. **156**, 593 (2011)
11. E. Yablonovitch, Phys. Rev. Lett. **58**, 2059 (1987)
12. V.I. Kopp, B. Fan, H.K.M. Vithana, A.Z. Genack, Opt. Lett. **23**, 1707 (1998)
13. A. Mekis, J.C. Chen, I. Kurland, S. Fan, P.R. Villeneuve, J.D. Joannopoulos, Phys. Rev. Lett. **77**, 3787 (1996)
14. M.J. Steel, R.M. Osgood Jr., J. Lightwave Technol. **19**, 495 (2001)
15. V.I. Kopp, A.Z. Genack, Phys. Rev. Lett. **89**, 033901 (2002)
16. I.J. Hodgkinson, Q.h. Wu, L. De Silva, M. Arnold, M.W. McCall, A. Lakhtakia, Phys. Rev. Lett. **91**, 223903 (2003)
17. F. Wang, A. Lakhtakia, Opt. Express **13**, 7319 (2005)
18. J. Gao, A. Lakhtakia, M. Lei, J. Nanophotonics **5**, 051502 (2011)
19. F. Wang, A. Lakhtakia, Opt. Commun. **215**, 79 (2003)
20. N.Y. Ha, Y. Ohtsuka, S.M. Jeong, S. Nishimura, G. Suzaki, Y. Takanishi, K. Ishikawa, H. Takezoe, Nat. Mater. **7**, 43 (2008)
21. J. Schmidtke, W. Stille, H. Finkelmann, Phys. Rev. Lett. **90**, 083902 (2003)
22. M.H. Song, N.Y. Ha, K. Amemiya, B. Park, Y. Takanishi, K. Ishikawa, J.W. Wu, S. Nishimura, T. Toyooka, H. Takezoe, Adv. Mater. **18**, 193 (2006)
23. I. Šolc, Czechoslov. J. Phys. **4**, 65 (1954)
24. P. Yeh, J. Opt. Soc. Am. **5**, 742 (1979)
25. M. Ozaki, M. Kasano, T. Kitasho, D. Ganzke, W. Haase, K. Yoshino, Adv. Mater. **15**, 974 (2003)

26. S.S. Choi, S.M. Morris, H.J. Coles, W.T.S. Huck, Appl. Phys. Lett. **91**, 231110 (2007)
27. I.L. Lyubchanskii, N.N. Dadoenkova, M.I. Lyubchanskii, E.A. Shapovalov, Th. Rasing, J. Phys. D, Appl. Phys. **36**, R277 (2003)
28. S. Kahl, A. Grishin, Appl. Phys. Lett. **84**, 1438 (2004)
29. M. Levy, R. Li, Appl. Phys. Lett. **89**, 121113 (2006)
30. M. Levy, A. Chakravarty, P. Kumar, X. Huang, in *Magnetophotonics: From Theory to Applications*, ed. by M. Inoue, M. Levy, A. Baryshev (Springer, Berlin, 2013), Chap. 7
31. M. Levy, A.A. Jalali, J. Opt. Soc. Am. B **24**, 1603 (2007)
32. F. Wang, A. Lakhtakia, Appl. Phys. Lett. **92**, 011115 (2008). The expression $\alpha = \sin^{-1}[\epsilon_g/\Delta^{(m)}]$ in this paper must be corrected to $\alpha = \tan^{-1}[\epsilon_g/\Delta^{(m)}]$
33. F. Wang, A. Lakhtakia, Phys. Rev. B **79**, 193102 (2009)
34. F. Wang, A. Lakhtakia, Proc. R. Soc. Lond. A **461**, 2985 (2005)
35. M.D. Pickett, A. Lakhtakia, Optik **113**, 367 (2002)
36. F. Wang, A. Lakhtakia, Phys. Rev. B **79**, 075115 (2011)
37. X. Huang, R. Li, H. Yang, M. Levy, J. Magn. Magn. Mater. **300**, 112 (2006)
38. A. Fedyanin, O. Aktsipetrov, D. Kobayashi, K. Nishimura, H. Uchida, M. Inoue, J. Magn. Magn. Mater. **282**, 256 (2004)
39. M. Levy, R. Li, Appl. Phys. Lett. **89**, 121113 (2006)
40. A. Lakhtakia, V.C. Venugopal, M.W. McCall, Opt. Commun. **177**, 57 (2000)
41. A. Lakhtakia, Opt. Commun. **275**, 283 (2007)
42. J. Li, L. Zhou, C.T. Chan, P. Sheng, Phys. Rev. Lett. **90**, 083901 (2003)
43. F. Wang, A. Lakhtakia, Z. Shi, SPIE Newsroom (2010). doi:10.1117/2.1201009.002581

Chapter 3
Electromagnetic Unidirectionality in Magnetic Photonic Crystals

Alex Figotin and Ilya Vitebskiy

Abstract Magnetization, either spontaneous or field-induced, is always associated with nonreciprocal circular birefringence which breaks the reciprocity principle and qualitatively changes electrodynamics of medium. In magnetic photonic crystals and other periodic structures involving magnetic components, broken reciprocity can result in electromagnetic unidirectionality, when the traveling waves can only propagate in one the two opposite directions. The unidirectional wave propagation can only occur if both time reversal and space inversion symmetries of the periodic structure are broken. During the last decade there have been numerous publications devoted to this kind of phenomenon. Our goal is to present some of those ideas.

3.1 Introduction

In this chapter we consider nonreciprocal effects in electromagnetic wave propagation in magnetic photonic crystals and other periodic structures involving magnetically polarized materials. The magnetic polarization can be spontaneous, as in ferrites or ferromagnets, or it can be induced by external magnetic field. In either case, any magnetically polarized medium has broken time reversal symmetry and does not support the Lorentz reciprocity [1]. This qualitatively changes electromagnetic properties of the medium. In a uniform substance, magnetic field or spontaneous magnetization can cause nonreciprocal circular birefringence resulting in magnetic Faraday rotation. In case of a non-uniform periodic structure, we can also have a strong asymmetry in forward and backward wave propagation. Specifically, if both time reversal and space inversion symmetries of the periodic structure are broken, light can propagate in one direction much faster or much slower than in the opposite direction. This phenomenon is essentially nonreciprocal and unique to

A. Figotin (✉)
University of California, Irvine, CA 92697, USA
e-mail: afigotin@uci.edu

I. Vitebskiy (✉)
Air Force Research Laboratory, Sensors Directorate, Wright Patterson AFB, OH 45433, USA
e-mail: ivitebsk@gmail.edu

M. Inoue et al. (eds.), *Magnetophotonics*, Springer Series in Materials Science 178,
DOI 10.1007/978-3-642-35509-7_3,

magnetic photonic crystals and some other nonreciprocal periodic structures. A fascinating consequence of spectral asymmetry is the phenomenon of electromagnetic unidirectionality [2–9]. In one scenario, a unidirectional structure, being perfectly transmissive for electromagnetic waves propagating in a certain direction, freezes the radiation of the same frequency propagating in the opposite direction [2, 3]. The frozen mode has nearly zero group velocity and greatly enhanced amplitude. In another scenario, a backward propagating mode might not exist at all [4–9]. The electromagnetic unidirectionality and the frozen mode regime are fundamentally new wave phenomena, nonexistent in uniform materials, both artificial and naturally occurring.

In this chapter, our focus is exclusively on electromagnetic unidirectionality. Since its discovery, there have been numerous publications devoted to different physical realizations of this phenomenon. Our goal is to present some of those ideas emphasizing the fundamental physical aspects of the phenomenon, as well as its practical importance.

Electromagnetic unidirectionality always implies strong asymmetry between forward and backward wave propagation. The very possibility of such an asymmetry can be established from symmetry considerations alone, which is the subject of the next section. Whether or not such an asymmetry results in electromagnetic unidirectionality depends on specific physical characteristics of the periodic structure. In the following sections, we analyze some important examples.

3.2 Bloch Waves in Periodic Structures with Broken Reciprocity

In spatially periodic structures, such as photonic crystals, the electromagnetic eigenmodes can be represented in the Bloch form

$$\Psi_k(r+a) = \Psi_k(z)\exp(ia\cdot k), \tag{3.1}$$

where k is the Bloch wave vector and a is a lattice translation. The relation between the wave vector, k, and the frequency, ω, is referred to as the Bloch dispersion relation. Real k correspond to propagating Bloch modes. In most cases, the dispersion relation is symmetric with respect to the wave vector

$$\omega(k) = \omega(-k). \tag{3.2}$$

Usually, the relation (3.2) can be viewed as a direct consequence of time reversal symmetry, R, and/or space inversion symmetry, I, of the periodic structure. Indeed, since either operation reverses the direction of the Bloch wave vector

$$Ik = -k; \qquad Rk = -k, \tag{3.3}$$

we have

$$\text{if } R\in G \text{ and/or } I\in G, \text{ then } \omega(k)=\omega(-k) \text{ for any } k, \tag{3.4}$$

where G is the space-time symmetry group of the periodic array. All nonmagnetic media always support time reversal symmetry. In addition, most of the homogeneous and periodic heterogeneous structures are centrosymmetric. As a consequence, the overwhelming majority of uniform materials and periodic structures display perfectly symmetric dispersion relation. If both, time reversal and space inversion symmetries are broken, still there might be some other symmetry operation that ensures the spectral symmetry (3.2).

Let G be the point symmetry group of the periodic structure, and $g \in G$ be a symmetry operation that changes the sign of the Bloch wave vector k. Obviously, the relation

$$gk = -k, \quad g \in G \tag{3.5}$$

provides a sufficient condition for spectral symmetry (3.2). Therefore, a necessary condition for spectral asymmetry

$$\omega(k) \neq \omega(-k) \tag{3.6}$$

is

$$gk \neq -k, \quad \text{for any } g \in G. \tag{3.7}$$

In other words, spectral asymmetry (3.6) is only possible if the point symmetry group G of the periodic structure does not include any operations changing k to $-k$.

Let us make a few remarks on the use of the above symmetry criteria.

To find which of the symmetry criteria (3.2) or (3.6) is satisfied, one can use, instead of the Bloch wave vector k, any other time-odd vector parallel to k. Examples of such time-odd vectors include the group velocity, $v_g(k)$, and the energy flux, $S(k)$, of the propagating Bloch mode. One can use v_g and/or S instead of k in (3.2) and (3.6) even if v_g or S are not parallel to k—the result will always be the same.

In 2D and 3D periodic structures it is possible that the condition (3.5) for spectral symmetry is satisfied for some, but not all directions of the Bloch wave number k. For instance, in the case of a 3D periodic structure, the condition (3.5) is satisfied for all directions of wave propagation only if this structure supports time reversal and/or space inversion symmetries. Otherwise, the criterion (3.5) can only be satisfied for some, but not all directions of wave propagation. For more examples see [2].

A bounded photonic structure with 3D periodicity can have a flat surface supporting surface waves. The surface symmetry is usually lower than that of the unbounded 3D periodic structure. In particular, a surface never supports space inversion symmetry. As a result, surface waves propagating along flat boundary of a magnetic photonic crystal can display asymmetric dispersion relation (3.6), while inside the photonic structure the Bloch dispersion relation can be perfectly symmetric. Examples of the kind were considered in [11, 12], as well as in [4–8]. Similar situation can develop with all kinds of 1D and 2D defect states, interfaces, and boundaries in 2D and 3D periodic magnetic structures.

Finally, note that the symmetry considerations based on the criteria (3.5) and (3.7) apply not only to electromagnetic waves, but also to any other Bloch excitation in periodic media, such as electrons in metals and semiconductors [10],

magnons, polaritons, etc. Also, the relations (3.5) and (3.7) have much farther reaching consequences than just the symmetry of the Bloch dispersion relations. For instance, the relation (3.5) also implies that for any linear or nonlinear wave, $\psi(r - vt)$, propagating along the specified direction, v, there exists a reciprocal, backward wave, $\psi(r + vt)$, propagating with equal and opposite velocity.

Naturally occurring substances displaying electromagnetic spectral asymmetry (3.6) have been known for decades (see, for example, [13–15], and references therein). They constitute a special class of crystalline materials known as magnetoelectrics [1]. The electrodynamics of magnetoelectric media can be described by standard time-harmonic Maxwell equations

$$\nabla \times E = i\frac{\omega}{c}\mu H, \qquad \nabla \times H = -i\frac{\omega}{c}\varepsilon E, \tag{3.8}$$

with bianisotropic constitutive relations

$$D = \varepsilon E + \xi H, \qquad B = \mu H + \zeta E. \tag{3.9}$$

Here ε and μ are electric permittivity and magnetic permeability tensors; ξ and ζ are tensors of linear magnetoelectric effect. The tensors $\zeta = \xi^T$ are odd with respect to time reversal R and space inversion I, implying that linear magnetoelectric effect is ruled out in all nonmagnetic and/or centrosymmetric structures

$$\text{if } R \in G \text{ and/or } I \in G, \text{ then } \xi = \zeta = 0. \tag{3.10}$$

Comparison of symmetry relations (3.4) and (3.10) shows that necessary conditions for linear magnetoelectric effect are similar to those of spectral asymmetry. A problem with single-phase magnetoelectric crystals is that the degree of electromagnetic spectral asymmetry there is usually negligible (10^{-4} or less). The situation is further aggravated by complicated and often unpredictable domain structure of natural magnetoelectric materials. As a consequence, the remarkable properties of magnetoelectrics featuring electromagnetic spectral asymmetry (3.6) are yet to find any practical use.

The above problems can be avoided in magnetic photonic crystals and other periodic structures involving magnetic components. Space inversion, I, can always be removed from the point symmetry group, G, of the periodic array by a proper choice of structural geometry, even if each individual constituent is a centrosymmetric material. When it comes to time reversal, R, it can only be eliminate by incorporating a material with spontaneous magnetic order (such as a ferromagnet or a ferrite) or by applying a *dc* magnetic field. In this way, the space-time symmetry group, G, of the periodic structure can always be made compatible with spectral asymmetry. Although such a structure might not display any static magnetoelectric effect, dynamically it will behave as an artificial magnetoelectric medium with exceptionally strong electromagnetic spectral asymmetry, unachievable in any single-phase bianisotropic material, natural or artificial.

3.3 Symmetry of Maxwell Equations in Magneto-Photonic Structures

At this point, all constitutive components of the periodic structure are presumed lossless. We assume also that each of the constitutive components is a uniform non-conducting material satisfying conventional constitutive relations

$$D = \varepsilon(\omega)E, \qquad B = \mu(\omega)H, \tag{3.11}$$

with Hermitian material tensors

$$\varepsilon^{\dagger}(\omega) = \varepsilon(\omega), \qquad \mu^{\dagger}(\omega) = \mu(\omega). \tag{3.12}$$

The dagger, †, denotes Hermitian conjugate. The property (3.12) of Hermiticity implies losslessness. The tensors $\varepsilon(\omega)$ and $\mu(\omega)$ are different in different components of the periodic array. The absence of magnetoelectric terms in the constitutive relations (3.11) implies that each uniform component, if it fills the entire space, has perfectly symmetric electromagnetic dispersion relation (3.2), which is the case with all nonmagnetic and an overwhelming majority of magnetic materials. At the same time we expect that a spatially periodic array of such components can support asymmetric dispersion relation (3.6). In other words, in a magnetic periodic structure, the property (3.6) of spectral asymmetry can be achieved by proper space arrangement of the constitutive components, rather than by using magnetoelectric (bianisotropic) materials.

From symmetry standpoint, a photonic crystal, being spatially periodic, can be viewed as an artificial macroscopic crystal. Therefore, every photonic crystal, or any other spatially periodic array, can be assigned certain magnetic symmetry group, G_M, which along with rotations, reflections, and translations might also include time reversal operation, R, combined with certain space transformations [1]. Knowing the magnetic symmetry group, G_M, of the periodic array, one can apply the criterion (3.7) to find whether or not one can expect asymmetric dispersion relation for a particular direction of the Bloch wave vector k. The spectral asymmetry can only occur if the symmetry group G_M is on the list of those compatible with linear magnetoelectric effect [1]. It does not mean, though, that the periodic structure will display any static magnetoelectric effect.

Finding the magnetic symmetry group, G_M, of a periodic array is a straightforward task. Indeed, knowing the geometry of the periodic array and the magnetic symmetry, $G_M(i)$, of each uniform constitutive component, one can immediately obtain the exact magnetic symmetry, G_M, of the periodic structure. By definition, the periodic array is invariant under operations from G_M. Therefore, if we substitute G in (3.7) with the magnetic symmetry group, G_M, we will get a rigorous necessary condition for spectral asymmetry.

At this point it is worth noting that the symmetry of the Maxwell equations (3.8) with the constitutive relations (3.11) can be higher than G_M. Indeed, each constitutive component, i, of the periodic structure is only represented by the respective

material tensors $\varepsilon_i(\omega)$ and $\mu_i(\omega)$ in (3.11). The space-time symmetry, $G(i)$, of the material tensors $\varepsilon_i(\omega)$ and $\mu_i(\omega)$ can be higher than the magnetic symmetry $G_M(i)$ of the material itself. For instance, both $\varepsilon_i(\omega)$ and $\mu_i(\omega)$, being second rank tensors, are always centrosymmetric, regardless of whether or not the material itself supports space inversion. In other words, the space-time symmetry of the material relations (3.11) in some of the constitutive components of the photonic crystal can be higher than the exact magnetic symmetry $G_M(i)$ of the respective materials. As a result, the symmetry group G of the Maxwell equations with the material relations (3.11) can be higher than the magnetic symmetry G_M of the periodic structure. If indeed the symmetry group G of Maxwell equations is higher than the magnetic symmetry group G_M, one can expect the situation where a particular effect, such as spectral asymmetry, is prohibited by G but allowed by $G_M \subset G$. In such a case, this particular effect can occur, but if it does, it is associated exclusively with physical processes unaccounted for by the Maxwell equations (3.8) with the conventional constitutive relations (3.11). All such interactions and effects are presumed negligible. They might include:

- electrostriction and/or magnetostriction at low frequencies, as described in [14, 28, 29],
- space dispersion, such as a reciprocal optical activity in chiral constitutive components,
- linear magnetoelectric effect in some of the constitutive components,
- surface effects at the photonic structure boundaries and at the interfaces between different constitutive components.

Hereinafter, we will focus exclusively on those space-time effects which are accounted for by the Maxwell equations (3.8) with the conventional constitutive relations (3.11). Thus, our symmetry consideration will be based on the space-time symmetry group, G, derived from the constitutive relations (3.11), rather than its subgroup, G_M. Note that in many cases, the two symmetries are simply identical ($G \equiv G_M$). But even if $G_M \subset G$, the use of the space-time symmetry, G, usually remains an excellent approximation, especially at IR and optical frequencies.

Unlike the time reversal symmetry, R, the space inversion, I, is always supported by both material tensors $\varepsilon(\omega)$ and $\mu(\omega)$ in any uniform material, regardless of the presence or absence of magnetic and/or electric polarization. To remove space inversion from space-time symmetry group G of the periodic array and, thereby, to allow for spectral asymmetry, one should choose a proper spatial arrangement of the constitutive components. To put it differently, the geometry of the photonic structure must be complex enough not to support space inversion. Note that space inversion is not an issue when it comes to surface waves or, more generally, any Bloch waves propagating along the interface of two different media or two different periodic arrays. Indeed, in the latter cases, the interface does not support space inversion, even if the media on both sides of the interface do.

3.3.1 Material Tensors of Magnetically Polarized Materials

Let us see how the presence of magnetization and/or *dc* magnetic field affects the constitutive relations (3.11) and results in violation of the reciprocity principle. More on this can be found in [1]. Consider the skew-symmetric parts of the material tensors $\varepsilon(\omega)$ and $\mu(\omega)$

$$\varepsilon_m = \frac{1}{2}\left(\varepsilon - \varepsilon^T\right), \qquad \mu_m = \frac{1}{2}\left(\mu - \mu^T\right). \tag{3.13}$$

In magnetic medium

$$\varepsilon_m \neq 0, \quad \text{and/or} \quad \mu_m \neq 0. \tag{3.14}$$

This is what distinguishes magnetically polarized medium from any other substance. In the absence of magnetic field and/or spontaneous magnetization, the permittivity and permeability tensors are symmetric at any frequency

$$\varepsilon = \varepsilon^T, \qquad \mu = \mu^T. \tag{3.15}$$

The relations (3.15) remain valid even in the presence of losses and/or gain.

The absorption and/or gain are determined by anti-Hermitian parts of the material tensors $\varepsilon(\omega)$ and $\mu(\omega)$

$$\varepsilon_a = \frac{1}{2}\left(\varepsilon - \varepsilon^\dagger\right), \qquad \mu_a = \frac{1}{2}\left(\mu - \mu^\dagger\right). \tag{3.16}$$

Without loss and gain, both $\varepsilon_a(\omega)$ and $\mu_a(\omega)$ in (3.16) are zeros, and the material tensors $\varepsilon(\omega)$ and $\mu(\omega)$ are Hermitian.

Note that the absorption and/or gain also break time reversal symmetry of the Maxwell equations (3.8) with constitutive relations (3.11). At the same time, neither absorption nor gain can affect Lorentz reciprocity. Therefore, if the periodic structure does not involve magnetic components (3.13), it cannot display spectral asymmetry (3.6), or any form of electromagnetic unidirectionality.

A properly balanced periodic array of loss and gain components can support regular, propagating Bloch modes with constant amplitude (see, for example, [30, 31], and references therein). The respective Bloch dispersion relations, though, will always be perfectly symmetric, as long as there are no magnetic components in the periodic structure.

Let us sum up this section. In a uniform, magnetically polarized substance, the imaginary skew-symmetric parts (3.13) of the material tensors $\varepsilon(\omega)$ and $\mu(\omega)$ are responsible for violation of Lorentz reciprocity [1]. If such a magnetic material is incorporated in a periodic composite structure, this can also cause the effect of spectral asymmetry (3.6), provided that the space-time symmetry, G, of the periodic array is low enough to satisfy the criterion (3.7). The criterion (3.7) is just a necessary condition for spectral asymmetry (3.6). Even if this condition is met, the effect of spectral asymmetry could be negligible or even ruled out by physical reasons different from those imposed by the space-time symmetry G. To find whether a photonic structure satisfying the criterion (3.7) displays spectral asymmetry, one has to go beyond the symmetry consideration and solve the Maxwell equations (3.8) in the non-uniform structure.

3.4 Electromagnetic Unidirectionality and the Frozen Mode Regime

In this and the following sections we consider several specific examples of periodic structures supporting strong spectral asymmetry and electromagnetic unidirectionality. Importantly, the existence of strong spectral asymmetry does not guarantee that a particular periodic structure can also display the phenomenon of electromagnetic unidirectionality, even in principle. In other words, the possibility of electromagnetic unidirectionality cannot be derived from symmetry consideration alone. Further in this section, we will focus on nonreciprocal periodic layered structures, also known as 1D magnetic photonic crystals, or periodic stacks. Periodic magnetic stacks are practically important (see, for example, [18–27] and references therein), relatively easy to analyze, and they display all important features associated with the phenomenon of electromagnetic unidirectionality, including the frozen mode regime [3, 17].

3.4.1 Periodic Layered Structures

Let us start with periodic stacks with just two different layers in a unit cell, as shown in the example in Fig. 3.1.

The space-time symmetry G of such a periodic array always supports space inversion with the center of inversion located in the middle of each uniform layer. Therefore, a periodic stack composed of two alternating layers will never display spectral asymmetry (3.6), regardless of the materials of the layers. Let us reiterate that referring to the space-time symmetry group G rather than to the true magnetic symmetry group G_M of the photonic crystal, we disregard those presumably insignificant effects which cannot be accounted for within the framework of time-harmonic Maxwell equation (3.8) with conventional constitutive relations (3.11). In most cases, though, the symmetry groups G and G_M are simply identical.

The simplest layered structure capable of supporting asymmetric Bloch dispersion relation is shown in Fig. 3.2. A unit cell of this periodic array has three layers—the minimum number of layers in a unit cell to remove inversion, I, from the space-time symmetry group G.

The magnetic F-layers have the magnetization M parallel to the z direction normal to the layers. The magnetization can be spontaneous, or field-induced. The respective material tensors are

$$\varepsilon(F)=\begin{bmatrix}\varepsilon_F & i\alpha & 0\\ -i\alpha & \varepsilon_F & 0\\ 0 & 0 & \bar{\varepsilon}_F\end{bmatrix},\qquad \mu(F)=\begin{bmatrix}\mu_F & i\beta & 0\\ -i\beta & \mu_F & 0\\ 0 & 0 & \bar{\mu}_F\end{bmatrix}. \tag{3.17}$$

The real parameters α and β are responsible for nonreciprocal circular birefringence (magnetic Faraday rotation). Both α and β are odd functions of frequency and vanish in the static limit of $\omega=0$. If the direction of magnetization is reversed, both α

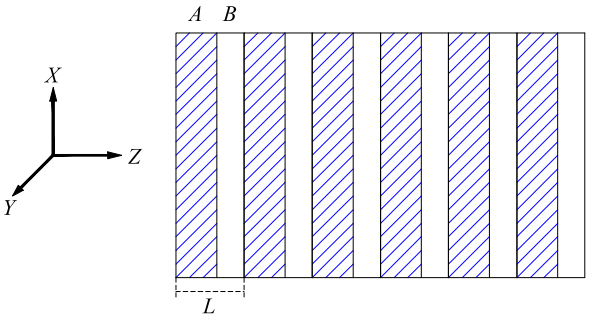

Fig. 3.1 Periodic stack with two layers A and B in a unit cell L. This stack always supports symmetric dispersion relation $\omega(k) = \omega(-k)$, regardless of the material of the layers and the direction of the Bloch wave vector k

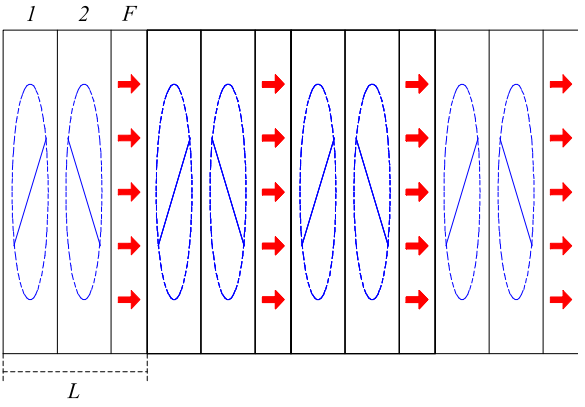

Fig. 3.2 Simplest periodic layered structure supporting asymmetric dispersion relation (3.6). A unit cell L includes three layers: a magnetic layer F with magnetization shown by the arrows, and two anisotropic dielectric layers A_1 and A_2 with different orientations φ_1 and φ_2 of the respective anisotropy axes in the x–y plane

and β in (3.17) also change sign, and so does the sense of Faraday rotation [1, 16]. In non-conducting magnetic materials, at microwave frequencies, the dominant contribution to circular birefringence usually comes from the parameter β, which can become particularly large in the vicinity of magnetic resonance. Some conducting materials placed in a very strong *dc* magnetic field can also display an α-related circular birefringence at microwave and THz frequencies. The latter effect, though, is accompanied by strong absorption, unless the mean-free-path of the charge carriers is much larger the respective Larmor (cyclotron) radius. At IR and optical frequencies, the dominant nonreciprocal contribution comes from α.

The birefringent A-layers are presumed nonmagnetic, although this is not a requirement. The respective permittivity and permeability tensors are

$$\varepsilon(A) = \begin{bmatrix} \varepsilon_A + \delta_A \cos 2\varphi_A & \delta_A \sin 2\varphi_A & 0 \\ \delta_A \sin 2\varphi_A & \varepsilon_A - \delta_A \cos 2\varphi_A & 0 \\ 0 & 0 & \bar{\varepsilon}_A \end{bmatrix}, \tag{3.18a}$$

$$\mu(A) = \begin{bmatrix} \mu_A + \Delta_A \cos 2\varphi_A & \Delta_A \sin 2\varphi_A & 0 \\ \Delta_A \sin 2\varphi_A & \mu_A - \Delta_A \cos 2\varphi_A & 0 \\ 0 & 0 & \bar{\mu}_A \end{bmatrix}. \tag{3.18b}$$

Table 3.1 Point symmetry group G of the periodic layered structure in Fig. 3.2 for different values of misalignment angle $\varphi = \varphi_1 - \varphi_2$ between the adjacent A-layers

Misalignment angle φ	Magnetic symmetry	Dispersion relation symmetry
$\varphi = 0$	$m'm'm$	$\omega(k) = \omega(-k)$ for all k
$\varphi = \pi/2$	$\bar{4}m'm'$	$\omega(k) = \omega(-k)$ for $k \parallel z$
$\varphi \neq 0, \pi/2$	$2'2'2$	$\omega(k) \neq \omega(-k)$ for $k \parallel z$

The term "nonmagnetic" implies that both material tensors (3.18a), (3.18b) are symmetric, in line with the relations (3.15). In the absence of absorption/gain, $\varepsilon(A)$ and $\mu(A)$ are also real. Note that from symmetry standpoint, whether or not the magnetic permeability $\mu(A)$ differs from unity has nothing to do with "magnetism", as long as the skew-symmetric part of $\mu(A)$ is zero. The parameters δ and Δ in (3.18a), (3.18b) describe the in-plane anisotropy (linear birefringence), while the angle φ_A defines the orientation of the principal axes of the tensors $\varepsilon(\omega)$ and $\mu(\omega)$ in the x–y plane. For simplicity, we presume that all A-layers are made of the same anisotropic dielectric material and have the same thickness. The only parameter that is different in the adjacent A-layers is the orientation φ_A.

A primitive cell in Fig. 3.2 comprises one F-layer and two A-layers with different orientations φ_1 and φ_2. The most critical parameter of this periodic structure is the misalignment angle $\varphi = \varphi_1 - \varphi_2$ between the adjacent A-layers. This angle determines the space-time symmetry group G of the stack, along with the symmetry of its electromagnetic dispersion relation. The results are summarized in Table 3.1. The periodic layered structure in Fig. 3.2 is the simplest and the most symmetric periodic stack supporting spectral asymmetry (3.6) of the Bloch dispersion relation. In this case, spectral asymmetry is only possible if the misalignment angle $\varphi = \varphi_1 - \varphi_2$ is not a multiple of $\pi/2$. More examples can be found in [2].

In order for the spectral asymmetry to be strong, the following physical conditions should be satisfied:

(1) At least one of the two gyrotropic parameters α and β of the magnetic material is large enough. Ideally, the ratio α/ε_F or β/μ_F should be larger than 0.2, but not too large.
(2) The in-plane linear birefringence in the A-layers is strong enough, but not too strong to suppress the nonreciprocal effects. Ideally, the ratio δ_A/ε_A or Δ_A/μ_A should be somewhere between 0.2 and 5.

A numerical example of electromagnetic dispersion relations of nonreciprocal periodic array in Fig. 3.2 is shown in Fig. 3.3. In accordance with Table 3.1, the spectral asymmetry (3.6) for $k||z$ develops only if the misalignment angle φ is not a multiple of $\pi/2$.

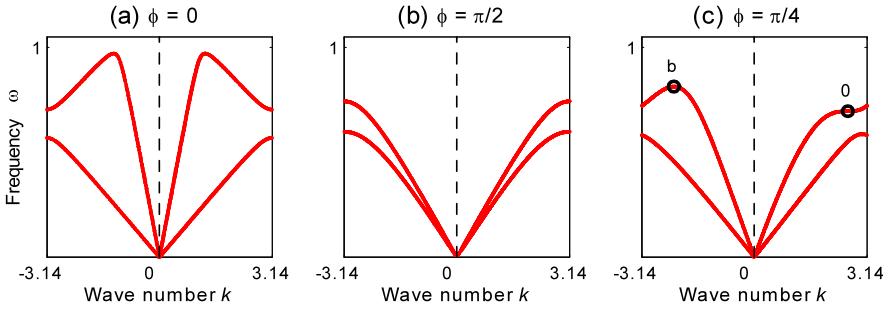

Fig. 3.3 Example of electromagnetic dispersion relations $\omega(k)$ of nonreciprocal periodic stack in Fig. 3.2. Only the two lowest frequency bands are shown. Three graphs correspond to three different values of the misalignment angle φ between adjacent A-layers. In the cases $\varphi = 0$ (no misalignment) and $\varphi = \pi/2$, the respective dispersion relation is symmetric with respect to the sign of the Bloch wave vector $k \parallel z$

3.4.2 Electromagnetic Unidirectionality

Strong spectral asymmetry has various physical consequences, one of which can be the effect of unidirectional wave propagation [2, 3]. Suppose that at $k = k_0$ one of the asymmetric spectral branches, $\omega(k)$, develops a stationary inflection point

$$\text{at } k = k_0 \text{ and } \omega = \omega_0 = \omega(k_0): \quad \frac{\partial \omega}{\partial k} = 0; \qquad \frac{\partial^2 \omega}{\partial k^2} = 0; \qquad \frac{\partial^3 \omega}{\partial k^3} > 0, \quad (3.19)$$

as shown in Fig. 3.4(a). At frequency $\omega = \omega_0$, there are two propagating Bloch waves: one with $k = k_0$ and the other with $k = k_1$. Obviously, only one of the two waves can transfer electromagnetic energy—the one with $k = k_1$ and the group velocity $v_g(k_1) < 0$. The Bloch eigenmode with $k = k_0$ has zero group velocity, $v_g(k_0) = 0$, and does not transfer energy. This latter eigenmode is referred to as the frozen mode, it is associated with stationary inflection point (3.19) of the Bloch dispersion relation. As one can see in Fig. 3.4(a), none of the two propagating eigenmodes with $\omega = \omega_0$ has positive group velocity and, therefore, none of the Bloch eigenmodes can transfer energy from left to right at this particular frequency! Thus, a periodic structure with the dispersion relation similar to that in Fig. 3.4(a), displays the property of unidirectional wave propagation at $\omega = \omega_0$.

Electromagnetic unidirectionality can be viewed as an extreme manifestation of spectral asymmetry (3.6). If spectral asymmetry happens to be weak, it does not formally rule out the phenomenon of electromagnetic unidirectionality, but it would obscure the effect. Indeed, weak Faraday rotation in the F layers and/or weak anisotropy in the A layers will result in a small value of the third derivative $\partial^3\omega/\partial k^3$ in (3.19). This, in turn, pushes the stationary inflection point ω_0 in Fig. 3.4(a) too close to the photonic band edge ω_b, as illustrated in Fig. 3.5. In the close proximity of the photonic band edge, both forward and backward waves become almost equally slow, which obscure the asymmetry in forward and backward wave propagation. Besides, in the vicinity of the photonic band edge ω_b, the periodic structure

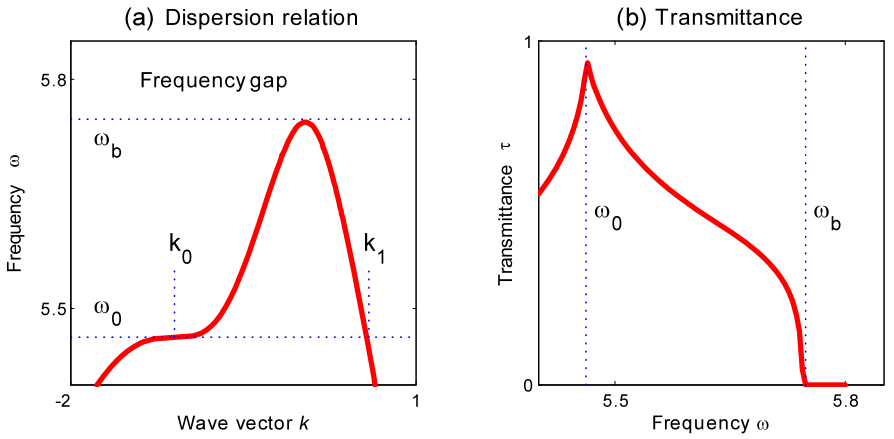

Fig. 3.4 (**a**) A fragment of asymmetric dispersion relation $\omega(k)$ of the periodic stack shown in Fig. 3.2. At $k = k_0$ and $\omega = \omega_0$ this spectral branch develops a stationary inflection point associated with electromagnetic unidirectionality and the frozen mode. The frequency ω_b designates the photonic band edge. (**b**) Frequency dependence of the transmittance, τ, of semi-infinite photonic slab with the dispersion relation in (**a**). The incident light propagates from left to right. At the frequency, ω_0, of stationary inflection point, the transmittance is close to unity, which implies that the incident wave is almost completely converted into the frozen mode with zero group velocity and drastically enhanced amplitude

becomes reflective, which implies that the incident light cannot be transmitted in the photonic crystal and converted into the slow frozen mode [17].

In cases of 2D and 3D photonic crystals, the spectral asymmetry (3.6) and electromagnetic unidirectionality do not require the presence of birefringent dielectric components in a unit cell of the periodic structure. The same is true for all kinds of periodic waveguides, photonic interfaces, and surface waves. Of course, the presence of magnetic materials with nonreciprocal constitutive relations (3.14) is still required.

3.4.3 Scattering Problem for Bounded Unidirectional Media. The Frozen Mode Regime

Consider a plane electromagnetic wave incident on a lossless, semi-infinite, unidirectional photonic structure with the electromagnetic dispersion relation shown in Fig. 3.4(a). The semi-infinite periodic structure occupies the right half-space, $z > 0$. The incident wave propagates in the positive direction along the z axis normal to the layers and hits the photonic crystal boundary at $z = 0$. At the slab boundary, a portion of the incident wave is reflected back to space and the rest of the incident radiation enters the semi-infinite photonic structure. Let S_I and S_R be the energy flux of the incident and reflected waves (at $z < 0$), and S_T be the energy flux of the wave transmitted inside the semi-infinite periodic structure (at $z > 0$). Due to energy

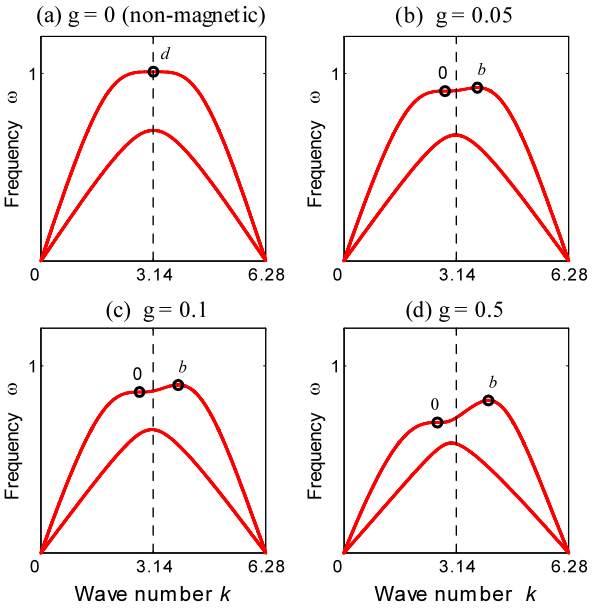

Fig. 3.5 Dispersion relation of the periodic stack in Fig. 3.2 for four different values of nonreciprocal circular birefringence, g. For any given g, the stack configuration is adjusted so that the dispersion curve $\omega(k)$ has a stationary inflection point 0, associated with the frozen mode regime. In the nonmagnetic limit (**a**), the stationary inflection point 0 merges with the frequency band edge (**b**) and they form a degenerate band edge (**d**)

conservation, $S_I + S_R = S_T$. The transmittance τ and reflectance ρ of semi-infinite medium are defined as

$$\tau = \frac{S_T}{S_I}, \qquad \rho = -\frac{S_R}{S_I}. \tag{3.20}$$

In the absence of losses and gain, the energy conservation implies that S_I, S_R, and S_T are independent of z, and also $\rho = 1 - \tau$.

Let v_g be the group velocity (along the z direction) of the transmitted Bloch mode inside the semi-infinite structure

$$\text{At } z > 0: \quad v_g = \frac{\partial \omega}{\partial k}. \tag{3.21}$$

The energy flux, S_T, of the transmitted Bloch wave can be expressed in terms of its energy density, W_T, and its group velocity, v_g

$$\text{At } z > 0: \quad S_T = W_T v_g. \tag{3.22}$$

According to (3.19) and Fig. 3.4(a), as $\omega \to \omega_0$, the wave number of the transmitted wave approaches k_0 and its group velocity, v_g, vanishes

$$v_g = \frac{\partial \omega}{\partial k} \propto |\omega - \omega_0|^{2/3} \to 0, \quad \text{as } \omega \to \omega_0.$$

Remarkably, in spite of the vanishing group velocity, the transmittance τ and the energy flux S_T remain finite even at $\omega = \omega_0$, as shown in Fig. 3.4(b). This implies that the energy density W_T inside the unidirectional slab (at $z > 0$) increases dramatically to offset the vanishing group velocity in (3.22)

$$W_T \propto W_I |\omega - \omega_0|^{-2/3}, \quad \text{as } \omega \to \omega_0,$$

where W_I is the incident light intensity. As a consequence, the incident wave with frequency close to ω_0 gets trapped inside the slab in the form of coherent frozen mode with drastically enhanced amplitude and vanishing group velocity [3, 17]. In reality, the frozen mode amplitude will be limited by such factors as absorption, nonlinear effects, imperfection of the periodic array, deviation of the incident radiation from a perfect plane monochromatic wave, finiteness of the photonic crystal dimensions, etc. Still, with all these limitations in place, the frozen mode regime is a very powerful effect and can be attractive for a variety of practical applications. Detailed analysis of this remarkable phenomenon can be found in [17] and references therein.

Consider now the case of a backward wave incidence on a semi-infinite unidirectional structure. Assume that similar unidirectional photonic crystal, with the same as before dispersion relation shown in Fig. 3.4(a), now occupies the left half-space, $z < 0$. The backward incident wave, coming from $z = +\infty$, propagates in the negative direction along the z axis and hits the photonic crystal boundary at $z = 0$. As $\omega \to \omega_0$, the wave number k of the transmitted Bloch mode at $z < 0$ approaches k_1, as shown in Fig. 3.4(a). The group velocity of the transmitted Bloch mode remains negative and large in magnitude

$$\text{At } z < 0: \quad v_g = \frac{\partial \omega}{\partial k} < 0, \quad \text{as } \omega \to \omega_0.$$

There will be no frozen mode regime in this case.

As expected, the scattering properties of a unidirectional semi-infinite medium are highly asymmetric. The frozen mode regime develops only for one of the two opposite directions of incident wave propagation.

Consider now forward and backward transmittance of a finite plane-parallel photonic slab with the dispersion relation shown in Fig. 3.4(a), in the vicinity of the stationary inflection point frequency, ω_0. The transmittance of a finite slab is usually defined as

$$t = \frac{S_P}{S_I},$$

where S_P is the energy flux of the wave exiting the slab from the opposite side. At first sight, the transmittance in the direction of zero group velocity (the forward transmittance, t_F) should be significantly different from the backward transmittance, t_B. A rigorous analysis, though, shows that the forward transmittance, t_F, averaged over the incident light polarization, is exactly equal to that of the backward transmittance, t_B:

$$\langle t_F \rangle = \langle t_B \rangle, \tag{3.23}$$

where the angle brackets $\langle \cdots \rangle$ denote averaging over incident light polarization. Importantly, the unidirectional photonic slab displays a pseudo-resonance behavior, regardless of which of the two opposite directions the incident radiation is coming from. In the vicinity of a stationary inflection point frequency, ω_0, the energy density in the middle of the plane-parallel photonic slab reaches

$$W_T \propto W_I N^2, \tag{3.24}$$

where N is the number of layers in the periodic stack. As opposed to the case of a common Fabry–Perrot resonance, the field intensity in (3.24) remains high within a relatively broad frequency range including the frozen mode frequency, ω_0, and it is not particularly sensitive to the shape of the photonic structure. For more details, see [17] and references therein.

The equality (3.23) is only valid in the absence of absorption and/or gain. Even a modest absorption, can result in a significant difference between the forward and the backward transmission. Such a behavior is reminiscent of a nonreciprocal linear isolator. If a nonreciprocal photonic crystal includes both lossy and gain component, a wave propagating in one direction can experience amplification, while the wave propagating in the opposite direction can be suppressed. The physical reasons for such a behavior are discussed in [18].

3.4.4 Nonreciprocal Waveguides

A necessary condition (3.7) for spectral asymmetry can be achieved not only in magnetic photonic crystals, but also in other nonreciprocal periodic structures, such as waveguides, periodic arrays of coupled resonators, etc. The non-uniform periodic structure provides strong spatial dispersion, while the magnetic component breaks the reciprocity. In some cases, the spectral asymmetry can result in electromagnetic unidirectionality in exactly the same way as in the case of magnetic layered structures. Namely, unidirectional wave propagation occurs at frequency ω_0 of stationary inflection point of the Bloch dispersion relations. But in the case of nonreciprocal waveguides and interfaces, there might be another, qualitatively different realization of electromagnetic unidirectionality, nonexistent in unbounded photonic crystals. An interesting example of the kind is provided by recently discovered edge waveguides formed at the interface between two photonic crystals, of which at least one is nonreciprocal (magnetic). As was first demonstrated in [4, 5] and later in [6, 7], in such a configuration, the one way light propagation can occur within a narrow but finite frequency range. This kind of electromagnetic unidirectionality is not related to a stationary inflection point of the Bloch dispersion relation, and there is no frozen mode regime in this case. Instead, this kind of unidirectionality is related to the fact that at certain frequency range, backward traveling modes do not exist at all.

Acknowledgements The research was supported through Dr. A. Nachman of the U.S. Air Force Office of Scientific Research and the Air Force Research Lab Metamaterial Portfolio.

References

1. L. Landau, E. Lifshitz, L. Pitaevskii, *Electrodynamics of continuous media* (Pergamon, New York, 1984)
2. A. Figotin, I. Vitebskiy, Phys. Rev. B **63**, 066609 (2001)

3. A. Figotin, I. Vitebskiy, Phys. Rev. B **67**, 165210 (2003)
4. S. Raghu, F. Haldane, arXiv:cond-mat/0602501v3
5. F. Haldane, S. Raghu, Phys. Rev. Lett. **100**, 013904 (2008)
6. Z. Wang, Y. Chong, J. Joannopoulos, M. Soljac, Phys. Rev. Lett. **100**, 013905 (2008)
7. Z. Yu, G. Veronis, Z. Wang, S. Fan, Phys. Rev. Lett. **100**, 023902 (2008)
8. Z. Wang, Y. Chong, J. Joannopoulos, M. Soljacic, Nature **461**, 772 (2009)
9. E. Yablonovitch, Nature **461**, 744 (2009)
10. I. Vitebsky, J. Edelkind, E. Bogachek, U. Landman, Phys. Rev. B **55**, 12566 (1997)
11. H. How, C. Vittoria, Phys. Rev. B **39**, 6823 (1989)
12. H. How, C. Vittoria, Phys. Rev. B **39**, 66331 (1989)
13. A. Freeman, H. Schmid, *Magnetoelectric Interaction Phenomena in Crystals* (Gordon and Breach, New York, 1979)
14. M. Fiebig, J. Phys. D, Appl. Phys. **38**, R123 (2005)
15. T. O'Dell, *The Electrodynamics of Magnetoelectric Media* (North-Holland, Amsterdam, 1970)
16. A. Gurevich, G. Melkov, *Magnetization Oscillations and Waves* (CRC Press, Boca Raton, 1996)
17. A. Figotin, I. Vitebskiy, Laser Photonics Rev. **5**, 201 (2011)
18. A. Figotin, I. Vitebskiy, Phys. Rev. B **77**, 104421 (2008)
19. M. Inoue et al., J. Phys. D, Appl. Phys. **39**, R151 (2006)
20. M. Inoue, T. Fujii, J. Appl. Phys. **81**, 5659 (1997)
21. M. Inoue, K. Arai, J. Appl. Phys. **83**, 6768 (1998)
22. M. Inoue, K. Arai, T. Fuji, M. Abe, J. Appl. Phys. **85**, 5768 (1999)
23. I. Lyubchanskii, N. Dadoenkova, M. Lyubchanskii, E. Shapovalov, T. Rasing, J. Phys. D, Appl. Phys. **36**, R277 (2003)
24. M. Levy, R. Li, Appl. Phys. Lett. **89**, 121113 (2006)
25. M. Levy, A.A. Jalali, J. Opt. Soc. Am. B **24**, 1603 (2007)
26. S. Khartsev, A. Grishin, J. Appl. Phys. **101**, 053906 (2007)
27. S. Kahl, A. Grishin, Appl. Phys. Lett. **84**, 1438 (2004)
28. C.-W. Nana, M. Bichurin, S. Dongb, D. Viehland, G. Srinivasan, J. Appl. Phys. **103**, 031101 (2008)
29. K. Bi, Y. Wang, D. Panb, W. Wua, Scr. Mater. **63**, 589 (2010)
30. C. Bender, S. Boettcher, Phys. Rev. Lett. **80**, 5243 (1998)
31. T. Kottos, Nat. Phys. **6**, 166 (2010)

Chapter 4
Magneto-Optics of Plasmonic Crystals

V.I. Belotelov, A.N. Kalish, and A.K. Zvezdin

Abstract Plasmonics has been attracting considerable interest as it allows localization of light at nanoscale dimensions. A breakthrough in integrated nanophotonics can be obtained by fabricating plasmonic functional materials. Such systems may show a rich variety of novel phenomena and also have huge application potential. In particular magnetooptical materials are appealing as they may provide ultrafast control of laser light and surface plasmons via an external magnetic field. Here we give a review of the state of the art in the area of magnetoplasmonics and consider a new metal–dielectric heterostructure: plasmonic crystal formed by a periodically perforated with slit or hole arrays noble metal film on top of a ferromagnetic dielectric film. It provides a significant enhancement of magneto-optical effects as proved by the observation of increase of the intensity and polarization rotation effects near Ebbesen's extraordinary transmission peaks by several orders of magnitude. Surface plasmon polaritons as well as waveguide modes play a decisive role in this enhancement. The plasmonic crystal can be operated in transmission, so that it may be implemented in devices for telecommunication, plasmonic circuitry, magnetic field sensing and all-optical magnetic data storage.

Abbreviations

SPP	surface plasmon polariton
TE	transverse electric
TM	transverse magnetic
TMOKE	transverse magneto-optical Kerr effect

V.I. Belotelov (✉) · A.N. Kalish
Prokhorov General Physics Institute, Russian Academy of Sciences, Moscow 119991, Russia
e-mail: belotelovvi@gmail.com

V.I. Belotelov · A.N. Kalish
Lomonosov Moscow State University, Moscow 119991, Russia

A.K. Zvezdin (✉)
Lebedev Physical Institute, Russian Academy of Sciences, Moscow 119991, Russia
e-mail: zvezdin@gmail.com

A.K. Zvezdin
Moscow Institute of Physics and Technology (State University), Dolgoprudny 141700, Russia

M. Inoue et al. (eds.), *Magnetophotonics*, Springer Series in Materials Science 178,
DOI 10.1007/978-3-642-35509-7_4,

4.1 Introduction

4.1.1 Magneto-Optics and Plasmonics

The magnetic field influence on light was discovered by M. Faraday in the middle of the 19th century [1]. Nowadays, magneto-optical effects are considered for nanophotonics applications requiring manipulation of light at gigahertz frequencies [2–4]. The magneto-optical effects allow manipulation with light polarization and intensity via medium magnetization. The magnetization can be controlled in turn by either external magnetic field which is the most straightforward approach or by the intense laser pulse of proper polarization [5–7]. The latter possibility could allow to pass to even shorter operation times lying at subpicosecond time scale.

A prospective example of the magneto-optical effects is the transverse magneto-optical Kerr effect (TMOKE) providing an intensity change of light reflected from a ferromagnetic metal if an applied external magnetic field is reversed [8]. The TMOKE allows one to investigate magnetic material properties and can be utilized in magneto-optical data storage [3, 9]. The relative change of the reflected light intensity in the TMOKE is on the order of 10^{-3}, limiting its applicability [3, 10]. The TMOKE's counterpart in transmission may also occur, for which a necessary condition is a difference between the opposite magnetic-film boundaries. However, it is difficult to observe because of the small transmission through ferromagnetic metals in addition to its small magnitude [11].

The other very important and well-known magneto-optical effect is the Faraday effect. In a magnetized medium the refractive indices for right- and left- handed circular polarized light propagating along the magnetization are different. This effect manifests itself in rotation of polarization plane as light propagates through a transparent magnetized medium along its magnetization. The Faraday effect is usually observed in transmitted light, though it is also present in reflection when light propagates back and forth in a magnetic film. In visible range specific Faraday rotation could be as large as several degrees per micron for rare-earth iron garnet films having high level of substitution with bismuth [3, 12, 13].

Apart from the two aforementioned effects the family of the magneto-optical effects also includes two other polarization rotation effects: the longitudinal and the polar Kerr effects observed in reflection configuration and the effect of magnetic circular dichroism observed in Faraday configuration. All of these effects are odd in magnetization.

There are also magneto-optical effects that are even in magnetization. One of them is the Cotton–Mouton or Voigt effect. This effect results from the difference of refractive indices of two components of light radiation, which are linearly polarized parallel and perpendicular to magnetization, when the light propagates in a transversely magnetized medium (the wavevector is perpendicular to the magnetization). A linearly polarized light that has its polarization plane oriented at an angle to the

magnetization direction becomes elliptically polarized after propagation through the medium.

The other even magneto-optical effect is called orientational effect. It was experimentally discovered for Ni films and was determined by a relative change δ of reflected light intensity when film's magnetization changes its orientation with respect to the plane of light incidence. Typical values of this effect for Ni are of about 10^{-3} [14].

It is this smallness which has been preventing an invasion of magneto-optics into applied nanophotonics so far. Therefore, it is essential to seek for strategies to enhance magneto-optical effects, for which there are several ways. While the potential of methods relying purely on material synthesis is almost exhausted, nanostructuring is very prospective for tailoring the optical properties of materials [15]. This approach reflects a new paradigm of modern optics in which optical properties are mainly determined by geometrical resonances rather than by electronic ones. An example of a fruitful magneto-optical implementation of this approach is a magnetophotonic crystal providing a considerable enhancement of the Faraday effect [16–18].

The other rather interesting approach to boost magneto-optical effects involves surface plasmon polaritons (SPP)—coupled oscillations of the electromagnetic field and the electron plasma in a metal which are localized and propagate along a metal/dielectric interface [19]. Nowadays, the field of plasmonics represents an exciting new area for the application of surface plasmons in which surface-plasmon-based circuits merge the fields of photonics and electronics at the nanoscale [20]. Indeed, SPPs can serve as a basis for constructing nanoscale photonic circuits that will be able to carry optical signals and electric currents [21]. Surface plasmons can also serve as a basis for the design, fabrication and characterization of subwavelength waveguide components [22]. In the framework of plasmonics, modulators and switches have also been investigated [23], as well as the use of SPPs as mediators in the transfer of energy from donor to acceptors molecules on opposite sides of metal films [24].

In the last years many significant discoveries were made in plasmonics. It was demonstrated that the strong electromagnetic field energy concentration arises at SPPs excitation. It leads to harsh increase of light-matter interaction efficiency and enhancement of optical effects like nonlinear effects and Raman scattering. Nevertheless, the potential of plasmonics has not yet been fully discovered and there are many directions for investigations in this area. In particular, introducing functional materials in plasmonics is very prosperous as they change their properties by external forces.

One possibility is to use magneto-optical functional materials. The marriage of plasmonics and magneto-optics looks mutually beneficial [25]. On the one hand, magnetic field is a nice tool to control SPPs, and on the other hand SPPs can be utilized to enhance magneto-optical effects. In this chapter we consider plasmonic structures containing magneto-optical materials and discuss current state of the art in this area.

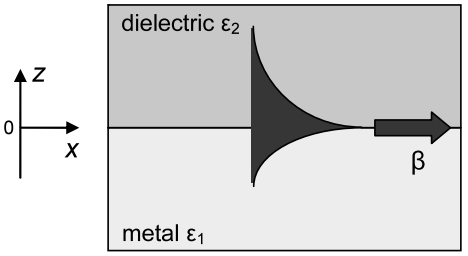

Fig. 4.1 The surface plasmon polariton (shown as the decaying electromagnetic field with maximum at $z = 0$) propagating along the metal–dielectric interface

4.1.2 Surface Plasmon Polaritons in Smooth and Perforated Metal–Dielectric Structures

The existence of self-sustained collective excitations of electron plasma and an electromagnetic field localized at the metal/dielectric interfaces was predicted by Ritchie in 50-s of the previous century [26]. Experimental proof of Ritchie's work followed shortly afterwards by a series of electron energy-loss experiments after which the term *surface plasmon* was coined to name the quanta of these collective oscillations [27]. Since then, there has been significant progress in investigations of SPPs, which played a key role in many problems of condensed matter and surface physics.

Frequency of collective plasma oscillations—plasma frequency—in a free electron gas is $\omega_p = (ne^2/m)^{1/2}$ (in SI units), where n is an equilibrium density, e and m are electron charge and mass, respectively. In the presence of a planar interface between a plasma medium and a nonconducting medium a surface plasmon mode appears. Its frequency is lower than that of the bulk plasma: $\omega_s = \omega_p/\sqrt{1+\varepsilon_2}$, where ε_2 is the permittivity of the nonconducting medium. If phase speed of the surface plasmon is compared with the speed of light c it can be coupled with an electromagnetic field thus originating the *surface plasmon polariton* mode. An SPP is a TM polarized wave having the following components of the electromagnetic field:

$$\begin{aligned} H_y &= A\exp(i\beta x + \gamma_1 z - i\omega t), \\ E_x &= -A\frac{i\gamma_1}{\omega\varepsilon_0\varepsilon_1}\exp(i\beta x + \gamma_1 z - i\omega t), \\ E_z &= -A\frac{\beta}{\omega\varepsilon_0\varepsilon_1}\exp(i\beta x + \gamma_1 z - i\omega t) \end{aligned} \tag{4.1}$$

for $z < 0$ (see Fig. 4.1) and

$$\begin{aligned} H_y &= A\exp(i\beta x - \gamma_2 z - i\omega t), \\ E_x &= A\frac{i\gamma_2}{\omega\varepsilon_0\varepsilon_2}\exp(i\beta x - \gamma_2 z - i\omega t), \\ E_z &= -A\frac{\beta}{\omega\varepsilon_0\varepsilon_2}\exp(i\beta x - \gamma_2 z - i\omega t) \end{aligned} \tag{4.2}$$

for $z > 0$. Here A is the SPP amplitude, γ_1 and γ_2 define decay rate of the electromagnetic field in both media, and β is the absolute value of the SPP wavevector. Boundary conditions at $z = 0$ lead to

$$\frac{\gamma_1}{\varepsilon_1} + \frac{\gamma_2}{\varepsilon_2} = 0. \tag{4.3}$$

This relation imposes two conditions on the real parts of the adjacent media permittivities ε_1' and ε_2': $\varepsilon_1' < 0$, $\varepsilon_2' > 0$, and $|\varepsilon_1'| > \varepsilon_2'$. Fulfillment of these conditions is necessary for the SPP wave localization at the interface. They are all satisfied, for example, for the case of a dielectric and a metal below plasma frequency. The permittivity of a noble metal can be described by the Drude model:

$$\varepsilon_1 = \varepsilon_{\text{ib}}(\omega) - \frac{\omega_p^2}{\omega^2 + i\nu\omega}, \tag{4.4}$$

where $\varepsilon_{\text{ib}}(\omega)$ is the part of the metal permittivity describing contribution of the interband electron transitions, ν is the free electron scattering rate, and ω is an angular frequency of light. Consequently, metal can sustain SPPs for the frequencies $\omega < \omega_p/\sqrt{\text{Re}(\varepsilon_{\text{ib}})}$. Here we neglected optical losses and frequency dependence of ε_{ib}.

The electromagnetic field decays in each of the two adjacent media at a rate of

$$\gamma_i = k_0 \sqrt{\frac{-\varepsilon_i^2}{\varepsilon_1 + \varepsilon_2}}, \tag{4.5}$$

with $i = 1, 2$, $k_0 = \omega/c$. It allows defining the attenuation length of the SPP in normal to the interface direction $l_{zi} = 1/\gamma_i$.

The dispersion of the SPP mode is given by

$$\beta = k_0 \sqrt{\frac{\varepsilon_1 \varepsilon_2}{\varepsilon_1 + \varepsilon_2}}. \tag{4.6}$$

Since both media can be absorptive the propagation constant β has both real and imaginary parts: $\beta = \beta' + i\beta''$. The latter determines the SPP propagation length along the interface l_x:

$$l_x = 1/\beta'' = \frac{2}{k_0} \frac{(\varepsilon_1')^2}{\varepsilon_1''} \left(\frac{\varepsilon_1' + \varepsilon_2}{\varepsilon_1' \varepsilon_2} \right)^{3/2}. \tag{4.7}$$

Here we assumed that optical losses in the dielectric are much smaller than that in the metal, so that $\varepsilon_1'' \gg \varepsilon_2''$ is satisfied for imaginary parts of the metal and dielectric permittivities ε_1'' and ε_2'', respectively.

A thin metal film can also support SPPs. In the case of a thin metal film of thickness h_m in the symmetric surrounding of a dielectric, the interaction of the electromagnetic field on both interfaces leads to two equations:

$$\tanh \gamma_1 h_m = -\frac{\gamma_2 \varepsilon_1}{\gamma_1 \varepsilon_2}, \tag{4.8a}$$

$$\tanh \gamma_1 h_m = -\frac{\gamma_1 \varepsilon_2}{\gamma_2 \varepsilon_1}. \tag{4.8b}$$

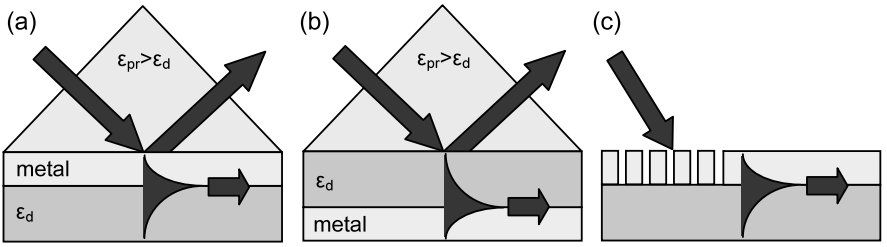

Fig. 4.2 SPP excitation configurations. (**a**) Kretschmann configuration. (**b**) Otto configuration. (**c**) Diffraction on a grating

It can be shown that (4.8a) corresponds to modes of odd vector parity ($E_x(z)$ is odd, $E_z(z)$ and $H_y(z)$ are even functions of z), while (4.8b) corresponds to modes of even vector parity ($E_x(z)$ is even, $E_z(z)$ and $H_y(z)$ are odd functions of z) [19].

Odd modes have the prominent feature that upon decreasing metal film thickness, the electromagnetic energy distribution shifts away from the metal film and the mode tends to become a plane wave in a bulk dielectric surrounding. This implies a drop in β'' and a significant increase of the SPP propagation length l_x [28]. That is why odd parity mode is usually called a *long-range* SPP. The even modes behave oppositely—their confinement to the metal film for thinner films increases and propagation length l_x becomes smaller.

For the case of non-symmetrical dielectric environment of the metal film a dispersion relation of the SPP is given by

$$\exp(-4\gamma_1 h_m) = \frac{\gamma_1/\varepsilon_1 + \gamma_2/\varepsilon_2}{\gamma_1/\varepsilon_1 - \gamma_2/\varepsilon_2} \frac{\gamma_1/\varepsilon_1 + \gamma_3/\varepsilon_3}{\gamma_1/\varepsilon_1 - \gamma_3/\varepsilon_3}, \tag{4.9}$$

where ε_3 is the dielectric permittivity of the second adjacent dielectric. A metal film in asymmetric environment also sustains two modes—a high index mode which is mostly concentrated in the high refractive index dielectric and a low index mode mostly concentrated in the low refractive index dielectric.

It is important to know that a wavevector of a free electromagnetic wave inside the dielectric given by $k_0\sqrt{\varepsilon_2}$ is less than the SPP wavevector at the metal/dielectric interface by a factor of $\sqrt{\varepsilon_1/(\varepsilon_1+\varepsilon_2)} > 1$. It prevents direct coupling of light to the SPP mode. That is why to excite SPPs some special experimental arrangements have been designed. The photon and SPP wavevectors can be matched by using either photon tunneling in the total internal reflection geometry (Kretschmann and Otto configurations) or diffraction effects (Fig. 4.2).

In the Kretschmann configuration (Fig. 4.2(a)), a metal film is illuminated through a dielectric prism at an angle of incidence θ greater than the critical angle for the total internal reflection [29]. If a dielectric constant of prism $\varepsilon_{\text{pr}} > \varepsilon_2$ then the momentum conservation law can be satisfied along the interface: $\beta = k_0\sqrt{\varepsilon_{\text{pr}}}\sin\theta$. At this angle of incidence the resonant light tunneling through the metal film occurs, and the light is coupled to the SPP at the lower interface and a sharp minimum is observed in reflection spectrum from the prism–metal interface indicating that the

light is efficiently coupled to SPPs. At this a significant electromagnetic energy concentration near the metal/dielectric interface is observed. The field intensity at the interface can exceed the one in the incident light by more than two orders of magnitude. The Kretschmann method is applicable for the case of not very thick metals ($h_m < 80$ nm). For thicker films the tunneling efficiency is too low.

Otto configuration allows SPP excitation at the upper interface of the metal (Fig. 4.2(b)). Here, the prism where the total internal reflection occurs is placed close to the metal surface, so that the photon tunneling occurs through the air gap between the prism and the surface [30].

Another way to provide the wavevector conservation for the SPP excitation is to use diffraction effects. It can be realized if either a metal or a dielectric is periodically perforated by a slit or hole array. Such gratings provide diffracted light with different in-plane wavevector components. If some of them coincides with the SPP wavevector then the light will be coupled to SPPs (Fig. 4.2(c)). In this case the momentum conservation law is written by

$$k_0\sqrt{\varepsilon_3}\sin\theta\mathbf{e}^{(\mathrm{in})} = \beta\mathbf{e}_{\mathrm{SPP}} + u_1\mathbf{G}_x + u_2\mathbf{G}_y, \tag{4.10}$$

where ε_3 is the dielectric constant of the medium above the metal/dielectric structure, θ is an angle of incidence, $\mathbf{G}_x$ and $\mathbf{G}_y$ are two reciprocal lattice vectors, $|\mathbf{G}_x| = 2\pi/d_x$, $|\mathbf{G}_y| = 2\pi/d_y$; d_x and d_y are periods of the grating in x- and y-directions; $\mathbf{e}^{(\mathrm{in})}$, $\mathbf{e}_{\mathrm{SPP}}$ are two in-plane unit vectors along the plane of light incidence and along the SPP propagation direction, respectively, u_1 and u_2 are integers. In the grating configuration SPPs can be excited on the both metal film interfaces.

Strictly speaking, the absolute value of the wavevector β of the grating SPP in (4.10) deviates from the one determined by (4.6), (4.8a) (4.8b), and (4.9). In the case of a metal grating with narrow slits/holes on a smooth dielectric this deviation is usually rather small and formulas for smooth interfaces are well applicable. The SPP dispersion in the structure of a smooth metal and perforated dielectric can be also approximately calculated via (4.6), (4.8a) (4.8b), or (4.9) but substituting a permittivity of the perforated dielectric with the one calculated from Lichtenecker equation: $|\varepsilon_2^{(\mathrm{eff})}| = (1-f)|\varepsilon_2| + f|\varepsilon_2^{(f)}|$, where f is the fraction coefficient, $\varepsilon_2^{(f)}$ is the dielectric function of the substance filling the slits/holes (usually, $\varepsilon_2^{(f)} = 1$) [31]. Usually, f is close in value to the fraction of the slit/hole volume with respect to the unit cell volume.

However, the periodicity of the slits/holes does not allow to describe SPP dispersion fully by the effective medium approach. This becomes mostly pronounced at $k = u(\pi/d)$ with an integer u, where the dispersion curve splits into two branches: low and high frequency and a band gap appears. This phenomenon is a general feature of any periodic structure with a period comparable with the wavelength of the wave propagating through it. Such periodic structures dealing with photons are called photonic crystals. That is why periodic metal-dielectric structures considered here can be referred to as *plasmonic crystals*. Plasmonic crystals allow tailoring dispersion of SPP in a desired way and concentration electromagnetic energy in a small volume near the metal/dielectric interface. The latter was shown recently to have a

great potential for ultrafast nanophotonics since it allows switching permittivity of gold by a short laser pulse at a time scale of several hundreds of femtoseconds [32].

The SPP dispersion in metal gratings with wide slits/holes cannot be described by smooth interface SPP model. The metal part of such structure should be considered rather like a periodic array of metal wires. In this case localized plasmonic resonances in each individual metal wire are excited [33]. Frequencies of these resonances depend strongly on the metal wire size and shape. If a grating of metal wires is deposited on the thin dielectric film then localized plasmonic modes couple with optical waveguide modes, resulting in the formation of a waveguide-plasmon polariton [34].

Localized surface plasmons play significant role in optical properties of metal nanoparticles. Usually, their frequencies can be determined in the non-retarded (electrostatic) approximation by solving Laplace's equation with suitable boundary conditions. The electrostatic approximation, which neglects the effects of retardation, is valid if the characteristic size of a system is small compared to the wavelength corresponding to the localized plasmon frequency. In this approximation frequency of the localized plasmon excited in a metal sphere is given by

$$\omega_l = \omega_p \left(\frac{l}{\varepsilon(l+1)+l} \right)^{1/2}, \tag{4.11}$$

where ε is a dielectric constant of a surrounding medium, and l is a number of multipole expansion ($l = 1$ for dipole excitation) [33].

4.1.3 Magneto-Optical Effects in Bulk Media

4.1.3.1 Description of Magneto-Optical Effects in Classical Electrodynamics

Particular properties of a medium in the macroscopic theory of the magneto-optical phenomena are defined by the form of $\hat{\varepsilon}$- and $\hat{\mu}$-tensors. It is enough to consider just the $\hat{\varepsilon}$-tensor, because the properties that we describe below are similar for $\hat{\varepsilon}$- and $\hat{\mu}$- tensors. Besides, for visible and near infrared light $\hat{\mu}$-tensor is approximately equal to the unit tensor. In the magnetically ordered state $\hat{\varepsilon}$-tensor depends on the order parameter. In ferromagnets the order parameter is magnetization **M**, in antiferromagnets it is the sublattice magnetization, and so on. We shall confine our discussion to ferromagnets.

Let us consider the simplest case of an optically isotropic ferromagnet. The presence of magnetization reduces the symmetry to the single-axis one. $\hat{\varepsilon}$-tensor can be represented as a sum of symmetric and antisymmetric tensors, which is given by [3]:

$$\hat{\varepsilon} = \begin{pmatrix} \varepsilon_0 & 0 & 0 \\ 0 & \varepsilon_0 & 0 \\ 0 & 0 & \varepsilon_0 \end{pmatrix} + ig(\mathbf{M}) \begin{pmatrix} 0 & -m_z & m_y \\ m_z & 0 & -m_x \\ -m_y & m_x & 0 \end{pmatrix} + b(\mathbf{M}) \begin{pmatrix} m_y^2 + m_z^2 & -m_x m_y & -m_x m_z \\ -m_x m_y & m_x^2 + m_z^2 & -m_y m_z \\ -m_x m_z & -m_y m_z & m_x^2 + m_y^2 \end{pmatrix}, \tag{4.12}$$

where $\mathbf{m} = \mathbf{M}/M$, ε_0 is the dielectric permittivity of the medium at $\mathbf{M} = 0$, $\mathbf{g} = g\mathbf{m}$ is the gyration vector. In an isotropic medium normally $\mathbf{g} = a\mathbf{M}$. If there is absorption, then

$$\varepsilon_0 = \varepsilon_0' + i\varepsilon_0'', \qquad g = g' + ig'', \qquad b = b' + ib'' \tag{4.13}$$

are complex functions of the frequency. The second terms in (4.12) and (4.13) define the gyrotropic effects: magnetic gyrotropic birefringence and magnetic circular dichroism. The last terms define optical magnetic anisotropy: magnetic linear birefringence and magnetic linear dichroism. The constants g and b become zero when $\mathbf{M}$ approaches zero.

Usually for the characterization of magneto-optical effects the magneto-optical (Voigt) parameter Q is used. It is defined as

$$Q = Q' + iQ'' = g/(\varepsilon_0 + b). \tag{4.14}$$

Normally, $|Q| \ll 1$. If $\hat{\mu}$-tensor can no longer be considered as a unit tensor then both Q and Q_M need to taken into account and the magneto-optical medium is called bi-gyrotropic.

In crystals the dependence of $\hat{\varepsilon}$-tensor on $\mathbf{M}$ is more complicated, namely

$$\varepsilon_{ik} = \varepsilon_{ik}^0 - ie_{ikl}g_l + \delta_{iklm}M_lM_m, \tag{4.15}$$

where $g_l = a_{lq}M_q$, e_{ikl} is the antisymmetric 3D-order pseudotensor (the Levi-Civita tensor). The polar tensors ε_{ik}^0, a_{lq}, δ_{iklm} are defined by the crystallographic symmetry.

4.1.3.2 Magneto-Optical Effects of Light Polarization Rotation

The magneto-optical Faraday effect manifests itself in a rotation of polarization plane of a linearly polarized light at an angle Φ when the light propagates along the medium magnetization $\mathbf{M}$. In the electromagnetic theory the Faraday effect can be explained as follows. When the medium magnetization has non-zero projection on the wave vector $\mathbf{k}_0$ of the incident radiation, two independent fundamental Maxwell's equations solutions are circular polarized waves with different refractive indices n_+ and n_-, respectively. At the output of the magnetic medium these waves gain phase shift and when added give linearly polarized wave with rotated polarization plane. That is why the Faraday effect is also called magnetic circular birefringence [35].

The angle of the light polarization plane rotation is given by

$$\Phi = \Phi_{\text{sp}}h = -\frac{k_0 g' h}{2n_0}, \tag{4.16}$$

where Φ_{sp} is the specific Faraday rotation (rotation of polarization plane of the wave per unit length of the sample, typical values of Φ_{sp} are 0.1–3°/μm), $n_0 = \frac{1}{2}(n_+ + n_-)$, h is sample's thickness.

If a medium is absorptive, the absorption coefficients of the right-and left- handed circular polarized light are different. This phenomenon is called magnetic circular dichroism. After transmission through a medium that exhibits such properties, the light changes its polarization from linear to elliptical. The elliptical polarization is characterized by the orientation angle Φ, which is analogous to the Faraday angle, and ellipticity Ψ. Ellipticity is calculated by

$$\Psi = -\frac{k_0 g'' h}{2n_0}. \tag{4.17}$$

Along with the magneto-optical effects that are observed in transmission, there is a number of effects that manifest themselves when light is reflected from a surface of a magnetized material. These are magneto-optical Kerr effects. There are three types of the Kerr effect, which are differentiated depending on a mutual orientation of the magnetization, with respect to both the wave propagation direction and the normal to the surface [36].

The complex polar Kerr effect consists of both the rotation of polarization plane and the appearance of the ellipticity if a linearly polarized light reflects from a sample surface and the sample is magnetized normally to this surface. If light falls from a vacuum perpendicularly to the sample surface, the expression for the complex polar Kerr effect takes the following form:

$$\tilde{\Phi}_K = \Phi_K + i\Psi_K = \frac{inQ}{n^2 - 1}, \tag{4.18}$$

where Φ_K is the Kerr rotation angle and Ψ_K is the ellipticity. The longitudinal Kerr effect also means both the rotation of polarization plane and the appearance of the ellipticity when a linearly polarized light reflects from a sample surface provided that the magnetization vector belongs to both the sample plane and the light incidence plane.

4.1.3.3 Odd Magneto-Optical Intensity Effect

Like the above-mentioned effects, the transverse magneto-optical Kerr effect (TMOKE) is linear in magnetization. The TMOKE may be observed only in absorbing materials if the magnetization lies in the sample plane but is perpendicular to the light incidence plane. For the p-polarization of the incident light (light polarization is in the incident plane) it is measured by the relative change in the reflected light intensity when the medium is remagnetized

$$\delta_p = \frac{I(\mathbf{M}) - I(-\mathbf{M})}{I(0)} = 2\,\mathrm{Im}\,\rho_{12}^p, \tag{4.19}$$

where $I(\mathbf{M})$ and $I(0)$ are the intensities of the reflected light in the magnetized and non-magnetized states, respectively,

$$\rho_{12}^p = \frac{r_{12}^p Q \sin\theta}{(\varepsilon - \sin^2\theta)^{1/2}}, \tag{4.20}$$

r_{12}^{p} is the conventional Fresnel coefficient for reflection:

$$r_{12}^{p} = \left(\varepsilon\cos\theta - \sqrt{\varepsilon - \sin^2\theta}\right)/\left(\varepsilon\cos\theta + \sqrt{\varepsilon - \sin^2\theta}\right),$$

and θ is the angle of incidence [3]. For the s-polarization (light polarization is perpendicular to the incidence plane) the TMOKE can be observed only in bi-gyrotropic media.

4.1.3.4 Second-Order in Magnetization Magneto-Optical Effects

If light propagates perpendicular to the medium magnetization then the Cotton-Mouton or Voigt effect arise [37]. This effect results from the difference of refractive indices of two components of the electromagnetic wave, which are linearly polarized parallel and perpendicular to the magnetization. That is why the Voigt effect is also called the effect of linear magnetic birefringence. A linearly polarized light having its polarization plane oriented at an angle to the magnetization direction becomes elliptically polarized after propagation through the medium.

The refractive index for the light component perpendicular to the magnetization is given by

$$n_{\perp} = \sqrt{\varepsilon + b - g^2/\varepsilon}, \tag{4.21}$$

while for the polarization along the magnetization it remains the same as the one for the non-magnetized medium $n_{\parallel} = \sqrt{\varepsilon}$. The Voigt effect is often revealed in experiment as a relative phase shift of the two polarization components per unit length of a sample:

$$B_V = (\omega/c)\left|\mathrm{Re}(n_{\parallel} - n_{\perp})\right|. \tag{4.22}$$

The Voigt effect is quadratic in magnetization, i.e. it is the second-order effect in the contrary to the Faraday effect which is linear in magnetization.

The linear magnetic birefringence also leads to the changes in light reflection and transmission coefficients when the medium magnetization is rotated in the plane of the magnetic film. Indeed, if for one orientation of magnetization it coincides with the incident light polarization then the reflection and transmission are the same as ones for the non-magnetized medium. In-plane magnetization rotation by 90° makes it perpendicular to the light polarization thus changing refractive index of the medium (see (4.21)) and the reflection and transmission coefficients. A second-order in magnetization magneto-optical effect can be defined by

$$\delta = \frac{I_{\parallel} - I_{\perp}}{I_{\parallel}}, \tag{4.23}$$

where $I_{\parallel(\perp)}$ is the reflected or transmitted intensity for the cases of the magnetization parallel (perpendicular) to the light polarization. It should be noted that $I_{\parallel} = I_0$, where I_0 is the reflection or transmission for a non-magnetized medium.

The even magneto-optical reflection and transmission effects were experimentally observed in monocrystalline and polycrystalline Fe, Ni, Co films [38–41]. For

the crystals the permittivity tensors usually has complicated form (4.15) and the even magneto-optical intensity effect becomes also very sensitive to the position of the magnetization and the plane of light incidence with respect to the crystallographic axes and its phenomenological description is rather cumbersome [42]. To emphasize on this feature a term *orientational magneto-optical effect* (OME) was introduced [40]. It was comprehensively experimentally studied for Ni films [14, 44].

The typical values of the orientational effect for Fe, Ni, and permalloy in the visible and near infrared spectral band are of the order of $\delta_{\mathrm{OME}} \sim (0.1\text{–}1) \times 10^{-3}$.

4.2 The Transverse Magneto-Optical Kerr Effect in Plasmonic Structures

4.2.1 State of the Art

Early papers on the interplay between SPPs and magneto-optics addressed SPPs propagating along the smooth surface of a ferromagnetic film [45–47] or along a smooth semiconductor surface in an external magnetic field [48, 49]. In that case, the magnetic field modifies the SPP wave vector but leaves its transverse magnetic polarization (TM) unchanged.

The SPP assisted increase of the TMOKE was reported. At the same time, it was shown in [50] that the most efficient enhancer of the TMOKE is the high-quality long range SPP. In other papers bimetallic systems of noble and ferromagnetic metals were considered. The SPPs propagate a long distance along the noble metal and air interface and they enhance the TMOKE taking place at the ferromagnetic surface [51–53]. Such an interesting concept of magneto-optical and plasmonic interfaces spaced by several tens of nanometers leads to further enhancement of the TMOKE by several times. It was also demonstrated that similar structures increase sensitivity of gas sensors [54].

One more approach is to substitute the ferromagnetic metal by a low absorptive noble one and to make the dielectric layer magnetized. It allows the long range SPPs to propagate exactly at the magnetized surface without any spacing which makes the TMOKE even larger [55]. It seems to be the optimal case for the smooth films. However, the specially tailored nanostructuring of plasmonic systems can allow more pronounced enhancement.

Nanostructured plasmonic systems were also investigated recently [56–64]. They mostly utilize periodicity to excite propagating plasmonic modes and to observe influence of SPPs on the TMOKE. That is why such a kind of structures can be attributed to the class of plasmonic crystals. There are several designs of a plasmonic crystal with magnetic media (Fig. 4.3).

A resonant increase of the TMOKE was reported for one-dimensional Co, Fe and Ni gratings [56, 62] (Fig. 4.3(a)). Though the propagation length of SPPs on ferromagnetic metals l_x (see (4.7)) is rather small and does not exceed several microns, it still counts several periods of the structure and the periodicity plays an

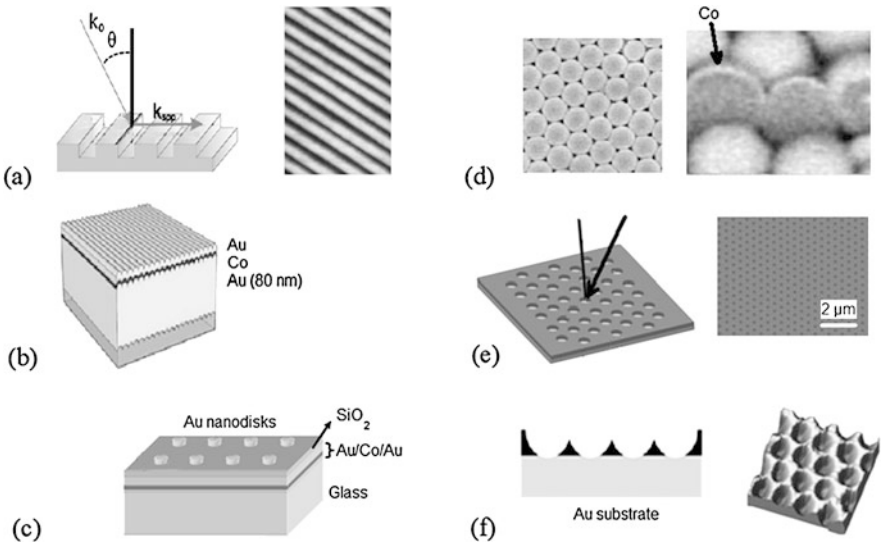

Fig. 4.3 Different types of plasmonic crystal with magnetic constituents. (**a**) 1D nickel grating: (*left*) schematics and (*right*) AFM image [56]. (**b**) Trilayer Au/Co/Au grating on a polycarbonate grating [57]. (**c**) Gold nanodiscs on the Au/Co/Au trilayer [58]. (**d**) 2D nanocorrugated magnetic film of cobalt on the top of PMMA colloidal crystal: (*left*) SEM image and (*right*) microphotography of the particles cross section made by focused Ga ion beam, the Co coverage is visible as a bright layer [59]. (**e**) 2D plasmonic crystal of cobalt: (*left*) schematic of the structure and (*right*) SEM image [60]. (**f**) 2D plasmonic crystal from self-assembled polymeric monolayers replicated on nickel on a gold substrate: (*left*) schematics and (*right*) AFM image [61]

important role in the SPP excitation and their interplay with magneto-optics. Several times increase of the TMOKE at the plasmonic resonances of the grating with respect to the smooth ferromagnets was reported [56]. Noble metal structures in a high external magnetic field also provide enhancement of the TMOKE [63]. Their magneto-optical properties are due to Lorentz force acting on free electrons in a magnetic field. The concept of hybrid noble-metal/ferromagnetic-metal multilayers was also applied to the plasmonic crystals [57, 64] (Fig. 4.3(b)). Since the overall optical losses for such systems are lower than those for pure ferromagnetic metals the effect of resonant increase of the TMOKE due to propagating SPPs in these structures is more pronounced.

As we will see further, the SPP mediated increase of the TMOKE is due to the shift of a SPP resonance in a transverse magnetic field. This shift happens only for propagating SPPs. Resonance frequency of the localized SPPs is hardly influenced by the magnetic field, and, consequently, no pronounced changes in the TMOKE at localized plasmonic resonances are observed. Nevertheless, the interaction of localized and propagating surface plasmon modes modify SPP dispersion and thus modify the TMOKE signal [65] (Fig. 4.3(c)). In addition to that, localized SPPs can also influence the second harmonic TMOKE which is experimentally shown in [66, 67].

The case of the transverse magnetization with respect to the SPP propagation direction is also interesting due to the fact that it enables the phenomenon of nonreciprocal optical transmission, in which the transmission coefficients of light through a plasmonic crystal from the gold side and from the substrate side are significantly different. In the case of perfectly conducting metal the plasmonic crystal at some optical frequencies can be almost perfectly transparent in one direction and can reflect almost all radiation coming from the other side [68]. This effect is also described in terms of the magnetization induced shift of plasmonic resonances.

The main disadvantage of most of the aforementioned approaches is that the optical losses associated with the presence of a ferromagnetic metal are still relatively high. This limits exploiting fully the potential gain of the combined concepts of nanostructuring and plasmonics in magneto-optics. If the ferromagnetic metals were avoided as in cases of pure semiconductors or noble metal systems, huge external magnetic fields exceeding several Tesla would be necessary to make the TMOKE at least comparable with the effect in ferromagnets. That is why it seems that the plasmonic crystals containing ferromagnetic dielectrics and noble metals can provide even better results.

4.2.2 Theory

4.2.2.1 Magnetoplasmons at a Smooth Metal–Dielectric Interface

For analyzing the TMOKE in plasmonic systems combining ferromagnetic dielectrics with noble metals we start from the case of a smooth interface between these media.

Using a linear approximation for the dependence of the permittivity tensor describing the ferromagnetic medium on the gyration (the magneto-optical parameter) this tensor is given by (4.12) with $m_x = m_z = 0$, $m_y = 1$ (the coordinate system is shown in Fig. 4.1, and the dielectric is magnetized along y-direction). The metallic layer is characterized by the dielectric function ε_1 (see e.g. (4.4)).

The necessary condition for the TMOKE occurrence is $[\mathbf{k} \times \mathbf{N}] \neq 0$, where $\mathbf{k}$ is the wave vector and $\mathbf{N}$ is the vector normal to the metal-dielectric interface. Moreover, the cross product $[\mathbf{M} \times \mathbf{N}]$ is also very important. It is non-zero near the surface of the magnetized film. The magnetic field breaks the symmetry with respect to time reversal, while the interface (and the $\mathbf{N}$ vector normal to it) breaks the space inversion. Interestingly, space–time symmetry breaking is characteristic of media with a toroidal moment $\boldsymbol{\tau}$ which has transformation properties similar to those of $[\mathbf{M} \times \mathbf{N}]$ [69]. Consequently, the problem of the SPP propagation along the interface of a transversely magnetized medium is similar to that of electromagnetic wave propagation in a bulk medium with a toroidal moment parallel to this direction. In electrodynamics, a toroidal moment is known to give rise to optical nonreciprocity as manifested by a difference between the wave vectors for waves propagating forward and backward with respect to the toroidal moment [70].

It follows from Maxwell's equations that, in contrast to all other possible magnetization directions, the transverse magnetization does not change the polarization state of the SPP but only changes its wavenumber κ. As a result, a TM polarized wave whose magnetic field $H_y(x,z) = H_y \exp(i\kappa x - \gamma_i|z|)$ is directed in the plane (in a coordinate system with the z-axis perpendicular to the plane and the x-axis directed along the SPP propagation) propagates along the smooth metal/gyrotropic dielectric interface. An explicit expression for the wavenumber of the SPP that propagates along the metal/gyrotropic medium interface is the following [71]:

$$\kappa = \kappa_0(1 + \alpha g), \tag{4.24}$$

where $\kappa_0 = k_0(\varepsilon_1\varepsilon_2/(\varepsilon_1 + \varepsilon_2))^{1/2}$ and $\alpha = (-\varepsilon_1\varepsilon_2)^{-1/2}(1 - \varepsilon_2^2/\varepsilon_1^2)^{-1}$. It follows from (4.24) that, in the first approximation, the wavenumber of the surface wave depends linearly on the film gyration g.

The nonreciprocity effect is a prominent inherent feature of the SPP-assisted TMOKE, as can clearly be seen for a smooth metal/dielectric interface. Far from the plasmonic resonance, one usually observes a monotonic, featureless reflection spectrum, and the TMOKE signal is quite small, even for metal ferromagnets. In contrast, at the SPP resonance, a pronounced dip appears in the reflection spectrum. Because the SPP wave vector differs for opposite magnetizations according to (4.24), the reflection dip shifts with magnetic field to smaller or higher frequencies and the TMOKE signal becomes enhanced by about an order of magnitude. In fact, in the frequency range of SPP generation, the TMOKE parameter δ is approximately equal to the product given by the frequency derivative of the reflection spectrum and the magnetic field induced frequency shift. Thus, the TMOKE enhancement through SPPs occurs even for a smooth interface. However, there are drawbacks to this approach. First, to excite SPPs at the interface between a metal and a magnetic film (in the Kretschmann geometry), the refractive index of the prism must be larger than the refractive index of the magnetic film, which is rather difficult to achieve. Second, sputtering of the opaque metal layer onto the dielectric reduces the transmission to almost zero, preventing operation in transmission. This is why it might be worth considering a hybrid approach that involves a perforated metal.

4.2.2.2 Magnetoplasmons in Plasmonic Crystals

Let us now turn to a plasmonic crystal in which the metallic layer is perforated by an array of parallel slits and the dielectric layer is magnetized along the slits (Fig. 4.4). At first we assume that the magnetic film is thick enough so we can neglect the influence of the non-magnetic substrate. In this case, the dielectric constant in the region of the metal and the gyrotropic dielectric is a periodic function of the coordinate x and a step function of the coordinate z:

$$\varepsilon(x,z) = \big(\varepsilon_1(x) - \varepsilon_2\big)\theta_H(z) + \varepsilon_2, \tag{4.25}$$

while the structure gyration remains a step function $g(z) = g\theta_H(-z)$, where $\theta_H(z)$ is the Heaviside function (the metal/dielectric interface coincides with the $z = 0$

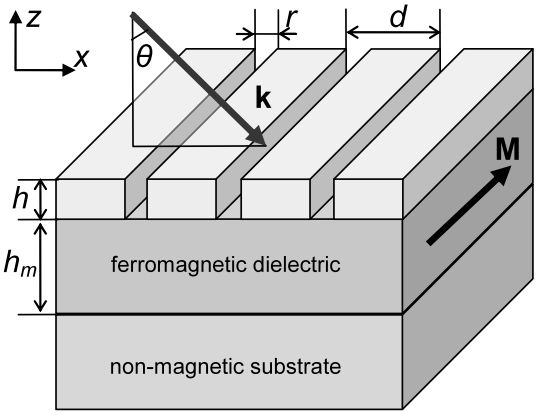

Fig. 4.4 Magnetoplasmonic crystal consisting of a metal grating on top of a planar ferromagnetic dielectric grown on a non-magnetic substrate. The magnetization **M** in the ferromagnetic layer is parallel to the slits, and the incident light is p-polarized; **k** is the wave vector of the incident wave [72]

plane). The incident light is p-polarized. The plane of incidence is perpendicular to **M**.

The excitation condition for SPPs is given by (4.10). For the one-dimensional plasmonic crystals (4.10) takes the form:

$$\kappa = k_0 \sin\theta + 2\pi m/d, \tag{4.26}$$

where d is the grating period and θ is the incidence angle.

Let us assume that the metal is thicker than the skin layer and the interaction between the SPPs at the two metal surfaces is negligible. From Maxwell's equations, we derive a differential equation for the complex amplitude of the magnetic field **H** and write it in an operator form [73]:

$$(\hat{L} + \hat{V})\mathbf{H} = \omega^2/c^2\mathbf{H}, \tag{4.27}$$

where the operator $\hat{V}$ represents the linear (in g) magneto-optical contribution. Since the dielectric constant is periodic along the x-axis, the magnetic field component H_y can be represented as a Bloch wave. Equation (4.27) can be transformed to an eigenvalue problem for the normalized Bloch envelope $u_\kappa(x, z)$ with the quasi-wavenumber κ [73]:

$$\left(\hat{L}' + \hat{V}'\right)u_\kappa = \omega^2/c^2 u_\kappa. \tag{4.28}$$

In the first order of the perturbation theory in g, it follows from (4.28) that the SPP excitation frequency in the magnetic case is shifted from that in the non-magnetic one:

$$\omega_n(\kappa, g) = \omega_{0n}(\kappa) + \Omega(g). \tag{4.29}$$

The shift value $\Omega(g)$ is linear in g and comes to zero if $\kappa = 0$. Moreover, $\Omega(g)$ is determined not only by the gyration and dielectric constants of the plasmonic crystal components but also by the field distribution at the interface, i.e., it depends on the grating parameters [73].

If the thickness of the metal is larger than the values of the skin layer and the width of the slits is much smaller than the SPP's wavelength then for $\omega(\kappa, g)$ (4.24)

keeps applicable. At this the magnetic field assisted SPP's frequency shift is given by

$$\frac{\Omega(g)}{\omega_{0n}(\kappa)} = -\frac{\kappa_0 \alpha}{mG} g. \tag{4.30}$$

4.2.2.3 Scattering Matrix Analysis

When the problem of light incidence on periodic structures is analyzed, it is convenient to use the scattering matrix method [74–76]. This method is efficient in searching for the system's eigenmodes that have a great effect on its optical properties.

When light is incident on a periodic structure, it is diffracted by the latter and the generated electromagnetic field can be represented as a superposition of incident, reflected, and transmitted plane waves with longitudinal wavenumbers $k_x^{(m)}$ that differ from the wavenumber of the incident wave $k_x^{(i)}$ by the reciprocal lattice vector mG. Generally, the complex amplitudes of the reflected and transmitted waves can be combined into a column $\mathbf{A}_{\text{scat}}$, while the amplitudes of the waves incident on the structure on both sides in all diffraction orders can be combined into a column $\mathbf{A}_{\text{in}}$. The complex amplitudes of the incident and scattered waves are related via the scattering matrix $\mathbf{S}$:

$$\mathbf{S}\mathbf{A}_{\text{in}} = \mathbf{A}_{\text{scat}}. \tag{4.31}$$

The scattering matrix ($\mathbf{S}$-matrix) is an adequate physical tool for describing the electromagnetic properties of materials that are significantly inhomogeneous on the subwavelength scale, for which the standard optical approaches suggesting wave front homogeneity in the lateral direction are inapplicable [74–76]. The possibility of finding the structure eigenmodes is among the advantages of the method. The dimension of the $\mathbf{S}$-matrix is determined by the dimension of the columns of amplitudes. The scattering matrix is calculated numerically.

The technique for calculating the scattering matrix of the problem is described, for example, in [75, 77]. The scattering matrix for multilayered structures is constructed recurrently. N layers homogeneous along the z-axis (in accordance with the designations of Fig. 4.4) and $N+1$ interfaces corresponding to them are selected in the structure. The complex amplitudes of the eigenmodes on different sides of each layer or interface are related via the transfer matrix $\mathbf{T}_i$ and the full transfer matrix for the entire structure is $\mathbf{T} = \prod_{i=1}^{2N+1} \mathbf{T}_i$. The form of the matrix $\mathbf{T}_i$ is determined by finding the eigenmodes for each layer and by taking into account the boundary conditions at the interface. A virtual interface for which the transfer matrix $\mathbf{T}_0$ and the scattering matrix $\mathbf{S}_0$ are unit ones is also selected in the external medium near the surface of the extreme layer. Denote the scattering matrix for the part of the structure contained between the virtual interface and the ith layer or interface by $\mathbf{S}_i$. For these matrices, there are recurrence relations that relate the components of $\mathbf{S}_i$ with those of $\mathbf{S}_{i-1}$ and $\mathbf{T}_i$. The sought-for scattering matrix for the entire structure is $\mathbf{S} = \mathbf{S}_{2N+1}$.

Since the eigenmodes can propagate through the structure without any external interaction, a nontrivial solution of the homogeneous problem with a zero column of incident wave amplitudes $\mathbf{A}_{\text{in}}$, $\mathbf{S}^{-1}\mathbf{A}_{\text{scat}} = 0$, corresponds to them. The existence of a nontrivial solution requires that

$$\det(\mathbf{S}^{-1}) = 0. \tag{4.32}$$

The scattering matrix is a function of the frequency and quasi-wavenumber. Generally, the solution of (4.32) is a pair of complex numbers κ and ω. However, the eigenmodes are excited by a wave with real κ and ω. Therefore, at least one of the two numbers should be assumed to be real depending on the specific problem [78, 79]. Here we consider the case where a plane wave is incident on an infinite periodic structure. The problem has a translation symmetry in the grating plane. Consequently, the intensity of the eigenmodes excited in it are also a periodic function and there is no damping of the waves that propagate in the lateral direction. This necessitates assuming κ to be real and ω to be complex. In fact, the problem is reduced to searching for a local minimum from the frequency $\det(\mathbf{S}^{-1})$ for κ from the first Brillouin zone.

We assume that the quasi-wavenumber is fixed and find the solution of (4.32) from the frequency. The solutions of (4.32) are generally complex: $\tilde{\omega}_p = \omega_p + i\gamma_p$. The zeroes of the determinant $\det(\mathbf{S}^{-1})$ are the poles of the determinant $\det(\mathbf{S})$. Assuming that the determinant of the scattering matrix is a meromorphic function of the complex frequency, we represent it as a series expansion:

$$\det(\mathbf{S}) = \sum_p \frac{D_p}{\omega - \tilde{\omega}_p} + D_0, \tag{4.33}$$

where p is an integer, $p \geq 1$, D_0 is an analytic function of the frequency. In accordance with the Kramers formulas, the complex amplitude of the mth diffraction order A_m can be represented by the ratio of the auxiliary determinant $\det(\mathbf{S}_m^{-1})$ in which the mth column is replaced by the column $\mathbf{A}_{\text{in}}$ and the determinant of the inverse scattering matrix:

$$A_m = \det\left(\mathbf{S}_m^{-1}\right) / \det\left(\mathbf{S}^{-1}\right). \tag{4.34}$$

Consequently, since $\det(\mathbf{S}) = 1/\det(\mathbf{S}^{-1})$, we find that near each pth pole of the determinant of the scattering matrix the complex amplitudes of the diffraction orders have a resonance feature and the complex amplitude of the mth diffraction order near the pole has the form

$$A_m = \frac{a_{pm}}{\omega - \tilde{\omega}_p} + b_{pm}. \tag{4.35}$$

4.2.2.4 Fano Resonances in Transmission and Reflection Spectra

The energy transmission, T_m, and reflection, R_m, coefficients in the mth propagating diffraction order are proportional to the sum of the squares of the amplitudes of two

mth-order waves that propagate in the substrate or in the medium above the grating and that are polarized mutually orthogonally (e.g., TE and TM polarizations). Thus, the intensity I_m of the transmitted or reflected radiation in the mth diffraction order depends on the squares of the amplitudes of the corresponding elements in the column $\mathbf{A}_{\text{scat}}$: $I_m = f(|A_m|^2)$. Therefore, the features of the reflection and transmission spectra are determined by the behavior of $|A_m|^2$. Calculating the intensity I_m using (4.35), we obtain

$$I_m \sim |A_m|^2 = \frac{(\omega - \omega_z)^2 + \gamma_z^2}{(\omega - \omega_p)^2 + \gamma_p^2} |b_{pm}|^2, \tag{4.36}$$

where

$$\omega_z = \omega_p\big[1 - \mathrm{Re}(q_{pm})\big], \qquad \gamma_z = \gamma_p\left[1 - \frac{\omega_p}{\gamma_p}\,\mathrm{Im}(q_{pm})\right], \quad q_{pm} = \frac{a_{pm}}{\omega_p b_{pm}}.$$

Consequently, the frequency dependences of R and T have a characteristic asymmetric profile with a maximum and a minimum following each other (or conversely, depending on the sign of $\mathrm{Re}(q_{pm})$), which is commonly called the Fano resonance [80–82]. A Fano resonance is widely known in many areas of physics as a result of interference of a resonant scattering and a nonresonant background that leads to an asymmetric line-shape.

The parameter q_{pm} is called the Fano parameter. It shows the ratio of the efficiencies of the resonant and nonresonant processes. In the problem of light–grating interaction, the resonant process is the excitation of eigenmodes in the system, such as quasi-waveguide waves, plasmon polaritons, slit modes, etc. At the same time, the nonresonant contribution to the intensity in the mth diffraction order is related to the radiation scattered by the diffraction grating without any excitation of eigenmodes. The amplitude of the wave in the mth diffraction order is the sum of two components: the resonant one arising from the excitation of eigenmodes and the nonresonant one. If the nonresonant process is negligible ($|q| \to \infty$), then the frequency dependence acquires the standard symmetric shape of a Lorentz curve. The width of the resonance curve depends on the dissipation parameter γ_p.

4.2.2.5 The TMOKE in Plasmonic Crystals

For the plasmonic crystals considered here (Fig. 4.4), the eigenmodes are the SPPs and the modes inside the slits [71]. Therefore, in our case, the **S**-matrix poles correspond to the excitation frequencies $\tilde{\omega}_p$ of surface waves and slit modes. As was shown above, the SPP excitation frequency in a transversely magnetized plasmonic crystal depends on gyration (i.e. on magnetization) (see (4.29)). Consequently, the Fano resonance curves are shifted in frequency relative to their positions for the non-magnetic case by $\Omega(g)$: $|A_m(g,\omega)|^2 = |A_m(0,\omega - \Omega(g))|^2$ (Fig. 4.5(a)). At low gyration values, the change in the resonance shape may be neglected. As a result, a change in the transmission and reflection coefficients which is characteristic

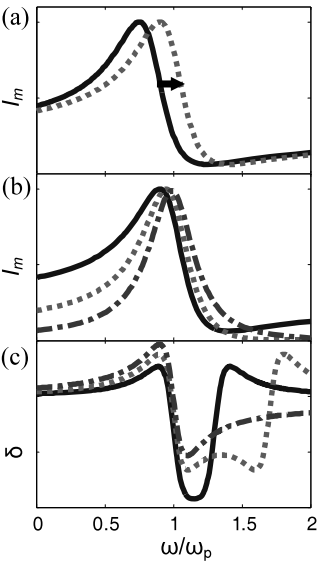

Fig. 4.5 (**a**) Fano resonance shift induced by the gyration vector in the transverse geometry, (**b**) Fano resonances, and (**c**) the magneto-optical effect δ for various Fano parameters q: $q = 0.3$ (*solid line*), 0.7 (*dashed line*), and 3.0 (*dash–dotted line*); $\gamma_p/\omega_p = 0.1$ [73]

of the TMOKE arises when the magnetization sign is reversed. Since $\Omega(g) \ll \omega$, the frequency dependence of ΔI, in fact, expresses the derivative of the function $|A_m(0,\omega)|^2$.

Compared to the case of homogeneous nonplasmonic films, the Kerr effect is enhanced [71]. It depends not only on the magneto-optical properties of the medium but also on the shape of the resonance curve: for sharper resonance peaks, the Kerr effect increases significantly. Since the width of the resonance peak is determined by dissipation, one might expect ΔI and δ characterizing the effect to depend on γ_p. If the nonresonant processes in the system are weak, i.e. $|q| \gg 1$, then the expressions for the maximum values of ΔI and δ follow from (4.35) and (4.36):

$$(\Delta I)_{\max} \sim \left(|A_m|^2\right)_{\max} \sim \frac{\Omega(g)}{\gamma_p^3}|a_{pm}|^2; \qquad (\delta)_{\max} = \frac{\sqrt{3}\Omega(g)}{\gamma_p}. \tag{4.37}$$

Both quantities decrease with increasing dissipation coefficient γ_p.

In the case of a significant nonresonant contribution (i.e., at low values of q), the absolute change in intensity ΔI remains as before, while the optical transmission and reflection spectra change their shape. As a result, the relative change in the intensity of light δ increases, in particular, because the denominator in (4.19) decreases. This is illustrated by Fig. 4.5.

Our qualitative analysis of the problem reveals that the plasmon reflection and transmission resonances in a transverse magnetic field are shifted in frequency depending on the magnitude and direction of the field virtually without changing their shape, which leads to an enhancement of the transverse Kerr effect [73].

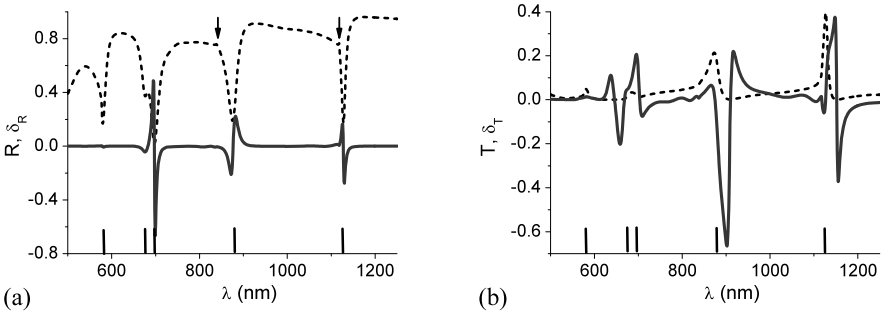

Fig. 4.6 (**a**) Spectra of the reflection coefficient (*dashed line*) and its relative change δ_R (*solid line*). (**b**) Spectra of the transmission coefficient (*dashed line*) and its relative change δ_T (*solid line*). The angle of light incidence is 20°. The plane of incidence is perpendicular to the slits, the light is *p*-polarized. The *arrows* mark the wavelengths of the Rayleigh–Wood anomalies. The structure parameters are $d = 430$ nm, $r = 40$ nm, and $h = 100$ nm (see Fig. 4.4) [73]

4.2.2.6 RCWA Analysis

For the electromagnetic modeling of reflection and transmission spectra and electromagnetic field distribution we use the rigorous coupled waves analysis (RCWA) technique [83] extended to the case of gyrotropic materials [84]. Since the heterostructure is periodic, the electromagnetic field components in each layer can be represented as a superposition of Bloch waves. Maxwell's equations are written in a truncated Fourier space. The electromagnetic boundary conditions are then applied at the interfaces between the substrate region, the individual grating slabs, and finally the upper surface of the structure. The sequential application of electromagnetic boundary conditions reduces the computing effort for the reflected and the transmitted diffracted field amplitudes to the solution of a linear system of differential equations. To improve convergence of the method we employed the correct rules of Fourier factorization presented in [84].

The following parameters are assumed: ε_1 is equal to the permittivity of gold taken from [85], and the values of ε_2 and g correspond to the bismuth substituted yttrium iron garnet film (e.g., $\varepsilon_2 = 5.06$ and $g = 0.01$ at the wavelength $\lambda = 1100$ nm) [3].

The transmission and reflection coefficients and their relative changes δ are plotted against the wavelength λ of the incident light in Fig. 4.6 [73]. The vertical lines mark the points on the wavelength scale that represent a particular wave mode calculated numerically from the solution of (4.32). The reflection minimum (transmission maximum) at $\lambda = 580$ nm corresponds to the SPP at the metal/air interface, while the reflection minima (transmission maxima) at $\lambda = 685$, 875, and 1128 nm correspond to the SPPs at the metal/magnetic interface. These features in the spectra are commonly called Wood's anomalies. In addition, a small reflection minimum is observed at $\lambda = 678$ nm near the main dip. It is related to the excitation of a Fabry–Pérot mode (cavity mode) characterized by localization of electromagnetic field energy inside the slits. In fact, in the wavelength range from 670 to 700 nm,

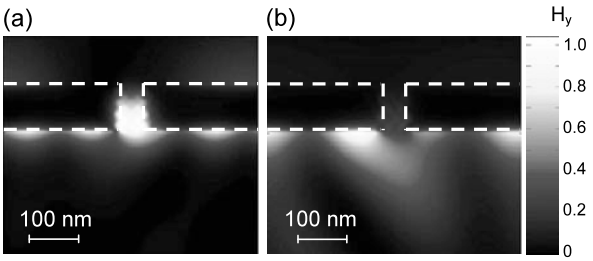

Fig. 4.7 Distribution of the square of the magnitude of the magnetic field component H_y (in relative units) at $\lambda = 680$ (**a**) and 875 (**b**) nm. The metallic grating is marked by the *dashed line*. The structure parameters are the same as those in Fig. 4.6 [73]

two types of modes are excited simultaneously in the structure: localized and surface plasmon polaritons. This is illustrated by Fig. 4.7, which presents the distribution of the square of the magnitude of the magnetic field component along the grating slits H_y. At $\lambda = 680$ nm, the electromagnetic field is concentrated both in the slit and at the interface with the dielectric. At the same time, at $\lambda = 875$ nm corresponding only to the SPP, the field is concentrated solely at the metal–dielectric interface.

The magneto-optical intensity effect is greatest at wavelengths near Wood's anomalies (the excitation of SPPs) at the interface with the magnetic substrate, due to strongest interaction with magnetic medium. In this case, δ reaches 70 %, suggesting a giant Kerr effect. Note that $\delta \sim 0.1$ % for a homogeneous magnetic film without metal coating. An additional peculiarity of the observation of the Kerr effect in this case is that it is easily observed in transmitted light, which is usually greatly complicated for homogeneous films due to the very low intensity of the transmitted radiation. In this case, δ is more than 20 % at 40 % transmission.

As for the other modes the interaction of electromagnetic field with the magnetic medium is much weaker, not all of the features in the transmission and reflection spectra are accompanied by an equally large enhancement of the intensity effect. Thus, for example, there is no enhancement of the intensity effect near the reflection minimum (transmission maximum) at a wavelength of 580 nm: the surface wave is localized at the metal–air interface, while the enhancement of the effect near the next reflection dip (at the wavelength of 677 nm) corresponding to the excitation of a slit mode is smaller.

Apart from several dips and peaks, the reflection spectra also exhibit features that are called Rayleigh–Wood anomalies [86] (marked by the arrows in Fig. 4.6). In this case, no enhancement of the intensity effect is observed. This is because the anomalies arise when one of the propagating diffraction orders disappears/appears and are determined by the grating period, i.e., they do not depend on the substrate gyration.

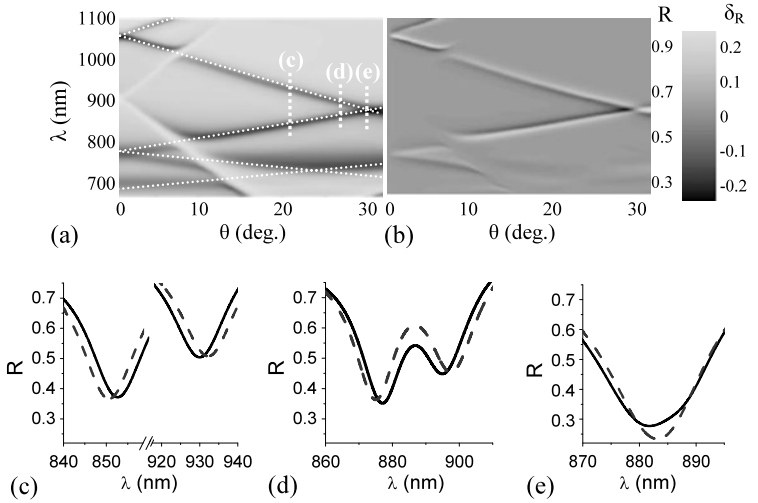

Fig. 4.8 (**a**)–(**b**) Dispersion of the reflection R (**a**) and the TMOKE δ_R (**b**) versus wavelength and incidence angle. *White dashed lines* indicate conditions for the curves (**c**)–(**e**). (**c**)–(**e**) Reflection spectra for the structure magnetized in two opposite directions $+\mathbf{M}$ (*solid line*) and $-\mathbf{M}$ (*dashed line*) for incidence angles of $\theta = 20°$ (**c**), $\theta = 28°$ (**d**), $\theta = 30°$ (**e**). The geometrical parameters are: $h = 130$ nm, $d = 900$ nm, $r = 35$ nm. The radiation is p-polarized [71]

4.2.2.7 The Dispersion Diagram and Brillouin Zone Edge Effects

As the TMOKE is correlated with the Wood anomalies its dispersion should follow the SPPs dispersion. Contour plots of the reflection and the TMOKE versus wavelength and incidence angle are shown in Fig. 4.8. The dispersion curves of the SPPs on the metal—dielectric surface are shown with white dotted lines and coincide well with the reflection minima. Rayleigh anomalies are also seen as two reflection maxima lines starting at $\lambda = 900$ nm.

The SPPs at the surface with the periodic relief get form of the Bloch waves. Different SPPs bands are seen in Fig. 4.8(a). The points of their intersection correspond to the standing SPPs at the edges of the first Brillouin zone. They are excited when $k_x^{(i)} = (2m + 1)G/2$. As a rule, standing SPPs originate band gaps, but at the diagram the gaps are not resolved because of the broadening of the reflection minima caused by SPP damping through the dissipation and scattering at the slits.

Intuitive reasoning hints that there should be some magneto-optical peculiarities at these regions of the dispersion diagram. At first glance, Fig. 4.8(b) demonstrates no pronounced features of the TMOKE there. It keeps following the SPPs curves even at the Brillouin zone edges. However, closer look does reveal one interesting peculiarity. Fig. 4.8(c)–(e) presents reflection spectra for different incidence angles measured for two opposite transverse magnetizations $+\mathbf{M}$ and $-\mathbf{M}$ (solid and dashed lines). The described above magnetization induced shift of the reflection minima takes place for incidence angles of 20° and 28°, the values of the minima being almost the same. However, for incidence angle of 30° no shift arises but,

on the contrary, the values of the reflection dips are no more equal. The origin of such different influence of the magnetization on the plasmonic crystal optical response lies in different nature of the SPPs involved. Indeed, in both former cases the light excites SPPs of wave numbers lying inside the Brillouin zone, while in the latter case it engenders SPPs of wave numbers corresponding to the Brillouin zone edge, i.e. $\kappa = (2m+1)G/2$. The "edge" SPPs are standing waves originating from the interference of two SPPs traveling in opposite directions. As the energy gap is smaller than the reflection minima bandwidths standing SPPs of two different orders of different sign are excited simultaneously. It leads to the cancellation of the magnetization shift effect but makes intensities of the reflection minima magnetization dependent. So, the enhanced TMOKE in the plasmonic structures can be caused either by the magnetization induced spectral shift of the reflection minima when the light excites the SPP of one order inside the first Brillouin zone or by the magnetization induced difference in the values of the reflection dips while standing SPPs of two different orders are excited simultaneously.

4.2.2.8 Effects of Waveguide Modes

If the magnetic film becomes thinner we should take into account the presence of the interface between the film and the substrate. In this case the eigenmodes that contribute to optical and magneto-optical response are not only the SPPs propagating along the two metal surfaces and cavity modes in the metal grating slits but also waveguide modes of the magnetic film [87].

Considering the magnetic layer placed between the metal without perforation and a substrate the following equations for eigenmodes dispersion relations can be obtained from Maxwell's equations with the corresponding boundary conditions:

$$\frac{\gamma_2}{\varepsilon_2}\left(\frac{\gamma_1}{\varepsilon_1}+\frac{\gamma_s}{\varepsilon_s}\right)+\left[\frac{\gamma_1}{\varepsilon_1}\frac{\gamma_s}{\varepsilon_s}+\left(\frac{\gamma_2}{\varepsilon_2}\right)^2+\frac{g\kappa}{\varepsilon_2^2}\left(\frac{\gamma_1}{\varepsilon_1}-\frac{\gamma_s}{\varepsilon_s}\right)\right]\tanh(\gamma_2 h_m)=0 \quad (4.38a)$$

for the SPPs at the metal/dielectric interface and

$$\frac{k_{z2}}{\varepsilon_2}\left(\frac{\gamma_1}{\varepsilon_1}+\frac{\gamma_s}{\varepsilon_s}\right)+\left[\frac{\gamma_1}{\varepsilon_1}\frac{\gamma_s}{\varepsilon_s}-\left(\frac{k_{z2}}{\varepsilon_2}\right)^2+\frac{g\kappa}{\varepsilon_2^2}\left(\frac{\gamma_1}{\varepsilon_1}-\frac{\gamma_s}{\varepsilon_s}\right)\right]\tan(k_{z2}h_m)=0 \quad (4.38b)$$

for the waveguide modes, where h_m is the magnetic layer height, $\gamma_i = (\kappa^2 - \varepsilon_i k_0^2)^{1/2}$, $k_{z2} = (\varepsilon_2 k_0^2 - \kappa^2)^{1/2}$, index s refers to the substrate. It follows from (4.38a), (4.38b) that the propagation constant κ of either type of eigenmode is dependent on magnetization.

If the magnetic layer is rather thin the SPPs dispersion law is close to one for the interface between the metal and the substrate: $\kappa = k_0[\varepsilon_1\varepsilon_s(\varepsilon_1+\varepsilon_s)^{-1}]^{1/2}$, so it is almost magnetization independent. With the increase of h_m the influence of magnetization on the SPP dispersion gets more pronounced according to (4.38a) and also the optical spectra acquire additional features related to the excitation of the waveguide modes that are also magnetic dependent as seen from (4.38b). If h_m exceeds the value $[-(\varepsilon_1+\varepsilon_2)]^{1/2}(k_0\varepsilon_2)^{-1}$, which is about 100 nanometers, the SPPs

dispersion becomes independent of the layer height and the dispersion law (4.38a) takes the form (4.24).

As the eigenmode's propagation constant κ is now dependent on magnetization the resonance wavelengths are shifted with respect to the non-magnetic case which leads to emergence of the TMOKE as described above.

For the case of the plasmonic crystal depicted in Fig. 4.4 the eigenmodes are leaky and they also contribute to the transmitted wave in the far field. That is why it is more correct to call the waveguide waves the quasi-waveguide ones. The dispersion laws for the quasi-waveguide modes and the SPPs are influenced by periodicity and the slits in the metal grating. However, if the slits are rather narrow being compared to the eigenmode wavelength the empty lattice approximation can be applied, according to which κ can be estimated from (4.38a), (4.38b) and (4.26). Near the center and the edges of the Brillouin zone ($\kappa = mG/2$) this approximation is not applicable as the wave propagation is strongly influenced by periodicity. The excitation of the quasi-waveguide modes and the SPPs at metal/magnetic interface is accompanied by resonant enhancement of the TMOKE as described above.

The results of the numerical simulations showing the transmission and the TMOKE dependence on the magnetic layer thickness are presented in Fig. 4.9.

The principal features on the TMOKE spectrum (Fig. 4.9(b)) are series of resonances that are dependent on the magnetic layer height and they are accompanied by transmission dips. These are the contributions of the magnetic layer quasi-waveguide modes excited by $\pm$second diffraction orders. Their excitation conditions estimated from (4.38b) and (4.26) are shown in Fig. 4.9(c) and there is rather nice correspondence with the transmission and TMOKE resonances. The difference can be explained by the only approximate applicability of the empty lattice approximation.

According to (4.38b) and (4.26) each quasi-waveguide mode in the plasmonic crystal is characterized by two integers m and n, the former denoting the diffraction order via which the mode is excited and the latter coming from solution of (4.38b) for fixed m. Within the spectral range shown in Fig. 4.9 the quasi-waveguide modes only with $m = \pm 2$ are excited. It should be noted that opposite signs of m correspond to opposite directions of modes propagation and hence according to the discussion above the signs of the TMOKE are opposite for $m = 2$ and $m = -2$, which is clearly seen in Fig. 4.9(b). For the case of normal incidence the difference in dispersion between modes with the same values of n but opposite values of m vanishes and so does the TMOKE since this situation corresponds to the quasi-momentum $\kappa = 0$ from the first Brillouin zone.

As we have already discussed the other features in transmission spectrum (Fig. 4.9(a)) do not demonstrate strong magneto-optical response. One of them is an increase in transmission at wavelengths of about 680 nm that is independent of the magnetic layer thickness. It is Fabry-Pérot resonance inside the slits of metallic grating. The transmission dips at wavelengths about 610 and 650 nm are related to the SPPs excitation at the metal/air interface and therefore they do not contribute much to the TMOKE.

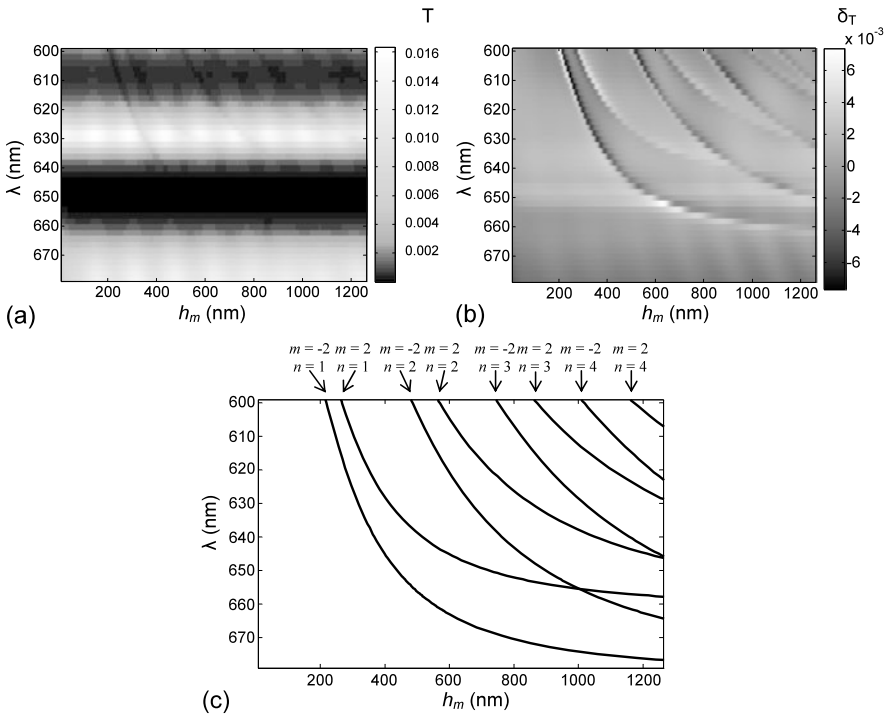

Fig. 4.9 (**a**) Contour plots for calculated transmission (**a**) and the TMOKE (**b**) versus incident light wavelength and height of the magnetic dielectric layer h_m. (**c**) The dispersion curves for the waveguide modes of the magnetic layer calculated from (4.38b) and (4.26) for $m = \pm 2$. The geometrical parameters are: $h = 150$ nm, $d = 595$ nm, $r = 110$ nm. The substrate is silica ($\varepsilon_s = 2.1$). The incidence angle is 2°, the radiation is p-polarized [87]

As it is seen from Fig. 4.9(a) the transmission dips related to the waveguide modes are not very prominent and are suppressed by other features caused by SPPs and cavity modes. As the magneto-optical response on the waveguide modes is the strongest the TMOKE becomes a powerful and efficient tool for their detection.

It should be noted that for rather large values of magnetic layer thickness the excitation of modes is less effective. Moreover, if the structure is illuminated with light with small coherence length the modes are not excited at all, so in our experiments they were not observed.

4.2.3 Experimental

4.2.3.1 Sample and Experimental Setup

Preliminary numerical modeling allowed us to design the sample, i.e. determine the gold grating period, gold thickness, and slit width, and to adjust the main SPP

resonances to the wavelength range of 650–850 nm [72], which is most suitable for magneto-optical experiments on bismuth iron garnets since the magneto-optical figure of merit given by the ratio of the specific Faraday rotation to the absorption is highest around 750 nm. In what follows we concentrate on the observation of the giant TMOKE in the magnetoplasmonic crystal in transmission.

The magnetic part of the magnetoplasmonic structure is a 2.5 μm thick bismuth-substituted rare-earth iron garnet film of composition $Bi_{0.4}(YGdSmCa)_{2.6}(FeGeSi)_5O_{12}$, grown by liquid phase epitaxy with a $Bi_2O_3 : PbO : B_2O_3$ melt on a gadolinium gallium garnet $Gd_3Ga_5O_{12}$ substrate with orientation (111). The film possesses uniaxial magnetic anisotropy in the direction perpendicular to the film plane. The specific Faraday rotation is 0.46°/μm at wavelength 633 nm. The magnetoplasmonic sample of structure shown in Fig. 4.4 was fabricated by the thermal deposition of the gold layer on the bismuth-substituted rare-earth iron garnet film and subsequent electron beam lithography combined with the reactive ion etching in Ar plasma. The sample was characterized by AFM and SEM imaging. The grating parameters obtained are gold layer height h is 120 nm, period d is 595 nm and the air groove width r is 110 nm.

For magneto-optical measurements we used a tungsten halogen lamp as a source of white light with stability better than 0.1 %. The light was focused on the sample into a spot with diameter of about 300 μm. The zero-order transmission signal was spectrally dispersed with a single monochromator (linear dispersion 6.28 nm/mm) and detected with a charge coupled device camera. The overall spectral resolution was below 0.3 nm. During measurement the sample was kept at room temperature.

4.2.3.2 The Giant Enhancement of the TMOKE

Results of the experimentally measured zero-order transmission for the configuration shown in Fig. 4.4 are presented in Fig. 4.10(b) [72]. Comparison with the calculated band structure (Fig. 4.10(a)) allows us to attribute the pronounced Fano resonance (1) in Fig. 4.10(b) to the Wood anomaly of the second band SPP at the air/gold interface, while the Fano resonances (2) and (3) are related to the second and third band SPP at the gold/magnetic-film interface. Finally, the prominent transmission peak (4) is attributed to the collective Fabry-Pérot cavity mode inside the slits.

The experimentally measured TMOKE parameter δ is defined in accordance to (4.19) with the transmission coefficient standing for I (Figs. 4.10(c), (d)). To ensure that the sample magnetization is oriented almost completely in the plane, a relatively large external magnetic field of 2000 Oe was applied. Outside of the resonances the absolute value of δ is very small. Actually in this case, δ cannot be measured experimentally, which means that it is below 10^{-3}. On this background, pronounced positive (brighter) and negative (darker) peaks are observed at which δ reaches up to 1.5×10^{-2} demonstrating a TMOKE increase by at least one order of magnitude. Electromagnetic modeling for the nonresonant case gives $\delta = 8 \times 10^{-4}$ implying an enhancement factor of about 20. Compared to the uncovered bare iron

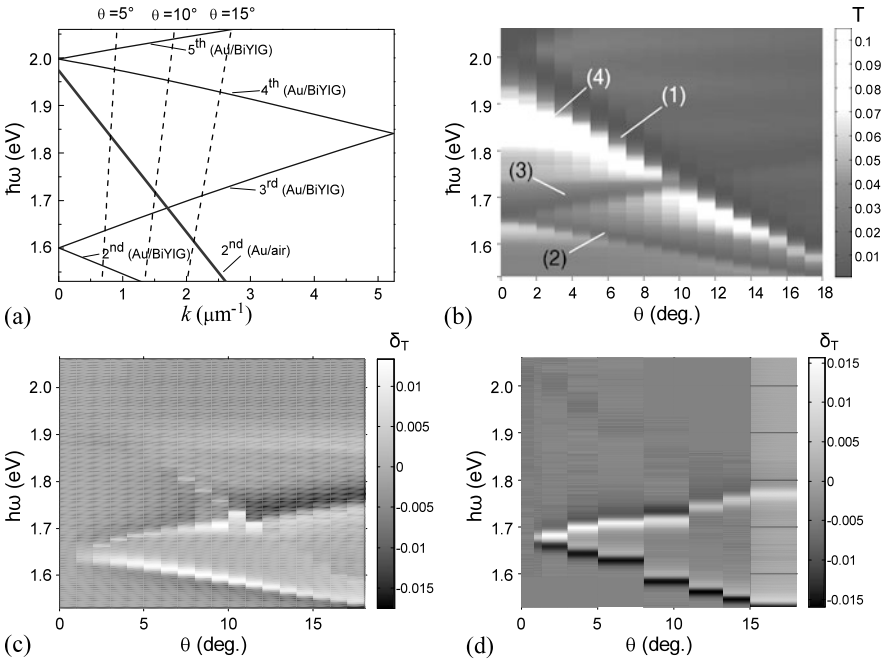

Fig. 4.10 (**a**) Dispersion diagram for SPPs at the gold/air interface (*thick solid line*) and at the gold/iron-garnet interface (*thin solid lines*), calculated in the empty lattice approximation within the first Brillouin zone (see (4.26) and (4.24)). The *dashed lines* indicate the dispersion curves for free space photons for $\theta = 5°$, 10° and 15°. (**b**)–(**d**) False-color plots showing experimentally measured transmission (**b**), the calculated TMOKE parameter δ_T (**c**), and the experimentally measured TMOKE parameter δ_T (**d**) as a function of photon energy (*vertical axis*) and the angle of incidence (*horizontal axis*). The geometrical parameters are: $h = 120$ nm, $d = 595$ nm, $r = 110$ nm. **M** is parallel to the slits and the incident light is p-polarized (as in Fig. 4.4). The in-plane magnetic field strength is 2000 Oe. The features labeled (1)–(4) are related to the SPPs or Fabry–Pérot eigenmodes [72]

garnet film, the enhancement factor is much larger, by about 10^3. From these results we can claim that a giant TMOKE has been observed in transmission. It should be noted that here we use a magnetic film with a relatively small concentration of bismuth. For iron garnets with a composition $Bi_3Fe_5O_{12}$ the specific Faraday rotation is about 6° at $\lambda = 630$ nm, 13 times larger than for our sample [3]. Since the δ-value is proportional to the gyration (and to the specific Faraday rotation), δ should be also 13 times larger than the one observed in our experiments, i.e. δ may exceed 0.2 by choosing right concentration of bismuth.

4.2.3.3 The TMOKE as a Tool for Probing SPPs

The regions of the enhanced TMOKE clearly correspond to the regions of SPP excitation at the gold/ferromagnet interface (compare Figs. 4.10(b) and (d)). No notable

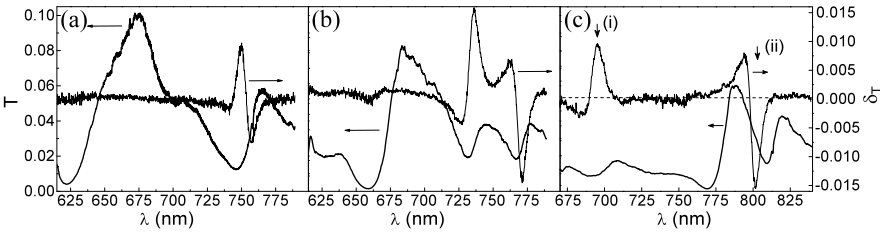

Fig. 4.11 Experimentally measured transmission (*thick curves*) and the TMOKE (*thin curves*) for three different incidence angles: (**a**) $\theta = 0.8°$; (**b**) $\theta = 5°$; (**c**) $\theta = 15°$ [72]. The parameters are the same as in Fig. 4.10

TMOKE increase is observed for other resonant regions, in agreement with the discussion above. This highlights the TMOKE's sensitivity to the excitation of different eigenmodes.

A close-up of the TMOKE spectral shape is shown in Fig. 4.11 [72]. For normal incidence the TMOKE is zero because of the symmetry of the incident light with respect to the structure (Fig. 4.11(a)). The magnetization induced shift of the SPP resonance frequency vanishes and there is degeneracy of the SPPs traveling forward and backward. When **k** is not normal to the surface, the symmetry is broken and the degeneracy is lifted. SPP modes propagating in opposite directions are excited at slightly different frequencies and the TMOKE appears. δ reaches almost 10^{-2} even if the incidence angle is as small as $\theta = 0.8°$ (Fig. 4.11(a)), in accordance with the Fano resonance for SPPs on the gold/magnetic-dielectric interface in the vicinity of the Γ point of the first Brillouin zone. Going from normal to slightly oblique incidence, the transmission spectrum, however, does not change notably, in contrast to the TMOKE spectrum. This demonstrates sensitivity of the TMOKE to the SPP modes in the structure. No measurable TMOKE signal is observed around the other features in the transmission spectrum, the peak at $\lambda = 675$ nm and the dip at $\lambda = 623$ nm.

When the incidence angle becomes larger (e.g. $\theta = 5°$, Fig. 4.11(b)), the eigenfrequencies of the two SPPs propagating in opposite directions differ significantly which gives rise to two Fano resonances in transmission. The TMOKE accompanies both resonances, but with opposite signs of δ, reflecting the fact that these resonances are due to SPPs propagating in opposite directions with respect to the cross product $[\mathbf{M} \times \mathbf{N}]$. This observation unravels another prominent feature of the TMOKE in magnetoplasmonic structures: through the sign of δ one can distinguish between resonances caused by SPPs propagating in opposite directions.

It should be noted that similar measurements for negative angles of incidence give the same value of δ but with opposite sign. This demonstrates that the observed effect is odd in magnetization and not an experimental artifact. Above some incidence angle (e.g. at $\theta = 15°$) the SPP resonance is barely detectable but the TMOKE still indicates its frequency position (see peak (i) of δ in Fig. 4.11(c)). Thus the TMOKE allows measurement of the energy spectrum of the SPP eigenmodes at a metal/ferromagnetic interface [72].

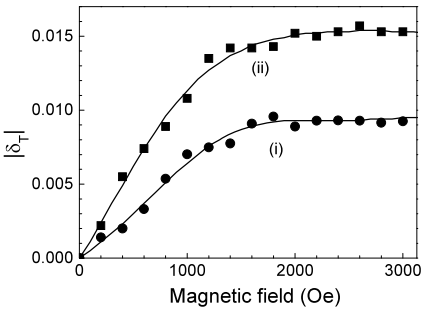

Fig. 4.12 The amplitudes of the two peaks (i) and (ii) in the TMOKE spectrum in (Fig. 4.11(c)) as a function of magnetic field [72]. The parameters are the same as in Fig. 4.10

The magnetic field dependence of δ is shown in Fig. 4.12 for the two main TMOKE peaks (i) and (ii) at $\theta = 15°$. At small magnetic fields the value of δ grows linearly with magnetic field, indicating that the in-plane component of the sample magnetization also has a linear dependence on magnetic field. Saturation takes place at the magnetic field strength of about 1600 Oe which is in nice agreement with the predicted micromagnetic properties of the magnetic film, namely with the value of the effective uniaxial magnetic anisotropy field. However, δ reaches relatively high values even for smaller fields. For example it is 5×10^{-3} at 300 Oe field, which by far exceeds the noise level and is easily measurable.

4.3 Even Magneto-Optical Intensity Effect in Plasmonic Structures

4.3.1 Plasmonic Crystal Based on a Magnetic Waveguide

In this Section we consider similar plasmonic crystal as for the case of the TMOKE with waveguide modes but having a dielectric layer magnetized perpendicular to the slits and in-plane (Fig. 4.13, top left). Such state of magnetization can cause some very interesting magneto-optical effects related to magnetization induced change in intensity of reflected/transmitted light. Unlike the TMOKE, this effect is magnetization-even and does not vanish at normal incidence [88]. In classical magneto-optics such phenomenon is known as the orientational magneto-optical effect (see Sect. 4.1.3.4). The orientational effect for smooth ferromagnetic metals was measured mainly at the reflection mode, since the transmission through metals is negligibly small. On the contrary, the magnetoplasmonic crystal considered here provides rather high transmission due to the effect of extraordinary optical transmission, making observation of the orientational effect easier. For the plasmonic crystal the light intensity depends on the angle between the in-plane magnetization and the direction of periodicity.

Optical properties of the considered system are strongly dependent on the guided modes excited in the system when the electromagnetic wave impinges the perforated metal. These are coupled SPPs and waveguide modes of the magnetized (gyrotropic)

dielectric layer. Due to the presence of the slit arrays in the metallic layer the waveguide modes scatter at the surface pattern and contribute into far-field intensity, i.e. into the observed transmission, which is why it would be more correct to call them quasi-waveguide [88].

4.3.2 Empty Lattice Approximation

For getting physical insight into the problem we start from study of a magnetized in-plane waveguiding layer of thickness h_m with a smooth semi-infinite metal on top and a dielectric on bottom. The presence of the slits in the metal will be taken into account later at the rigorous modeling. For the optical frequency range the magnetic layer is described by the dielectric tensor (4.12) with $m_x = 1$, $m_y = m_z = 0$. Permittivity of the metal is characterized by the dielectric function ε_1 and the dielectric constant of the substrate is ε_3.

At the demagnetized state $g = 0$ and the eigenmodes of the planar dielectric waveguide are TE and TM polarized waves having the longitudinal wavenumber β with the dispersion law determined by the transcendent equation:

$$\gamma_2 h_m = \arctan(\alpha_1/\alpha_2) + \arctan(\alpha_3/\alpha_2) + \pi q, \tag{4.39}$$

where $\gamma_{1,3} = (\beta^2 - \varepsilon_{1,3}k_0^2)^{1/2}$, $\gamma_2 = (\varepsilon_2 k_0^2 - \beta^2)^{1/2}$, $\alpha_i = \gamma_i/\varepsilon_i$ for the TM modes, $\alpha_i = \gamma_i$ for the TE modes, and q is an integer.

The presence of the periodical perforation of the metallic wall of the waveguide is taken by

$$\beta = \frac{2\pi}{d} q_1 + k_\parallel, \tag{4.40}$$

thus selecting all possible values of β. Here $k_\parallel$ is the in-plane part of the incident light wave vector and q_1 is an integer. Equation (4.40) expresses the empty lattice approximation for estimation of eigenmodes dispersion in periodic media that can be applied for the frequencies far from bandgaps.

Magnetization directed along the x-axis leads to change in the waveguide modes properties [89]. The electromagnetic fields of the waves in the waveguide and the neighboring media can be represented in the form

$$\begin{aligned}
\mathbf{E}_{1,3}(x, y, z, t) &= \mathbf{E}_{1,3} \exp\big(i\big(\beta x + i\gamma_{1,3}|z| - \omega t\big)\big), \\
\mathbf{E}_2(x, y, z, t) &= \big[K_1 \mathbf{e}_1 \exp(i\gamma_+ z) + K_2 \mathbf{e}_2 \exp(-i\gamma_+ z) + K_3 \mathbf{e}_3 \exp(i\gamma_- z) \\
&\quad + K_4 \mathbf{e}_4 \exp(-i\gamma_- z)\big] \exp\big(i(\beta x - \omega t)\big),
\end{aligned} \tag{4.41}$$

where $\mathbf{E}_i$ is the electric field amplitude in the ith layer; $\mathbf{e}_1$, $\mathbf{e}_2$, $\mathbf{e}_3$, and $\mathbf{e}_4$ are the unit vectors specifying the normal waves in the magnetic medium; and $\gamma_\pm$ are the z-components of their propagation constants.

The solution of Maxwell's equations reveals that in the linear in g approximation the dispersion equation (4.39) is not affected by magnetization. Unlike the TMOKE

the magnetization induced shift of the eigenfrequencies is quadratic in g, leading to intensity magneto-optical effect that is even in g. But this effect is rather small, and the main contribution to the orientational effect comes from the change in field distribution.

In the linear in gyrotropy approximation Maxwell's equations lead to the following relations:

$$\begin{aligned}
\gamma_{\pm}^2 &= k_0^2\varepsilon_2 - \beta^2 \mp gk_0\beta/\sqrt{\varepsilon_2},\\
e_{1,2x} &= \mp\frac{\gamma_+}{\beta - gk_0/\sqrt{\varepsilon_2}}e_{1,2z},\\
e_{1,2y} &= -i\frac{k_0\sqrt{\varepsilon_2}}{\beta - gk_0/(2\sqrt{\varepsilon_2})}e_{1,2z},\\
e_{3,4x} &= \mp\frac{\gamma_-}{\beta + gk_0/\sqrt{\varepsilon_2}}e_{3,4z},\\
e_{3,4y} &= i\frac{k_0\sqrt{\varepsilon_2}}{\beta + gk_0/(2\sqrt{\varepsilon_2})}e_{3,4z}.
\end{aligned} \tag{4.42}$$

Let us denote the y-components of electric and magnetic fields amplitudes by C_i^{TE} and C_i^{TM}:

$$\begin{aligned}
E_{1,3y}(x,z,t) &= C_{1,3}^{\mathrm{TE}}\exp\bigl(i\bigl(\beta x + i\gamma_{1,3}|z| - \omega t\bigr)\bigr),\\
H_{1,3y}(x,z,t) &= C_{1,3}^{\mathrm{TM}}\exp\bigl(i\bigl(\beta x + i\gamma_{1,3}|z| - \omega t\bigr)\bigr).
\end{aligned} \tag{4.43}$$

For the field components the following relations are valid: for the "TE-like" modes:

$$\begin{aligned}
C_3^{\mathrm{TE}} &= A_1 C_1^{\mathrm{TE}},\\
C_1^{\mathrm{TM}} &= iQA_2 C_1^{\mathrm{TE}},\\
C_3^{\mathrm{TM}} &= iQA_3 C_1^{\mathrm{TE}},
\end{aligned} \tag{4.44a}$$

for the "TM-like" modes:

$$\begin{aligned}
C_3^{\mathrm{TM}} &= B_1 C_1^{\mathrm{TM}},\\
C_1^{\mathrm{TE}} &= iQB_2 C_1^{\mathrm{TM}},\\
C_3^{\mathrm{TE}} &= iQB_3 C_1^{\mathrm{TM}},
\end{aligned} \tag{4.44b}$$

where Q is the magneto-optical parameter (see (4.14)), the coefficients A_i and B_i do not depend on magnetization and all of them with the exception of A_1 and B_1 are odd in β. The excitation conditions and efficiency of the two classes of modes are different and depend on the incident light polarization and on the media surrounding the waveguide.

4.3.3 Physical Origin of the Effect

Thus the coupling between the TE and TM field components emerges in the magnetized layer. The manifestation of this effect in the optical transmission and reflection spectra can be expected. Let us now assume that the demagnetized plasmonic crystal is illuminated by linearly polarized light with the electric field vector perpendicular to the slits and parallel to the plane of the modes propagation. Only quasi-waveguide TM modes are excited in the dielectric layer at frequencies determined by (4.39). At frequency equal to one of the TE mode's eigenfrequencies ω_{TE} which can be found from (4.39) and (4.40) no waveguiding takes place and reflection/transmission spectra generally have no peculiarities at around ω_{TE}. However, if the plasmonic crystal is magnetized then a quasi-waveguide wave can be excited at the frequency near ω_{TE} as the "TE-like" mode has all components of the electric and magnetic field including those of the incident linearly polarized wave. This leads to the redistribution of transmitted, reflected and absorbed energy, and the spectrum should acquire a resonant feature. The value of the transmission change depends on g. Consequently, at around ω_{TE} one should expect a kind of the magneto-optical effect expressed as $\delta = (T_0 - T_M)/T_0$, where T_M and T_0 are the transmission coefficients of light through the magnetized and not magnetized structures, respectively.

On the other hand, the coupling between the TE and TM field components can cause polarization rotation for the transmitted light. However, at the normal incidence according to (4.40) the modes with opposite sign of β are excited with the same efficiency. As was mentioned above, the coefficients A_2, A_3, B_2 and B_3 in (4.44a), (4.44b) are odd in β, and due to symmetry reasons the total contribution to the TE component is zero. So the Faraday rotation can be observed only for oblique incidence.

The excitation of quasi-waveguide "TM-like" modes can also cause the magneto-optical intensity effect, though usually it is much weaker.

4.3.4 RCWA Analysis

To approve this reasoning and to characterize the effect, quantitatively numerical calculations based on RCWA algorithm have been performed [83, 84] (brief description is provided in Sect. 4.2.2.6). The following parameters are assumed: ε_1 is equal to the permittivity of gold taken from [85], the values of ε_2 and g correspond to the bismuth substituted yttrium iron garnet film (e.g., $\varepsilon_2 = 5.06$ and $g = 0.01$ at $\lambda = 1100$ nm) [3], and $\varepsilon_3 = 2.1$ (silica substrate). The radiation is normally incident and linearly polarized so that the electric field vector is perpendicular to the slits. It is seen from Fig. 4.13 that the zero-order transmission for the magnetized system T_1 has pronounced dips at $\lambda = 1102$, 1060 and 1200 nm, while the transmission for the demagnetized system T_0 does not have such features implying that the orientational

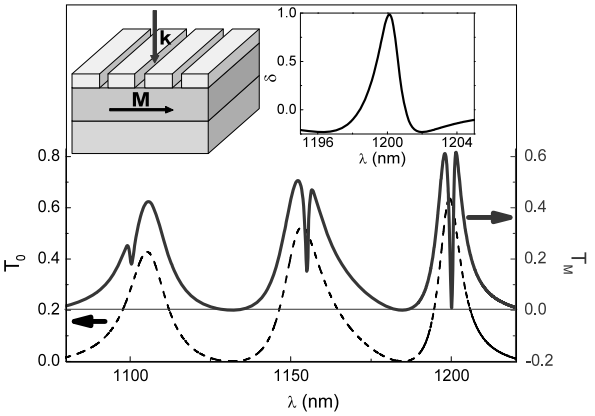

Fig. 4.13 *Top left*: Schematic of the magnetoplasmonic crystal. *Top right*: spectrum of the magneto-optical effect $\delta = (T_0 - T_M)/T_0$. *Bottom*: spectra of the zero-order transmission T_0 and T_M of the non-magnetized (*dashed line*) and magnetized (*solid line*) plasmonic crystal, respectively. The metal layer thickness h is 362 nm, the magnetic layer thickness h_m is 1935 nm, the grating period d is 552 nm, the slits width r is 55 nm. The radiation is normally incident and linearly polarized so that the electric field vector is perpendicular to the slits [88]

effect takes place [88]. The narrow spectral width of the observed peak indicates that the effect has a resonance nature.

The maximum value of δ is attained at $\lambda = 1200$ nm, which coincides with the position of the T_0 peak. The value of δ reaches almost 100 % at the maximum (Fig. 4.13 top right). At the same time, the orientational effect for the single uniform magnetic layer is only 0.01 % even at oblique incidence at large angles. So the enhancement of the effect due to the presence of the perforated metal grating is about four orders of magnitude, which allows referring to it as a giant orientational effect.

It should be noted that the effect under consideration is even with respect to the magnetization. Indeed, the change in the sign of the gyration g does not change the transmission: $T(g) = T(-g)$. Consequently, the effect should be quadratic in g at least for small gyrations g. The corresponding dependence shown in Fig. 4.14 confirms this inference.

It should be noted that peaks of the orientational effect are not always coincident to the maxima of transmission T_0. For example, the resonance of δ at 1102 nm is evidently shifted from the transmission peak. Moreover, modeling of the spectra for the structures with some other geometrical parameters demonstrates that these two features of the transmission spectra are not directly related. However, it is possible to make peaks of δ and of the transmission be coincident, which is the case of the structure in Fig. 4.13 at the wavelength of 1200 nm. Here, the effect becomes more pronounced and easier to be observed and applied.

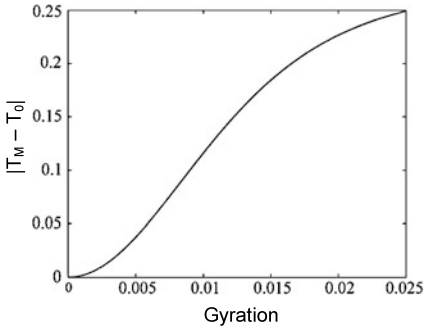

Fig. 4.14 Dependence of the magneto-optical effect magnitude on the gyration g. The metal layer thickness h is 302 nm, the magnetic layer thickness h_m is 883 nm, the grating period d is 886 nm, the slits width r is 88 nm, and the dielectric constant of the substrate $\varepsilon_3 = 1$. The wavelength λ is 1013 nm. The radiation is normally incident and linearly polarized so that the electric field vector is perpendicular to the slits [89]

4.3.5 The Giant Orientational Effect. Rayleigh–Wood Anomalies

It follows from the aforementioned qualitative analysis that the optical properties associated with the presence of the gyration in the structure should be expected upon excitation of quasi-waveguide modes of the dielectric layer. In order to confirm this hypothesis, we investigated the mutual dependences of the structure parameters (the height and the width of metal steps, the period, the magnetic layer thickness, and the permittivities of the materials in the structure) at which similar properties manifest themselves.

Firstly, it should be noted that the wavelength at which the effect is observed does not correlate with the maxima of the transmission. However, the effect is most pronounced when the corresponding wavelengths coincide with each other. This case is illustrated in Fig. 4.13. Moreover, it was revealed that the wavelength at which the intensity of transmitted light changes does not depend on grating parameters, such as the slit width and the metal film thickness. However, a change in the grating period, the permittivity of the materials, and the thickness of the dielectric leads to a shift in the minimum of the transmission. This suggests that the effect is due to the waveguide modes.

Figure 4.15 proves it quantitatively [88]. The maxima of the orientational effect are attained at the parameters favorable for the TE-like modes. The value of δ is not constant along the modes dispersion curves and it becomes the largest near the grating periods d supporting Rayleigh–Wood anomalies [90] on the metal-magnetic dielectric interface (shown by dash-dotted vertical lines in Fig. 4.15). Actually, this means that the effective angle of the mode propagation, which is calculated from the formula

$$\vartheta_{\text{prop}} = \arcsin\left(\frac{\lambda}{d\sqrt{\varepsilon_2}} q_1\right), \tag{4.45}$$

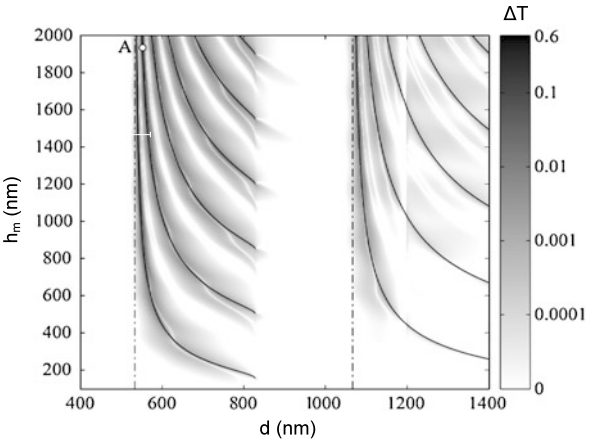

Fig. 4.15 The magneto-optical effect $\Delta T = |T_M - T_0|$ versus h_m and d at $\lambda = 1200$ nm. *Solid lines* represent conditions for the excitation of the "TE-like" eigenmode calculated by (4.39) and (4.40). The other parameters of the structure are the same as for Fig. 4.13. Point A indicated parameters for the former structure [88]

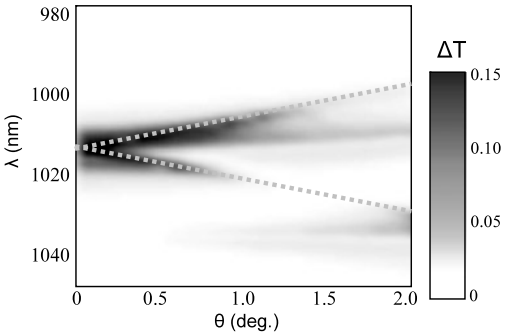

Fig. 4.16 Dependence of the magneto-optical effect magnitude $\Delta T = |T_M - T_0|$ on the angle of incidence and the radiation wavelength. The values of ΔT are plotted along the *right vertical axis*. The plane of incidence of light is perpendicular to slits of the metal grating. The parameters are the same as in Fig. 4.14. The dispersion curves for the second order "TE-like" waveguide modes (*dashed lines*) are shown for comparison [89]

is close to 90° and, in the plane-wave approximation, the mode can be considered as propagating almost parallel to the surface of the dielectric layer. This propagation increases the effective optical path of the mode in the magnetic layer, which, in turn, enhances the magneto-optical effect.

The vertical band in Fig. 4.15 for values of d from 829 nm to 1067 nm does not provide any pronounced orientational effect. The reason for that is a violation of the total internal reflection conditions for the modes of the first order in q_1 (see (4.40)) for structures with $d > 829$ nm (at the fixed wavelength $\lambda = 1200$ nm). The band ends at $d = 1067$ nm because of the excitation of the waveguide modes family of the second order ($q_1 = 2$ in (4.40)).

The dispersion of the magneto-optical effect ΔT and the "TE-like" waveguide modes is shown in Fig. 4.16. In the case of oblique incidence, apart from the change in the intensity, there appears a rotation of plane of polarization of transmitted and

reflected light. However, now we consider only the change in the intensity. As before, the magnitudes of the effect are largest in the vicinity of the excitation of the waveguide modes.

In accordance with theoretical predictions, the numerical analysis confirms that the excitation of quasi-waveguide "TM-like" modes does not produce the pronounced intensity magneto-optical effect.

4.4 Polarization Rotation Magneto-Optical Effects in Plasmonic Structures

4.4.1 State of the Art

If a structure is magnetized perpendicular to the sample's plane or in-plane but along the direction of the SPPs or waveguide mode propagation then the magneto-optical effects of polarization rotation arise. These are the Faraday effect, and the polar and longitudinal Kerr effects (see Sect. 4.1.3.2).

The SPPs and the waveguide modes of smooth semiconductors in the presence of an external magnetic field in both configurations were considered in [91, 92]. It was shown that the magnetic field does not introduce any linear in magnetization terms in the modes dispersion but it induces electromagnetic field components.

The polarization rotation magneto-optical effects were studied in different types of smooth multilayered metal/dielectric structures with either metallic or dielectric component magnetized [93–96]. Probably, the first experimental demonstration of the influence of the plasmonic modes on the Faraday effect was published in [97]. Without making reference to surface plasma waves, author of [97] reported an optically enhanced Kerr rotation in thin iron films, magnetized in the longitudinal orientation, near what has become identified as the plasmon angle.

In some papers [95, 96] the polar or longitudinal Kerr effect enhancement was claimed but it was usually accompanied by decrease in the intensity of the signal. The SPPs-assisted pronounced increase of the Faraday effect was reported in the Bi-substituted iron garnet film covered with thin corrugated silver and gold layers [93]. It was assumed that the main contribution in the enhancement of the Faraday effect in such systems is made by the polarization rotation of the SPPs excited on the metal/dielectric interface.

Faraday and Kerr effects in periodic metal–dielectric structures were also considered recently [59–61, 98–103]. In particular, Diwekar et al. [98] experimentally investigated the Kerr effect upon reflection of visible light from a perforated cobalt film magnetized perpendicular to the surface. It was revealed that, in the vicinity of the region of anomalous transmission of light, the Kerr effect is reduced by one order of magnitude. There is a number of works dealing with the metal–dielectric structures characterized by a considerable enhancement of the Faraday effect [99–101]. In those works, a magnetic medium was placed either inside holes in the metal [99], or the metal itself was ferromagnetic [100, 101].

A 2D plasmonic crystal in a Co film was investigated recently in [60] (Fig. 4.3(e)). The 2D hole array was found to influence not only on the magneto-optical Kerr signal but also on the magnetic properties of the structure. Thus, there is an increase of the coercive field of the in-plane magnetization with increasing hole diameter and an appearance of out-of-plane magnetization components.

The plasmonic crystals of perforated gold on top of the smooth thick ferromagnetic layer similar to the ones considered in the previous sections were also investigated by measuring the cross-polarized transmission and polar Kerr rotation as a function of external magnetic field [102]. Although the effects of plasmons on these processes were observed, the enhancement of the magneto-optical effects via SPPs was not clearly demonstrated.

Though most of the periodic structures were fabricated by means of electron beam lithography and subsequent etching some other fabrication approaches were also used. Thus, the authors of [59] fabricated a 2D plasmonic crystal by sputtering Co or Ni on top of PMMA colloidal crystal (Fig. 4.3(d)). It was found that there are some resonance peculiarities in the Kerr rotation spectra. They were attributed to the SPPs resonances and to the resonances related to the multiple reflections from the colloidal crystal substrate and from the nanostructured film. Torrado et al. [61] also use self-assembling method (Fig. 4.3(f)). They prepared a plasmonic crystal from a polymeric monolayers replicated on nickel. The SPP assisted increase of the polar and transverse Kerr effects due to the excitation of Ni SPPs modes is reported. However, the effect of disorder was shown to decrease the amount of that enhancement. One more magnetoplasmonic periodic structure was fabricated by depositing Co/Pt multilayers on arrays of polystyrene spheres [103].

A significant amount of research was paid recently to the Faraday and Kerr effects in the structures with localized SPP resonances [104–117]. In recent paper by Bonanni et al. [105] nickel nanoferromagnets are studied. Strong and tunable correlation between the localized plasmons and the longitudinal Kerr effect is shown. The authors also demonstrated an existence of a phase shift in Kerr rotation produced by the combination of the anisotropic polarizability and the magneto-optical properties of the nickel nanoparticles.

Magneto-optical activity induced by strong magnetic fields in gold nanoparticles was studied in [106, 107].

The effect of magnetization-induced second harmonic generation in chiral nickel microstructures was investigated in [108].

The enhancement of the Kerr rotation due to localized SPPs was also found in the systems of Ni nanowires [109], in Au/Co/Au nanosandwiches [110, 111] and in ferrimagnetic garnet films incorporating Au particles [112–115]. Authors of [111] pointed out that shape anisotropy of the ferromagnetic nanoparticles might be an additional degree of freedom which allows further increase of the magneto-optical effects.

An increase of the polar Kerr effect due to localized surface plasmons has also been predicted for granular ferromagnetic composites [116].

In spite of a rather large number of papers devoted to the increase of the Faraday and Kerr effect in plasmonic structures the physical nature of this increase has not

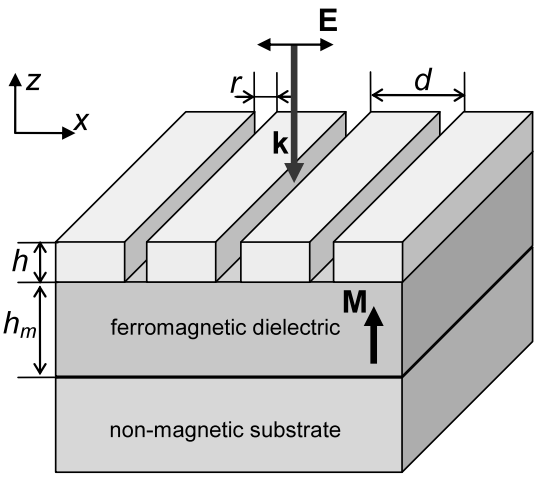

Fig. 4.17 Magnetoplasmonic crystal consisting of a metal grating on top of a planar ferromagnetic dielectric grown on a non-magnetic substrate. The magnetization **M** in the ferromagnetic layer is perpendicular to the plane, and the incident light is normally incident and linearly polarized so that the electric field vector is perpendicular to the slits; **k** is the wave vector of the incident wave

been discussed clearly so far. There seems to be several mechanisms of the enhancement. One of them is related to the significant increase of the local electromagnetic field in the vicinity of the metal structures at the plasmonic which modifies the spin–orbit coupling controlling magneto-optical effects. Spin-dependent interface effects were discussed to explain a large magnetic field-dependent modulation of particle transparency observed in Co/Au core/shell microparticles [118].

The other mechanism takes into account that excitation of the SPP mode leads to the changes in the polarization of the near-field of the structures and thus modifies the response in the optical far field. Finally, excitation of plasmonic or waveguide modes can bring increase of the polarization rotation due to the increase of the effective propagation length of light through the magnetic part of the structure.

It should be noted that the increase of the Faraday and Kerr rotation was reported recently for pure dielectric systems at the wavelengths of waveguide mode resonances [119, 120].

4.4.2 Plasmonic and Waveguide Mechanisms of Faraday Rotation Enhancement

In this section we consider the polarization rotation magneto-optical effects in the plasmonic crystal similar to the ones considered above but having a dielectric layer magnetized perpendicular to the sample's plane (Fig. 4.17) [121].

At the nonresonant frequencies the Faraday rotation is close to that of a single magnetic film and is defined by the film's thickness. At the eigenmodes excitement the resonant features of the magneto-optical response is expected. The eigenmodes that are essential for magneto-optical behavior are the surface plasmon polariton at the metal/dielectric interface and the waveguide modes of the dielectric layer.

The analysis similar to that performed in Sect. 4.3 reveals that for the dielectric layer magnetized along z-axis equations similar to (4.39), (4.41), (4.43), and (4.44a), (4.44b) are valid. Thus, there are the two types of the waveguide modes, namely "TE-like" and "TM-like" ones. Neglecting the perforation of the metallic layer dispersion equation of them is the following:

$$\gamma_2 h_m = \arctan(\alpha_1/\alpha_2) + \arctan(\alpha_3/\alpha_2) + \pi q, \tag{4.46}$$

where indices 1, 2, 3 stand for the metal, the magnetic dielectric and the substrate, respectively, $\gamma_{1,3} = (\beta^2 - \varepsilon_{1,3}k_0^2)^{1/2}$, $\gamma_2 = (\varepsilon_2 k_0^2 - \beta^2)^{1/2}$, $\alpha_i = \gamma_i/\varepsilon_i$ for the "TM-like" modes, $\alpha_i = \gamma_i$ for the "TE-like" modes, and q is an integer. The SPP can be treated as a "TM-like" mode with the imaginary value of γ_2. The electromagnetic fields of the waves in the waveguide and the neighboring media have the form:

$$\begin{aligned}
&\mathbf{E}_{1,3}(x,y,z,t) = \mathbf{E}_{1,3}\exp\big(i\big(\beta x + i\gamma_{1,3}|z| - \omega t\big)\big),\\
&\mathbf{E}_2(x,y,z,t) = \big[K_1\mathbf{e}_1\exp(i\gamma_+ z) + K_2\mathbf{e}_2\exp(-i\gamma_+ z) + K_3\mathbf{e}_3\exp(i\gamma_- z)\\
&\qquad + K_4\mathbf{e}_4\exp(-i\gamma_- z)\big]\exp\big(i(\beta x - \omega t)\big),
\end{aligned} \tag{4.47}$$

where $\mathbf{E}_i$ is the electric field amplitude in the ith layer; $\mathbf{e}_1$, $\mathbf{e}_2$, $\mathbf{e}_3$, and $\mathbf{e}_4$ are the unit vectors specifying the normal waves in the magnetic medium; and $\gamma_\pm$ are the z-components of their propagation constants. Let us denote the y-components of electric and magnetic fields amplitudes by C_i^{TE} and C_i^{TM}:

$$\begin{aligned}
E_{1,3y}(x,z,t) &= C_{1,3}^{\mathrm{TE}}\exp\big(i\big(\beta x + i\gamma_{1,3}|z| - \omega t\big)\big),\\
H_{1,3y}(x,z,t) &= C_{1,3}^{\mathrm{TM}}\exp\big(i\big(\beta x + i\gamma_{1,3}|z| - \omega t\big)\big).
\end{aligned} \tag{4.48}$$

For the field components the following relations are valid: for the "TE-like" modes:

$$\begin{aligned}
C_3^{\mathrm{TE}} &= \tilde{A}_1 C_1^{\mathrm{TE}},\\
C_1^{\mathrm{TM}} &= iQ\tilde{A}_2 C_1^{\mathrm{TE}},\\
C_3^{\mathrm{TM}} &= iQ\tilde{A}_3 C_1^{\mathrm{TE}}
\end{aligned} \tag{4.49a}$$

for the "TM-like" modes:

$$\begin{aligned}
C_3^{\mathrm{TM}} &= \tilde{B}_1 C_1^{\mathrm{TM}},\\
C_1^{\mathrm{TE}} &= iQ\tilde{B}_2 C_1^{\mathrm{TM}},\\
C_3^{\mathrm{TE}} &= iQ\tilde{B}_3 C_1^{\mathrm{TM}},
\end{aligned} \tag{4.49b}$$

where Q is the magneto-optical parameter (see (4.14)), the coefficients $\tilde{A}_i$ and $\tilde{B}_i$ do not depend on magnetization and they are different from the similar coefficients in (4.44a), (4.44b). Since both "TM-like" and "TE-like" modes have all six nonzero components the p-polarized incident wave originates the TE components in the reflected and transmitted waves at the excitation of either mode. Unlike the longitudinal geometry, in the present case the coefficients $\tilde{A}_i$ and $\tilde{B}_i$ are even in β, so

that at the normal incidence the Faraday effect does not vanish. The even intensity effect described in Sect. 4.3 is also present but is less pronounced compared to the longitudinal geometry due to the difference in coefficients A_i and B_i in (4.44a), (4.44b) and $\tilde{A}_i$ and $\tilde{B}_i$ in (4.49a), (4.49b).

The Faraday rotation can be considered qualitatively as a result of conversion of TE–TM field components. Two mechanisms for resonant behavior of the Faraday effect are possible. Let the incident wave be p-polarized. Firstly, at the frequency ω_{TM}, favorable for the TM mode or the SPP excitation, it partly converts to the TE mode. But since the excitation condition for the TE mode is not fulfilled, it comes out of the structure contributing to the far field. The enhancement of the Faraday effect is due to the fact that the effective path of the TM mode or the SPP is larger than in nonresonant case. Secondly, at the frequency ω_{TE} the TM wave comes out of the structure partly converting to the TE mode. At this the TE mode has large effective path that causes the enhancement of the Faraday effect. Thus the mechanism for the Faraday rotation enhancement depends on the type of the excited eigenmode.

4.4.3 RCWA Analysis

4.4.3.1 Plasmonic Structure Without Waveguide Modes

To approve this reasoning numerical simulations for various kinds of plasmonic structure were performed by means of RCWA technique [83, 84] (brief description is provided in Sect. 4.2.2.6). We start with the case of thick magnetic film ($h_m \gg \lambda$), so that waveguide modes are not efficiently excited [122]. The optical properties are affected only by the SPPs that are quasi-TM polarized.

The magnetic layer and the substrate are assumed to have the same refractive index, so there are no reflections on the interface between them and no guiding effects in the magnetic part of the system are present (see Fig. 4.17). The thickness of the magnetic layer is $h_m = 1$ μm. The metallic grating is golden with the parameters $d = 800$ nm, $r = 100$ nm, and $h = 50$ nm. The dielectric layer is assumed to be Bi:YIG, with $\varepsilon_2 = 5.5$ and $g = 0.01$. The dielectric permittivity of gold was taken from [85].

Optical and magneto-optical responses of the grating are shown in Fig. 4.18. Several sets of anomalies in the transmission and Faraday rotation spectra can be seen. For the transmission these are maxima followed by minima, while for the Faraday rotation these are resonance peaks.

Wavelengths for the transmission minima and the Faraday rotation peaks are presented in Table 4.1 in comparison with the calculated Rayleigh's and SPPs wavelength. The Rayleigh's anomalies appear when the mth diffracted order ($m > 0$) becomes tangent to the grating surface. Consequently, it takes place at

$$\lambda_{\mathrm{R}} = \frac{\sqrt{\varepsilon_2} d}{m}(\sin\theta + 1), \tag{4.50}$$

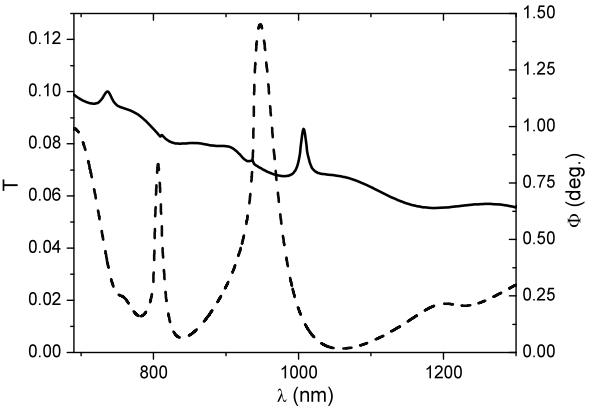

Fig. 4.18 Transmission (*dashed line*) and the Faraday rotation spectra (*solid line*) of the magnetic plasmonic crystal without the guiding layer (see for parameters in the text). The light is normally incident and linearly polarized so that the polarization is perpendicular to the slits of the grating [122]

Table 4.1 The SPPs wavelengths λ_{SP} (first column) calculated via (4.51), wavelengths λ_1 for maxima of the Faraday rotation (second column), wavelengths λ_2 for the transmission minima (third column), and Rayleigh's wavelengths λ_R (fourth column) calculated for the grating (see for parameters in the text). In the brackets: v/m is a vacuum-metal interface, m/d is metal-dielectric interface, numbers denote the orders of SPPs or Rayleigh's anomalies

λ_{SP} (nm)—SPP excitation	λ_1 (nm) for Φ_{max}	λ_2 (nm) for T_{min}	λ_R (nm)—Rayleigh anomalies
738 (3, m/d)	736	782	–
814 (1, v/m)	811	839	806
1006 (3, m/d)	1007	1058	947

where θ is an angle of incidence. The SPPs wavelength can be estimated via the empty lattice approximation:

$$\lambda_{SP} = \frac{\sqrt{\varepsilon_2}d}{m}\left(\sin\theta + \alpha(\lambda_{SP})\right), \tag{4.51}$$

where $\alpha(\lambda) = \sqrt{\varepsilon_1/(\varepsilon_1+\varepsilon_2)}$, ε_1 and ε_2 are the dielectric permittivities of the metal and dielectric, respectively.

One can see from Table 4.1 that the Faraday angle maxima coincide almost exactly to the SPPs wavelengths but not to the transmission minima which confirms the qualitative model presented above.

It is instructive to note that the shape of the Faraday peak is Lorentzian like. It emphasizes the role of resonant processes in the phenomenon of the magneto-optical effects enhancement and explains almost perfect coincidence of the maxima with the conditions for the SPPs excitation. The role of the propagating diffraction orders here is negligible.

For most of the practical cases it is important to acquire large rotation of the polarization plane and high optical transmission. It follows from the previous discussion that minima of the transmission are shifted from the SPPs wavelengths while the wavelengths of the Faraday peaks almost coincide with them. The shift of the

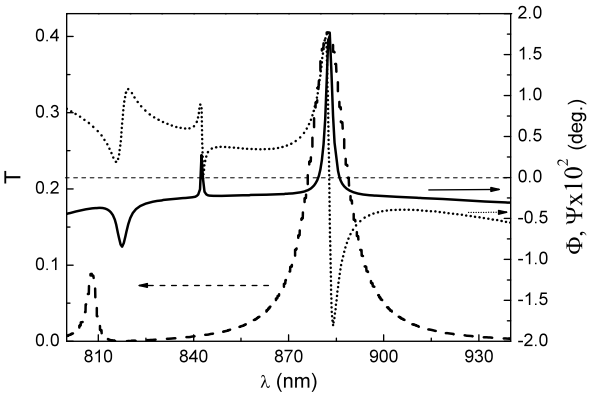

Fig. 4.19 Spectra of the optical transmission (*dashed line*), the Faraday rotation (*solid line*) and the ellipticity (*dotted line*) of the plasmonic crystal of Au grating of thickness 65 nm and uniform Bi:YIG film of thickness 535 nm; $d = 750$ nm, $r = 75$ nm (see Fig. 4.17). The permittivity of the substrate is equal to 1 [123, 124]

minima depends on the relative strength of the nonresonant input and can vary in its value. Consequently, it is possible to get Faraday rotation peak at not vanishing transmission. However, the transmission is not sufficiently high. In this sense, the bilayer metal-dielectric gratings are much more advantageous, as they allow making the transmission and Faraday rotation peak coincident. The main parameter of the bilayer systems is the thickness of the dielectric layer that allows reaching this coincidence.

4.4.3.2 One-Dimensional Plasmonic Structure with Waveguiding Layer

Now let us turn to the case of the magnetic film thickness comparable to wavelength, and at this the waveguide modes become essential [123, 124]. As shown in Fig. 4.19 the Faraday rotation demonstrates both negative and positive peaks. Furthermore, the positive Faraday rotation peak at $\lambda = 883$ nm corresponds to more than four times enhancement being compared to the single magnetic layer of the same thickness placed in optically matched surrounding medium which has the Faraday angle of -0.47 deg. In addition to that, the positive Faraday rotation peak coincides to the resonance in transmission, allowing about 40 % of the incident energy flux to be transmitted. At the same time, the negative Faraday maximum at $\lambda = 818$ nm corresponds to almost negligible transmission. The peaks of the Faraday angle are accompanied by the abrupt changes of the light ellipticity. However, the ellipticity becomes zero at the resonance wavelength and the transmitted light remains linearly polarized, but with substantial rotation of the polarization plane.

Using (4.46) within the empty lattice approximation one can obtain the result that the following quasi-waveguide modes are excited: (i) TM mode at $\lambda = 814$ nm, (ii) TE modes at $\lambda = 844$ nm and $\lambda = 879$ nm. The comparison of these values

with the resonant features of the Faraday angle demonstrates that the negative and positive peaks correspond to the TM and TE modes excitation, respectively. It agrees well with the theoretical reasoning of the resonant behavior of the Faraday angle at the eigenmodes excitation and consequent increase of effective interaction length and moreover confirms the existence of the two mechanisms for its enhancement.

The effective interaction length is determined by the mode's lifetime which is inversely proportional to its resonance width $\Delta\omega$. The latter depends on the optical absorption in metal and in magnetic film, and on the mode's leakage into the far field as well. If the losses are negligibly small, then the relative resonance width is about $\Delta\omega/\omega = 5 \times 10^{-4}$. At this the resonant value of the Faraday angle is 14° that is 75 times higher than for the single film. For the real losses the resonance width is $\Delta\omega/\omega = 3 \times 10^{-3}$ that is six times lower, and the Faraday angle is 1.9° that is seven times lower. So one can conclude that $\Phi \sim (\Delta\omega)^{-1}$.

The Faraday rotation resonances corresponding to the TE modes are of prime practical significance. Firstly, at these resonances the Faraday effect enhancement by an order of magnitude or even higher can be achieved. Moreover, the Faraday angle maxima can be adjusted to transmission maxima. It comes from the following reasoning. Faraday angle peaks are caused by TE modes excitation so their spectral position depends mostly on magnetic film thickness h_m and the grating period. The transmission peak depends not only on magnetic film properties but also on the grating parameters such as the slit width and the grating thickness. Thus by tuning various geometrical parameters the coincidence of a transmission peak and a Faraday angle peak can be achieved.

It is very important to note that while the accordance between the negative Faraday rotation maxima and zeros of the transmission preserves for different geometrical parameters of the metal/dielectric heterostructure, the accordance between the positive Faraday angle peaks and transmission maxima is very sensitive to them, especially to the thickness of the dielectric film h_m. Thus for a little bit different values of h_m the positive peaks of the Faraday rotation and transmission maxima shift differently and do not coincide any more. This observation points out on the different nature of the negative and positive Faraday rotation resonances.

The dependence of the Faraday effect and transmission on the thickness h_m at $\lambda = 883$ nm are shown in Fig. 4.20. The values of h_m favorable for the propagation of TE or TM modes inside the dielectric slab are marked with solid and dashed lines, respectively, indicating the existence of the relation between the Faraday angle resonances and the waveguide modes. The transmission peaks marked by (1) are caused by excitation of localized modes. As we have just discussed the Faraday angle peaks correspond to the TE or TM modes resonances. At the same time, the transmission maxima do not correlate with such resonances and are mainly determined by the field distribution in the metal part of the plasmonic crystal. At $h_m = 537$ nm the Faraday angle maxima coincides with the transmission peak. Besides there are periodic oscillations of the Faraday angle and the transmission (with maxima marked by (2)), which are caused by interference of the wave transmitting through the magnetic film without modes excitation.

The close relation between main features of the optical and magneto-optical properties of the considered system and modes of the electromagnetic field in the

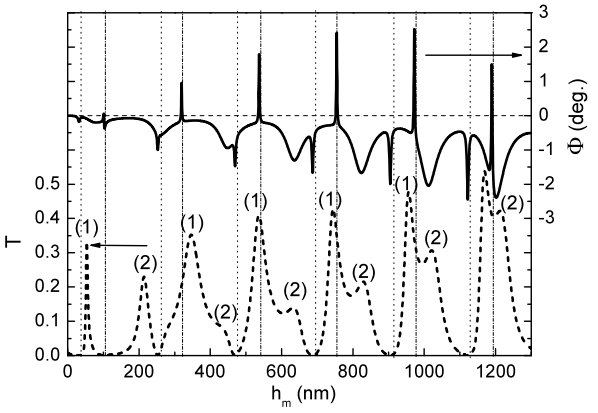

Fig. 4.20 Optical transmission (*dashed line*) and the Faraday rotation (*solid line*) versus the thickness h_m of the magnetic layer. Geometrical parameters of the Au-BiYIG film are the same as in Fig. 4.19; $\lambda = 883$ nm. *Vertical dashed* and *dotted lines* depict the position of the TE mode and TM mode resonances in the dielectric slab, respectively (see for details the text) [123, 124]

magnetic film is underscored by Fig. 4.21, where optical transmission and the Faraday angle versus the magnetic film thickness are shown for three different dielectric constants of the substrate. For the wavelength $\lambda = 840$ nm and grating period $d = 750$ nm two diffraction orders become propagating into the magnetic layer. The modes associated with them can be denoted as TE1, TE2, TM1, and TM2. As long as the dielectric constant of the substrate $\varepsilon < 1.255$, the condition of the total internal reflection is satisfied for both diffraction orders and all four modes are quasi-waveguide. Resonance features in transmission and Faraday rotation related to these modes are apparent. Thus, for the case of $\varepsilon = 1.25$ zeros of transmission and negative peaks of the Faraday rotation correspond to the resonances of TM1 and TM2 modes (Fig. 4.21(b)); positive peaks of the Faraday rotation coincide with resonances of TE1 and TE2 modes. For higher values of ε the total internal reflection for the first diffraction order is no longer present and only TE2- and TM2-modes remain localized in the dielectric layer. That is why in the graph for $\varepsilon = 1.6$ there are only one negative and only one positive Faraday effect resonances, corresponding to TM2 and TE2 modes excitation, respectively (Fig. 4.21(c)).

One needs to pay attention to the optical transmission. As it is anticipated by the preliminary discussion the transmission should strongly depend on the parameters of the metallic constituent of the heterostructure. This is fully proved by the Fig. 4.22(a), where a pronounced shift of the extraordinary optical transmission resonance with the increase of the metal layer thickness is present. Such transmission peak behavior emphasizes the role of the electromagnetic field distribution in the metal and near the metal/dielectric interface. At the same time, the Faraday angle is only weakly dependent on the metal thickness (Fig. 4.22(b)), since it is mostly determined by the field distribution inside the dielectric layer.

The electromagnetic field distribution in the plasmonic crystal is shown in Fig. 4.23, demonstrating the distribution of the absolute values of the electric field components E_x and E_y for three different thicknesses of the dielectric layer, corresponding to the extraordinary optical transmission peak ($h_m = 200$ nm), and Faraday rotation positive ($h_m = 322$ nm) and negative ($h_m = 471$ nm) resonances (see Fig. 4.20). Analysis of Fig. 4.23 confirms the assertions on the relation between

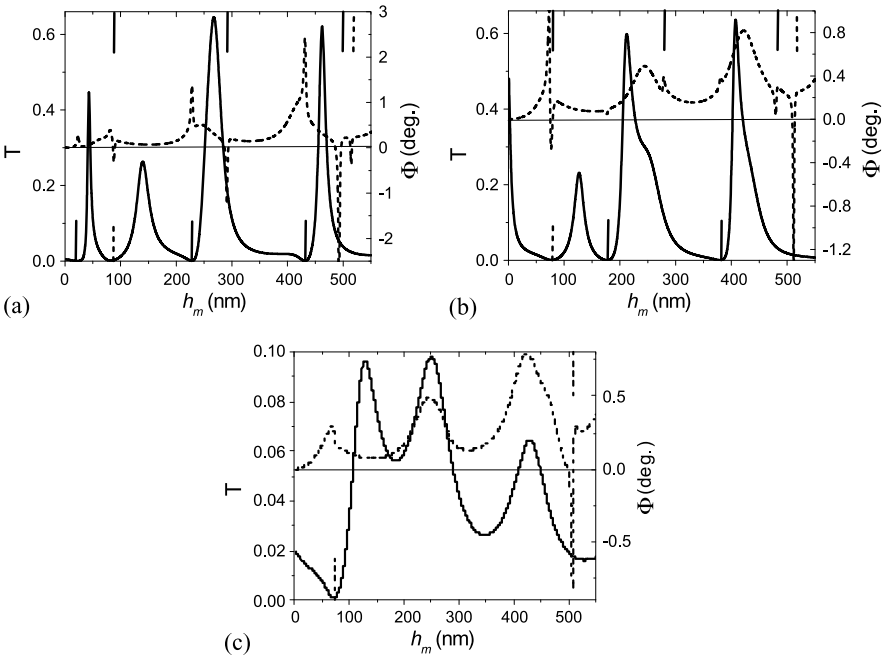

Fig. 4.21 Optical transmission (*solid line*) and the Faraday rotation (*dashed line*) versus the thickness h_m of the magnetic layer are shown for three different values of the dielectric constant of the substrate: (**a**) $\varepsilon = 1$, (**b**) $\varepsilon = 1.25$, (**c**) $\varepsilon = 1.6$. Thickness of Au grating is 70 nm, $d = 750$ nm, $r = 100$ nm (see Fig. 4.17); $\lambda = 840$ nm. *Solid* and *dotted lines* in the upper part of the graphs depict the position of the TE1- and TE2-modes, respectively. *Solid* and *dotted lines* in the bottom part of the graph depict the position of the TM1- and TM2-modes, respectively (see for details in the text) [124]

modes peculiarities and optical/magneto-optical features of the structure. Indeed, at the optical transmission resonance (Figs. 4.23(a), (b)) most of the energy of the E_x component is concentrated on the metal/dielectric interface hinting on the SPPs-like wave. We should notice here that the E_x component is associated to the incident polarization, as the incident wave is assumed to be polarized perpendicularly to the slits. At the dielectric layer thickness corresponding to the negative resonance of the Faraday effect the value of the E_x component is rather weak, while the E_y component is increased, suggesting that at this case it is TE mode which is quasi-waveguide (Figs. 4.23(c), (d)). On the contrary, when the dielectric film thickness has a value supporting positive peak of the Faraday angle most of the field energy is in its E_x component inside the dielectric layer (Figs. 4.23(e), (f)).

In [125, 126] it was emphasized that the Faraday rotation in the periodic systems is strongly related with the group velocity V_g and gets its maximum values at the vanishing of V_g. In the case of magnetic photonic crystals this dependence for the specific Faraday angle can be written by

$$\Phi_{\text{sp}} = \langle Q \rangle \omega / 2V_g, \tag{4.52}$$

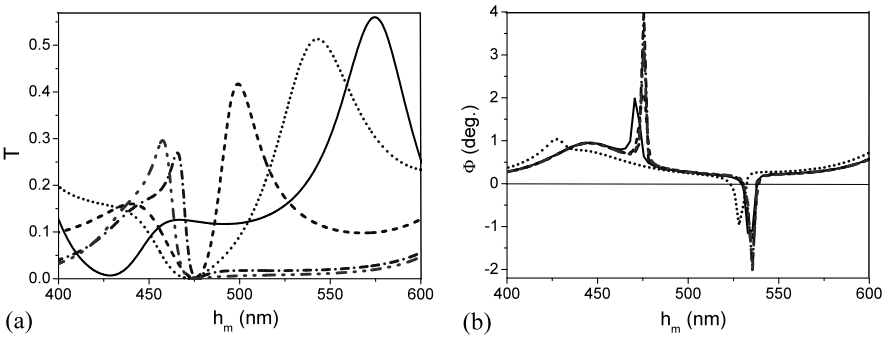

Fig. 4.22 Optical transmission (**a**) and the Faraday rotation (**b**) versus the thickness h_m of the magnetic layer for several different thicknesses of the metallic layer h: 40 nm (*solid lines*), 75 nm (*dotted lines*), 100 nm (*dashed lines*), 150 nm (*dash-dotted lines*), and 200 nm (*dash-dot-dotted lines*). Geometrical parameters of the Au-BiYIG film are the same as in Fig. 4.19; $\lambda = 883$ nm [123]

where $\langle Q \rangle$ is the matrix element of the Voigt parameter Q (see (4.14)) calculated in the volume of the single lattice cell of the system. Equation (4.52) demonstrates the strong correlation between the Faraday effect enhancement and the slow light effect. In the case of plasmonic crystals the mechanism is similar. At normal incidence the eigenmodes are excited at the Γ point of the Brillouin zone that corresponds to the bandgap edges. At this the excited modes experience decrease of the group velocity and the effective time of the interaction of a mode with the magnetic media and the conversion to the opposite mode increases. So the Faraday effect is enhanced. This reasoning is confirmed by Fig. 4.24 where the dispersion of the Faraday angle is plotted. The Faraday angle at the oblique incidence is smaller since the slow light effect does not take place.

It is not only the Faraday effect that acquires peculiarities in the plasmonic crystal. Indeed, it can be seen from Fig. 4.25 that the Kerr rotation is also enhanced at around $\lambda = 880$ nm. Note that the term *Kerr effect* here should be treated in the generalized sense, i.e. it includes not only light polarization rotation and ellipticity originated from the metal/ferromagnetic interface, but also magneto-optics of the reflected waves propagating through the bulk of the system.

4.4.3.3 Fishnet-Like Structure

Magneto-optical effects can be enhanced even more significantly in the cascaded metallic structures containing two perforated metal layers separated by a magnetic layer [124]. The advantages of the cascaded films for optical features of metal/dielectric structures have already been shown in [127], and here we report on their applicability in the magneto-optics area. The addition of the second metallic grating onto the bottom surface of the magnetic layer changes the conditions for the leaking modes in the dielectric slab allowing additional increase of the efficiency of the magneto-optical interaction and further decrease of the group veloc-

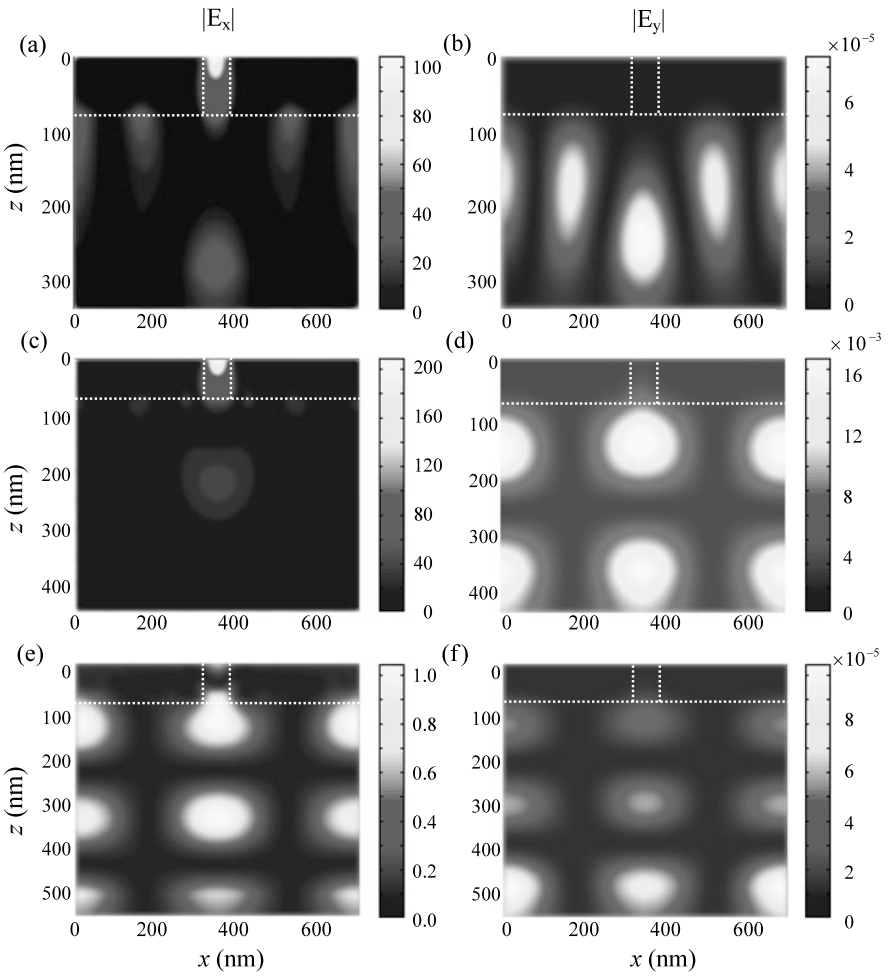

Fig. 4.23 Distribution of the electric field amplitudes $|E_x|$ and $|E_y|$ in the plasmonic crystal at three different values of the dielectric layer thickness: (**a**)–(**b**) $h_m = 200$ nm; (**c**)–(**d**) $h_m = 322$ nm; and (**e**)–(**f**) $h_m = 471$ nm. The other parameters are the same as in Fig. 4.20 [123]

ity at the resonance point. In Fig. 4.26(a) the transmission and the Faraday rotation spectra for one of the possible cascaded films design are shown. Both peaks finely coincide providing 17 times enhancement of the Faraday effect and 43 % of transmitted energy at wavelength $\lambda = 884$ nm. The dependences on the thickness of the magnetic film (see Fig. 4.26(b)) reveal again that the negative Faraday angle peaks happen at the negligible transmission, while positive Faraday angle maxima do not obviously correlate with any features of transmission spectra. As in the case of the metal/dielectric bilayers, the position of the positive Faraday maxima is determined by the TE mode resonances of the dielectric slab and can be adjusted by its thickness. The resonances of transmission are mainly dependent on

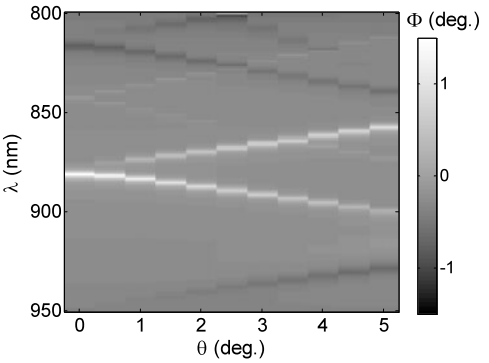

Fig. 4.24 The Faraday angle vs. the wavelength and the incidence angle. The parameters are the same as in Fig. 4.19

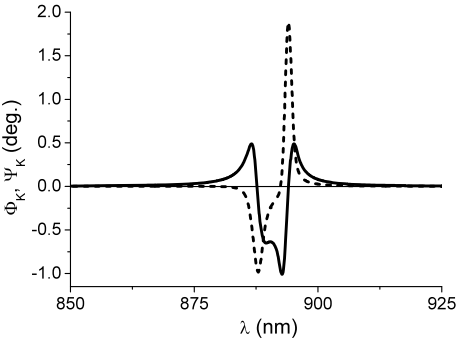

Fig. 4.25 Spectra of the Kerr rotation (*solid line*) and ellipticity (*dashed line*) of the bilayer system of Au grating of thickness 75 nm and uniform Bi:YIG film of thickness 538 nm; $d = 750$ nm, $r = 75$ nm (see Fig. 4.17) [124]

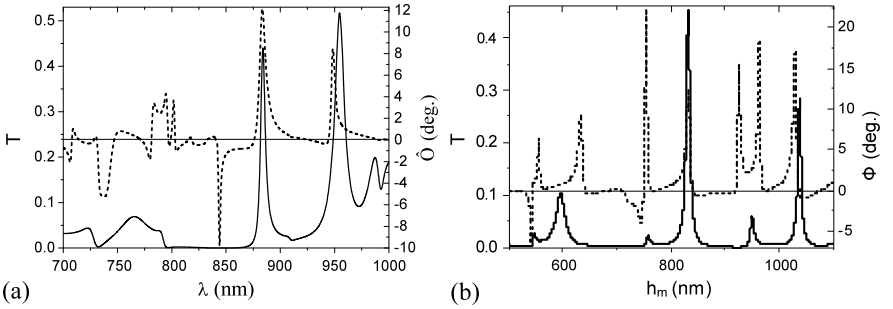

Fig. 4.26 Optical transmission (*solid line*) and the Faraday rotation (*dashed line*) versus (**a**) wavelength λ ($h_m = 832$ nm) and (**b**) the magnetic layer thickness h_m (λ = 884 nm) for the case of cascaded metal/dielectric film (see for details in the text). The geometrical parameters of both metallic gratings are the same: $d = 832$ nm, $r = 301$ nm, the thickness is 194 nm [124]

the parameters of the metallic gratings. Since there are two independent gratings in the cascaded systems the control of the transmission peak position becomes easier.

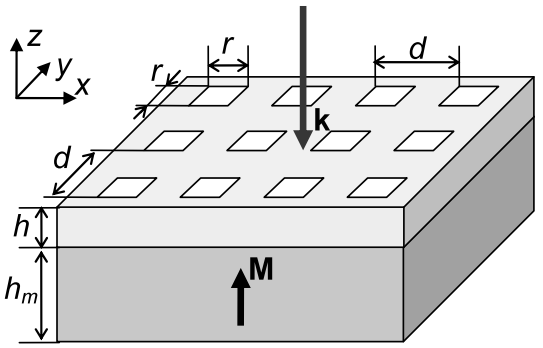

Fig. 4.27 The two-dimensional magnetic plasmonic crystal. Metallic plate (upper layer) is periodically perforated with the square hole arrays. Holes constitute a square lattice of period d. The size of each hole is r. Dielectric layer (lower layer) of thickness h_m is magnetized in polar geometry (along OZ-axis). The light with the wavevector **k** is normally incident

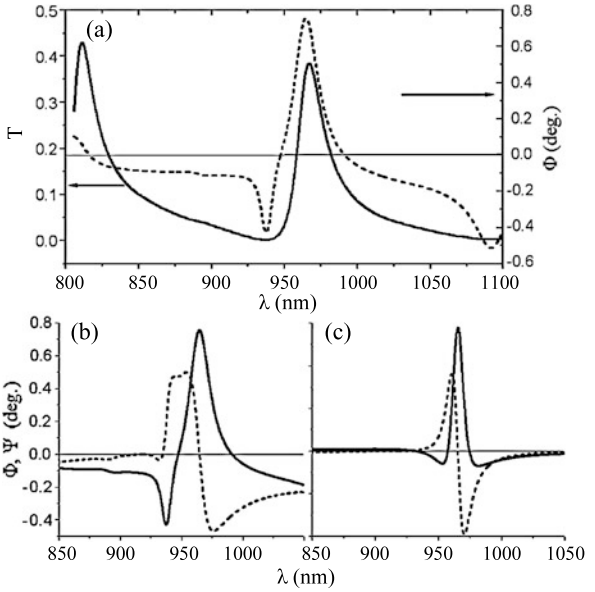

Fig. 4.28 Spectra of the optical transmission (*solid line* on (**a**)), Faraday rotation (*dashed line* on (**a**) and *solid line* on (**b**)), and ellipticity (*dashed line* on (**b**)), Kerr rotation (*solid line* on (**c**)) and ellipticity (*dashed line* on (**c**)) of the bilayer system of perforated Au film of thickness 68 nm and uniform Bi:YIG film of thickness 118 nm; $d = 750$ nm, $r = 395$ nm (see Fig. 4.27) [128]

4.4.3.4 Two-Dimensional Plasmonic Crystal

Finally, we consider the similar effects in two-dimensional plasmonic crystals shown in Fig. 4.27 [128, 129].

The results of the calculations of transmission and magneto-optical effects in the considered system are shown in Fig. 4.28. The Faraday and Kerr effects are described by the angles Φ_F and Φ_K, which stand for the Faraday and Kerr rotation of light polarization, and angles Ψ_F and Ψ_K denoting Faraday and Kerr ellipticity of light polarization, respectively.

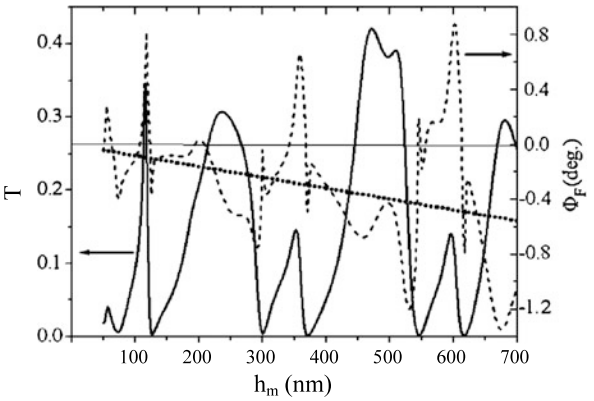

Fig. 4.29 Faraday rotation (*dashed line*) and transmission (*solid line*) versus the thickness h_m of the magnetic layer. Geometrical parameters of the Au-BiYIG film are the same as in Fig. 4.28; $\lambda = 963$ nm. *Dotted line* represents the Faraday rotation for the same single magnetic layer placed in optically matched surrounding medium [128]

Transmission spectrum of the Au/Bi:YIG bilayer has several transmission resonances, which are related to the light coupling with surface waves in the films. At the same time, at the vicinity of some transmission peaks a pronounced enhancement of the magneto-optical effects is found. Namely, at $\lambda_{\max} = 963$ nm where the transmission reaches 35 percent the Faraday and Kerr rotations get positive values of $\Phi_F = 0.78^\circ$ and $\Phi_K = 0.63^\circ$, respectively. This corresponds to their enhancement by nine times in comparison with the case of the same single magnetic layer surrounded by optically matched medium. Ellipticity of transmitted/reflected light polarization gets increased as well, but their positive and negative extrema happen at slightly different wavelengths and the ellipticity is almost zero at the resonance of the magneto-optical rotation. Consequently, transmitted and reflected electromagnetic waves at $\lambda_{\max} = 963$ nm are linearly polarized.

Optical and magneto-optical spectra presented in Fig. 4.28 correspond to the magnetic film thickness $h_m = 118$ nm. Under change of the thickness h_m all spectra substantially modify, which is demonstrated in Fig. 4.29 where the optical transmission and the Faraday rotation at $\lambda = 963$ nm versus thickness h_m are shown. It is vivid that for the given wavelength the optimal value of h_m is close to 118 nm. Positive and negative resonances in the Faraday rotation also happen for some other thicknesses but all of them correspond to smaller enhancement level. At some other incident wavelength the shape of the thickness dependences would modify and the optimization would take place for different h_m. Similar to one-dimensional plasmonic crystals, the resonances of the transmission and Faraday rotation do not fully correlate and their matching appear only for narrow interval of the film thickness values.

4.5 Conclusion

Here we have presented current situation in the area of plasmonics conjugated with magneto-optics. Main stress was made on the structures having three important features. Namely, they are (i) plasmonic, (ii) periodically nanostructured, and (iii) mag-

netic. The main aim of this chapter was to identify how the first two features affect the magneto-optical properties of the structure and in particular whether they can be used to enhance the magneto-optical effects. This has been accomplished exemplary by addressing several main magneto-optical effects such as the transverse Kerr effect, the Faraday effect and the even magneto-optical transmission effect. Thus, numerical calculations showed that the TMOKE for bare iron garnet film is very small $\delta \sim 10^{-4}$, both for transmitted and reflected light. When the film is covered by a smooth gold layer, the TMOKE is resonantly enhanced up to $\delta \sim 5 \times 10^{-3}$ but it can be observed only in reflection while the transmission almost vanishes. If the second feature—nanostructuring—comes into play extraordinary optical transmission appears with a giant TMOKE δ reaching 1.5×10^{-2}. Similar resonant increase is also demonstrated for the other magneto-optical effects.

There are several physical mechanisms responsible for the enhancement of the magneto-optical effects in plasmonic structures. In particular, they include (i) magnetization induced shift of plasmonic and waveguide mode frequencies in the magnetic transverse configuration, (ii) magnetization induced coupling of TM- and TE-modes of the gyrotropic waveguide in polar or longitudinal configurations, and (iii) influence of the local electromagnetic field in the vicinity of the metal structures at the plasmonic resonances on the spin-orbit coupling.

The appearance of the magneto-optical effects depends on the orientation of magnetization in the sample, which can be easily controlled by relatively small external magnetic field on the order of 100 Oe. With these parameters magnetic plasmonic crystals are very promising for applications in ultra high sensitivity devices and optical data processing. Plasmonic crystals are also promising for optical control of a medium magnetization. Enhancement of the inverse Faraday effect in plasmonic crystal was already shown theoretically [130]. Recent progress in the femtosecond control of the magnetization in conjunction with the concept of plasmonic crystal opens a possibility for modulation of light intensity and polarization in the plasmonic crystals at ultra fast terahertz rates.

Acknowledgements We would like to thank I.A. Akimov, M. Pohl, D.R. Yakovlev, and M. Bayer (TU Dortmund University, Germany) for their invaluable help in experimental demonstration of the enhanced TMOKE. We thank A.S. Vengurlekar, Achanta Venu Gopal, and S. Kasture (Tata Institute of Fundamental Research, India) for providing the plasmonic crystal structures and discussing the related results. We also thank E.A. Bezus, D.A. Bykov, and L.L. Doskolovich (Image Processing Systems Institute, RAS, Russia) for their help in electromagnetic modeling of optical properties of plasmonic structures. We are also grateful to K. Alameh, A.A. Fedyanin, H. Giessen, N.A. Gippius, V.A. Kotov, M. Levy, A.P. Sukhorukov, S.G. Tikhodeev, M. Vanwolleghem, and M. Vasiliev for fruitful discussions.

The work was supported by the Russian Foundation for Basic Research (RFBR, projects Nos. 12-02-33100, 12-02-31298, 11-02-00681), the Federal Targeted Program "Scientific and Scientific-Pedagogical Personnel of the Innovative Russia", and the Russian Presidential Fellowship SP-124.2012.5.

References

1. M. Faraday, *Experimental Researches in Electricity*, vol. 3 (Adamant Media Corp, Boston, 2005)
2. P.N. Prasad, *Nanophotonics* (Wiley, Hoboken, 2004)
3. A.K. Zvezdin, V.A. Kotov, *Modern Magnetooptics and Magnetooptical Materials* (IOP, Bristol, 1997)
4. V.I. Belotelov, V.A. Kotov, A.K. Zvezdin, Curr. Prog. Multiferroics Magnetoelectr. **79**, 1135 (2006)
5. A.V. Kimel, A. Kirilyuk, P.A. Usachev, R.V. Pisarev, A.M. Balbashov, Th. Rasing, Nature **435**, 655 (2005)
6. A. Kirilyuk, A.V. Kimel, Th. Rasing, Rev. Mod. Phys. **82**, 2731 (2010)
7. K. Vahaplar, A.M. Kalashnikova, A.V. Kimel, D. Hinzke, U. Nowak, R. Chantrell, A. Tsukamoto, A. Itoh, A. Kirilyuk, Th. Rasing, Phys. Rev. Lett. **103**, 117201 (2009)
8. J. Kerr, Philos. Mag. **3**, 321 (1877)
9. M. Mansuripur, *The Physical Principles of Magneto-Optical Recording* (Cambridge University Press, Cambridge, 1998)
10. G.S. Krinchik, V.A. Artem'ev, Zh. Eksp. Teor. Fiz. **53**, 1901 (1967) [Sov. Phys. JETP **26**, 1080 (1968)]
11. A.V. Druzhinin, I.D. Lobov, V.M. Mayevskiy, G.A. Bolotin, Phys. Met. Metallogr. **56**, 58 (1983)
12. M. Vasiliev, M. Nur-E-Alam, V.A. Kotov, K. Alameh, V.I. Belotelov, V.I. Burkov, A.K. Zvezdin, Opt. Express **17**, 19519 (2009)
13. S. Kahl, S.I. Khartsev, A.M. Grishin, K. Kawano, G. Kong, R.A. Chakalov, J.S. Abell, J. Appl. Phys. **91**, 9556 (2002)
14. G.S. Krinchik, E.A. Gan'shina, Zh. Eksp. Teor. Fiz. **65**, 1970 (1974) [Sov. Phys. JETP **38**, 983 (1974)]
15. A.K. Sarychev, V.M. Shalaev, *Electrodynamics of Metamaterials* (World Scientific, Singapore, 2007)
16. M. Inoue, K. Arai, T. Fujii, M. Abe, J. Appl. Phys. **85**, 5768 (1999)
17. M. Levy, H.C. Yang, M.J. Steel, J. Fujita, J. Lightwave Technol. **19**, 1964 (2001)
18. A.K. Zvezdin, V.I. Belotelov, Eur. Phys. J. B **37**, 479 (2004)
19. S.A. Maier, *Plasmonics: Fundamentals and Applications* (Springer, New York, 2007)
20. E. Ozbay, Science **311**, 189 (2006)
21. S.I. Bozhevolnyi (ed.), *Plasmonics Nanoguides and Circuits* (Pan Stanford, Singapore, 2008)
22. S.A. Maier, M.D. Friedman, P.E. Barclay, O. Painter, Appl. Phys. Lett. **86**, 071103 (2005)
23. A.V. Krasavin, N.I. Zheludev, Appl. Phys. Lett. **84**, 1416 (2004)
24. P. Andrew, W.L. Barnes, Science **306**, 1002 (2004)
25. I.A. Akimov, V.I. Belotelov, A.V. Scherbakov, M. Pohl, A.N. Kalish, A.S. Salasyuk, M. Bombeck, C. Brüggemann, A.V. Akimov, R.I. Dzhioev, V.L. Korenev, Yu.G. Kusrayev, V.F. Sapega, V.A. Kotov, D.R. Yakovlev, A.K. Zvezdin, M. Bayer, J. Opt. Soc. Am. B **29**, A103 (2012)
26. R.H. Ritchie, Phys. Rev. **106**, 874 (1957)
27. E.A. Stern, R.A. Ferrell, Phys. Rev. **120**, 130 (1960)
28. D. Sarid, Phys. Rev. Lett. **47**, 1927 (1981)
29. E. Kretschmann, H. Raether, Z. Naturforsch. A **23A**, 2135 (1968)
30. A. Otto, Z. Phys. Hadrons Nucl. **216**, 398 (1968)
31. H. Ragossnig, A. Feltz, J. Eur. Ceram. Soc. **18**, 429 (1998)
32. M. Pohl, V.I. Belotelov, I.A. Akimov, S. Kasture, A.S. Vengurlekar, A.V. Gopal, A.K. Zvezdin, D.R. Yakovlev, M. Bayer, Phys. Rev. B **85**, 081401(R) (2012)
33. U. Kreibig, M. Vollmer, *Optical Properties of Metal Clusters* (Springer, Berlin, 1995)
34. A. Christ, S.G. Tikhodeev, N.A. Gippius, J. Kuhl, H. Giessen, Phys. Rev. Lett. **91**, 183901 (2003)

35. R.V. Pisarev, *Physics of Magnetic Dielectrics* (Nauka, Leningrad, 1974)
36. G.S. Krinchik, *Physics of Magnetic Phenomena* (Moscow State University Press, Moscow, 1985)
37. W. Voigt, *Magneto und Elektrooptic* (Teubner, Leipzig, 1908)
38. C.N. Afonso, F. Briones, J. Phys. F, Met. Phys. **10**, 1253 (1980)
39. R. Carey, B.W.J. Thomas, I.V.F. Viney, G.H. Weaver, J. Phys. D, Appl. Phys. **1**, 1679 (1968)
40. R.R. Birss, N. Collings, M.R. Parker, Phys. Lett. A **51**, 13 (1975)
41. C.N. Afonso, J.L. Vincent, F. Briones, J. Phys. D, Appl. Phys. **10**, 753 (1977)
42. G.A. Bolotin, Fiz. Met. Metalloved. **39**, 731 (1975)
43. G.S. Krinchik, V.S. Gushchin, Zh. Eksp. Teor. Fiz., Pis. Red. **10**, 35 (1969) [JETP Lett. **10**, 24 (1969)]
44. B. Donovan, T. Medcalf, Proc. Phys. Soc. **86**, 1179 (1965)
45. P.E. Ferguson, O.M. Stafsudd, R.F. Wallis, Physica B+C **86–88**, 1403 (1977)
46. J.J. Burke, G.I. Stegeman, T. Tamir, Phys. Rev. B **33**, 5186 (1986)
47. R.K. Hickernell, D. Sarid, Opt. Lett. **12**, 570 (1987)
48. G.C. Aers, A.D. Boardman, J. Phys. C, Solid State Phys. **11**, 945 (1978)
49. M.S. Kushwaha, Surf. Sci. Rep. **41**, 1 (2001)
50. N. Bonod, R. Reinisch, E. Popov, M. Nevière, J. Opt. Soc. Am. B **21**, 791 (2004)
51. V.V. Temnov, G. Armelles, U. Woggon, D. Guzatov, A. Cebollada, A. Garcia-Martin, J.-M. Garcia-Martin, T. Thomay, A. Leitenstorfer, R. Bratschitsch, Nat. Photonics **4**, 107 (2010)
52. J.B. González-Díaz, A. García-Martín, G. Armelles, J.M. García-Martín, C. Clavero, A. Cebollada, R.A. Lukaszew, J.R. Skuza, D.P. Kumah, R. Clarke, Phys. Rev. B **76**, 153402 (2007)
53. E. Ferreiro Vila, X.M. Beñdana Sueiro, J.B. González-Díaz, A. García-Martín, J.M. García-Martín, A. Cebollada Navarro, G. Armelles Reig, D. Meneses Rodríguez, E. Muñoz Sandoval, IEEE Trans. Magn. **44**, 3303 (2008)
54. M.G. Manera, G. Montagna, E. Ferreiro-Vila, L. González-García, J.R. Sánchez-Valencia, A.R. González-Elipe, A. Cebollada, J.M. Garcia-Martin, A. Garcia-Martin, G. Armelles, R. Rella, J. Mater. Chem. **21**, 16049 (2011)
55. B. Sepúlveda, L.M. Lechuga, G. Armelles, J. Lightwave Technol. **24**, 945 (2006)
56. A.A. Grunin, A.G. Zhdanov, A.A. Ezhov, E.A. Ganshina, A.A. Fedyanin, Appl. Phys. Lett. **97**, 261908 (2010)
57. C. Clavero, K. Yang, J.R. Skuza, R.A. Lukaszew, Opt. Lett. **35**, 1557 (2010)
58. G. Armelles, J.B. González-Díaz, A. García-Martín, J.M. García-Martín, A. Cebollada, M.U. González, S. Acimovic, J. Cesario, R. Quidant, G. Badenes, Opt. Express **16**, 16104 (2008)
59. M.V. Sapozhnikov, S.A. Gusev, B.B. Troitskii, L.V. Khokhlova, Opt. Lett. **36**, 4197 (2011)
60. G. Ctistis, E. Papaioannou, P. Patoka, J. Gutek, P. Fumagalli, M. Giersig, Nano Lett. **9**, 1 (2009)
61. J.F. Torrado, J.B. González-Díaz, G. Armelles, A. García-Martín, A. Altube, M. López-García, J.F. Galisteo-López, A. Blanco, C. López, Appl. Phys. Lett. **99**, 193109 (2011)
62. D.M. Newman, M.L. Wears, R.J. Matelon, I.R. Hooper, J. Phys. Condens. Matter **20**, 345230 (2008)
63. Y.M. Strelniker, D.J. Bergman, Phys. Rev. B **77**, 205113 (2008)
64. G. Armelles, A. Cebollada, A. García-Martín, J.M. García-Martín, M.U. González, J.B. González-Díaz, E. Ferreiro-Vila, J.F. Torrado, J. Opt. A, Pure Appl. Opt. **11**, 114023 (2009)
65. J.F. Torrado, J.B. González-Díaz, M.U. González, A. García-Martín, G. Armelles, Opt. Express **18**, 15635 (2010)
66. T.V. Murzina, I.A. Kolmychek, A.A. Nikulin, E.A. Gan'shina, O.A. Aktsipetrov, Pis'ma Zh. Eksp. Teor. Fiz. **90**, 552 (2009) [JETP Lett. **90**, 504 (2009)]
67. I.A. Kolmychek, T.V. Murzina, O.A. Aktsipetrov, Proc. SPIE **7394**, 739424 (2009)
68. A.B. Khanikaev, S.H. Mousavi, G. Shvets, Y.S. Kivshar, Phys. Rev. Lett. **105**, 126804 (2010)

69. V.M. Dubovik, L.A. Tosunyan, Fiz. Elem. Chastits At. Yadra **14**, 1193 (1983) [Sov. J. Part. Nucl. **14**, 504 (1983)]
70. A.N. Kalish, V.I. Belotelov, A.K. Zvezdin, Proc. SPIE **6728**, 67283D (2007)
71. V.I. Belotelov, D.A. Bykov, L.L. Doskolovich, A.N. Kalish, A.K. Zvezdin, J. Opt. Soc. Am. B **26**, 1594 (2009)
72. V.I. Belotelov, I.A. Akimov, M. Pohl, V.A. Kotov, S. Kasture, A.S. Vengurlekar, A.V. Gopal, D.R. Yakovlev, A.K. Zvezdin, M. Bayer, Nat. Nanotechnol. **6**, 370 (2011)
73. V.I. Belotelov, D.A. Bykov, L.L. Doskolovich, A.N. Kalish, A.K. Zvezdin, Zh. Eksp. Teor. Fiz. **137**, 932 (2010) [J. Exp. Theor. Phys. **110**, 816 (2010)]
74. D.M. Whittaker, I.S. Culshaw, Phys. Rev. B **60**, 2610 (1999)
75. S.G. Tikhodeev, A.L. Yablonskii, E.A. Muljarov, N.A. Gippius, T. Ishihara, Phys. Rev. B **66**, 045102 (2002)
76. M. Nevière, E. Popov, R. Reinisch, J. Opt. Soc. Am. A **12**, 513 (1995)
77. N. Chateau, J.-P. Hugonin, J. Opt. Soc. Am. A **11**, 1321 (1994)
78. A. Archambault, T.V. Teperik, F. Marquier, J.J. Greffet, Phys. Rev. B **79**, 195414 (2009)
79. A.B. Akimov, A.S. Vengurlekar, T. Weiss, N.A. Gippius, S.G. Tikhodeev, Pis'ma Zh. Eksp. Teor. Fiz. **90**, 398 (2009) [JETP Lett. **90**, 355 (2009)]
80. U. Fano, Phys. Rev. **124**, 1866 (1961)
81. S. Fan, W. Suh, J.D. Joannopoulos, J. Opt. Soc. Am. A **20**, 569 (2003)
82. M. Sarrazin, J.-P. Vigneron, Europhys. News **38**(3), 27 (2007)
83. M.G. Moharam, D.A. Pommet, E.B. Grann, T.K. Gaylord, J. Opt. Soc. Am. A **12**, 1077 (1995)
84. L. Li, J. Opt. A, Pure Appl. Opt. **5**, 345 (2003)
85. D. Palik (ed.), *Handbook of Optical Constants of Solids* (Edward Academic, Orlando, 1985)
86. R.W. Wood, Phys. Rev. **48**, 928 (1935)
87. V.I. Belotelov, I.A. Akimov, M. Pohl, A.N. Kalish, S. Kasture, A.S. Vengurlekar, A.V. Gopal, V.A. Kotov, D. Yakovlev, A.K. Zvezdin, M. Bayer, J. Phys. Conf. Ser. **303**, 012038 (2011)
88. V.I. Belotelov, D.A. Bykov, L.L. Doskolovich, A.N. Kalish, V.A. Kotov, A.K. Zvezdin, Opt. Lett. **34**, 398 (2009)
89. V.I. Belotelov, D.A. Bykov, L.L. Doskolovich, A.N. Kalish, A.K. Zvezdin, Fiz. Tverd. Tela **51**, 1562 (2009) [Phys. Solid State **51**, 1656 (2009)]
90. A. Hessel, A.A. Oliner, Appl. Opt. **4**, 1275 (1965)
91. M.S. Kushwaha, P. Halevi, Phys. Rev. B **35**, 3879 (1987)
92. M.S. Kushwaha, P. Halevi, Phys. Rev. B **38**, 12428 (1988)
93. V.E. Kochergin, A.Yu. Toporov, M.V. Valeiko, Pis'ma Zh. Eksp. Teor. Fiz. **68**, 376 (1998) [JETP Lett. **68**, 400 (1998)]
94. V.I. Safarov, V.A. Kosobukin, C. Hermann, G. Lampel, J. Peretti, C. Marlière, Phys. Rev. Lett. **73**, 3584 (1994)
95. C. Hermann, V.A. Kosobukin, G. Lampel, J. Peretti, V.I. Safarov, P. Bertrand, Phys. Rev. B **64**, 235422 (2001)
96. B. Sepúlveda, L.M. Lechuga, G. Armelles, J. Lightwave Technol. **24**, 945 (2006)
97. J. Judy, IEEE Trans. Magn. **6**, 563 (1970)
98. M. Diwekar, V. Kamaev, J. Shi, Z.V. Vardeny, Appl. Phys. Lett. **84**, 3112 (2004)
99. A.B. Khanikaev, A.V. Baryshev, A.A. Fedyanin, A.B. Granovsky, M. Inoue, Opt. Express **15**, 6612 (2007)
100. Y.H. Lu, M.H. Cho, J.B. Kim, G.J. Lee, Y.P. Lee, J.Y. Rhee, Opt. Express **16**, 5378 (2008)
101. V.I. Belotelov, A.K. Zvezdin, J. Magn. Magn. Mater. **300**, e260 (2006)
102. G.A. Wurtz, W. Hendren, R. Pollard, R. Atkinson, L. Le Guyader, A. Kirilyuk, Th. Rasing, I.I. Smolyaninov, A.V. Zayats, New J. Phys. **10**, 105012 (2008)
103. L. Wang, C. Clavero, Z. Huba, K.J. Carroll, E.E. Carpenter, D. Gu, R.A. Lukaszew, Nano Lett. **11**, 1237 (2011)
104. E.Th. Papaioannou, V. Kapaklis, P. Patoka, M. Giersig, P. Fumagalli, A. Garcia-Martin, E. Ferreiro-Vila, G. Ctistis, Phys. Rev. B **81**, 054424 (2010)

105. V. Bonanni, S. Bonetti, T. Pakizeh, Z. Pirzadeh, J. Chen, J. Nogués, P. Vavassori, R. Hillenbrand, J. Åkerman, A. Dmitriev, Nano Lett. **11**, 5333 (2011)
106. B. Sepúlveda, J.B. González-Díaz, A. García-Martín, L.M. Lechuga, G. Armelles, Phys. Rev. Lett. **104**, 147401 (2010)
107. G.-X. Du, S. Saito, M. Takahashi, IEEE Trans. Magn. **47**, 3167 (2011)
108. V.K. Valev, A.V. Silhanek, W. Gillijns, Y. Jeyaram, H. Paddubrouskaya, A. Volodin, C.G. Biris, N.C. Panoiu, B. De Clercq, M. Ameloot, O.A. Aktsipetrov, V.V. Moshchalkov, T. Verbiest, ACS Nano **5**, 91 (2011)
109. J.B. González-Díaz, A. García-Martín, G. Armelles, D. Navas, M. Vázquez, K. Nielsch, R.B. Wehrspohn, U. Gösele, Adv. Mater. **19**, 2643 (2007)
110. J.B. González-Díaz, A. García-Martín, J.M. García-Martín, A. Cebollada, G. Armelles, B. Sepúlveda, Y. Alaverdyan, M. Käll, Small **4**, 202 (2008)
111. G.X. Du, T. Mori, S. Saito, M. Takahashi, Phys. Rev. B **82**, 161403 (2010)
112. S. Tomita, T. Kato, S. Tsunashima, S. Iwata, M. Fujii, S. Hayashi, Phys. Rev. Lett. **96**, 167402 (2006)
113. S. Tkachuk, G. Lang, C. Krafft, O. Rabin, I. Mayergoyz, J. Appl. Phys. **109**, 07B717 (2011)
114. R. Fujikawa, A.V. Baryshev, J. Kim, H. Uchida, M. Inoue, J. Appl. Phys. **103**, 07D301 (2008)
115. H. Uchida, Y. Masuda, R. Fujikawa, A.V. Baryshev, M. Inoue, J. Magn. Magn. Mater. **321**, 843 (2009)
116. A.A. Zharov, V.V. Kurin, J. Appl. Phys. **102**, 123514 (2007)
117. I.D. Mayergoyz, G. Lang, L. Hung, S. Tkachuk, C. Krafft, O. Rabin, J. Appl. Phys. **107**, 09A925 (2010)
118. K.J. Chau, M. Johnson, A.Y. Elezzabi, Phys. Rev. Lett. **98**, 133901 (2007)
119. B. Bai, J. Tervo, J. Turunen, New J. Phys. **8**, 205 (2006)
120. K. Fang, Z. Yu, V. Liu, S. Fan, Opt. Lett. **36**, 4254 (2011)
121. A.N. Kalish, V.I. Belotelov, D.A. Bykov, L.L. Doskolovich, A.K. Zvezdin, Opt. Zh. **77**, 62 (2010) [J. Opt. Technol. **77**, 784 (2010)]
122. V.I. Belotelov, L.L. Doskolovich, V.A. Kotov, E.A. Bezus, D.A. Bykov, A.K. Zvezdin, Proc. SPIE **6728**, 67281M (2007)
123. V.I. Belotelov, L.L. Doskolovich, V.A. Kotov, E.A. Bezus, D.A. Bykov, A.K. Zvezdin, Opt. Commun. **278**, 104 (2007)
124. V.I. Belotelov, L.L. Doskolovich, V.A. Kotov, E.A. Bezus, D.A. Bykov, A.K. Zvezdin, Proc. SPIE **6581**, 65810S (2007)
125. V.I. Belotelov, A.K. Zvezdin, J. Opt. Soc. Am. B **22**, 286–292 (2005)
126. V.I. Belotelov, A.N. Kalish, V.A. Kotov, A.K. Zvezdin, J. Magn. Magn. Mater. **321**, 826 (2009)
127. Y.-H. Ye, J.-Y. Zhang, Opt. Lett. **30**, 1521 (2005)
128. V.I. Belotelov, L.L. Doskolovich, A.K. Zvezdin, Phys. Rev. Lett. **98**, 077401 (2007)
129. V.I. Belotelov, L.L. Doskolovich, V.A. Kotov, A.K. Zvezdin, J. Magn. Magn. Mater. **310**, e843 (2007)
130. V.I. Belotelov, E.A. Bezus, L.L. Doskolovich, A.N. Kalish, A.K. Zvezdin, J. Phys. Conf. Ser. **200**, 092003 (2010)

Chapter 5
Magnetorefractive Effect in Magnetoresistive Materials

Alexander Granovsky, Yurii Sukhorukov, Elena Gan'shina, and Andrey Telegin

Abstract In this chapter, we survey early and later experimental and theoretical results on the magnetorefractive effect in: (i) all-metal multilayers and granular alloys with giant magnetoresistance, (ii) metal–insulator multilayers and nanocomposites with tunnel magnetoresistance, (iii) bulk single- and polycrystals, thin films and heterostructures of manganites with colossal magnetoresistance, focusing on recent developments that have led to a better understanding of the magnetorefractive effect in the infrared and visible range of spectrum and to the recognition of unsolved problems and possible routes for the magnetorefractive effect enhancement. The possible applications of the magnetorefractive effect are also discussed.

Abbreviations

MRE	magnetorefractive effect
MO	magneto-optical
IR	infrared
SOI	spin–orbit interaction
MR	magnetoresistance

5.1 Introduction

Discovered by Michael Faraday in 1845, the Faraday effect was the first experimental evidence that light interacts with magnetized media. Later, numerous magneto-optical (MO) effects, odd- and even-parity in magnetization, linear and non-linear relative to a light intensity were discovered and widely used in physics and technique [1]. Being observed in a wide spectral range, from microwaves to infrared, ultraviolet and X-ray wavelengths, in metals, semiconductors, oxides, gases and liquids MO phenomena provide a basis for magnetophotonics, which operates with

A. Granovsky (✉) · E. Gan'shina
Faculty of Physics, M.V. Lomonosov Moscow State University, Moscow 119991, Russia
e-mail: granov@magn.ru

Y. Sukhorukov · A. Telegin
Institute of Metal Physics, Russian Academy of Sciences, Yekaterinburg 620990, Russia

M. Inoue et al. (eds.), *Magnetophotonics*, Springer Series in Materials Science 178,
DOI 10.1007/978-3-642-35509-7_5, © Springer-Verlag Berlin Heidelberg 2013

charges, spins of electrons, and photons. By means of magnetophotonics the ultra-fast manipulation of light characteristics is possible by an external magnetic field. On the other hand, ultra-fast control and manipulation of magnetization is done by light [2]. Photons do not interact directly with magnetic moments, they do this through relativistic effects such as the spin–orbit interaction (SOI). This is why the MO effects are very weak even for advanced MO materials. For example, the change in intensity of reflected light under magnetization of ferromagnetic materials does not exceed 0.1 % in the visible [1]. Numerous efforts during last years were devoted to searching for novel MO materials [1], enhancing the Faraday and Kerr effects in artificial structures, for example, in magnetophotonic crystals [3], and seeking new MO effects that are not determined by a weak SOI. Recently, this activity has been triggered by rapid progress in optoelectronics, optical communication, all-optical computers, ultra-fast magnetic recording, holography, etc.

One of such promising phenomena is the magnetorefractive effect (MRE) [4–7], which is a high-frequency response on magnetoresistance (MR) and manifests itself in magnetic field-induced changes in the coefficients of infrared light reflection (R), transmission (I), and absorption (A) in magnetic materials having large magnetoresistance (MR). MRE parameters are called magnetoreflection, magnetotransmission and magnetoabsorption of light, respectively:

$$\frac{\Delta R(H)}{R} = \frac{R(H) - R(H=0)}{R(H=0)}, \tag{5.1}$$

$$\frac{\Delta I(H)}{I} = \frac{I(H) - I(H=0)}{I(H=0)}, \tag{5.2}$$

$$\frac{\Delta A(H)}{A} = \frac{A(H) - A(H=0)}{A(H=0)}. \tag{5.3}$$

It is assumed in (5.1)–(5.3) that the sample is completely demagnetized in the external magnetic field of $H = 0$, i.e. the average magnetization M is zero. If it is not the case, one can to use values of R, I, A at $H = H_c$, where H_c is the coercivity. Another phenomenon related to the MRE is the change in the radiated intensity (emissivity) in external magnetic fields [8].

Since the dc conductivity $\sigma = \sigma(\omega = 0)$ of magnetic materials exhibiting any type of large MR (for example, anisotropic, giant, tunnel, or colossal MR) changes significantly upon magnetization, the ac conductivity $\sigma(\omega)$ also depends on magnetic field. The diagonal part of effective permittivity ε_d, which by definition determines the complex refractive index $\tilde{n} = n - ik$, is written as

$$\varepsilon_d(\omega, H, T) = \varepsilon' - i\varepsilon'' = (n - ik)^2 = \varepsilon_r(\omega, H, T) - i\frac{4\pi\sigma(\omega, H, T)}{\omega}, \tag{5.4}$$

and therefore also is a function of H. In this formula n is refractive index, k is index of extinction, and $\varepsilon_r(\omega, H, T)$ term is associated with displacement current and interband optical transitions; ω is the light frequency, T stands for the temperature of a material. The second term in (5.4) describes the MRE. Thus, the origin of MRE is the high-frequency MR. As an example, Fig. 5.1 demonstrates the strict correlation between magnetoreflection of infrared light for a nanocomposite $Co_x(Al_2O_3)_{1-x}$

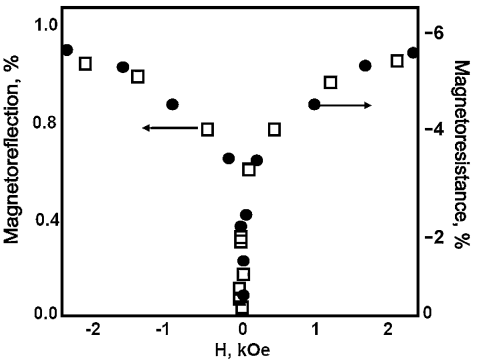

Fig. 5.1 Magnetic field dependences of magnetoreflection and magnetoresistance for a $Co_{43}Al_{22}O_{35}$ nanocomposite at the incident angle $\varphi = 10°$ and frequency $\nu = 1130\ cm^{-1}$ at room temperature

and its MR [9]. It should be underlined that, for this structure and the parameters of experiment (see the caption to Fig. 5.1), the change in reflection due to the MRE is at least two or three orders of magnitude larger than that for the transverse MO Kerr effect.

The frequency, temperature, and field dependences of $\sigma(\omega, H, T)$ and the MRE parameters (5.1)–(5.3) depend on the type of MR and of materials under consideration. In contrast to traditional MO phenomena the MRE is not attributed to the SOI but is associated with MR, hence, the magnetoreflection and magnetotransmission of light due to the MRE in high-magnetoresistive materials can reach values of 10–20 % that are giant for magneto-optics. The MRE is nongyrotropic phenomenon i.t it is an even-parity function of magnetization.

It is worth to discuss the definition of the MRE in more detail. The term "magnetorefractive effect" means that the indices n and k change in the presence of an external magnetic field H. Generally, this term can be used for any mechanisms of magnetoreflection, magnetotransmission, and magnetoabsorption in arbitrary materials, even in insulators [10] or paramagnetic and diamagnetic metals and semiconductors without or with very small MR. For example, such effects in non-magnetic semiconductors, which are sometimes referred to as magnetoplasma phenomena (see [11, 12]), have been known for more than 50 years. However, they are relatively weak even in a strong magnetic field and can be observed only in a narrow frequency range [11] at low temperatures. The effects of magnetoreflection and magnetotransmission may be caused by the following:

- influence of the Lorentz force on charge carriers' transport [11, 12];
- changes in the concentration of charge carriers, in the electronic structure, in the probability of interband optical transitions [13], due to the Fermi level shift or the displacement of the mobility edge [14] by a strong magnetic field;
- magnetic field-induced phase transitions and phase separation [43];
- the change of the effective polaron mass [15], due to the dynamic Jahn–Teller effect [16];
- a strong suppression of polarons [17] by a magnetic field, etc. (see discussion below).

All this eventually leads to changes in the permittivity. Initially, these effects were not considered as manifestations of the MRE, because Jacquet and Valet [4] introduced this term in 1995 only for magnetoreflection and magnetotransmission of infrared radiation (IR) in metallic multilayers with giant MR. Later, the term MRE, which characterizes the high-frequency response to MR, had been applied to any systems with a significant value of MR, including those with giant, tunneling, and colossal MR, not only in the IR spectral region but also in the microwave [18, 19] and visible range [16]. Recently, this term has been used for all the mechanisms providing magnetoreflection and magnetotransmission that are not determined by the SOI [10, 13–17]. Although, strictly speaking, this is not consistent with the initial definition of Jacquet and Valet [4], we will also use the term MRE in a broad sense to refer to different mechanisms of magnetoreflection and magnetotransmission rather than only to a high-frequency response to MR, every time, whenever possible, specifying the cause of these effects.

In this chapter, firstly, we will briefly survey early experimental and theoretical results on the MRE in: (i) all-metal multilayers and granular alloys with giant magnetoresistance, (ii) metal–insulator multilayers and nanocomposites with tunnel magnetoresistance, (iii) manganites with colossal magnetoresistance, and magnetophotonic crystals. Secondly, we will focus on recent developments, which have led to better understanding of the MRE and to the recognition of unsolved problems and possible routes for the MRE enhancement.

5.2 MRE in All-Metal Multilayers and Granular Alloys with Giant MR

5.2.1 Introductory Remarks

The permittivity tensor for a medium magnetized along the z axis has the form of

$$\widehat{\varepsilon} = \begin{pmatrix} \varepsilon_{xx} & \varepsilon_{xy} & 0 \\ \varepsilon_{yx} & \varepsilon_{yy} & 0 \\ 0 & 0 & \varepsilon_{zz} \end{pmatrix}. \tag{5.5}$$

It follows from symmetry considerations that $\varepsilon_{xx} = \varepsilon_{yy}$ and $\varepsilon_{xy} = -\varepsilon_{yx}$. The non-diagonal components are linear, while the diagonal components of $\widehat{\varepsilon}$ are quadratic in magnetization M, i.e.

$$\varepsilon_{xx} = \varepsilon_d\left(1 + bM^2\right); \qquad b = b_a + b_{\mathrm{MRE}}; \qquad \varepsilon_{xy} = aM. \tag{5.6}$$

Here, b_a characterizes the contribution due to induced anisotropy of the magnet [20, 21], which is on second order of the SOI, while b_{MRE} describes the MRE contribution. The non-diagonal elements of the permittivity tensor are responsible for the MO Kerr and Faraday effects, which are linear in the SOI and magnetization, and also may lead to the even-parity MO effect. Note that the so-called orientation MO effect, which is also even-parity in magnetization [20, 21], is associated

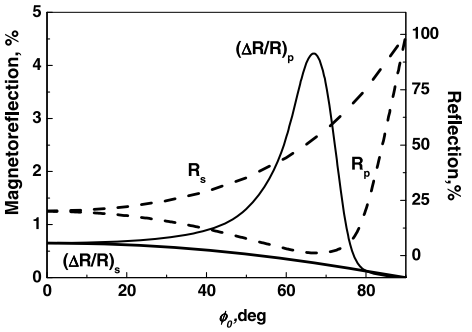

Fig. 5.2 Dependencies of the magnetorefractive effect in reflection mode (magnetoreflection) and the reflection coefficient on an incident angle of s- and p-polarized light for an insulating nanocomposite (below the percolation threshold): $\frac{\Delta\rho}{\rho} = -3\ \%$, $n = 2.5$, $k = 0.5$

both with the contribution $\varepsilon_d b_a M^2$ to the diagonal elements and with non-diagonal terms ε_{xy}. Consequently, the results of MRE measurements always contain the contribution from these even-parity MO effects along with the true MRE. As a rule, the even-parity MO effects are discarded in the analysis of the MRE based on the following arguments. The contributions of induced anisotropy and non-diagonal terms to magnetoreflection and magnetotransmission are approximately the square of the MO factor Q [21], i.e. are quadratic in the SOI. The MO factor Q in the visible spectral region for most materials does not exceed 0.01 and there are no grounds to expect an increase in this factor in the IR spectral region. Consequently, the even-parity MO effects may lead to a change in R upon magnetization by no more than 0.1 %. Thus, the influence of the even-parity MO effects on the MRE can be neglected in all cases when the MRE exceeds 0.1 %. At first glance these arguments look reasonable. Nevertheless, in spite of the induced anisotropy term is quadratic in the SOI, the corresponding contribution to magnetoreflection may be compared with linear MO effects because of different role of degenerate states near Fermi energy and different MO transitions in the even-parity MO effects, which are due to the diagonal and non-diagonal terms in (5.5). A good example of such possibility is given in Ref. [21]. It is not without precedent for effects related to the SOI. For example, anisotropic MR is also quadratic in the SOI but may reach 4 % at room temperature and 20 % at low temperatures. Thus, it should be taken into account that even-parity MO effects can give a noticeable contribution to magnetoreflection and magnetotransmission; especially in the case of materials with giant MO phenomena in the visible spectral range.

If a function of $\widehat{\varepsilon}\ (\omega, H, T)$ is known, then, using the Fresnel formulas, it is not difficult to calculate the MRE parameters (5.1)–(5.3) for an arbitrary angle and polarization of incident light in the cases of thick samples or thin films on substrates [9, 22]. Without interference effects and backscattering from a substrate magnetoreflection increases with an angle of incidence for p-polarized light [22], reaches maximum at an angle close to the Brewster angle and then decreases (Fig. 5.2). In contrast to the MO Kerr effect, the MRE exists at normal incidence and weakly depends on polarization of light at small angles of incidence [22].

The MRE theory differs for "good" (high-conductivity) metallic systems (all-metal multilayers and granular alloys with giant MR) and "poor" (low-conductivity)

metals (multilayers and nanocomposites with tunnel MR or manganites with colossal MR) because of different mechanisms of MR and frequency dependences of conductivity $\sigma(\omega, H)$. For "good" metals, $\sigma(\omega)$ satisfies the Drude–Lorentz law, which makes the theory quite simple.

5.2.2 Theory

The MRE theory for all-metal multilayers was developed by Jaquet and Valet [4] (see also discussion in [23–25]). The theory is based on: (i) the phenomenological theory of spin-dependent scattering in the bulk and interfaces of ferromagnetic layers in the current perpendicular to plane (CPP) geometry of giant MR, (ii) the Drude–Lorentz law for $\sigma(\omega, H)$, and (iii) the self-averaging limit [26] for averaging all parameters of multilayers, including the relaxation time, conductivity and permittivity. It is also assumed that only intraband scattering is responsible for the MRE, which is consistent with the initial definition of this effect, and that the electronic structure is the same for ferromagnetic and antiferromagnetic alignments of magnetic moments of ferromagnetic layers. The same approach was used by Granovsky et al. [5] for the case of granular alloys but with the theory of Zhang–Levy [26] for giant MR in granular alloys as the starting point.

These theories [4, 5] are very similar to each other, as was shown in Ref. [27], and are oversimplified. However, they can give qualitative description of the experiment in the IR range of spectrum in most cases. Since these models were discussed in detail in several papers [25, 27–29], here we do not give details but only discuss some useful relations and limitations of the theory.

If the MRE is due to only intraband optical transitions ($\varepsilon_r = \text{const}(H)$) and the Drude–Lorentz law is valid ($\sigma(\omega) = \frac{\sigma(\omega=0)}{1+i\omega\tau}$, where τ is the relaxation time), then magnetoreflection tends to zero at visible and at far infrared wavelengths; thus it reaches a maximum value at an intermediate frequency [6, 27]. It follows immediately from (5.4) that if the frequency of light is large, the second term in (5.4) $\frac{4\pi\sigma(\omega,H,T)}{\omega}$ is small compared with the first one $\varepsilon_r = \text{const}(H)$ and $\frac{\Delta R(H)}{R} \to 0$; in the Hagen–Rubens limit $\omega\tau \ll 1$ the energy of photons is on contrary too small to provide optical intraband transitions, which also gives $\frac{\Delta R(H)}{R} \to 0$. The corresponding expression in the Hagen–Rubens limit ($\omega\tau \ll 1$) is as follows [5, 6, 27]:

$$\frac{\Delta R(H)}{R} = -\frac{1}{2}(1-R)\frac{\Delta\rho(H)}{\rho} \quad (\omega\tau \ll 1), \tag{5.7}$$

$$\frac{\Delta\rho(H)}{\rho} = \frac{\rho(H)-\rho(H=0)}{\rho(0)}, \tag{5.8}$$

where $\frac{\Delta\rho(H)}{\rho}$ is MR. It follows from (5.7) that one should expect large values of the MRE in materials with large MR but small reflection R, a strict correlation between field dependences of MRE and MR, and opposite signs of these parameters.

Let us discuss the limitations of the theory. First, the self-averaging limit is valid only when the mean-free path of electrons is much larger than all characteristic lengths, namely, the thickness of layers or granular diameter. In that sense the self-averaging limit is equivalent to the effective medium approximation. Obviously, it does not work well in the case of multilayers and granular alloys with giant MR [30]. Second, the theory is phenomenological because it is based on a phenomenological approach to the MR theory. Since this approach is not appropriate for quantitative description of MR it is difficult to expect it for the MRE. Third, models contain numerous parameters, and it is difficult to determine them independently. For example, transport and electronic parameters of thin ferromagnetic and paramagnetic layers may differ significantly from those for bulk materials and may depend on their thickness. Fourth, the models do not use realistic electronic structures and do not take into account interband optical transitions. It was shown in [13] that the last point is very important in the near-IR range.

5.2.3 Experiment

The MRE in the reflection geometry was reproducibly observed in the near-IR region in NiFe/Cu/Co/Cu multilayers and, for transmitted light [4], in trilayers Fe/Cr/Fe [31] and spin-valve structures [32], in Co/Cu multilayers [25], and in Fe/Cr multilayers ([29] and references therein). Magnetoreflection is as large as 5.4 % for Co/Cu multilayers exhibiting 65 % MR at room temperature, and, for the multilayers having about 1–4 % MR, it is less than 1 % [25]. The authors of Ref. [29] succeeded in explaining magnetoreflection in Fe/Cr multilayers at $\lambda > 9$ μm even quantitatively and determined the important for spintronics parameter of spin asymmetry of scattering, which was in good agreement with first-principle calculations [29]. It was shown that in the long-wave limit the theory of Jaquet and Valet is quite appropriate for explaining experimental data [29], but it does not work well at shorter wavelengths. Both for Co/Cu and Fe/Cr multilayers the role of interband optical transitions (the first term in (5.4)) becomes more and more important [13, 29] with approaching the visible range.

Recently, magnetic, optical, MO properties, MR, magnetoreflection and magnetotransmission of a seven-layer Cr(28 Å)/Fe(36 Å)/Cr(13 Å)/Fe(18 Å)/Cr(13 Å)/Fe(36 Å)/Cr(28 Å) structure have been studies over a wide field and temperature range in the spectral region from 0.8 to 10 μm [33]. The authors measured MRE and MR in the Voigt and Faraday geometry and the field dependences of the magnetotransmission and MR were found to correlate. However, there is no linear correlation between the temperature dependences neither of the magnetotransmission and MR nor between the magnitudes of these effects measured in the Voigt and Faraday geometry. The calculations performed in terms of the MRE theory of Jaquet and Valet [4] qualitatively described the obtained experimental data. The model calculations demonstrate that, apart from the film thickness and related multiple light reflections from substrate and possible interference effects, the effective relaxation

time of charge carriers and the plasma frequency strongly affect both the magnitude and the spectral dependence of the MRE. However, a quantitative explanation of the obtained spectra requires a theory that does not use the self-averaging limit and takes into account the realistic band structure, or at least two groups of carriers (*s* and *d* electrons), even-parity MO effects, the effect of a magnetic field on interband optical transitions, and the change in the band structure at the conditions when the orientation of the magnetic moments in the layers changes.

The above conclusion is also true for granular metal–metal alloys with giant MR. Besides, the theory does not take into account also neither a distribution in size of grains and distance between them nor the presence of magnetic ions in the matrix between grains. The MRE was experimentally measured for granular Co–Ag alloys [27, 28, 34], and, in sufficiently strong magnetic fields, it was less than 1 % [27, 28] because MR in granular alloys is not as large as in multilayers. The correlation between the MRE and MR was clearly demonstrated. The detailed analysis of the MRE in granular alloys in the framework of the theory of Granovsky et al. [5] revealed the influence of different model parameters on the MRE behavior [27, 28].

5.3 MRE in Nanostructures Exhibiting Tunnel MR

5.3.1 Theory

The theory of the MRE in metal–insulator multilayers with tunnel MR was developed in [35]. The authors used the same approach as was developed for metal–metal multilayers [23, 24] but took into account the tunneling between ferromagnetic layers. This calculation predicts a quite small effect in magnetoreflection, when the thickness of insulator layers is greater than 1 nm.

A different approach was suggested in Ref. [7] for the case of metal–insulator nanocomposites with a metal volume fraction close to the percolation threshold. The tunnel junction between adjacent granules, responsible for *ac* current in metal–insulator nanocomposites can be thought of as a capacitor [36, 37]. Then the optical conductivity of granular metal–insulator alloys with a composition close to the percolation threshold can be written as

$$\sigma(\omega, H) = \frac{1 + i\frac{\varepsilon_{\text{int}}}{4\pi}\omega\rho(H)}{\rho(H)}, \tag{5.9}$$

where ε_{int} is the dielectric constant of the insulator between granules. For simplicity in (5.9), a flat capacitor was considered, and the authors did not average (5.9) over the grain size distribution and distances between them since only a few tunnel junctions are responsible for a charge transport when approaching the percolation threshold. Then it immediately follows from (5.4) and the Fresnel formulas for a semi-infinite medium model (air and thick sample) at normal incidence that

$$\frac{\Delta R}{R} = -(1-R)\frac{\Delta\rho}{\rho}k^2\left[\frac{3n^2-k^2-1}{(n^2+k^2)[(1-n)^2+k^2]}\right], \tag{5.10}$$

$$\frac{\Delta I}{I} = \frac{1}{2}\frac{\Delta\rho}{\rho}Ik^2\frac{2n^2+n}{n^2+k^2}, \tag{5.11}$$

where optical constants correspond to the demagnetized state.

Equation (5.9) is valid if the tunneling probability does not depend on frequencies those are expected for infrared wavelengths [37]. In fact, the tunneling probability does not depend on frequency ω if $\omega\tau \ll 1$, where τ is the tunneling time. Since τ is about d/v_F, where v_F is the electron velocity at the Fermi level and d is the mean distance between adjacent granules responsible for tunneling, one can estimate τ as 10^{-15}–10^{-16} s that is in an agreement with more strict considerations [37]. It means that the tunneling probability is suppressed only at the ultra-violet wavelengths. Besides, one can neglect photon-assistant tunneling because of a low intensity of light in the experiment. It should be noticed the following limitations of this simple approach. First, (5.9) is based on the assumption that the same tunneling junctions in nanocomposites are responsible for both *dc* and *ac* current. If *ac* current flows through other junctions with larger distances between granules, one can expect significant decrease of the MRE. Second, it was assumed in the model that the capacitance between grains does not depend on relative orientations of granular magnetic moments, so predicted in [38] (but not confirmed by experiments) possible effects of electron–electron interaction on magnetocapacitance were not taken into account. Third, only single-barrier tunneling was considered, although resonant double-barrier tunneling might be important as well. Finally, (5.9) is valid only in the vicinity of the percolation threshold. To consider a wider range of compositions, one should average the optical conductivity over granules' size distribution and distances between granules. In a strict sense, the developed theory of the MRE in nanocomposites is valid only in the immediate vicinity of the percolation transition, since the high-frequency current is apparently redistributed between different conduction channels as frequency varies. Thus, (5.9) can be viewed only as an initial step for the qualitative interpretation of the MRE in nanocomposites.

According to (5.10) the MRE frequency dependence in nanocomposites differs from that for metallic granular alloys; the MRE can be negative as well as positive and it is large if reflectivity is small. Formally, (5.10) and (5.7) are similar but for metallic systems reflectivity R is much larger, which makes the MRE in nanocomposites more pronounced in a wider spectral range even at equal MR. Using the Fresnel formulas it is straightforward to generalize the above approach to an arbitrary incident angle and polarization. Besides, it is not difficult to apply the approach to the three-layer model (air-sample-substrate) when the MRE can be enhanced due to interference of light [7]. It should be underlined that, since nanocomposites are partly transparent, light reflected from substrate and interference effects are more significant for them than for metallic systems.

At last, there is another mechanism of the MRE in nanocomposites, which is not due to spin-dependent tunneling at all. It is well known that light interacts with optical phonon modes in case of non-metallic systems. Kravets et al. [10, 15] discovered that this interaction in dielectrics depends on the magnetic field. The effect

can be observed in strong magnetic fields at an incident angle close to the Brewster angle in a certain frequency region in the infrared band. This effect was attributed to the influence of the applied magnetic field on an effective mass of polaron [15]. As a rule, this effect is small, $\frac{\Delta R}{R}$ is less than 0.6 % at 12 kOe for Al_2O_3 and MgO, which are typical dielectric components of magnetic nanocomposites. Apparently, this effect is not described by (5.9) because it occurs due to the first term in (5.6).

5.3.2 Experiment

The experimental data on the MRE in nanocomposites [18–23] clearly indicate the existence of spin-dependent tunneling at high frequencies, including that from the near infrared range. The spin-dependent tunneling is of primary importance for all high frequency applications of devices based on tunneling and for spintronics. A significant (up to 1.5 %) magnetoreflection was found in metal–dielectric films, such as Co–Al–O, CoFe–MgF, CoFeZr–SiO_n, Fe-SiO_2 and CoFe-Al_2O_3 [7, 9, 22, 39, 40]. The effect is observed only in compositions that are close to the percolation threshold and that are characterized by a significant tunnel MR.

Recently, a detailed experimental study of the MRE in nanocomposites CoFe-Al_2O_3 and multilayers CoFe/Al_2O_3 has been conducted [39]. The nanocomposites samples were close to the percolation threshold, exhibited tunnel MR about 7 % and $\frac{\Delta R}{R}$ about 0.7 %. The MRE in multilayered structures of [CoFe(1.3 nm)/Al_2O_3(3 nm)]$_{10}$ with MR of 5.5 % had $\frac{\Delta R}{R} = 2.5$ % in spite of the insulator spacer was quite thick. This relatively large value of the MRE in metal–insulator multilayers was attributed to the interference effects. Besides, two found peculiarities in the MRE spectra at $\lambda = 6.7$ and 8.1 μm were explained by the magnetic field induced changes in optical vibration modes.

Thus magnetoreflection and magnetotransmision in metal–insulator nanocomposites have at least two mechanisms: the first one is the high-frequency spin-dependent tunneling between adjacent grains, which is intrinsic MRE; the second one is the influence of the magnetic field on vibration modes in insulator spacers between grains. The second mechanism was studied by precise measurements in [40] for nanocomposites $(CoFe)_x(Al_2O_3)_{1-x}$ and $(CoFe)_x(HfO_2)_{1-x}$. IR reflection spectra were recorded within 2.5–25 μm region using a Fourier transform IR reflection spectrometer with 4 cm^{-1} resolution and liquid-nitrogen-cooled HgCdTe detector. The angle of s- or p-polarized light incident with respect to the film normal was equal to 65°, close to the Brewster angle. This allowed analyzing possible mechanisms. Surprisingly, magnetoreflection was quite small in comparison with the above mentioned data, less than 0.5 %, in spite of a strong magnetic field of 12 kOe and of the same order of MR. The data clearly indicate that, besides the intrinsic MRE, there is a contribution from the insulator component at certain frequencies, corresponding to vibration modes. To explain the experimental data on optical properties, the authors used the effective medium approximation for dielectric permittivity of a two-component composite, a phenomenological Lorentz model

for the dielectric permittivity of an insulator, and (5.7) for magnetoreflection in the Hagen–Rubens limit for metallic systems, supposing that MR in this expression is tunneling MR. The explanation is not consistent because (5.7) does not work for metal–insulator composites and is valid only for giant MR metallic materials with the Drude–Lorentz behavior of optical conductivity. Perhaps, the similarity between (5.7) and (5.10) allowed obtaining qualitative explanation. Nevertheless, the origin of the contribution from the insulator component is not quite clear. This contribution is small (even at the Brewster angle) that makes difficult its investigation. Several possible mechanisms can be considered as responsible of these peculiarities at certain vibrating frequencies. It is quite reasonable to assume that the characteristic vibrating frequencies and electron–phonon interaction depend on the applied magnetic field but there is no corresponding theory. Besides, as it was mentioned in Ref. [40], since numerous doped and undoped with transition metals insulators exhibit room-temperature ferromagnetism, supposed to originate from percolating magnetic polarons (see, for example [41]), it is also possible that such magnetic polarons appear in nanocomposites in the vicinity of structural defects in the insulator matrix. In this case an external magnetic field will influence magnetic polarons' behavior that can lead to a corresponding contribution to magnetoreflection. However, such an interesting mechanism is questionable because the peculiarities at the vibrating frequencies in nanocomposites [40] and bulk insulators [10] are very similar.

To conclude this section, we would like to stress that the study of the MRE in systems with tunnel junctions makes possible to shed light on spin-dependent tunneling in a wide frequency range, and a lot of problems in this field are far from being well understood.

5.4 MRE in Manganites Exhibiting Colossal Magnetoresistance

5.4.1 Introductory Remarks

Manganites constitute a class of systems that is important for fundamental researches due to reach physics underlying their unique features and due to a wide diversity of their structural, magnetic, magnetotransport, MO and mechanical properties [43–45]. For MRE applications, it is necessary either to increase the amplitude of the effect or to decrease the strength of control fields. In addition, it is important to find materials or structures for which a significant MRE is observed also in the visible spectral range. Since the MRE is primarily controlled by the MR value, the interest in the MRE in manganites exhibiting colossal MR, which may be much larger than giant or tunnel MR, is quite obvious. However, it is not the sole reason because the inverse problem, namely, developing of a new type of MO spectroscopy, based on the MRE spectra measurements, is also important for investigation of such complicated materials as manganites.

The effect of magnetotransmission in manganites with colossal MR was discovered in 1997 in experiments with an $La_{0.9}Sr_{0.1}MnO_3$ single crystal in mid-IR wavelengths at low temperatures [46] and was later studied in experiments with many other manganites (see [47–51] and references therein). An important advance was that, in $La_{0.67}Sr_{0.33}MnO_3$ films, the value of magnetotransmission above room temperature and in a field of 8 kOe was as large as 6 % [47]. The corresponding quantity for the composition of $La_{0.8}Ag_{0.1}MnO_{3+\delta}$ was as large as 15 % [49], the record value for room temperatures. Even stronger magnetotransmission effects ~30 % were observed in the $La_{0.9}Sr_{0.1}MnO_3$ single crystal at $T_C = 140$ K when the concentration of strontium was lower than the percolation threshold [46] and about ~50 % for $La_{0.35}Pr_{0.35}Ca_{0.3}MnO_3/SrTiO_3$ thin film [52] at $T = 170$ K and $H = 8$ kOe. Magnetoreflection in manganite films is also larger than in nanostructures with the giant and tunnel MR [53]. Recently, the MRE has been demonstrated also for visible wavelengths [14, 16, 17].

Although it is natural to assume that these giant magnetotransmission and magnetoreflection effects are manifestations of the high-frequency MR (or in other words, of the intrinsic MRE) because they are observed in systems with colossal MR, this assumption implies the strict correlation between the MRE parameters (see (5.1)–(5.3)) and MR, whereas this correlation is often violated for temperature and concentration dependences of magnetotransmission and magnetoreflection in the studied samples. Currently, there is no quantitative and, in some cases, even qualitative theoretical description of these effects. The absence of a consistent theory of the high-frequency conductivity and MR of manganites hinders consistent description of the MRE in such systems. In manganites, the mechanisms of conductivity and MR are substantially more complicated than those in nanostructures with giant or tunnel MR. MR in manganites is determined by at least two different main mechanisms, namely, (i) an increase in the volume fraction of the ferromagnetic phase with a simultaneous decrease in the volume fraction of the more resistive antiferromagnetic phase during magnetization (this leads to colossal MR) and (ii) the tunnel MR, which is observed in weakly doped manganites, in polycrystals, in systems with a variant structure, and in heterostructures [46–49, 54–56]. Besides phase separation, manganites are characterized by a strong electron–phonon and electron–electron interaction, the Jahn–Teller effect and the influence of magnetic fields on electronic structure. Therefore, magnetotransmission and magnetoreflection in manganites can also be due to numerous mechanisms, as the high-frequency tunnel MR, the high-frequency colossal MR, magnetic field induced shift of the Fermi energy or of the fundamental optical absorption edge, a change of electronic structure and electron–phonon interaction in a magnetic field, the Jahn–Teller effect etc. The theory of the MRE in metal nanostructures with giant MR described above in Sect. 5.2.2 is not appropriate for manganites because they are "poor" (high-resistive) metals, where the Drude–Lorentz law is invalid and the origin of colossal MR is not connected with the spin-dependent scattering. The approach to the high-frequency spin-dependent tunneling in nanocomposites described in Sect. 5.3.2 cannot also be applied to manganites directly because tunneling in manganites occurs in completely different geometries and conditions. In manganites magnetic field influences on tunneling across weak-conducting grain boundaries in poly- and nanocrystals [42, 43],

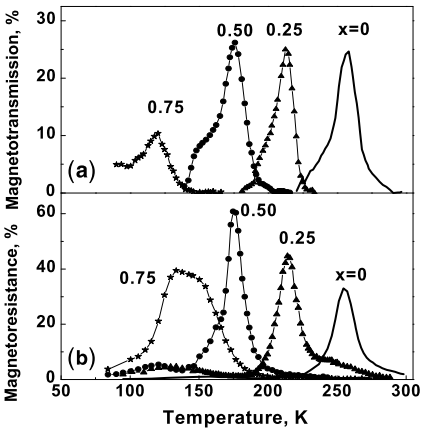

Fig. 5.3 Temperature dependences of the absolute values of (**a**) magnetotransmission at wavelength $\lambda \sim 6.7$ μm and (**b**) magnetoresistance of $(La_{1-x}Pr_x)_{0.7}Ca_{0.3}MnO_3$ ($0 \leq x_{Pr} \leq 0.75$) films grown on a $SrTiO_3$ substrate in an out-of-plane magnetic field of 8 kOe

or across high-angle boundaries of structural domains in thin films with a variant structure [48, 49], and through interfaces in multilayered structures and heterostructures [56, 61, 77]. In addition, tunneling is not responsible for the colossal MR. The developing of the theory of high-frequency colossal MR based on a model of *ac* current in percolating two-phase composite in the effective medium approximation is only in the very beginning [57].

5.4.2 Magnetotransmission in the IR Range of Spectrum

Since the first observation of magnetotransmission in manganites in 1997 [46], the origin of this effect has been a subject of intense research. It was shown that magnetotransmission takes place in the IR range of the spectrum in single crystals, single-crystalline and polycrystalline thin films and thin films heterostructures (see [46, 51, 53–56] and references therein). It was established that magnetotransmission at temperatures $T > 100$ K in a magnetic field up to 10 kOe is an optical response on the colossal MR, i.e. it can be viewed as the intrinsic MRE. Magnetotransmission is of the same sign as the colossal MR (which corresponds to the MRE theory), alike MRE reaches a maximum in the narrow interval of $\Delta T = \pm 20$ K around the Curie temperature T_C, and weakly depends on a magnetic field orientation relative to a sample surface. The magnitude of magnetotransmission can be as high as 50 % [52].

Both magnetotransmission magnitude and the temperature, at which magnetotransmission exhibits maximum, strongly depend on isovalent and non-isovalent substitution of rare earth metals ions as well as on a doping level [58, 59]. Figure 5.3 shows an example of magnetotransmission for the isovalent substitution La^{3+} by Pr^{3+} ions in the case of $(La_{1-x}Pr_x)_{0.7}Ca_{0.3}MnO_3$ ($0 \leq x_{Pr} \leq 0.75$) thin films: both the temperature position of the maximum in magnetotransmission $(\frac{\Delta I(\omega,H)}{I})_{max}$ and the position of the MR maximum $(\frac{\Delta\rho}{\rho})_{max}$ shift synchronously with increase

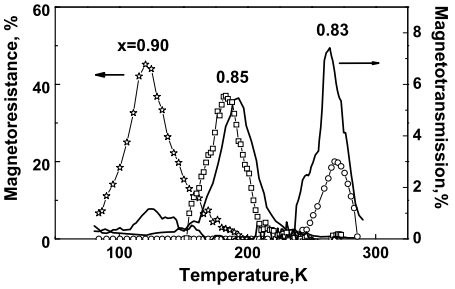

Fig. 5.4 Temperature dependences of the absolute values of magnetotransmission at a wavelength of $\lambda \sim 9$ μm (*solid lines*) and magnetoresistance (*open symbols*) of La_xMnO_3 ($0.83 \leq x_{La} \leq 0.90$) films in an out-of-plane magnetic field of 8 kOe

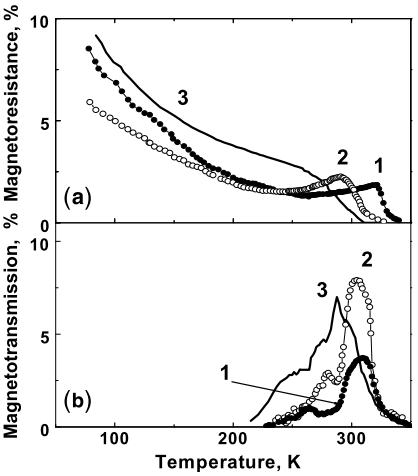

Fig. 5.5 Temperature dependences of the absolute values of magnetoresistance (**a**) and magnetotransmission (**b**) at an out-of-plane magnetic field of 8 kOe and a wavelength of $\lambda \sim 6$ μm for $La_{0.8}Ag_{0.1}MnO_{3+\delta}$ films of different thicknesses grown on $ZrO_2(Y_2O_3)$ substrates: (*1*)—500 nm, (*2*)—800 nm, (*3*)—1 μm

of a doping level from $x_{Pr} = 0$ to the percolation threshold ($x_{Pr} = 0.75$), and an amplitude of $(\frac{\Delta I(\omega,H)}{I})_{max}$ does not change (Fig. 5.3(a)), while $(\frac{\Delta\rho}{\rho})_{max}$ increases (Fig. 5.3(b)).

A different behavior was observed for a non-isovalent substitution and in the presence of vacancies in the rare earth metal sub-lattice. For example (Fig. 5.4), in La_xMnO_3 ($0.83 \leq x_{La} \leq 1.10$) thin films magnetotransmission and MR reach their maximum values at different x_{La} [59]. Thus the strict correlation between magnetotransmission and MR is violated in the temperature range of dominant contribution of the colossal MR both at isovalent and non-isovalent substitutions.

By analogy with an observed optical response of manganites with the colossal MR and of nanocomposites with the tunnel MR, one can also expect a low temperature optical response on a tunnel contribution to MR in manganites with a variant structure [48, 49]. But, surprisingly, it is not the case. Figure 5.5(a) clearly shows two contributions to MR in thin films $La_{0.8}Ag_{0.1}MnO_{3+\delta}/ZrO_2(Y_2O_3)$ with a variant structure: low temperature tunnel MR and colossal MR with a maximum at T_C. Magnetotransmission was not observed in the range of dominant tunnel MR (Fig. 5.5(b)) but existed at T_C [48]. Anyhow, further experiments are needed to answer whether an optical response on tunnel MR in manganites exists or not. At

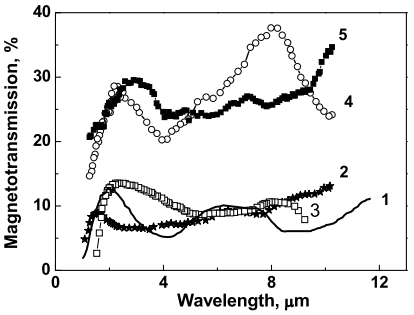

Fig. 5.6 Spectra of the absolute values of magnetotransmission of (*1*)—$La_{0.83}MnO_3$ film at temperature $T = 268$ K, (*2*)—$La_{0.82}Na_{0.18}MnO_{3+\delta}$ (303 K), (*3*)—$La_{0.9}Ag_{0.1}MnO_{3+\delta}$ (305 K), (*4*)—$La_{0.7}Ca_{0.3}MnO_3$ (265 K) and (*5*)—$(La_{0.5}Pr_{0.5})_{0.7}Ca_{0.3}MnO_3$ (176 K) in an out-of-plane magnetic field of 8 kOe

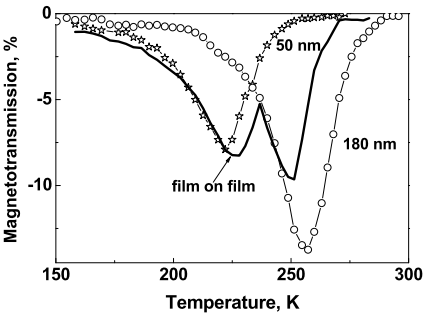

Fig. 5.7 Temperature dependences of magnetotransmission the $La_{0.7}Ca_{0.3}MnO_3$ single films of different thickness at a wavelength of $\lambda \sim 6$ μm in an out-of-plane magnetic field of 8 kOe. *Solid line* is for a structure of these adjoined films

least, there is evidence in the case of charge and magnetic inhomogeneous crystals $La_{5/8-y}Pr_yCa_{3/8}MnO_3$ that its optical conductivity depends on a magnetic field of 120 kOe at $T = 4.2$ K, whereas $T_C = 120$ K [60].

Magnetotransmission spectra in non-stoichiometric and doped lanthanum manganites show that the effect is quite large in a wide IR spectral range from 1.4 to 12 μm (Fig. 5.6). The spectra profile depends on a doping level, charge, and magnetic inhomogeneities, and on mechanical stresses [47–59].

Thus magnetotransmission in the IR spectral range is determined by the influence of a magnetic field on interaction with light both localized and delocalized charge carriers. Therefore the temperature and field dependences of magnetotransmission are quite different at different wavelengths. The choice of a wavelength of 6 μm for measurements of field and temperature dependences of magnetotransmission was done because this wavelength is far from the fundamental absorption edge and optical modes at 3 and 8–10 μm (Fig. 5.6).

Figure 5.7 demonstrates the effect of superposition in magnetotransmission from two adjacent thin films. In this experiment, the $La_{0.7}Ca_{0.3}MnO_3$ thin film with a thickness of 50 nm and $T_C \sim 220$ K was placed directly on the top of another $La_{0.7}Ca_{0.3}MnO_3$ film with a thickness of 180 nm and $T_C \sim 260$ K. As a result magnetotransmission of two films is neither a weighted average of two contributions

nor a simple sum of two contributions but a superposition of the separate contributions (Fig. 5.7). The discovery of this effect triggered investigations of MRE in heterostructures based on manganites with colossal MR. Such investigations were aimed at development of novel multifunctional MO materials and showed results promising for applications. For example, it became possible to enhance magnetotransmission up to 40 % in the heterostructure ferrite/manganite due to an additional sub-magnetization by the ferrite film [55] or to obtain a weak temperature dependent magnetotransmission in heterostructures composed from $Sm_{0.55}Sr_{0.45}MnO_3$ and $Nd_{0.55}Sr_{0.45}MnO_3$ possessing different T_C [61]. Since manganites are partly transparent for a light, it is also possible to use them as components of magnetophotonic crystals [62] and, as predicted in [6] and discussed in [14, 62], reach giant responses in magnetotransmission and magnetoreflection.

5.4.3 *Magnetoreflection and Magnetotransmission of Manganites $La_{0.7}Ca_{0.3}MnO_3$ in the IR and Visible Spectral Range*

The experimental data on the MRE in manganites in the IR range are contradictory, scarce, and exist either only for magnetoreflection (see [54, 60, 63–66]) or for magnetotransmission (see [46–53, 55–59] and references therein) often in a limited ranges of wavelengths, fields, and temperatures without comparison with the data for bulk crystals or polycrystals of the same composition and analysis for films of various thicknesses. Reflection from a substrate used for a fabrication of a film may significantly change the MRE spectra profile–enhance or suppress the MRE signal at certain wavelengths; also it may change the sign of magnetoreflection [53]. A sample surface roughness and inhomogeneity of composition and an impurity distribution across the skin-depth or along the surface may also affect magnetoreflection.

Recently, magnetoreflection has been discovered in the visible range for thin films of $La_{2/3}Ca_{1/3}MnO_3$ and $(Pr_{0.4}La_{0.6})_{0.7}Ca_{0.3}MnO_3$ [16, 17]. Magnetoreflection for an incident angle of 45° and a magnetic field of 7 kOe reaches 2 % at temperatures near T_C. The effect was attributed to the influence of the magnetic field on polarons [17]. But this mechanism is under debate in Ref. [14], where a competition between mechanisms such as the contribution from even-parity MO effects and the influence of magnetic field on the electronic structure is under discussion. The MRE was investigated only in the reflection mode in Refs. [16, 17].

In this section, we will discuss last results of an extended research of the MRE in $La_{0.7}Ca_{0.3}MnO_3$ bulk crystals and thin films, both in the reflection and transmission modes [53, 67], in a wide spectral range from IR to visible wavelengths [14]. We will focus only on several important features; details on samples' fabrication and experimental setups can be found in Refs. [14, 53, 56].

Let us compare magnetoreflection and MR for two $La_{0.7}Ca_{0.3}MnO_3$ single crystals of the same composition, grown up in almost identical conditions, but possessing a slightly different homogeneity. The lines with open symbols in Fig. 5.8 show

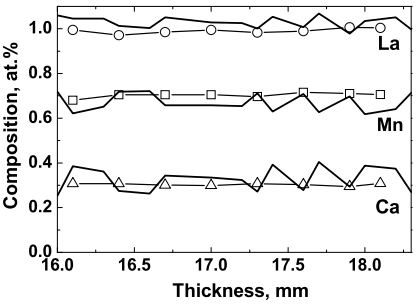

Fig. 5.8 Distributions of La, Ca and Mn ions along an arbitrary line in the basal plane of sample 1 (*open symbols*) and sample 2 (*solid lines*) for $La_{0.7}Ca_{0.3}MnO_3$ crystals at a depth of 2 μm measured at $T = 295$ K

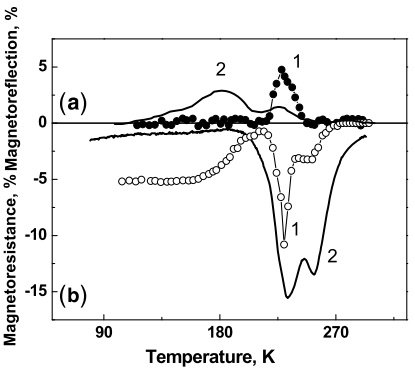

Fig. 5.9 Temperature dependences of (**a**) magnetoreflection at $\lambda = 12.5$ μm in a magnetic field of 3.5 kOe and (**b**) magnetoresistance for sample 1 and sample 2 of $La_{0.7}Ca_{0.3}MnO_3$ crystals in an out-of-plane magnetic field of 15 kOe

the distributions of La, Ca and Mn ions along an arbitrary line in the basal plane of sample 1 at a depth of 2 μm. It is seen that this sample is free of strong variations in the composition of $La_{0.7}Ca_{0.3}MnO_3$. The composition of sample 2 slightly fluctuates along the surface; its quality is still high but a mosaic structure is presented [67].

Figure 5.9 shows that magnetoreflection and MR of these samples exhibit different features. For both samples $\Delta R/R$ is opposite in sign to MR, that is, in an agreement with the MRE theory (see (5.7) and (5.10)). For high-quality sample 1, the bands of maximum values of $\Delta R/R$ and MR and characteristic temperatures (close to T_C) of maxima coincide with each other that are also in an agreement with the MRE theory [6]. Besides, (5.7) gives a maximum value of $\Delta R/R$ about 5 % that is close to the experimental one (Fig. 5.9). At last, the frequency dependence of $\Delta R/R$ (Fig. 5.10) is characterized by a maximum around 12–15 μm, which is also in an agreement with simple estimations for metallic systems (in accord with Ref. [5], $\Delta R/R$ reaches a maximum around $\omega \sim \tau^{-1}$, where $\tau \sim 5 \times 10^{-15}$ s is the relaxation time). Thus these data clearly indicate that magnetoreflection for high-quality sample 1 is a high-frequency response on the colossal MR, in other words, due to the true or intrinsic MRE.

In contrast to sample 1, magnetoreflection of sample 2 has two bands (Fig. 5.9). These bands originate from the presence of two main ferromagnetic phases with different conductivities, MR and T_C. It is worth mentioning that the MRE response from these two phases is stronger than the MR response. It means that the MRE can

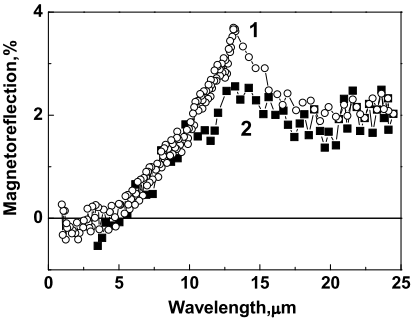

Fig. 5.10 Spectral dependences of magnetoreflection for sample 1 and sample 2 of $La_{0.7}Ca_{0.3}MnO_3$ crystals in a magnetic field of 3 kOe at $T = 230$ K

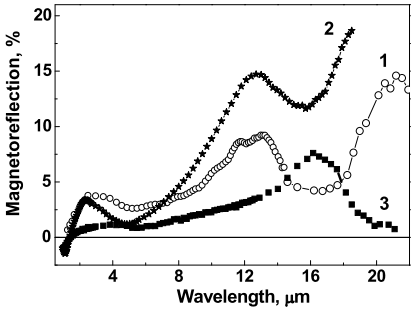

Fig. 5.11 Spectral dependences of the magnetoreflection for $La_{0.7}Ca_{0.3}MnO_3$ films with thickness 150 nm (*1*) and 300 nm (*2*) and $La_{0.9}Ag_{0.1}MnO_{3+\delta}$ film with thickness 450 nm (*3*) in a magnetic field of 3 kOe at temperatures corresponding to the maxima of effects

be used as a method for effective contactless structural characterization of surface layers.

There is no magnetoreflection associated with the low temperature tunnel MR in both samples (Fig. 5.9). The same result was obtained for magnetotransmission of $La_{0.8}Ag_{0.1}MnO_{3+\delta}/ZrO_2(Y_2O_3)$ films with variant structure [48]. As said in Sect. 5.1, there is no a good explanation of such behavior. One can suppose that this contribution to the MRE is suppressed by additional temperature dependences of optical indices at low temperatures (see (5.10)) or that the second term in (5.4) becomes too small in the case of tunneling in manganites (shunting effect of more conductive paths). Coming now to the MRE in thin films, we should take into account both strain stresses inherent in films and the reflection from substrates. Both factors can significantly change the MRE spectra and enhance magnetoreflection or magnetotransmission. This is demonstrated in Fig. 5.11 for the case of weakly stressed thick films $La_{0.7}Ca_{0.3}MnO_3$ and $La_{0.9}Ag_{0.1}MnO_3$ [14]. One can see that the spectra are similar to those for bulk crystals but differ in detail; multiple passages of light through the film enhance $\Delta R/R$ up to 20 %, to a giant value for magneto-optics indeed.

The most dramatic changes may occur in strongly stressed thin films due to appearance of optical resonances. Such resonance-like behavior in the MRE spectra was observed in $La_{0.7}Ca_{0.3}MnO_3$ thin films (Fig. 5.12) in the vicinity of spectral position of minimum reflectance at $\lambda \sim 14$ μm, which is before the first phonon line [53]. The analogous but less pronounced resonance was observed for the same films in Ref. [54]. The origin of this optical resonance is not quite clear but it be-

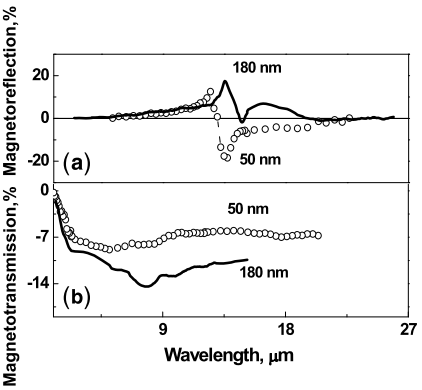

Fig. 5.12 Spectra of magnetoreflection (**a**) in an in-plane magnetic field of 3 kOe and magnetotransmission (**b**) in an out-of-plane magnetic field of 8 kOe for the $La_{0.7}Ca_{0.3}MnO_3$ films of different thickness measured at temperatures of the maximum response

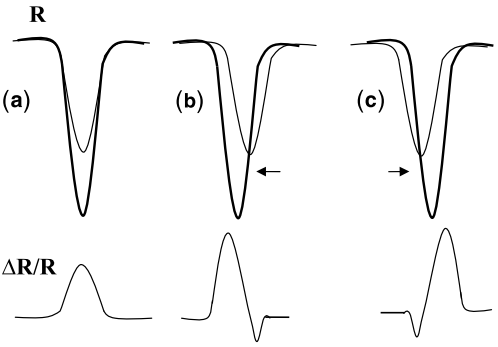

Fig. 5.13 Schematic spectral dependence of reflectance R in the presence of the magnetic field and the corresponding change in magnetoreflection $\Delta R/R$. The spectral position of the minimum R is not shifted (**a**), is shifted towards smaller wavelengths (**b**), and is shifted towards larger wavelengths (**c**) in the magnetic field

comes apparent in strain stressed thin films, for example, in the film with a thickness of 50 nm. The authors of Ref. [54] supposed that this resonance in $\Delta R/R$ is due to the deformation modes of MnO_6 octahedrons. The specific features of this resonance are as follows: (i) a deep minimum in reflectivity R spectra; (ii) enhancement of magnetoreflection $\Delta R/R$; (iii) $\Delta R/R$ changes its sign; (iv) absence of any signature of this resonance in magnetotransmission. These features can be explained if the magnetic field shifts the spectral position of the resonance. The scheme in Fig. 5.13 shows a possible behavior of $\Delta R/R$. The shift of the resonance frequency might be due to an influence of the magnetic field on the deformation modes or on the electron–phonon interaction. It is worth to notice that such resonance-type features may be induced not only by the magnetic but also by electric field or by applied stresses.

In the cases of weakly stressed films and single crystals the temperature and field dependences of $\Delta R(T, H)/R$ and $\Delta I(T, H)/I$ in the IR spectral range from the one side and those for $\Delta\rho(T, H)/\rho$ from the other side are alike [53], as it is expected in the MRE theory. Especially it is true close to T_C (Fig. 5.14). In the case of strongly stressed thin films such correlation is not so good because of resonance-type behavior in $\Delta R(T, H)/R$. It is not of surprise because the MRE theory does not take into account a resonance-type behavior of magnetoreflection.

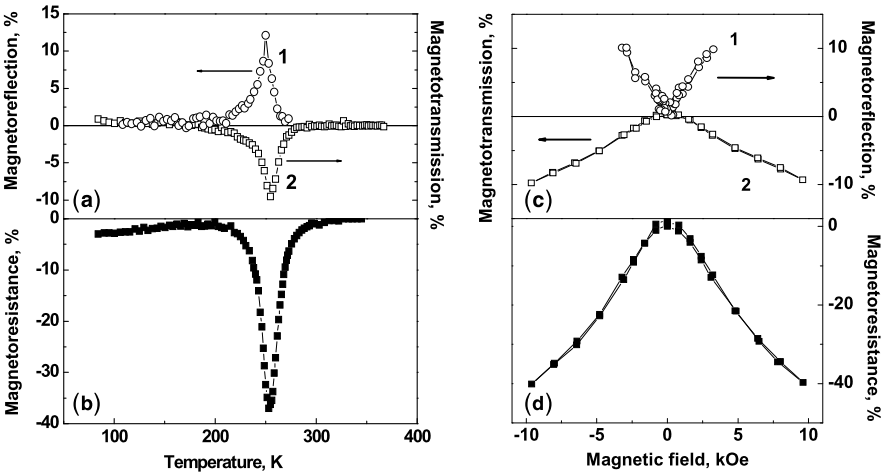

Fig. 5.14 Temperature dependences of (**a**) the magnetoreflection at in-plane $H = 3$ kOe (*1*), the magnetotransmission at out of-plane field 8 kOe (*2*) for wavelengths at which effects are maximal and (**b**) the magnetoresistance at out of-plane field 8 kOe. Field dependences of (**c**) the magnetoreflection (*1*) and magnetotransmission (*2*), and (**d**) the magnetoresistance of the $La_{0.7}Ca_{0.3}MnO_3$ film of the thickness 50 nm at $T = 255$ K in the same geometries

The MRE theory based on a high-frequency response on MR failed in the case of magnetoreflection and magnetotransmission in the visible spectrum. In accordance with the theory, $\Delta R/R$ has to be positive and magnetotransmission has to be negative when MR is negative, but it is not the case at $\lambda < 0.9$ μm (Fig. 5.15) [14]. Magnetoreflection and magnetotransmission in $La_{0.7}Ca_{0.3}MnO_3$ thin films change their signs at $\lambda < 0.9$ μm and their spectra become very complicated without any evidence of correlation with MR. For shorter wavelengths, a minimum appears in magnetotransmission around 0.6 μm and $\Delta R/R$ changes its sign again from the negative to positive one (Fig. 5.15). In the case of $La_{0.9}Ag_{0.1}MnO_3$ films, $\Delta R/R$ keeps its sign in the visible range [14]. The same is true for $La_{5/8-y}Pr_yCa_{3/8}MnO_3$ at $T = 4.2$ K in magnetic fields up to 120 kOe [60].

The most important finding is that magnetotransmission in $La_{0.7}Ca_{0.3}MnO_3$ thin films even in the visible range reaches ~2 % in a relatively weak magnetic field of 3 kOe, oriented in parallel with thin film surface. It makes this effect promising for application. Previously such large effect in magnetotransmission was observed only in a very strong magnetic field, in $Nd_{0.7}Sr_{0.3}MnO_3$ at $T < T_C$ in 89 kOe [65].

Thus, as judged from the sign of the observed spectra and their complicated structure in a wavelength range of 0.5–0.9 μm, magnetoreflection and magnetotransmission of the manganite films in the visible region of the spectrum have a different nature as compared to the MRE effect observed in the IR spectral region, which is associated exclusively with a high-frequency response on MR. The temperature and field dependences of $\Delta R/R$ and magnetotransmission studied in the visible region also support this conclusion [10, 13, 14, 16, 17, 21, 60, 65]. The origin of this behavior is currently under debate [14] and several mechanisms are considered as

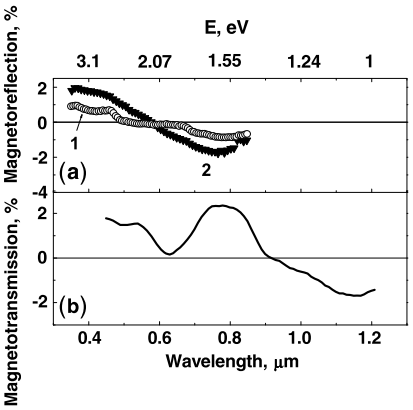

Fig. 5.15 Spectra of (**a**) magnetoreflection in an out-of-plane magnetic field of 11 kOe for the $La_{0.7}Ca_{0.3}MnO_3$ films with thicknesses of 50 nm (*1*) and 320 nm (*2*) at $T = 265$ K; (**b**) magnetotransmission for $La_{0.7}Ca_{0.3}MnO_3$ film with a thickness of 180 nm at $T = 265$ K and in an in-plane magnetic field of 2.8 kOe

possible candidates for explanation: (i) influence of the magnetic field on interband transitions [13, 14]; (ii) influence of the magnetic field on the effective mass of non-magnetic polarons [10]; (iii) suppression of the Jahn–Teller effect under the action of the magnetic field [16]; (iv) even-parity MO effects [7, 14, 17, 21]; (v) influence of magnetic field on the magnetic polarons [17].

In our opinion, the mechanism of the MRE in the visible range of spectrum in manganites is as follows. The electronic structure of manganites is more sensitive to variations in the magnetic field in comparison with other less complex materials. As a result, the probability of an interband transition may depend on the magnetic field. Since interband transitions are responsible for the dielectric permittivity and optical indices in the visible range (the first term in (5.4)), reflectivity and transmission of the visible light may also depend on the magnetic field. The manganites under investigation in the visible region are characterized by two fundamental absorption bands at approximately 1.5 eV (0.82 μm) and 3.5 eV (0.35 μm) [68, 69]. Therefore the probability of an interband transition is very high for this range, which is also in a favor of the supposed scenario. This mechanism should work fairly well over a wide range of temperatures both in the paramagnetic region and at low temperatures. However, it can be especially pronounced in the vicinity of the Curie temperature during the metal–insulator phase transition. In this case, the applied magnetic field can lead to a change either in the electron density of states, or, what amounts to approximately the same thing, in the relative fraction of delocalized charge carriers, as well as to a change in the band width, a shift of the bands with respect to each other, or a change in the wave functions, which, in turn, leads to a change in the oscillator strength. To confirm or to neglect this scenario, the first-principle calculations of electronic band structure of manganites in the presence of the magnetic field are needed. Besides, we cannot completely exclude the possible contributions from other mechanisms, listed above. Perhaps, all of them work in competition.

5.5 Possible Applications of the MRE

To understand advantages and disadvantages of the MRE in comparison with conventional MO effects, let us compare the MRE magnitude in the reflection mode with the transverse Kerr effect, which results in the change of intensity of reflected *p*-polarized light under the magnetization, and the MRE in the transmission mode with the Faraday effect.

In the IR range, say for $\lambda > 1$ μm, the parameter of the transverse effect Kerr effect (δ) as a rule does not exceed 10^{-3} a.u. [51]. Sometimes it is difficult to measure the corresponding Kerr signal, whereas magnetoreflection in materials with the giant MR (Sect. 5.2) or tunnel MR (Sect. 5.3) is about 1 % at normal incidence and can be as high as ∼10 % in manganites with the colossal MR (Sect. 5.4) at room temperature in reasonable magnetic fields.

In the visible range, manganites exhibit quite large MO effects (Fig. 5.16), the parameter δ can reach 3 % at certain frequencies (see [14] and references therein) and at the angles of incidence 50–67 degs. It is worth to remind the reader that the transverse Kerr effect does not exist at normal incidence of light. Since magnetoreflection in manganites in this range significantly increases with the angle of incidence (see Sect. 5.2) and is about 2 % at normal incidence, we can conclude that the MRE in the reflection mode is at least two orders of magnitude larger than the transverse Kerr effect in the IR range and can be also in several times larger in the visible range.

The difference is more pronounced in the case of magnetotransmission in manganites. The Faraday rotation is too small in the infrared range (Fig. 5.16) but is about ∼40000 deg/cm in the visible range [70–72]. For the manganite $La_{0.7}Ca_{0.3}MnO_3$ film with a thickness of 320 nm, the magnitude of the Faraday rotation does not exceed 1.3°, which, in accordance with the Malus' law, should lead to a change in the intensity by approximately 0.05 %. This change in the intensity of the light transmitted through the sample due to the Faraday rotation is one order of magnitude smaller than the value of magnetotransmission in the visible spectral region, which is no less than 0.7 % in a magnetic field of 1 kOe. So, in the same geometry and the same magnetic field, the MRE in the reflection and transmission modes is larger than even-parity MO Kerr and Faraday effects in the IR as well as in visible spectral ranges. Besides, the MRE is nongyrotropic in the visible and IR spectral regions; as a consequence, it has become possible to avoid the use of light analyzers and polarizers in optical circuits, which can be of great practical importance. Of course, it is an advantage only for nongyrotropic schemes. Since manganites exhibit strong MO response, it is possible to utilize both gyrotropic and nongyrotropic effects in one device.

The MRE can be used for development contactless magnetic sensors, modulators of the IR and visible light, magnetic lens, attenuators, detectors of temperature [55, 61, 73–77] and so on. The MRE in the reflection mode makes possible to effectively control MR of the key elements of spintronics—spin-valves—during their production; this was proposed in several works [6, 8, 27].

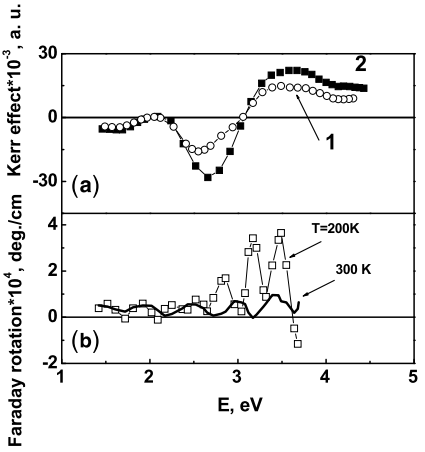

Fig. 5.16 Spectra of (**a**) transversal Kerr effect for $La_{0.7}Ca_{0.3}MnO_3$ (*1*) and $La_{0.9}Ag_{0.1}MnO_3$ (*2*) films at $T = 80$ K in $H = 3.5$ kOe and (**b**) Faraday rotation for a $La_{0.7}Ca_{0.3}MnO_3$ film at different temperatures in a magnetic field of 2 kOe [70]

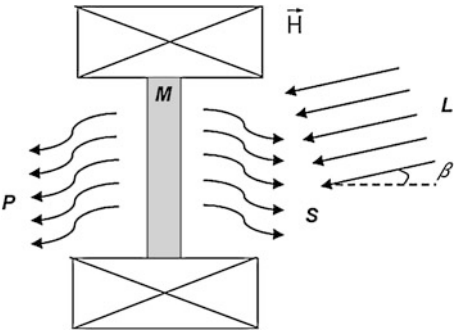

Fig. 5.17 Scheme of modulation: ***M***—the magneto-optical element, ***L***—incident natural light, ***P***—transmitted and ***S***—reflected unpolarized light, ***H***—the source of the controlling magnetic field directed in plane or out of plane to the surface of the magneto-optical element

Before discovery of strong magnetoreflection in manganites, a scheme of a light modulator was based on magnetotransmission [74–77]. Recently, it has been proposed a novel scheme [78], in which modulation of light occurs simultaneously in the reflection as well as in transmission modes for unpolarized light (Fig. 5.17). It is worth mentioning that this scheme can work at any orientation of the magnetic field.

Besides technical applications, the MRE can be used in physics for contactless investigation of MR, spin asymmetry, high-frequency tunneling, surface inhomogeneity, magnetic and non-magnetic polarons, deformation modes and so on.

5.6 Conclusions

Significant progress in studying the MRE in different structures exhibiting giant, tunnel and colossal magnetoresistance has been achieved in last years. It was unambiguously shown that for the IR spectral region the MRE in multilayers, granular alloys, nanocomposites and manganites is associated with the high-frequency MR

and it is in at least one or two orders of magnitude greater than the conventional MO phenomena. In the visible region the MRE has been observed in manganites thin films. It is not as large as in the IR region but in several times greater than effects in magnetoreflection and magnetotransmission associated with MO Kerr and Faraday effects.

Being quite large, in some cases up to 20–30 %, these are giant magnitudes for magneto-optics, nongyrotropic, non-dependent on orientation of magnetic field and light polarization at small angles of light incidence, the MRE can be successfully used in magnetophotonic. In particular, the MRE is of interest for contactless measurements of the MR in nanostructures, MO magnetic sensors, high-speed modulators, and field-controlled optical elements.

However, many problems need to be studied further. First of all, we hope that measurement of angular, polarization, temperature, frequency, and field dependences of magnetoreflection and magnetotransmission for manganites will help to clarify the origin of the MRE in the visible range. We think that the MRE in the visible range is predominantly determined by the change in the electronic structure under the action of the applied magnetic field but other mechanisms, mentioned in Sect. 5.4.3, may also be in competition. For example, the relative role of even-parity in magnetization for MO phenomena is not clear up to now. Secondly, it should be emphasized that the MRE has not been studied yet in the cases of thin films with anisotropic magnetoresistance and in the Heusler alloys with a large MR in the vicinity of the martensitic transition important for underlying physics and application. Thirdly, there is no experimental evidence of the magnetocapacitance effect, which was predicted in magnetic tunnel junction metal/insulator/metal (see Sect. 5.4). The list of important problems includes also (i) development of the theory of spin-dependent tunneling in magnetically non-uniform media at high frequencies and of the theory of the MRE in manganites; (ii) search for materials characterized simultaneously with weak absorption, high MRE and weak operating field; (iii) development of a technology for forming multilayer structures and magnetophotonic crystals, containing manganite and nanocomposite films; (iv) extension of the frequency range of applications toward the microwave and millimeter range of the spectrum; (v) development of steady ground for novel MRE spectroscopy of magnetic materials.

We hope that our brief review will stimulate experimental and theoretical study of the MRE in various magnetic nanostructures.

Acknowledgements This work was partially supported by the Russian Foundation of Basic Research Nos. 10-02-00038, 12-02-31505, by the Presidium of RAS grant 12-П-2-1034 and by the grant of the President of Russia MK-1048.2012.2.

References

1. A. Zvezdin, V. Kotov, *Modern Magnetooptics and Magnetooptical Materials* (IOP, Boston, 1997), p. 386

2. A. Kirilyuk, A.V. Kimel, Th. Rasing, Rev. Mod. Phys. **82**, 2731 (2010)
3. M. Inoue, R. Fujikawa, A. Baryshev, A. Khanikaev, P.B. Lim, H. Uchida, O. Aktsipetrov, A. Fedyanin, T. Murzina, A. Granovsky, J. Phys. D, Appl. Phys. **39**, R151 (2006)
4. J.C. Jacquet, T. Valet, in *Proceedings of the Materials Research Society Magnetic Ultrathin Films, Multilayer and Surfaces*, vol. 384, ed. by E. Marinero (Materials Research Society, Pittsburg, 1995), p. 477
5. A.B. Granovskii, M.V. Kuzmichev, J.P. Clerc, J. Exp. Theor. Phys. **89**, 955 (1999)
6. A.B. Granovskii, E.A. Gan'shina, A.N. Yurasov, V. Boriskina, S.G. Yerokhina, A.B. Khanikaev, M. Inoue, A.P. Vinogradov, Yu.P. Sukhorukov, J. Commun. Technol. Electron. **52**, 1065 (2007)
7. I.V. Bykov, E.A. Gan'shina, A.B. Granovskii, V.S. Guschin, A.A. Kozlov, A.M. Likhter, S. Ohnuma, J. Exp. Theor. Phys. **96**, 1104 (2003)
8. S.M. Stirk, S.M. Thompson, J.A. Matthew, Appl. Phys. Lett. **86**, 102505 (2005)
9. I.V. Bykov, E.A. Gan'shina, A.B. Granovskii, V.S. Guschin, A.A. Kozlov, T. Masumoto, S. Ohnuma, Phys. Solid State **47**, 281 (2005)
10. A.F. Kravets, Yu.I. Dzhezherya, V.G. Kravets, E.S. Klimuk, J. Exp. Theor. Phys. **99**, 1189 (2004)
11. E.D. Pailik, G.B. Wright, Optical Properties of III–V Compounds, in *Semiconductors and Semimetals*, vol. 3 (Academic Press, New York, 1967)
12. D.J. Bergman, Ya.M. Strelniker, Phys. Rev. Lett. **80**, 857 (1998)
13. R.J. Baxter, D.G. Pettifor, E.Y. Tsymbal, D. Bozec, J.A.D. Matthew, S.M. Thompson, J. Phys. Condens. Matter **15**, L695 (2003)
14. Yu.P. Sukhorukov, A.V. Telegin, A.B. Granovsky, E.A. Gan'shina, A. Zukov, J. Gonsalez, G. Herranz, J.M. Caicedo, A.N. Yurasov, V.D. Bessonov, A.R. Kaul', O.Yu. Gorbenko, I.E. Korsakov, J. Exp. Theor. Phys. **114**, 141 (2012)
15. V.G. Kravetz, Opt. Spectrosc. **98**, 405 (2005)
16. D. Hrabovsky, J.M. Caicedo, G. Herranz, I.C. Infante, F. Sanchez, J. Fontcuberta, Phys. Rev. B **79**, 052401 (2009)
17. J.M. Caicedo, M.C. Dekker, K. Dörr, J. Fontcuberta, G. Herranz, Phys. Rev. B **82**, 140410 (2010)
18. A.B. Rinkevich, L.N. Romashev, V.V. Ustinov, J. Exp. Theor. Phys. **90**, 834 (2000)
19. A.N. Yurasov, A.B. Granovsky, S.P. Tarapov, J.P. Clerc, J. Magn. Magn. Mater. **300**, e52 (2006)
20. G.S. Krinchik, V.S. Gushchin, JETP Lett. **10**, 24 (1969)
21. E.A. Gan'shina, A.V. Zenkov, G.S. Krinchik, A.S. Moskvin, A.Yu. Trifonov, JETP Lett. **72**, 154 (1991)
22. A.B. Granovskii, M. Inoue, J.P. Clerk, A.N. Yurasov, Phys. Solid State **46**, 498 (2004)
23. R. Atkinson, P.M. Dodd, N.F. Kubrakov, A.K. Zvezdin, K.A. Zvezdin, J. Magn. Magn. Mater. **156**, 159 (1996)
24. N.F. Kubrakov, A.K. Zvezdin, K.A. Zvezdin, V.A. Kotov, R. Atkinson, JETP Lett. **87**, 600 (1998)
25. M. Vopsaroiu, D. Bosec, J.A.D. Mattew, S.M. Thompson, C.H. Marrows, M. Perez, Phys. Rev. B **70**, 214423 (2004)
26. S. Zhang, P.M. Levy, J. Appl. Phys. **73**, 5315 (1993)
27. R.T. Mennicke, D. Bosec, V.G. Kravets, M. Vopsaroiu, J.A.D. Matthew, S.M. Thompson, J. Magn. Magn. Mater. **303**, 92 (2006)
28. V.G. Kravets, D. Bosec, J.A.D. Matthew, S.M. Thompson, Phys. Rev. B **65**, 054415 (2002)
29. I.D. Lobov, M.M. Kirillova, A.A. Makhnev, L.N. Romashev, V.V. Ustinov, Phys. Rev. B **81**, 134436 (2010)
30. A. Vedyaev, A. Granovsky, A. Kalitsov, M. Chshiev, JETP Lett. **85**, 1204 (1997)
31. S. Uran, M. Grimsditch, E. Fullerton, S.D. Bader, Phys. Rev. **57**, 2705 (1998)
32. J.J. van Driel, F.R. de Boer, R. Coehoorn, G.H. Rietjens, E.S.J. Heuvelmans-Wijdenes, Phys. Rev. B **61**, 15321 (2000)

33. V.V. Ustinov, Yu.P. Sukhorukov, M.A. Milyaev, A.B. Granovskii, A.N. Yurasov, E.A. Gan'shina, A.V. Telegin, JETP Lett. **108**, 260 (2009)
34. M. Gester, A. Schlapka, R.A. Pickford, S.M. Thompson, J.P. Camplin, J.K. Eve, E.M. McCash, J. Appl. Phys. **85**, 5045 (1999)
35. V.I. Belotelov, A.K. Zvezdin, V.A. Kotov, A.P. Pyatakov, Phys. Solid State **45**, 1957 (2003)
36. S.T. Chui, H. Liangbin, Appl. Phys. Lett. **80**, 283 (2002)
37. M. Buttiker, R. Landauer, Phys. Rev. Lett. **49**, 1739 (1982)
38. H. Kaiju, S. Fujita, T. Morozumi, K. Shiiki, J. Appl. Phys. **91**, 7430 (2002)
39. V.G. Kravets, Opt. Spectrosc. **102**, 717 (2007)
40. V.G. Kravets, L.G. Popernko, A.F. Kravets, Phys. Rev. B **79**, 144409 (2009)
41. J.M.D. Coey, P. Stamnov, R.D. Gunning, M. Venkatesan, K. Paul, New J. Phys. **12**, 053025 (2010)
42. E.L. Nagaev, *Colossal Magnetoresistance and Phase Separation in Magnetic Semiconductors* (Imperial College Press, London, 2002), p. 476
43. E. Dagotto, *Nanoscale Phase-Separation and Colossal Magnetoresistance* (Springer, Berlin, 2002), p. 463
44. M.B. Salomon, J. Marcela, Rev. Mod. Phys. **73**, 583 (2001)
45. G. Rao, in *New Trends in the Characterization of CMR-Manganites and Related Materials*, ed. by K. Barner (Research Singpost, New York, 2005), p. 29
46. N.N. Loshkareva, Yu.P. Sukhorukov, B.A. Gizhevskii, A.A. Samokhvalov, V.E. Arkhipov, V.E. Naish, S.G. Karabashev, Ya.M. Mukovskii, Phys. Status Solidi A **164**, 863 (1997)
47. Yu.P. Sukhorukov, A.P. Nossov, N.N. Loshkareva, E.V. Mostovshchikova, A.V. Telegin, E. Favre-Nicolin, L. Ranno, J. Appl. Phys. **97**, 103710 (2005)
48. O.V. Melnikov, Yu.P. Sukhorukov, A.V. Telegin, E.A. Gan'shina, N.N. Loshkareva, A.R. Kaul', O.Yu. Gorbenko, A.N. Vinogradov, I.B. Smoljak, J. Phys. Condens. Matter **18**, 3753 (2006)
49. Yu.P. Sukhorukov, A.V. Telegin, E.A. Gan'shina, N.N. Loshkareva, A.R. Kaul', O.Yu. Gorbenko, E.V. Mostovshchikova, O.V. Mel'nikov, A.N. Vinogradov, Tech. Phys. Lett. **31**, 484 (2005)
50. Yu.P. Sukhorukov, E.A. Gan'shina, B.I. Belevtsev, N.N. Loshkareva, A.N. Vinogradov, D.G. Naugle, K.D.D. Rathnayaka, A. Parasiris, J. Appl. Phys. **91**, 4403 (2002)
51. E. Ganshina, N. Loshkareva, Yu. Sukhorukov, E. Mostovshchikova, A. Vinogradov, L. Nomerovannaya, J. Magn. Magn. Mater. **300**, 62 (2006)
52. Yu.P. Sukhorukov, N.N. Loshkareva, E.A. Gan'shina, A.R. Kaul', O.Yu. Gorbenko, K.A. Fatieva, Tech. Phys. Lett. **25**, 551 (1999)
53. A.B. Granovskii, Yu.P. Sukhorukov, A.V. Telegin, V.D. Bessonov, E.A. Gan'shina, A.R. Kaul', I.E. Korsakov, O.Yu. Gorbenko, J. Gonsalez, J. Exp. Theor. Phys. **112**, 77 (2011)
54. R.F.C. Marques, P.R. Abernethy, J.A.D. Matthew, C.O. Paiva-Santos, L. Perazolli, M. Jafelicci Jr., S.M. Thompson, J. Magn. Magn. Mater. **272–276**, 1740 (2004)
55. Yu.P. Sukhorukov, N.N. Loshkareva, E.A. Gan'shina, A.R. Kaul', A.A. Kamenev, O.Yu. Gorbenko, A.V. Telegin, Phys. Met. Metallogr. **107**, 579 (2009)
56. Yu.P. Sukhorukov, A.V. Telegin, E.A. Gan'shina, E.A. Stepantsov, A.N. Vinogradov, F. Lombardi, D. Winkler, Tech. Phys. **55**, 1161 (2010)
57. A.N. Yurasov, T.N. Bakhvalova, A.V. Telegin, Yu.P. Sukhorukov, A.B. Granovsky, Solid State Phenom. **190**, 381 (2012)
58. Yu.P. Sukhorukov, N.N. Loshkareva, E.A. Gan'shina, A.R. Kaul', O.Yu. Gorbenko, E.V. Mostovshchikova, A.V. Telegin, A.N. Vinogradov, I.K. Rodin, Phys. Solid State **46**, 1241 (2004)
59. Yu.P. Sukhorukov, N.N. Loshkareva, E.V. Mostovshchikova, A.S. Moskvin, E.V. Zenkov, E.A. Gan'shina, I.K. Rodin, A.R. Kaul', O.Yu. Gorbenko, A.A. Bosak, J. Magn. Magn. Mater. **258–259**, 274 (2003)
60. H.J. Lee, K.H. Kim, T.W. Noh, B.G. Kim, T.Y. Koo, S.-W. Cheong, Y.J. Wang, X. Wei, Phys. Rev. B **65**, 115118 (2002)

61. Yu.P. Sukhorukov, E.A. Gan'shina, A.R. Kaul', O.Yu. Gorbenko, N.N. Loshkareva, A.V. Telegin, M.S. Kartavtseva, A.N. Vinogradov, Tech. Phys. **53**, 716 (2008)
62. M. Inoue, A. Khanikaev, A. Baryshev, in *Nanoscale Magnetic Materials and Applications*, ed. by J.P. Liu, E. Fullerton, O. Gutfleisch, D.J. Sellmyer (Springer, Berlin, 2009), pp. 627–660
63. Y. Okimoto, Y. Tokura, J. Supercond. **13**, 271 (2000)
64. J.H. Jung, H.J. Lee, T.W. Noh, Y. Moritomo, Y.J. Wang, X. Wei, Phys. Rev. B **62**, 8634 (2000)
65. J.H. Jung, H.J. Lee, T.W. Noh, E.J. Choi, Y. Moritomo, Y.J. Wang, X. Wei, Phys. Rev. B **62**, 481 (2000)
66. S.G. Kaplan, M. Quijada, H.D. Drew, D.B. Tanner, G.C. Xiong, R. Ramesh, C. Kwon, T. Venkatesan, Phys. Rev. Lett. **77**, 2081 (1996)
67. Yu.P. Sukhorukov, A.V. Telegin, A.B. Granovskii, E.A. Gan'shina, S.V. Naumov, N.V. Kostromitina, L.V. Elohina, J. Gonsalez, J. Exp. Theor. Phys. **111**, 353 (2010)
68. O. Ripeka Mercier, R.G. Buckley, A. Bittar, H.J. Trodahl, E.M. Haines, J.B. Metson, Y. Tomioka, Phys. Rev. B **64**, 035106 (2001)
69. M. Quijada, J. Cerne, J.R. Simpson, H.D. Drew, K.H. Ahn, A.J. Millis, R. Shreekala, R. Ramesh, M. Rajeswari, T. Venkatesan, Phys. Rev. B **58**, 16093 (1998)
70. E.A. Gan'shina, V.S. Guschin, O.V. Shabanova, in *Proceedings of the Conference on Advanced Magneto-Resistive Materials* (Institute of Metal Physics UD of RAS, Yekaterinburg, 2001), p. C2
71. J.F. Lawler, J.G. Lunney, J.M.D. Coey, Appl. Phys. Lett. **65**, 3017 (1994)
72. Yu.P. Sukhorukov, A.S. Moskvin, N.N. Loshkareva, I.B. Smoliak, V.E. Arkhipov, Ya.M. Mukovskii, A.V. Shmatok, Tech. Phys. **46**, 778 (2001)
73. A.R. Kaul', O.Yu. Gorbenko, N.N. Loshkareva, Yu.P. Sukhorukov, E.V. Mostovshchikova, Phys. Low-Dimens. Struct. **7/8**, 12 (2003)
74. Yu.P. Sukhorukov, N.N. Loshkareva, A.V. Telegin, E.V. Mostovshchikova, V.L. Kuznetsov, A.R. Kaul', O.Yu. Gorbenko, E.A. Gan'shina, A.N. Vinogradov, Tech. Phys. Lett. **29**, 904 (2003)
75. O.Yu. Gorbenko, A.R. Kaul', O.V. Melnikov, E.A. Gan'shina, A.Yu. Ganin, Yu.P. Sukhorukov, N.N. Loshkareva, E.V. Mostovshchikova, Thin Solid Films **515**, 6395 (2007)
76. Yu.P. Sukhorukov, A.V. Telegin, N.N. Loshkareva, A.R. Kaul', E.A. Gan'shina, Bulletin **30** (2009). Patent RU 88165 U1, 09.06.2009
77. Yu.P. Sukhorukov, B.A. Gizhevskii, N.N. Loshkareva, A.R. Kaul', O.Yu. Gorbenko, A.V. Telegin, Patent RU 2346315 C1, 10.02.2009, Bulletin 4, 2009
78. Yu.P. Sukhorukov, A.V. Telegin, V.D. Bessonov, A.B. Granovskii, B.A. Gizhevskii, A.R. Kaul', E.A. Ganshina, I.E. Korsakov, Patent RU 2439637 C1, 10.01.2012, Bulletin 1, 2012

Chapter 6
Magneto-Photonic Bragg Waveguides, Waveguide Arrays and Non-reciprocal Bloch Oscillations

Miguel Levy, Ashim Chakravarty, Pradeep Kumar, and Xiaoyue Huang

Abstract This chapter discusses optical transmission and waveguide mode propagation in one-dimensional periodic structures fabricated in magneto-optic ridge waveguides and waveguide arrays. The scattering process in multimode waveguide Bragg reflectors is analyzed. Elliptical birefringence plays an important role in stop band formation. Large band gap detuning in mixed-mode-order scattering is found, with important applications to magnetically controlled optical switching. The chapter also presents an analysis of non-reciprocal and unidirectional Bloch oscillations in asymmetric magneto-optic waveguide arrays.

6.1 Introduction

The last decade and a half has witnessed a number of optical propagation and polarization studies in magneto-photonic layered and waveguide structures. Interesting scientific and technological possibilities open up due to the combination of non-reciprocal effects such as Faraday rotation, the non-reciprocal-phase-shift effect in waveguides, and band gap engineering. Photon trapping in magneto-optic non-reciprocal resonant cavities has been shown to lead to significant Faraday rotation enhancement [1–5]. Stop band and polarization response to magnetic bias in waveguide micro-cavities and Bragg reflectors have also been studied and used to examine applications to optical switches and sensors [6–8]. Other authors have explored electromagnetic unidirectionality in periodic magnetic stacks and two-dimensional magneto-photonic crystals [9, 10] as well as magnetically controllable band gaps in one-dimensional helicoidal magneto-photonic crystals [11]. Flat-top response in multiple resonator one-dimensional magneto-photonic crystals [12] and large polarization rotations in waveguide non-reciprocal Bragg systems have been examined [13–15]. Other studies have analyzed band gap formation, local normal mode coupling and Bloch states in elliptically birefringent magneto-photonic periodic stacks [16–19].

M. Levy (✉) · A. Chakravarty · P. Kumar · X. Huang
Physics Department, Michigan Technological University, Houghton, MI 49931, USA
e-mail: mlevy@mtu.edu

M. Inoue et al. (eds.), *Magnetophotonics*, Springer Series in Materials Science 178,
DOI 10.1007/978-3-642-35509-7_6,

Here we present a discussion of one-dimensional periodic structures in multimode magneto-photonic waveguides and waveguide arrays in magneto-optic films. In particular, asymmetric coupling between different-order waveguide modes and the presence of elliptical birefringence are shown to lead to significant polarization and stop band tuning effects. Non-reciprocal and unidirectional propagation are also analyzed in asymmetric waveguide arrays. Applications to optical switching are discussed.

The existence of high-order waveguide modes in addition to the fundamental mode results in a rich complex of dispersion curves and qualitative changes in band gap formation. The multimode regime plays an important role in the systems under consideration, leading to wave-vector and frequency splitting for each fundamental to high-order mode scattering processes. This particular type of splitting permits magnetically controlled transmittance, strong near-band-edge polarization effects and the possibility of magneto-photonic-crystal-based magnetic switches and sensors. The essence of the effect can be traced to inter-modal back-reflection between different mode-orders and mode helicity dependence of the transmittance. Of particular interest is mode conversion and mode hybridization upon helicity reversals under asymmetric back-reflection in Bragg gratings. Some degree of Bloch mode reconfiguration upon magnetization reversals does take place, as discussed in this chapter, impacting the stop bands.

Elliptical birefringence, the difference in phase speed between elliptically polarized normal modes, arises naturally in magneto-optic waveguides due to the combined effects of magneto-optic gyrotropy and shape anisotropy [13–16]. Stress birefringence, due to lattice mismatch between waveguide film and substrate also contributes to the effect. We show that it is possible to induce significant changes in the stop band spectral dispersion in elliptically birefringent multimode waveguides through hybridized coupling between different forward and partially back-reflected elliptically polarized waveguide modes. This stop band reconfiguration is traced to the transmutation of elliptical normal modes into hybrid modes, through their effect on mode propagation in the waveguide. The stop bands for these normal modes are detuned from each other due mostly to the large birefringence of the high-order back-reflected modes.

Large near-band-edge polarization changes are induced through elliptically birefringent photonic crystal asymmetric backscattering. The polarization changes are due to the interplay between Faraday rotation and linear birefringence. These changes come about from the partial selective reflection of positive and negative helicity normal modes.

We also examine the application of the non-reciprocal phase shift effect to asymmetric magneto-optic waveguide arrays. The possibility of unidirectional Bloch oscillatory motion in arrays forming Wannier–Stark ladders is examined. In the late 1920s and early 1930s F. Bloch and C. Zener predicted the phenomenon of Bloch oscillations (BO), comprising oscillatory behavior of quantum particles in a periodic potential subject to constant external force [20, 21]. In the last two decades the idea of a discrete-optical system (e.g. a waveguide array) exhibiting diffraction-less propagation of an optical beam has drawn attention to the possibility of visualizing

the oscillatory motion in the spatial domain with controlled beam dynamics [22–24]. Here we extend the analysis of the Bloch oscillatory phenomenon to unidirectional propagation in magneto-optic media.

This chapter is divided into the following sections. Section 6.1: Introduction. Section 6.2: Fabrication and characterization of ridge waveguides and distributed Bragg reflectors in magneto-optic films. Section 6.3: Stop-bands in magneto-optic Bragg reflectors and Bragg filters. Section 6.4: Stop-bands and back-reflection processes in magneto-optic elliptically birefringent media: stacked-layer model. Section 6.5: Non-reciprocal and unidirectional optical Bloch oscillations in asymmetric magneto-optic waveguide arrays.

6.2 Fabrication and Characterization of Ridge Waveguides and Distributed Bragg Reflectors in Magneto-Optic Films

Photolithography is used to pattern ridge waveguide structures on the magneto-optic iron garnet films. Electron-beam lithography (EBL) and focused ion beam (FIB) patterning enable us to form one-dimensional photonic band gap structures on the ridge waveguides. The first technology is mainly based on a converted JEOL JSM-6400 scanning electron microscope (SEM) for the fabrication of our structures, and the second one on a Hitachi FB-2000A focused-ion-beam system. Both technologies have shown good results for patterning Bragg gratings having periods of more than 0.3 μm.

6.2.1 Photolithography and Plasma Etching

The typical steps involved in the photolithographic process are sample-cleaning in acetone, isopropanol, and de-ionized-water; photo-resist layer formation by spin-coating; soft baking; mask alignment, exposure, and development; and hard-baking.

Our processing involves the use of positive photo-resist Rohm & Haas SC1827^{TM} spin-coating on the sample using hexa-methyl-disilazane (HMDS) as an adhesive layer. A two-step spin-coating at 500 rpm followed by 2000 rpm is applied. The substrate is then pre-baked for 4 minutes at 100 °C. An Electronic Vision Group (EVG) 620 mask aligner is used to expose the ∼1 to 2 μm-thick layer of photo-resist for 10–15 seconds at a 15–20 mW/cm^2 ultra-violet power density. Line widths on the mask range from 1 to 10 μm. Post exposure processing entails development in an Rohm & Haas MF319^{TM} solution followed by a 20 minute hard-bake at 100 °C. Ion-milling in an argon-ion plasma at 170–210 μA/cm^2, 700 V beam voltage, 10–20 sccm argon gas flow-rate and 8×10^{-5}–4×10^{-4} Torr pressure, transfers the pattern into the iron-garnet film at an approximate rate of 14 nm/min. Acetone, isopropanol, and de-ionized-water are used to remove the resist after milling. Sidewall damage from the plasma milling is treated by dipping the sample into an ortho-phosphoric acid bath for 12–15 seconds at 100 °C and rinsing in de-ionized water.

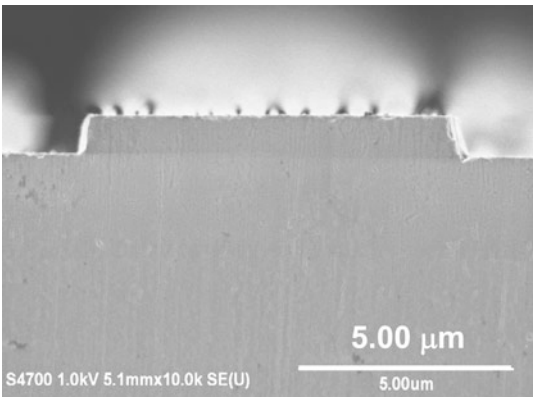

Fig. 6.1 SEM micrograph, cross sectional view of a ridge waveguide in an iron garnet film with polished facet

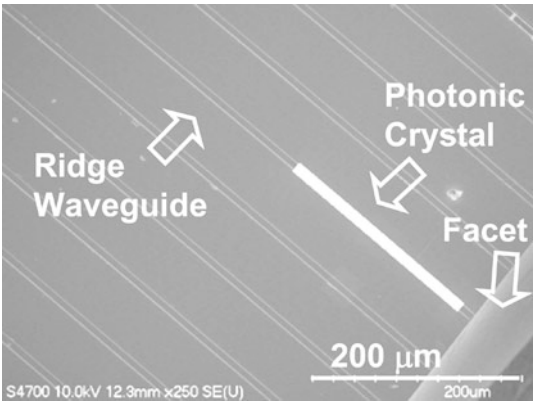

Fig. 6.2 SEM micrograph of several ridge waveguides with polished facet fabricated in a $Bi_{0.8}Gd_{0.2}Lu_{2.0}Fe_5O_{12}$ film. The white area on one of the waveguides near the facet corresponds to a Bragg grating patterned by focused-ion beam milling. First published in Physical Review B by some of the present authors, Ref. [19] Fig. 4

Facet lapping follows the ridge waveguide patterning. Diamond lapping films of different grain coarseness are used sequentially from coarser to finer, down to a 0.3 μm grain diamond lapping film finish. An SEM micrograph of a ridge waveguide cross section after facet lapping is shown in Fig. 6.1. Figure 6.2 shows an angled top view of several ridge waveguides patterned in the film.

6.2.2 Electron Beam Lithography

Electron beam lithography (EBL) is a high resolution patterning technique where high energy electrons (10 to 100 keV) expose electron-sensitive resists such as poly (methylmethacrylate) (PMMA). Proper conductive metal layer coating has to be employed to avoid severe electron charging during exposure. Otherwise undesired results such as unfocused exposure area, and lack of full exposure of the polymer layer may occur. Proper metal (Au) coating is very important for the success of EBL patterning. The metal coating usually requires more than 50 nm of gold for a 400 nm

Table 6.1 Beam current (standard value for each aperture) and beam diameter (calculated value) for FB-2000A

Aperture (μm)	Beam mode			
	M1		M0	
	Beam current (nA)	Beam dia. (nm)	Beam current (nA)	Beam dia. (nm)
500	11–15	1000		
300	4–8	250		
200	2–3.5	120	0.4–0.8	800
100	0.4–0.8	60	0.1–0.3	250
50	0.1–0.3	40	0.02–0.05	60
20	0.015–0.04	35	0.004–0.01	20
6	0.001–0.005	35	0–0.002	10

PMMA layer. Conductive taping near the target spot always improves the patterning results.

A proper selection of electron dose is also very important for the fabrication of good Bragg gratings in the resist mask because full exposure depends on a balance between the polymer thickness and incoming electron density. We have found that after a 200 nm-thick PMMA layer is spun on the garnet film, a dose of 350 μC/cm^2 at 10 pA current should be used for electron-beam exposure. The patterning is controlled with a Nabity nanometer pattern generation system (NPGS).

Once the pattern is formed on the resist, we tested pattern transfer via ion implantation and wet etching. The ion implantation induces local damage on the garnet film surface that results in selective etching when the sample is immersed in ortho-phosphoric acid. Here, again, the ion implantation condition is critical for a good pattern transfer. Argon-ion implantation at 270 keV and 1×10^{14} cm^{-2} yields ∼100 nm deep grating grooves upon wet etching in ortho-phosphoric acid.

6.2.3 Focused Ion Beam Milling

The focused ion beam method performs mask-free milling. A focused beam of gallium ions is accelerated to an energy of 5–50 keV (30 keV in our case) and scanned over the surface of the sample. A Nabity NPGS control system was added to our FIB model for vector-patterning purposes. The aperture, whose size varies from 6 μm to 500 μm, controls the beam current and spot size. There are two beam modes in the single-beam Hitachi FB-2000A model: M1 for working beam mode and M0 for imaging beam mode. Detailed beam configurations can be found in Table 6.1. Usually, we choose M1-100 for grating milling and M0-50 for imaging. The selection is based on a balance between the milling time and desired depth.

The interaction of the ion beam with the sample results in ejection of atoms from the surface (sputtering) and the production of secondary electrons and ions.

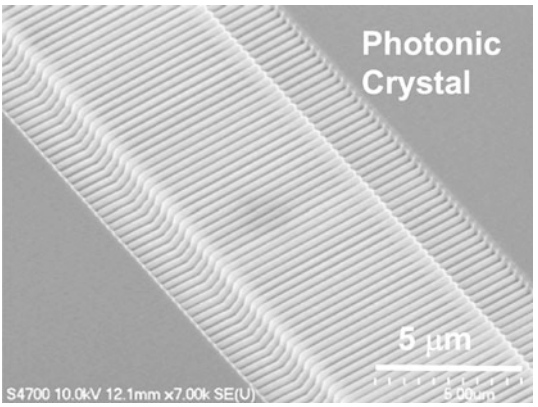

Fig. 6.3 Bragg grating patterned on a 5 µm-wide 0.8 µm-ridge height ridge waveguide in an iron garnet film. First published in Physical Review B by some of the present authors, Ref. [19] Fig. 4

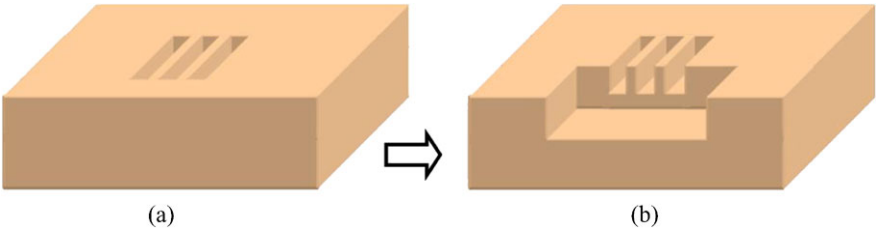

Fig. 6.4 Method of measuring grating groove depth: (**a**) Grooves are patterned near a facet. (**b**) A large cube was removed by milling. The depth is then measured by SEM

The secondary charged particles can be collected, and their signals are amplified and displayed to form an image of the surface. An imaging resolution below 500 angstroms is possible. Figure 6.3 shows a grating structure patterned on an iron-garnet ridge waveguide by FIB patterning.

The depth of the grooves directly affects the Bragg filter strength and finesse of resonant cavities patterned into the ridge waveguide. So it is very important to be able to precisely control this mill depth parameter. A way has been developed to calibrate experimentally the groove depths through FIB patterning and SEM characterization. The procedure is illustrated below.

First, the grooves are patterned near a mirror-finish polished facet edge as shown in Fig. 6.4(a). By milling away a large cube of material at the edge, the cross section profile of the gratings can be imaged from the facet side as shown in Fig. 6.4(b). The sample is then observed by SEM and the depth of the grooves is measured. Typical groove dimensions are ~150 nm wide and ~700 nm deep.

The FIB exposure dose is determined by the product of beam current and exposure time. Figure 6.5(a) shows the groove-depth dependence versus FIB line doses for a typical design groove-width of 100 nm and a bismuth-substituted iron garnet film sample. Depth ranges from 400 to 800 nm as the line dose increases from 50 to 200 nC/cm. The trend towards saturation is due to substantial re-deposition and backscattering for ion milling deeper into the material for this line width. We point

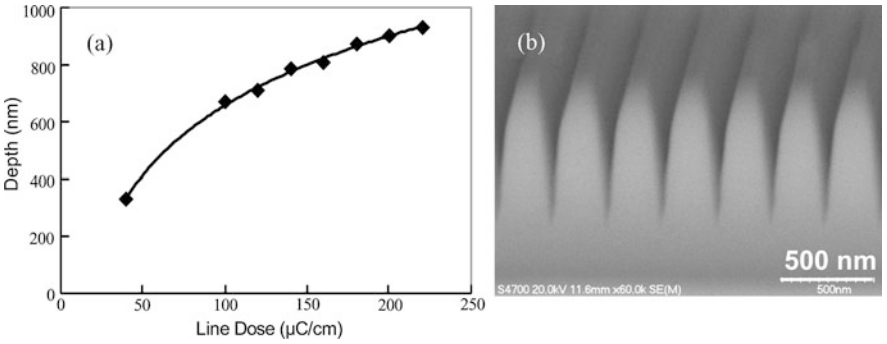

Fig. 6.5 (**a**) Characterization of FIB milled groove depths with line dose. (**b**) Scanning—electron micrograph showing typical groove cross section in a liquid-phase-epitaxially grown $Bi_{0.8}Gd_{0.2}Lu_{2.0}Fe_5O_{12}$ iron garnet film

out, however, that multiple and alternative beam scans in the transverse (along the groove length) and longitudinal (parallel to the grating axis) directions can reduce re-deposition and yield deeper and straighter grooves. Figure 6.5(b) is an SEM image of typical FIB-patterned grooves cross section.

A certain degree of ion implantation, sidewall damage and re-deposition occurs with the ion milling that will negatively affect the optical performance of the Bragg filters. These effects can be treated with an acid etch post-treatment by immersing the patterned sample into a solution of ortho-phosphoric acid at 75 °C for 10–15 seconds and rinsing in de-ionized water. A markedly improved optical response, with more pronounced transmittance stop bands is achieved as a result.

6.2.4 Optical Measurements

The optical transmittance and output polarization spectra are studied by end-fire fiber coupling from a 1480–1580 nm tunable laser source (Ando AQ4321A) in a magnetic field parallel to the waveguide axis as shown in Fig. 6.6. The laser has a 0.001 nm wavelength resolution and 7.9 mW (9 dBm) maximum, 0.079 mW (−11 dBm) minimum output power. Lensed fiber tips focus the laser spot onto the sample input facet.

Two configurations are used to magnetize the samples. Measurements that do not require variable magnetic fields are performed by placing the sample on a thin rectangular neodymium block-magnet plate fitted to the sample stage, return flux oriented parallel to the ridge waveguide axis (North and south poles parallel to the input and output sample facets). The return flux produces fields several hundred oersted strong and is strong enough to saturate the in-plane magnetization of the iron garnet film. To obtain data for the reversed magnetization direction, or for transverse magnetization, we rotate the neodymium (∼cm-wide) block-magnet 180° or 90°

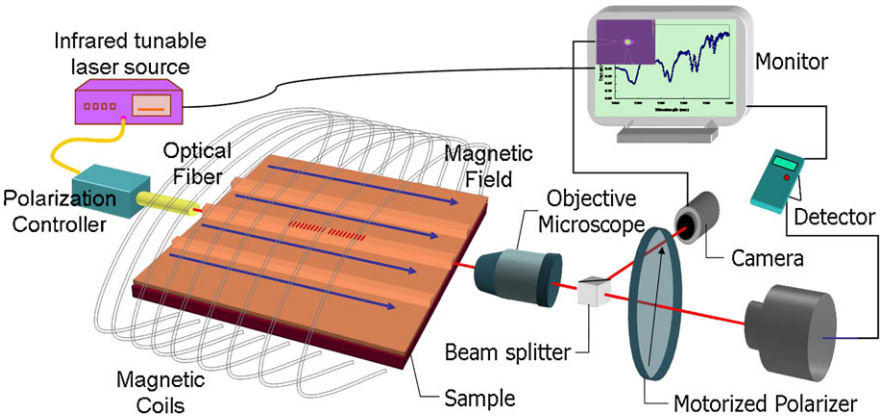

Fig. 6.6 Schematic illustration of the optical measurement setup

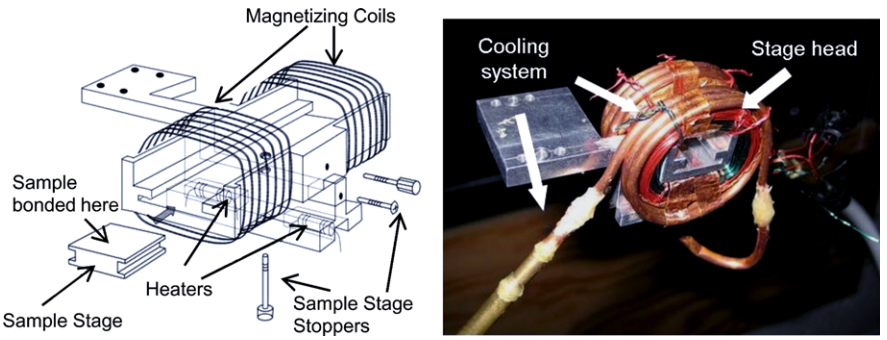

Fig. 6.7 (*Left*) Schematic depiction of the sample stage kit; (*right*) the photograph of the sample stage kit with integrated cooling system

about the normal to the plate, keeping the sample orientation relative to the input beam unchanged.

Measurements that require variable magnetic fields, such as hysteresis loops, use a set of homemade magnetic coils equipped with a homemade water cooling system. The coils and the cooling tubes are all integrated into a customized sample stage as shown in Fig. 6.7.

The sample is first bonded to a sliding stage and then inserted into the middle of the coils; two stage stoppers are used to fix the position of the slider. A small water cooling system made of copper tubes keeps the stage from heating up at larger currents ($\sim$1 A). The current to generate the magnetic fields is produced by a programmable power supply which produces a self-stabilized step current with 1 mA precision ($\pm$0.1 Oe). Fields of 40 Oe, generated at less than 0.5 A are enough to saturate the in-plane magnetization in $Bi_{0.8}Gd_{0.2}Lu_{2.0}Fe_5O_{12}$ films.

Transmittance spectra as a function of wavelength are acquired by recording the output light intensity emerging from the waveguide sample. A computer-driven Lab-

view interface to the laser source drives the wavelength scan, with controllable step-size down to 0.2 nm. The input polarization from a single-mode optical fiber is adjusted through a digital polarization controller (Agilent 11896A). Depending on the requirements of the experiment, the input polarization can be set to linearly horizontal or quasi-transverse-electric (TE), linearly vertical or quasi-transverse-magnetic (TM), circular or elliptical. The helicity, ellipticity and semi-major axis orientation of elliptically polarized inputs are prepared as explained in Sect. 6.2.5 below. The output beam emerging from the waveguide passes through a 10× microscope objective and is split into two beams by a 50 % non-polarizing beam-splitter. One beam is directed into an infrared photo-detector connected to a Newport power meter, with responsivity better than 0.9 A/W at 1550 nm (sub-nW power detection sensitivity). A motorized rotatory Glan–Thompson polarizer with sub-degree precision can be interposed between the sample and the photo-detector to analyze the polarization or record the transmittance at a given linear polarization, as described below. Polarization states are measured by recording the Stokes parameters or by performing a full 360° analyzer scan with the Glan–Thompson polarizer. The other beam is directed to an infrared Hamamatsu recording camera and monitors the output spot shape and intensity. The camera can be equipped with a beam-profile analyzer (Spiricon LBA-710PC).

6.2.5 Beam Preparation

Linear, circular and elliptical polarization states are prepared using a beam-collimator, a quarter-wave plate, a polarization controller and a linear polarizer. The optical beam from the fiber-pigtailed laser source goes through the polarization controller, a lensed fiber coupled to the output of the controller and a beam collimator. It is then allowed to go either directly to the Glan-Thompson polarizer to prepare linear-polarization or through the quarter-wave plate to prepare elliptical polarization states. In the former case, the controller is adjusted to minimize the output for the orthogonal polarization state. Extinction ratios of 1 to 4,000 (power) are obtained with dark readings of ∼35 nW for 150 μW light.

For elliptical polarizations, the quarter-wave-plate's fast axis orientation defines the semi-major axis of the input polarization state. To configure the input beam ellipticity (the ratio of the semi-minor to semi-major axes amplitudes of the polarization ellipse), a linear polarizer placed after the quarter-wave plate is oriented so that its transmission axis forms an angle $\frac{\pi}{2} - \theta$ relative to the latter's fast axis, with $\tan\theta$ equal to the desired ellipticity of the beam. The polarization controller is then adjusted to minimize the intensity of the transmitted light emerging from these two optical components for said configuration. The light coming out of the lensed fiber has the desired polarization.

An ellipticity check is done to confirm the polarization state of the beam by measuring its intensity directly from the lensed fiber for all 360° orientations of the

polarizer axis in steps of 0.1°. The measured ellipticity of a beam is given by the following expression:

$$Ellipticity = \sqrt{\frac{I_{\min}}{I_{\max}}},$$

where $I_{\min}$ and $I_{\max}$ are the measured minimum and maximum intensities of the beam. The polarizer-angle corresponding to the minimum intensity denotes the semi-minor axis orientation of the elliptical polarization state.

Stokes parameters are used to decide the beam's helicity. From the four Stokes parameters S_j ($j = 0$–3), the sign of S_3 determines the helicity of the propagating beam. In a Poincaré sphere representation, a beam with polarization coordinate (s_1, s_2, s_3) for normalized Stokes parameters $s_j = \frac{S_j}{S_0}$ is located in the upper hemisphere if S_3 is positive and polarized in the counter-clockwise sense as observed from the source, or in the clockwise sense as observed from the detector point of view (positive helicity). For a negative value of S_3 the beam carries the opposite (negative) helicity.

Experimentally, S_3 can be measured using a quarter-wave plate and a linear polarizer. The beam intensity $I(\theta, \varphi)$, where θ, φ are the linear polarizer axis and quarter-wave plate fast axis orientations, respectively, is first measured just with the linear polarizer at $\theta = 0°$ and 90°. Subsequently it is measured by inserting the quarter-wave plate ($\varphi = 90°$) into the beam path with the linear polarizer set at $\theta = 45°$. S_3 is given by

$$S_3 = I\left(0°, 0°\right) + I\left(90°, 0°\right) - 2I\left(45°, 90°\right).$$

6.3 Stop-Bands in Magneto-Photonic Bragg Reflectors and Bragg Filters

Multimode $Bi_{0.8}Gd_{0.2}Lu_{2.0}Fe_5O_{12}$ garnet films are used for our experimental tests. These are 2.7 μm-thick grown by liquid phase epitaxy (LPE) on (100)-oriented gadolinium gallium garnet (GGG) substrates. The films have planar magnetic anisotropy and in-plane coercivity of a few Oe. A specific Faraday rotation characterized for propagation normal to the films of 83°/mm was recorded at 1550 nm. A second set of $Bi_{1.28}Lu_{1.69}Gd_{0.03}Fe_{3.65}Ga_{1.35}O_{12}$ films 2.8 μm-thick grown on (100)-oriented GGG were also tested and gave results consistent with the first set. These films have a specific Faraday rotation of 95°/mm at 1550 nm wavelength and planar magnetization anisotropy.

6.3.1 Mode Indices

Waveguide modes are characterized by prism coupling in un-patterned films. Four TE and TM modes are supported by the slab waveguide for transverse

magnetization. The refractive indices of the four TE waveguide modes in the $Bi_{0.8}Gd_{0.2}Lu_{2.0}Fe_5O_{12}$ garnet films are 2.2930, 2.2497, 2.1781, and 2.0765, from fundamental to third order, respectively. Linear birefringence, defined as the difference between TE and TM mode indices, are 0.0005, 0.0047, 0.0120 and 0.0210, respectively.

Waveguide ridges with 600 nm ridge height are patterned on the films by standard photolithography and plasma etching. A one-dimensional photonic crystal or distributed Bragg reflector is formed by focused ion beam milling. Grating grooves are 700 nm-deep, with a period of ∼343 nm. The thickness of the film at the tip of the grating ridges is reduced by about 100 nm due to overlap milling. The ridge waveguides are ∼1.0 to 1.5 mm-long with the Bragg filter (200 μm in length) are positioned at different distances from the input facet, from 10 to 100 μm to ∼500 μm away from one of the facets. The latter are prepared by polishing both input and output ends of the waveguide as described in the fabrication section. For frequencies away from the Bragg condition, the photonic structure on the slab slightly modifies the effective index and character of the allowed waveguide modes, resulting in quasi-TE and quasi-TM modes with dominant in-plane (quasi-TE) or out-of-plane (quasi-TM) polarizations for transverse magnetization. Effective indices of the quasi-TE and quasi-TM modes can be determined by analysis of the stop band spectrum.

6.3.2 Stop Bands in Transversely Magnetized Bragg Filters

Stop bands are produced by the partial back-reflection of waveguide modes in the magneto-photonic Bragg filters. For transverse magnetization, quasi-TE and quasi-TM modes behave as normal modes. That means that, once launched, these modes maintain their polarization state.

For multimode waveguides the contra-directional coupling of modes of different order is allowed. Multiple stop bands form as a result of the contra-directional coupling of fundamental forward-propagating modes to different back-reflected waveguide mode orders, as shown in Fig. 6.8. These multiple stop bands appear because the optical wave incident in the grating region and the back-reflected wave satisfy the phase matching condition $\boldsymbol{\beta}_{\text{back}} = \boldsymbol{\beta}_{\text{incident}} + q\mathbf{K}$ [25]. Here $\boldsymbol{\beta}_{\text{incident}}$ and $\boldsymbol{\beta}_{\text{back}}$ are the propagation vectors of the incident and back-reflected waves, respectively; $\mathbf{K}$ is the grating vector pointing in the direction of the ridge waveguide axis and related to the grating period Λ by $|\mathbf{K}| = 2\pi/\Lambda$. $q = 0, \pm 1, \pm 2, \ldots$, indicate the order of the coupling. The vectors $\boldsymbol{\beta}_{\text{incident}} + q\mathbf{K}$ are called space harmonics and are produced as a result of the spatial modulation of the dielectric permittivity in the grating region. Notice that waveguide mode propagation depends not only on the permittivity of the waveguide core but also on the permittivity of the cladding and cover, so that a relief grating introduces spatial modulation. The stop bands form when the space harmonics match the propagation vectors of allowed waveguide modes traveling in the backward direction. Several stop bands occur because the waveguides

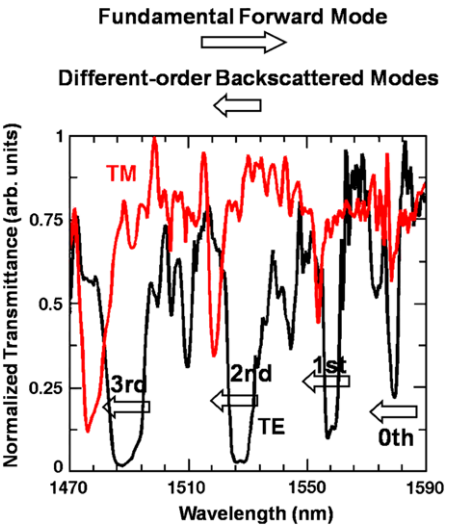

Fig. 6.8 Normalized transmittance of a waveguide Bragg reflector fabricated in a 2.7-μm-thick $Bi_{0.8}Gd_{0.2}Lu_{2.0}Fe_5O_{12}$ film. The spectrum displays several stop bands corresponding to back-reflections into different-order modes for TE and TM fundamental mode inputs. The spectra are taken for transverse magnetization in order not to mix the modes. First published in Physical Review B by some of the present authors, Ref. [19] Fig. 3

are multimode. The order of the coupling is -1, that is, first order contra-directional coupling.

The mode character of the forward traveling and back-reflected waves has been determined by an analysis of the stop band spectrum. This information was supplemented by beam-propagation simulations to estimate that more than 90 % of the coupled optical power in the forward direction is in the fundamental mode. A commercial optical-waveguide simulation package distributed by RSoft Design was used for this purpose. Back-reflected modes have different propagation vectors $|\boldsymbol{\beta}_b^{(m)}| = \frac{2\pi}{\lambda} n_b^{(m)}$, where m is the mode order and $n_b^{(m)}$ its effective or mode index. These modes satisfy the phase-matching condition $\boldsymbol{\beta}_b = \boldsymbol{\beta}_f - \mathbf{K}$ sequentially, from fundamental back-reflection at the longest-wavelength stop band, through first, second and higher-orders towards shorter wavelengths in the stop band spectrum. Figure 6.8 labels the stop bands according to this trend. Stop band center-wavelengths computed from the Bragg condition, as well as calculated stop bands based on power transfer efficiency show very good agreement with the experimental data, with average departures of 2 nm (0.15 %) and less than 5 nm between calculation and experiment. Power transfer efficiency is a function of the phase mismatch $|\boldsymbol{\beta}_b - (\boldsymbol{\beta}_f - \mathbf{K})|$.

6.3.3 Stop Bands in Longitudinally Magnetized Bragg Filters

6.3.3.1 Normal Modes

Activation of the gyrotropy upon longitudinal magnetization couples quasi-TE and quasi-TM modes. The normal modes are no longer quasi-TE and quasi-TM but elliptically polarized in the transverse direction. The simultaneous presence of shape

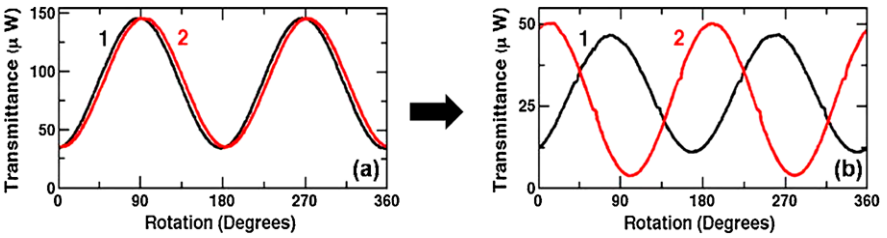

Fig. 6.9 Polarization response for plain waveguide of a normal mode (*curve 1*) and a reversed-helicity mode (*curve 2*) having the same ellipticity and semi-major axis orientation. The figure plots polarization analyzer 360°-scans, showing overlapping inputs into the waveguide (**a**) and different outputs (**b**) after propagating through a 1.2 mm-long waveguide. First published in Physical Review B by some of the present authors, Ref. [19] Fig. 5

anisotropy, lattice mismatch strain, and magnetic anisotropy establishes the elliptical birefringence, where opposite-helicity states advance at different phase speeds through the guide. Once launched into the waveguide elliptically polarized inputs can be shown to propagate with minimal change to their polarization state, as discussed below. It is in this sense that we speak of elliptically polarized normal modes.

An exact treatment of a birefringent magneto-gyrotropic waveguide requires solving the wave equation in the waveguide core and the cladding, matching boundary conditions. Here we use an alternative approach for the expressed purpose of obtaining expressions for the polarization state of the elliptical eigenmodes. The mode indices for all supported TE and TM waves in the waveguide are measured experimentally in transverse magnetization. For each TE/TM pair of a given mode order, the wave is treated as propagating in an anisotropic material having refractive indices for transverse horizontal and vertical polarizations equal to those of the given TE and TM waveguide modes in transverse magnetization. The elliptical polarization and mode indices for longitudinal magnetization are obtained by solving the dielectric permittivity eigenvalue problem in the presence of non-reciprocal gyrotropy. Thus, we approximate the diagonal components ε_{xx} and $\varepsilon_{yy}$of the relative permittivity matrix with the relative permittivity scalars (the squares of the mode indices for transverse magnetization) of the corresponding fundamental or high-order TE and TM modes. This approach works extremely well in predicting the elliptical polarization state of the normal modes of the waveguides.

Based on this formulation, elliptically polarized optical beams are prepared corresponding to the different normal mode polarization states. A saturation magnetic field of 300 Oe collinear with the waveguide axis in the forward and backward directions is used to magnetize the sample. The waveguides are fabricated in $Bi_{0.8}Gd_{0.2}Lu_{2.0}Fe_5O_{12}$ films. The response in plain 6 μm-wide ridge waveguides without Bragg filters confirm that the beams propagate with minimal changes to their polarization state over distances of 1 mm.

Figure 6.9 plots the polarization response of an elliptical normal mode (Stokes parameter $s_3 = 0.48$) and a reversed helicity mode ($s_3 = -0.48$) having the same ellipticity. Shown are 360° analyzer scans of the input (Fig. 6.9(a)) and output

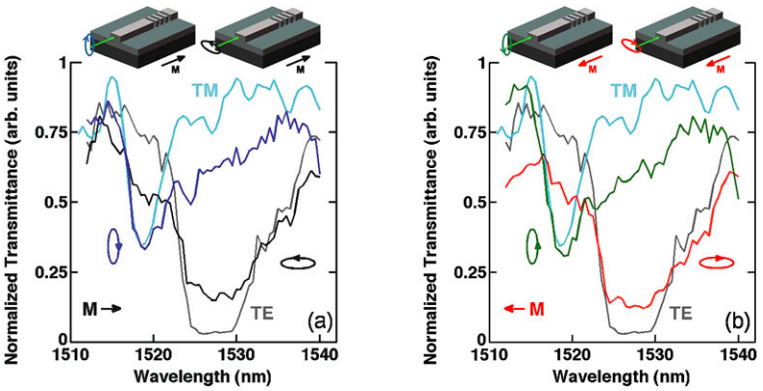

Fig. 6.10 Experimentally acquired transmittance profiles for fundamental-forward to second-order-backward propagating mode stop bands (normalized to the transmittance of a plain waveguide) for horizontally and vertically oriented elliptical normal mode inputs in a longitudinal magnetic field, (**a**) in the beam propagation direction and (**b**) opposite to the propagation direction. Normal mode helicity reverses upon reversal of magnetic field direction. Stop bands for TE and TM inputs are shown for comparison

(Fig. 6.9(b)), where 0° and 180° correspond to the orientation of the semi-minor axis. Figure 6.9(b) shows that the reversed helicity mode deviates significantly from the input, whereas the normal mode remains largely unaltered to within experimental accuracy ($\Delta s_3 \leq 0.05$). Ellipticity is preserved to $\Delta s_3 \leq 0.05$ or better. Deviations of less than 8° in semi-major axis orientation over a 1.2 mm waveguide length are routinely recorded for the normal mode. Our measurements confirm that the reversed helicity mode becomes normal upon reversal of the magnetization. Normal mode analysis at different wavelengths in the 1525 ± 5 nm range shows that their polarization state remains largely wavelength independent.

6.3.3.2 Distributed Bragg Reflectors and Elliptical Normal Modes

Normal mode beams are launched from the feeder (far) side toward the Bragg reflector, positioned 100 μm away from the output facet. Transmittance spectra for fundamental forward to high-order (first, second and third) as well as fundamental backscattered mode stop bands are measured. Normal mode polarization states are prepared at the center-wavelength of the TE stop bands, with no significant input polarization-state departures observed for ±20 nm wavelength detuning away from the center-wavelength. For normal modes with semi-major axis in the vertical direction, the stop band shows large detuning relative to the horizontally oriented normal mode. The reason for this detuning can be traced to the large birefringence between the high-order normal modes that take part in the back-reflection process.

Figure 6.10 displays measured normal mode transmittance for a fundamental forward-mode to second-order backscattered mode stop bands. Figure 6.10(a) corresponds to the stop bands of two elliptically polarized normal mode beams when

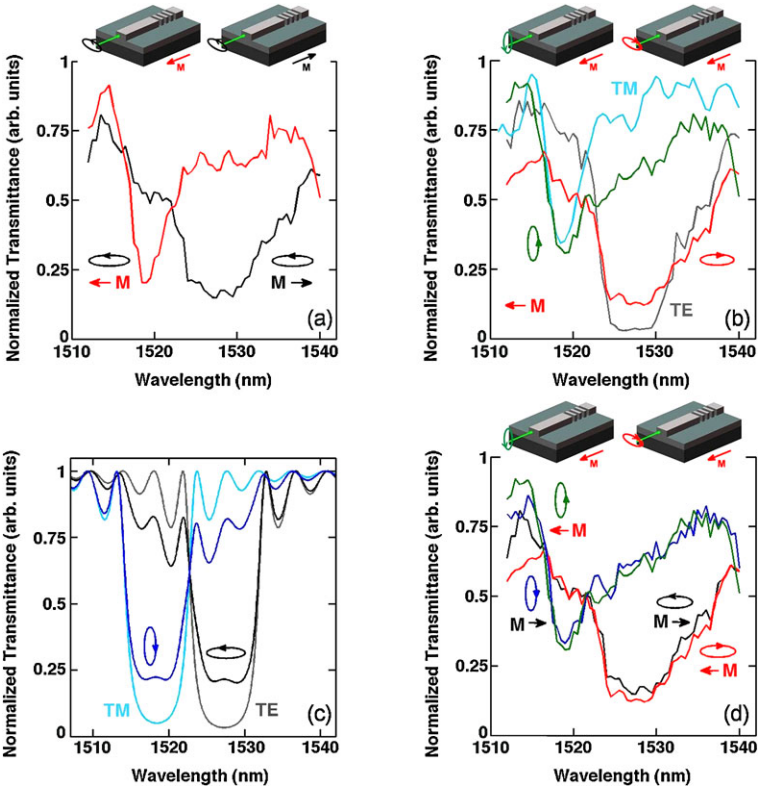

Fig. 6.11 Transmittance profiles of fundamental-forward to backward-propagating second-order–mode stop bands for elliptical normal-modes inputs and their corresponding reversed helicity modes (in normalized units to the transmittance of a plain waveguide). Experimentally measured strong stop band reconfiguration due to mode conversion is shown for reversed-helicity mode (not normal) stop bands in (**a**) *red* and (**b**) *green curves*. (**c**) The plot shows theoretically calculated stop bands for opposite helicity elliptical normal modes. (**d**) Stop bands for simultaneous helicity and magnetization reversals obtained experimentally showing that simultaneous reversal reproduces the stop bands

the magnetic field points in the light propagation direction. The stop bands for quasi-TE and quasi-TM modes (transverse magnetization) are also plotted for reference. Upon magnetization reversal the gyration vector is reversed and so is the normal mode helicity. Figure 6.10(b) plots the normal mode stop bands for reverse magnetic field and opposite helicity modes, showing that the stop bands remain largely unchanged.

Strong reconfiguring of the normal mode stop bands occur upon magnetization reversal without reversing the input beam helicity. These can be traced to the transmutation of normal modes into hybrid modes upon magnetization reversal and subsequent polarization changes of the beam in the feeder section of the waveguide. Strong stop band reconfiguration due to mode conversion are shown in Fig. 6.11.

Stop band spectra of these modes for both forward and backward magnetic field configurations were recorded for fundamental to second-order back-reflected modes. The black and blue curves in Figs. 6.11(a) and (b) plot the transmittance profiles of the horizontal and vertically oriented normal mode, respectively. Different responses, shown in the red and the green curves were obtained after magnetization reversal for the same horizontal and vertical inputs.

Of particular note is the very large spectral detuning of the stop bands upon magnetization reversal, as it may have useful applications to optical switching devices. In particular, it should be noted that reconfiguration of the stop band upon magnetization reversal or input-polarization helicity reversal can thus convert a stop band into a pass band, enabling optical switching. This detuning is a direct consequence of the inter-modal backscattering from fundamental to second-order mode. The large refractive index difference between different helicity backscattered modes is responsible for this detuning.

Mode conversion into the reverse-helicity normal mode in the waveguide feeder section is almost complete, as the stop band shifts to the one corresponding to that mode. These results agree remarkably well with stop band calculations based on the theoretical model presented in Sect. 6.4, as shown in Fig. 6.11(c). The difference between experimental and modeled back-reflection contrast for vertically and horizontally oriented polarization states is ascribed to differences in grating coupling strengths in the waveguide, not accounted for in the theoretical model. Mode conversion and strong stop band reconfiguration was reproducibly observed in all samples tested.

A change in helicity from positive to negative for the horizontal normal mode and from negative to positive for the vertical normal mode together with a change in magnetization direction restores the original normal modes spectral response (Fig. 6.11(d)). Thus, a change in helicity together with magnetization reversal preserves the normal-mode character of the mode and yields an unchanged stop band. These results are repeatable and have been reproduced in several samples.

6.3.3.3 Bloch Mode Reconfiguration upon Magnetization Reversal

The effect of Bloch mode reconfiguration on stop band restructuring upon magnetization reversal is studied experimentally by examining the Bragg filter response to normal mode inputs launched into an input facet ~10 μm-away from the magneto-photonic crystal structure. We compare these results to stack model calculations for asymmetric scattering from forward fundamental to second-order back-reflected modes in 200 μm-long gratings with 345 nm period patterned on $Bi_{0.8}Gd_{0.2}Lu_{2.0}Fe_5O_{12}$, 2.7-μm-thick ridge waveguides. The theoretical treatment is discussed in Sect. 6.4.

Upon magnetization reversal mode hybridization effects in the small 10 μm feeder section (Fig. 6.2) are minimal. A comparison of the experimental transmittance for forward- (normal mode) and backward pointing magnetization (not normal

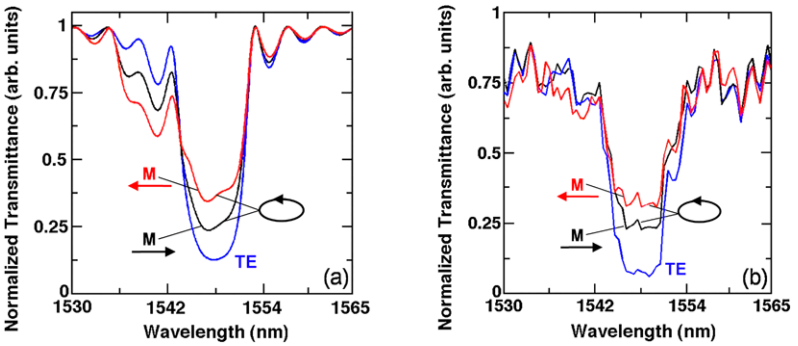

Fig. 6.12 Second-order back-reflected mode transmittance profile for horizontal elliptical normal mode input stop band (*black curve*) and corresponding reversed-helicity mode input (*red curve*) for a photonic crystal ~10 μm away from the input facet. (**a**) Theoretically calculated stop band reconfiguration calculated theoretically using the stack model in Sect. 6.4. (**b**) Experimentally measured stop bands. The stop bands for TE input are shown for comparison

mode) is shown in Fig. 6.12. These results are reproducible and show that the stop band changes are real, though not very large.

Theoretical calculations (Fig. 6.12(a)) based on the model described in Sect. 6.4 agree very well with these measurements. Bloch mode reconfiguration as a result of magnetization reversal is due to helicity reversals in the local normal modes in the photonic crystal. This reconfiguration impacts the coupling of the input polarization to the Bloch state. Forward propagating modes, but especially backscattered high-order modes exhibit strong departures from circular polarization (thin ellipses) impacting the transmittance upon helicity reversal. Magnetization reversal rotates the orientation of the semi-major axis of the normal mode polarization affecting back-reflection even if the input polarization and its helicity are not altered. This is also what we observe experimentally, as shown in Fig. 6.12(b).

6.4 Stop-Bands and Back-Reflection Processes in Magneto-Optic Elliptically Birefringent Media: Layered-Stack Model

In order to account for the coupling between differently polarized elliptically birefringent optical modes in the waveguide *Bragg reflectors* we present a layered-stack model that locally mimics the mode index and polarization state of the propagating wave. The diagonal components of the dielectric permittivity matrix in this model are allowed to acquire values corresponding to the squares of local effective mode refractive indices in the waveguide. In other words, the diagonal components ε_{xx} and ε_{yy} are approximated by the squares of the mode indices for transverse magnetization for the corresponding fundamental or high-order TE and TM modes. Asymmetric scattering between different forward and backward propagating modes is treated by the model.

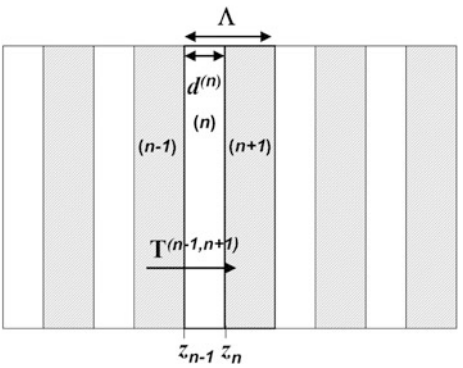

Fig. 6.13 Layered stack used for modeling the transmittance for inter-modal back-reflection. The model makes use of a bilayer unit cell with period Λ. Propagation is in the z-direction, normal to the layer planes. First published in Physical Review B by some of the present authors, Ref. [19] Fig. 1

The basic geometry of the model is depicted in Fig. 6.13. Plane waves impinge normally on the periodic stack structure consisting of alternating elliptically birefringent magneto-optic layers. The model, based on the treatment presented in [17, 18], is quite general and does not impose any constraints on the relative linear birefringence, gyrotropy, or thickness of the layers.

The electromagnetic wave equation in any particular layer of the stack is given by

$$\left(k_0^2\tilde{\varepsilon} - k^2\mathbf{I} + \mathbf{kk}\right)\cdot\mathbf{E}_0 = 0, \tag{6.1}$$

where $\mathbf{E}_0$ is the plane wave amplitude, $\mathbf{kk}$ is a dyadic product of the wave vector, $\mathbf{I}$ is the 3×3 identity matrix, and $k_0^2 = \omega/c$. c is the speed of light in vacuum and ω is the angular frequency. The dielectric permittivity matrix $\tilde{\varepsilon}$ of the birefringent magneto-optic crystal magnetized along the direction of light propagation (z-direction) in a given layer has the form:

$$\tilde{\varepsilon} = \begin{pmatrix} \varepsilon_{xx} & \pm ig & 0 \\ \mp ig & \varepsilon_{yy} & 0 \\ 0 & 0 & \varepsilon_{zz} \end{pmatrix}. \tag{6.2}$$

The above relation assumes no absorption of light in the medium, with ε_{xx}, ε_{yy}, ε_{zz} and g having real values. The condition for elliptical birefringence is given by $\varepsilon_{xx} \neq \varepsilon_{yy}$, and the magneto-optical gyrotropy is parameterized by the off-diagonal components $\pm ig$.

By solving the wave equation, (6.1), upon normal incidence of a monochromatic plane wave propagating parallel to the z axis the elliptical eigenmodes and their refractive indices in any particular layer are given by [17, 18]:

$$\hat{e}_\pm = \frac{1}{\sqrt{2}}\begin{pmatrix} \cos\alpha \pm \sin\alpha \\ \pm i\cos\alpha - i\sin\alpha \\ 0 \end{pmatrix}, \tag{6.3}$$

where

$$\tan(2\alpha) = \frac{\varepsilon_{yy} - \varepsilon_{xx}}{2g},$$

$$n_{\pm}^2 = \bar{\varepsilon} \pm \sqrt{\Delta^2 + g^2},$$

$$\bar{\varepsilon} = \frac{\varepsilon_{yy} + \varepsilon_{xx}}{2},$$

and

$$\Delta = (\varepsilon_{yy} - \varepsilon_{xx})/2.$$

$n_{\pm}$ are the mode indices of the elliptical eigenmodes. When the direction of magnetization is opposite to the direction of the beam propagation, the gyration vector of the media is reversed and as a result the helicity of the eigenmodes is also reversed. A magnetization reversal yields eigenmodes

$$\hat{e}_{\pm}^{r} = \frac{1}{\sqrt{2}} \begin{pmatrix} \pm\cos\alpha + \sin\alpha \\ -i\cos\alpha \pm i\sin\alpha \\ 0 \end{pmatrix},$$

where the superscript r indicates helicity reversal [19].

A transfer matrix formulation can be built based on this model to calculate the transmittance of the stack in Fig. 6.13, as described in [17, 18]. The dielectric permittivity matrix in adjacent layers of the stack can be modeled by adjusting the diagonal components (TE and TM mode index values) to account for differences in ridge height and index contrast in the grating.

In order to formulate an expression for the transfer matrix, [17, 18] express the Bloch mode in an arbitrary layer n of the stack in terms of local elliptically polarized normal waveguide modes. Forward and backward traveling waves are allowed to correspond to different mode-orders to account for fundamental to high-order back-reflections. Thus, for any given layer n of the stack the field vector is expressed as:

$$\begin{aligned}\mathbf{E}(z,t) = {} & \hat{e}_{+}^{f} E_{01} \exp\big(i\omega n_{+}^{f}(z - z_n)/c\big) + \hat{e}_{+}^{b} E_{02} \exp\big(-i\omega n_{+}^{b}(z - z_n)/c\big) \\ & + \hat{e}_{-}^{f} E_{03} \exp\big(i\omega n_{-}^{f}(z - z_n)/c\big) + \hat{e}_{-}^{b} E_{04} \exp\big(-i\omega n_{-}^{b}(z - z_n)/c\big). \quad (6.4)\end{aligned}$$

Here $i = \sqrt{-1}$ for a light-wave of frequency ω propagating in the z-direction. The superscripts f and b refer to the forward and backward propagating modes, and z_n is the position of the interface. The mode indices $n_{\pm}^{f,b}$ are assumed to correspond to local waveguide normal modes of opposite helicity. The E_{0j}, $j = 1$–4 are partial-wave amplitude constants with z_n as the location of the interface between two arbitrary layers n and $n + 1$ in the media. The elliptical polarization-state unit-vectors $\hat{e}_{\pm}^{f,b}$, in the form $\hat{e}_{\pm}(\alpha^{f,b})$, are the elliptically polarized waveguide normal modes propagating in the forward and backward direction, respectively. Notice that forward and backward propagating normal modes have different elliptical polarizations.

The transfer matrix is the calculated by solving for the wave propagation from one layer to the next and matching boundary conditions at the interface, for the two-layered unit cell in Fig. 6.13. For the full crystal it is then obtained by repeated multiplication of the two-layered transfer matrix. The transfer matrix from layer $n-1$ to layer $n+1$ can be shown to be

$$\mathbf{T}^{(n-1,n+1)} = \left(\mathbf{P}^{(n+1)}\right)^{-1}\left(\mathbf{D}^{(n+1)}\right)^{-1}\mathbf{D}^{(n)}\left(\mathbf{P}^{(n)}\right)^{-1}\left(\mathbf{D}^{(n)}\right)^{-1}\mathbf{D}^{(n-1)},$$

where

$$\mathbf{D}^{(n)} = \begin{pmatrix} \cos\alpha_f^{(n)} & \cos\alpha_b^{(n)} & -\sin\alpha_f^{(n)} & -\sin\alpha_b^{(n)} \\ n_{+,f}^{(n)}\cos\alpha_f^{(n)} & -n_{+,b}^{(n)}\cos\alpha_b^{(n)} & -n_{-,f}^{(n)}\sin\alpha_f^{(n)} & n_{-,b}^{(n)}\sin\alpha_b^{(n)} \\ \sin\alpha_f^{(n)} & \sin\alpha_b^{(n)} & \cos\alpha_f^{(n)} & \cos\alpha_b^{(n)} \\ n_{+,f}^{(n)}\sin\alpha_f^{(n)} & -n_{+,b}^{(n)}\sin\alpha_b^{(n)} & n_{-,f}^{(n)}\cos\alpha_f^{(n)} & -n_{-,b}^{(n)}\cos\alpha_b^{(n)} \end{pmatrix}$$

and

$$\mathbf{P}^{(n)} = \begin{pmatrix} \exp(-i\frac{\omega}{c}n_{+,f}^{(n)}d_n) & 0 & 0 & 0 \\ 0 & \exp(i\frac{\omega}{c}n_{+,b}^{(n)}d_n) & 0 & 0 \\ 0 & 0 & \exp(-i\frac{\omega}{c}n_{-,f}^{(n)}d_n) & 0 \\ 0 & 0 & 0 & \exp(i\frac{\omega}{c}n_{-,b}^{(n)}d_n) \end{pmatrix}.$$

d_n is the thickness of layer n.

6.5 Non-reciprocal and Unidirectional Optical Bloch Oscillations in Asymmetric Magneto-Optic Waveguide Arrays

In the late 1920s and early 1930s Felix Bloch and Clarence Zener predicted a remarkable phenomenon, based on the ideas of newly founded quantum mechanics [20, 21]. That phenomenon is now known as Bloch oscillations (BO). They proposed that electrons in a crystalline medium would exhibit oscillatory trajectories in space and time when subject to a uniform external force. However, in the absence of any experimental evidence, the phenomenon was intriguing but unconfirmed for many years. The first experimental evidence confirming Bloch oscillations was reported in 1960 when Chynoweth et al. [26] observed an evenly spaced energy spectrum, a Wannier-Stark ladder [27], for electrons in a crystal placed in an external direct-current (DC) field. It is claimed by some authors that these and other initial results in the 1960s and 70s were inconclusive because of the smallness of the effect [28]. Since then, however, further experimental tests have conclusively confirmed the phenomenon in different particle systems such as electrons in semiconductor superlattices, cold atoms in optical lattices and electromagnetic waves in periodic dielectric systems [29–33]. In the last two decades the idea of a discrete-optical

system exhibiting diffraction-less propagation of an optical beam has drawn attention to the possibility of visualizing the oscillatory motion in the spatial domain. As an example of particular relevance, photons in an array of evanescently coupled waveguides with a transverse effective refractive index ramp have been shown to perform periodic oscillatory motion with controlled beam dynamics [22–24, 34].

In the present study we extend the BO phenomenon idea to unidirectional propagation in optical media. Prior work on this subject has dealt mostly with reciprocal phenomena [22–24, 34]. Recently, S. Longhi [33] predicted non-reciprocal (NR) and unidirectional BO as a result of gain and/or loss in pseudo-Hermitian systems. Subsequently some of the authors of this chapter showed the existence of non-reciprocal and unidirectional BO in passive waveguide arrays for Hermitian systems [35, 36]. Here we present a theoretical treatment demonstrating that it is possible to attain cancellation of Bloch oscillatory motion in the optical regime in one-propagation direction in the absence of gain or loss. We consider wave propagation in optical media characterized by gyrotropic dielectric permittivity tensors that are strictly Hermitian in character.

In particular, we show that normal modes of the waveguide array can exhibit different phase coherence lengths in opposite directions and even significantly different coherence and decoherence characteristics in the two directions. A key role is played by the transverse-magnetic (TM) mode non-reciprocal phase shift (NRPS) effect, due to the confinement of light in magnetized asymmetric waveguides. This NRPS effect critically depends on the introduction of unequal spatial gradients in the gyrotropy parameter and in the refractive index across dissimilar waveguide interfaces [37, 38].

Wave propagation in an array of ridge waveguides of different thicknesses is considered in the presence of an in-plane transverse magnetic field. For each individual waveguide in the array, assuming lossless continuous wave (cw) propagation, coupled-mode theory yields the following equation of motion for the modal amplitude $a_n^{f,b}$ in the nth waveguide [22]:

$$i\frac{da_n^{f,b}}{dz} + \delta\beta^{f,b} n a_n^{f,b} + \boldsymbol{\kappa}^{f,b}\left(a_{n-1}^{f,b} + a_{n+1}^{f,b}\right) = 0. \tag{6.5}$$

Here f and b denote the forward (FW) and backward (BW) directions. The wavenumber ($\beta = (2\pi/\lambda) \cdot n_{\text{eff}}$) of the $n = 0$ guide has been separated out. $\boldsymbol{\kappa}^{f,b}$ are the inter-waveguide coupling constants, in the FW and BW directions, λ is the wavelength in vacuum, n_{eff} is the waveguide-mode index, and $\delta\beta^{f,b}$ is the difference in waveguide-mode wavenumber between adjacent waveguides.

The light coupled into the central waveguide at the input facet can be described as a linear combination of normal modes, the mth mode propagation constant given by $\beta_0 + m\delta\beta$. β_0 is the propagation constant of the zeroth normal mode. Refocusing of the optical beam occurs when the normal modes recover an integer multiple of their initial phases, so that the Bloch oscillation period is $L_B = 2\pi/\delta\beta$, [22].

In the waveguide array (Fig. 6.14(a)) the magnetization $\mathbf{M}$ is transverse to the propagation direction. The permittivity tensor of the magnetic garnet layer is given

by

$$\hat{\varepsilon} = \begin{pmatrix} \varepsilon & 0 & ig \\ 0 & \varepsilon & 0 \\ -ig & 0 & \varepsilon \end{pmatrix}.$$

Here propagation is along the z-direction and the magnetization points in the y-direction. The off-diagonal component g is the gyrotropic parameter, directly related to the specific Faraday rotation (θ_F) via $g = (\theta_F.\lambda.\sqrt{\varepsilon})/\pi$ [38]. We take ε and g to be real numbers, making the model system lossless. This is a good approximation for magnetic garnets, such as bismuth/rare-earth-substituted iron garnets, in the near IR regime, where loss is small.

In the following we first develop a basic theory for non-reciprocal optical BO in an array consisting of garnet-based waveguides (e.g. Bi or rare-earth-substituted yttrium iron garnet (YIG) over $Gd_3Ga_5O_{12}$ substrate). We then extend it to unidirectional optical BO in a silicon platform with bonded [39] or sputter-deposited [40] magnetic garnet cover layers.

The dielectric tensor $\hat{\varepsilon}$ is spatially dependent, with different values in the film, cover and substrate regions of the waveguide. For modes that propagate in the z-direction ($\sim \exp(i\beta z)$) quasi-transverse-magnetic (TM) modes ($H_y \gg H_x, H_z$, where **H** is the optical magnetic field component), obey [37, 38]

$$\left(\varepsilon \partial_x \frac{1}{\varepsilon} \partial_x + \partial_y^2 - \beta^2 + \omega^2 \mu_0 \varepsilon_0 \varepsilon - \beta \frac{g}{\varepsilon} \partial_x + \beta \varepsilon \cdot \partial_x \frac{g}{\varepsilon^2}\right) H_y = 0. \tag{6.6}$$

The linear terms in the propagation parameter β combine into $\beta \varepsilon H_y \partial_x (g/\varepsilon^2)$ producing non-reciprocal propagation for different vertical gradients $\partial_x (g/\varepsilon^2)$ at dissimilar interfaces. The difference in propagation constant between FW and BW system modes ($\Delta\beta^{(\mathrm{nr})} = \beta^f - \beta^b$) is given in perturbation theory by

$$\Delta\beta^{(\mathrm{nr})} = \frac{2\mathrm{Re} \iint dx\, dy\, (\partial_x H_y) H_y^* (ig/\varepsilon^2)}{\iint dx\, dy\, |H_y|^2 \varepsilon^{-1}}, \tag{6.7}$$

where the superscript nr stands for non-reciprocal [37].

The inter-modal propagation constant difference between FW and BW directions is

$$\begin{aligned} \delta\beta^f_{m+1,m} - \delta\beta^b_{m+1,m} &= \beta^f_{m+1} - \beta^f_m - \left(\beta^b_{m+1} - \beta^b_m\right) \\ &= \Delta\beta^{(\mathrm{nr})}_{m+1} - \Delta\beta^{(\mathrm{nr})}_m = \Delta\left(\Delta\beta^{(\mathrm{nr})}\right)_{m+1,m}, \end{aligned} \tag{6.8}$$

where m labels the normal mode [35]. Thus the phase matching responsible for Bloch oscillatory motion in a given direction is affected by the magnetic non-reciprocity. Assuming that Bloch-like oscillation conditions are met in the FW direction, the following expression describes BW propagation:

$$i\frac{da^b_n}{dz} + \left(\delta\beta^f - \Delta\left(\Delta\beta^{(\mathrm{nr})}_n\right)\right) n a^b_n + \kappa^b \left(a^b_{n-1} + a^b_{n+1}\right) = 0. \tag{6.9}$$

Here $\delta\beta^f$ and $\Delta(\Delta\beta_n^{(\mathrm{nr})})$ refer to differences between adjacent waveguides in the array. Equation (6.9) suggests that in the BW direction Bloch-like oscillations occur with Bloch period $\frac{2\pi}{\delta\beta^f - \Delta(\Delta\beta^{(\mathrm{nr})})}$. This establishes that an optical beam launched into the central waveguide shows dissimilar Bloch periods in opposite directions of propagation, exhibiting non-reciprocal BO in the presence of magneto-optical effect.

Moreover, it is possible to violate the conditions for Bloch oscillatory motion in one direction while preserving them in the opposite. Equal magnitudes in $\delta\beta^f$ and $\Delta(\Delta\beta^{(\mathrm{nr})})$ will result in the wavenumber step $\delta\beta^b$ being canceled out completely, thus suppressing the oscillatory motion in the backward direction.

Equation (6.8) states that the difference between the propagation constants for FW and BW waves is equal to the difference in non-reciprocal propagation constants. Thus, an array structure with inter-modal wavenumber difference $\delta\beta^f = \Delta(\Delta\beta^{\mathrm{nr}})$ will satisfy the conditions for Bloch oscillatory motion in the FW direction with period $2\pi/\Delta(\Delta\beta^{\mathrm{nr}})$, while in the BW direction $\delta\beta^b = \delta\beta^f - \Delta(\Delta\beta^{\mathrm{nr}}) = 0$, resulting in a diffractive beam spread, analogous to the behavior of a homogeneous array [22]. We note here that a large $\Delta(\Delta\beta^{\mathrm{nr}})$ is critical for practical realizations.

The array structure presented below can be made to satisfy these conditions. It consists of a ridge-waveguide array in silicon-on-insulator (SOI) with a bonded or sputter-deposited cerium-substituted yttrium iron garnet (Ce:YIG) cover [39, 40]. A schematic depiction of the array structure is shown in Fig. 6.14(a). The high index contrast between core and cladding layers and large NRPS effect of the SOI array with iron garnet cover is very well suited for unidirectional BO. Initial estimates of the non-reciprocal effect for this case were carried out using a slab-waveguide formulation presented in [41]. However, finite ridge-width effects were taken into account through a perturbation theory approach [37] using (6.7).

A 3-D semi-vectorial beam-propagation method based on a finite difference algorithm was used to simulate the array model. Mode indices and field profiles are obtained through the correlation method [42]. The calculated NRPS values were found to vary approximately linearly with mode-order propagation constants as shown in Fig. 6.14(b). The plot depicts nearly equally spaced β and $\Delta\beta^{\mathrm{nr}}$ values, representing the Wannier–Stark ladder in the waveguide array system [22].

When a beam is launched into the central guide in the FW direction, an eigenmode spectrum is observed as shown in Fig. 6.15(a). We notice that all the normal modes have identical profile with consecutive modes shifted by a waveguide step, constituting an optical equivalent of the Wannier–Stark states in the electronic case [22]. In the FW direction each normal mode maintains a constant amplitude and width ($\sim$10 µm), whereas in the BW direction the modes diffract out as shown in Figs. 6.15(b) and (c), respectively. It is important to note here that the system modes themselves do not exhibit BO motion, rather it is their superposition that does.

The array consists of nine waveguides (see Fig. 6.14(a)) made of a Si ($n_f = 3.44$) core on a SiO_2 ($n_s = 1.45$) substrate with Ce:YIG ($n_c = 2.22$) cover layer, wherein the thickness (0.26 to 0.5 µm) and the width (0.6 to 0.15 µm) have been adjusted to yield a constant $\delta\beta^f$ of about 700 m^{-1} in the FW direction. We note here that

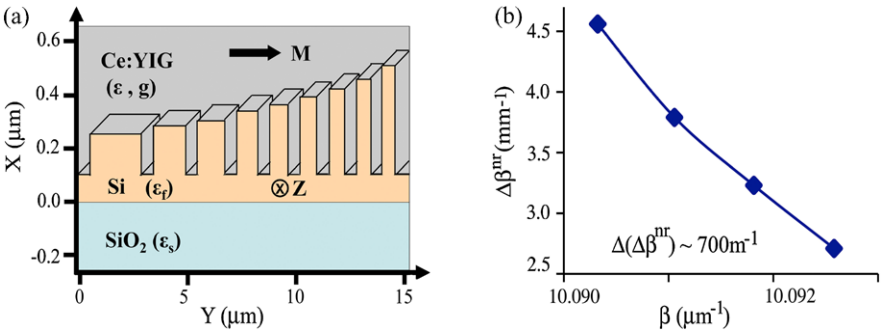

Fig. 6.14 (**a**) Schematic depiction of the waveguide array highlighting geometrical differences in the ridges leading to an effective index ramp (widths are scaled up and separations scaled down 4× to fit in the sketch); (**b**) plot showing nearly equally spaced NRPS $\Delta\beta^{nr}$ and propagation constant β for adjacent normal modes of the array

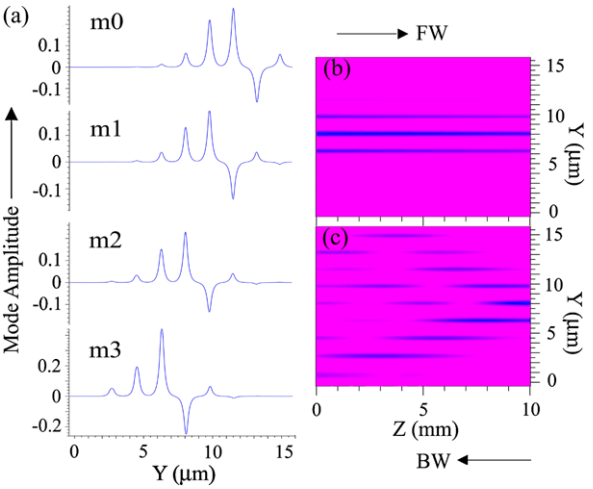

Fig. 6.15 (**a**) Field profiles of the normal modes of the array in the FW direction. (**b**) A typical normal mode of the array showing constant amplitude and width in the FW direction and, (**c**) diffractive spread in the BW direction

the wavelength range tolerated by the device is about 4 nm (1550 ± 2 nm). The device will show unidirectional Bloch oscillations within this wavelength range for any given design wavelength. However, the device is also fully scalable within a very broad wavelength range, from 1300 to 1600 nm. As for design sensitivity, deviations of up to 4 % in the ridge height and 2 % in the ridge width are tolerated and result in unidirectional Bloch oscillations. Our calculations show that the device is more sensitive to the dimensional changes in the ridges that are closer to the center of the array than those away from the center.

A constant coupling parameter $\kappa \sim 605\ \mathrm{m}^{-1}$ corresponds to the inter-waveguide separation ~2 μm design. The ensuing $\delta\beta^f$ yields a Bloch period (L_B) of about 9 mm and a lateral beam spread of ~11 μm for forward propagation. For a 0.2-μm-wide beam launched into the center waveguide the beam exhibits BO motion with a

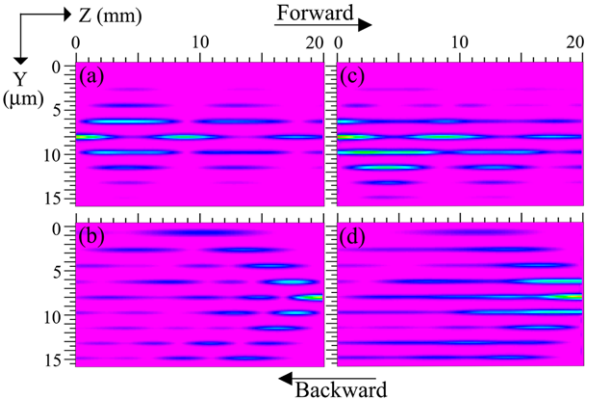

Fig. 6.16 (**a**) Beam evolution for single guide excitation in the FW direction showing BO motion, and (**b**) the BW direction, showing diffractive beam spread; (**c**) beam evolution for wide beam excitation in the FW direction, showing BO motion with the beam mostly confined to the high index side, and (**d**) the BW direction, showing diffractive beam spread

period close to 9 mm and lateral spread ∼11 μm, as shown in Fig. 6.16(a). A wider beam 6-μm-wide launched at the input facet of the array exhibits BO motion with a similar period $L_B \sim 9$ mm, with the light largely confined to the high index side with lateral spread ∼4 waveguides as shown in Fig. 6.16(c) [22].

A large NRPS is produced by reversing the propagation or the magnetization direction for the given design, with $\Delta(\Delta\beta^{nr}) \sim 700\ m^{-1}$. This is calculated performing the integration in (6.7) for a typical value of $g \sim 0.0086$ at $\lambda = 1.55$ μm with a Ce:YIG cover layer. The large index contrast between the Si core and the Ce:YIG cover plays a critical role to realize this strong NRPS. The modification of the inter-waveguide $\delta\beta$ caused by the non-reciprocal $\Delta(\Delta\beta^{nr})$ in the BW direction counters $\delta\beta^f$ and induces a $\delta\beta^b \sim 0$. The index ramp vanishes and an unlimited lateral beam spread is observed for both single guide excitation (0.2-μm-wide) and broad beam (6-μm-wide) excitation, as expected ($L_B = 2\pi/(\delta\beta^f - \Delta(\Delta\beta^{nr})) \sim \infty$) and shown in Figs. 6.16(b) and (d), respectively.

Silicon-based hybrid structures with magnetic garnet cover layers can yield NRPS as large as ∼7.0 rad/mm, as demonstrated in recent work by Mizumoto and co-workers [39]. The model system presented here has a similar garnet/SOI composition, making it possible to predict unidirectional optical BO phenomena for array lengths of less than 1 cm.

An important technological consequence of unidirectional Bloch oscillations (BO) in magneto-optic media is that it enables the design and fabrication of multi-functional on-chip devices that can function as optical isolators, amplifiers, switches, filters and routers *all in one*. For example the unidirectionality of the Bloch oscillatory phenomenon can be used for optical isolation purposes since the input beam is transversely confined and can be refocused into a single channel in the forward direction, while a backward traveling beam will diffract away from the central channel. At the same time, the same isolator device can also be used as a fast optical switch. A reversal of the magnetization direction in the cover layer will switch off the output beam as the beam switches from Bloch oscillation into a diffracting beam as a result of the magnetization reversal. This is because a magnetization reversal is equivalent to a reversal in propagation direction in these non-reciprocal

devices. The forward diffracting beam is either guided away or absorbed out. Moreover, the spread and refocusing of the waveguide excitation into a single channel in the forward direction may be used in other applications, such as non-saturated amplification in a semiconductor amplifier array. Although signals from several input channels may be amplified in a wide domain of the array thus spreading the power in a non-saturated fashion, they are refocused and leave the array through a single channel.

In summary, we predict and analytically establish the existence of unidirectional Bloch oscillations in asymmetric garnet/SOI waveguide media with transverse magnetization. It is shown that an array can be constructed with a constant wavenumber step in one propagation direction that simultaneously violates the conditions for standard Bloch oscillatory motion in the opposite. Under such conditions the counter-propagating waves behave differently, with Bloch oscillatory motion in one direction and unlimited beam spread in the opposite, as a result of the TM mode NRPS effect.

Acknowledgements This material is based upon work supported by the National Science Foundation under Grants Nos. 0856650 and 0520814. The authors thank Dr. Vincent J. Fratello and Integrated Photonics, Inc. for the LPE-grown iron garnet films. The material in Sects. 6.3 and 6.4 is partially based on the treatment published by some of the present authors in Physical Review B, Ref. [19]. The material presented in Sect. 6.5 is partially based on the treatment published by some of the present authors in Refs. [35] and [36].

References

1. M. Inoue, K. Arai, T. Fuji, M. Abe, J. Appl. Phys. **83**, 6768–6770 (1998)
2. M. Inoue, K. Arai, T. Fujii, M. Abe, J. Appl. Phys. **85**, 5768–5770 (1999)
3. M.J. Steel, M. Levy, R.M. Osgood Jr., J. Lightwave Technol. **18**, 1297–1308 (2000)
4. M.J. Steel, M. Levy, R.M. Osgood Jr., IEEE Photonics Technol. Lett. **12**, 1171–1173 (2000)
5. S. Kahl, A.M. Grishin, Phys. Rev. B **71**, 205110 (2005)
6. N. Dissanayake, M. Levy, A. Chakravarty, P.A. Heiden, N. Chen, J. Fratello, Appl. Phys. Lett. **99**, 091112 (2011)
7. N. Dissanayake, M. Levy, A.A. Jalali, V.J. Fratello, Appl. Phys. Lett. **96**, 181105 (2010)
8. Z. Wu, M. Levy, V.J. Fratello, A.M. Merzlikin, Appl. Phys. Lett. **96**, 051125 (2010)
9. A. Figotin, I. Vitebsky, Phys. Rev. B **67**, 165210 (2003)
10. M. Vanwolleghem, X. Checoury, W. Smigaj, B. Gralak, L. Magdenko, K. Postava, B. Dagens, P. Beauvillain, J.-M. Lourtioz, Phys. Rev. B **80**, 121102 (2009). (R)
11. F. Wang, A. Lakhtakia, Phys. Rev. B **79**, 193102 (2009)
12. M. Levy, H.C. Yang, M.J. Steel, J. Fujita, J. Lightwave Technol. **19**, 1964–1969 (2001)
13. M. Levy, R. Li, Appl. Phys. Lett. **89**, 121113 (2006)
14. R. Li, M. Levy, Appl. Phys. Lett. **86**, 251102 (2005)
15. X. Huang, R. Li, H. Yang, M. Levy, J. Magn. Magn. Mater. **300**, 112–116 (2006)
16. M. Levy, R. Li, A.A. Jalali, X. Huang, J. Magn. Soc. Jpn., Suppl. **30**, 561–566 (2006)
17. M. Levy, A.A. Jalali, J. Opt. Soc. Am. B **24**, 1603–1609 (2007)
18. A.A. Jalali, M. Levy, J. Opt. Soc. Am. B **25**, 119–125 (2008)
19. A. Chakravarty, M. Levy, A.A. Jalali, Z. Wu, A.M. Merzlikin, Phys. Rev. B **84**, 094202 (2011)
20. F. Bloch, Z. Phys. **52**, 555 (1928)
21. C. Zener, Proc. R. Soc. Lond. A **145**, 523–529 (1934)

22. U. Peschel, T. Pertsch, F. Lederer, Opt. Lett. **23**, 1701–1703 (1998)
23. R. Morandotti, U. Peschel, J.S. Aitchison, H.S. Eisenberg, Y. Silberberg, Phys. Rev. Lett. **83**, 4756–4759 (1999)
24. T. Pertsch, P. Dannberg, W. Elflein, A. Bräuer, F. Lederer, Phys. Rev. Lett. **83**, 4752–4755 (1999)
25. H. Nishihara, M. Haruna, T. Suhara, *Optical Integrated Circuits* (McGraw-Hill, New York, 1985)
26. A.G. Chynoweth, G.H. Wannier, R.A. Logan, D.E. Thomas, Phys. Rev. Lett. **5**, 57–58 (1960)
27. G.H. Wannier, Phys. Rev. **117**, 432–439 (1960)
28. E.E. Mendez, G. Bastard, Phys. Today **34**, 42 (1993)
29. C. Waschke, H.G. Roskos, R. Schwedler, K. Leo, H. Kurz, K. Kohler, Phys. Rev. Lett. **70**, 3319–3322 (1993)
30. M. Ben Dahan, E. Peik, J. Reichel, Y. Castin, C. Salomon, Phys. Rev. Lett. **76**, 4508–4511 (1996)
31. S.R. Wilkinson, C.F. Bharucha, K.W. Madison, Q. Niu, M.G. Raizen, Phys. Rev. Lett. **76**, 4512–4515 (1996)
32. K.G. Makris, R. El-Ganainy, D.N. Christodoulides, Z.H. Musslimany, Phys. Rev. Lett. **100**, 103904 (2008)
33. S. Longhi, Phys. Rev. Lett. **103**, 123601 (2009)
34. S. Longhi, Laser Photonics Rev. **3**(3), 243–261 (2009)
35. M. Levy, P. Kumar, Opt. Lett. **35**, 3147–3149 (2010)
36. P. Kumar, M. Levy, Opt. Lett. **36**, 4359–4361 (2011)
37. N. Bahlmann, M. Lohmeyer, O. Zhuronmkyy, H. Dötsch, P. Hertel, Opt. Commun. **161**, 330–337 (1999) and references therein
38. H. Dötsch, P. Hertel, B. Lührmann, S. Sure, H.P. Winkler, M. Ye, IEEE Trans. Magn. **28**, 2979–2984 (1992)
39. H. Yokoi, Y. Shoji, T. Mizumoto, Jpn. J. Appl. Phys. **43**, 5871–5874 (2004)
40. T. Uno, S. Noge, J. Eur. Ceram. Soc. **21**, 1957–1960 (2001)
41. R.L. Espinola, T. Izuhara, M.-C. Tsai, R.M. Osgood Jr., H. Dotsch, Opt. Lett. **29**, 941–943 (2004) and references therein
42. M.D. Feit, J.A. Fleck, Appl. Opt. **19**, 1154–1164 (1980)

Chapter 7
Magnetophotonic Crystals: Experimental Realization and Applications

M. Inoue, A.V. Baryshev, T. Goto, S.M. Baek, S. Mito, H. Takagi, and P.B. Lim

Abstract The most striking feature of photonic crystals, compared with homogeneous optical materials, is the existence of photonic band gaps. The band gaps are responsible for resonant light coupling to constituents of photonic crystals in both the cases where periodicity is ideal or broken by defects introduced intentionally. What if photonic crystals are made of magnetic materials? *May magnetism bring about new advances in the field of photonic crystals where not only amplitudes but also polarization states are controlled by the spin subsystem?* Below we will discuss *magnetophotonic crystals* and show that light confinement in their non-reciprocal magnetic constituents results in new magneto-optical phenomena. This chapter reviews studies on magnetophotonic crystals with various designs; it focuses on their experimental realizations, theoretical analysis and application to spatial light modulators.

7.1 Introduction

The electrodynamics of inhomogeneous artificial materials has experienced rapid development. Advances in experimental and applied electrodynamics are connected with the rising potential of modern fabrication techniques, allowing creation of tiny periodical structures with characteristic lengths (periodicity) comparable to or even smaller than the wavelength of light. Among representatives of such structures are photonic crystals (PCs) [1–5] and their remarkable extension—magnetophotonic

M. Inoue (✉) · T. Goto · S.M. Baek · S. Mito · H. Takagi · P.B. Lim
Department of Electrical and Electronic Information Engineering, Toyohashi University of Technology, Toyohashi, Aichi 441-8580, Japan
e-mail: inoue@ee.tut.ac.jp

A.V. Baryshev (✉)
Electronics-Inspired Interdisciplinary Research Institute, Toyohashi University of Technology, Toyohashi, Aichi 441-8580, Japan
e-mail: barysh.alex@gmail.com

A.V. Baryshev
Ioffe Physical-Technical Institute, St. Petersburg 194021, Russia

M. Inoue et al. (eds.), *Magnetophotonics*, Springer Series in Materials Science 178,
DOI 10.1007/978-3-642-35509-7_7,

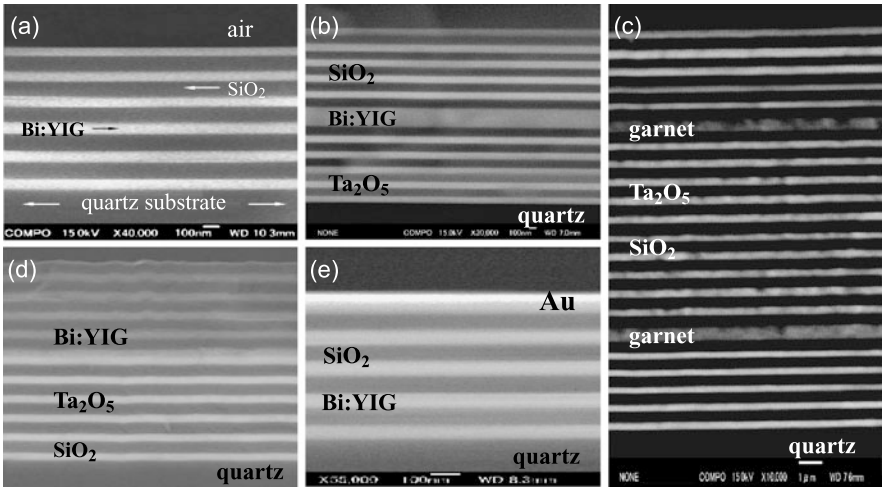

Fig. 7.1 Scanning electron microscopy images of 1D magnetophotonic crystals: (**a**) garnet/SiO_2 multilayer, (**b**) Fabri–Pérot microcavity, (**c**) dual microcavity, (**d**) and (**e**) Tamm structures

crystals (MPCs) [6–19]. Studies on MPCs were motivated by fundamental and practical interest to enhancing magneto-optical (MO) responses of existing MO materials and possibilities of controlling the flow of light by external magnetic fields. Looking back and ahead on can state that MPCs revealed themselves as fruitful media exhibiting new physical phenomena that are attractive for various applications.

Initial theoretical studies on MPCs deal with light propagation in discontinuous magnetic media with a 1D structure [6–8], where the Faraday rotation is analyzed using the matrix approach. 1D structures considered in these works are multilayer films composed of bismuth-substituted yttrium iron garnet (Bi:YIG) and SiO_2, which are piled up in an arbitrary sequence. For such multilayers, the enhancement both in transmittance and in the Faraday rotation angle θ_F is shown to originate from the localization of light caused by the multiple interference [20, 21]. Theoretical analysis shows that *the angle of Faraday rotation increases as the degree of light localization rises* (see Chap. 1). The largest enhancement of θ_F can be obtained in 1D MPCs with a microcavity structure, where a garnet layer is sandwiched between two Bragg reflectors [8, 13]. Following theoretical predictions, 1D MPCs were fabricated by different techniques and their experimental evaluation was performed. Below we will discuss experimental MPCs made by sputtering. Qualitative distinctions among various MPCs will be reviewed. As for MPCs' structural parameters and fabrication details, they can be found in works cited in the present chapter.

To start our consideration, let us recall peculiarities of a wave propagating through a one-dimensional (1D) PC and later through a 1D MPCs shown in Fig. 7.1(a). Let the PC be a periodical system of layers with dielectric constants of ε_1 and ε_2 and thicknesses of d_1 and d_2. The electromagnetic fields at the differ-

ent surfaces of a single layer are linearly connected due to linearity of the Maxwell equations:

$$\begin{pmatrix} E \\ H \end{pmatrix}_{\text{left}} = T \begin{pmatrix} E \\ H \end{pmatrix}_{\text{right}}, \tag{7.1}$$

where T is a transfer matrix. For one homogeneous layer, the T-matrix takes the form of

$$T = \begin{pmatrix} \cos(\frac{\omega}{c}\sqrt{\varepsilon}d) & i\sqrt{\varepsilon}\sin(\frac{\omega}{c}\sqrt{\varepsilon}d) \\ \frac{i}{\sqrt{\varepsilon}}\sin(\frac{\omega}{c}\sqrt{\varepsilon}d) & \cos(\frac{\omega}{c}\sqrt{\varepsilon}d) \end{pmatrix}. \tag{7.2}$$

As follows from (7.2), the T-matrix of a system of layers is equal to the product of the T-matrices of all layers. In an infinite periodical system, Bloch's theorem asserts that the eigensolution is changed only by the phase at propagation through a unit cell consisting of two layers:

$$\begin{pmatrix} E \\ H \end{pmatrix}_{\text{left}} = e^{ik_{\text{Bl}}a} \begin{pmatrix} E \\ H \end{pmatrix}_{\text{right}}. \tag{7.3}$$

If we compare (7.3) and (7.1), one may find that $e^{ik_{\text{Bl}}a}$ is an eigenvalue of the T-matrix of the unit cell, where k_{Bl} is the Bloch wave vector. For a 1D PC with such a unit cell, we arrive at a dispersion relation:

$$\begin{aligned} \cos(k_{\text{Bl}}a) = \cos\left(\frac{\omega}{c}\sqrt{\varepsilon_1}d_1\right)\cos\left(\frac{\omega}{c}\sqrt{\varepsilon_2}d_2\right) \\ - \frac{1}{2}\left(\sqrt{\frac{\varepsilon_1}{\varepsilon_2}} + \sqrt{\frac{\varepsilon_2}{\varepsilon_1}}\right)\sin\left(\frac{\omega}{c}\sqrt{\varepsilon_1}d_1\right)\sin\left(\frac{\omega}{c}\sqrt{\varepsilon_2}d_2\right), \end{aligned} \tag{7.4}$$

where $a = d_1 + d_2$ is a thickness of the unit cell. For small frequencies, we will get $k_{\text{Bl}} = \frac{\omega}{c}\sqrt{\frac{\varepsilon_1 d_1 + \varepsilon_2 d_2}{a}}$. This means that the dispersion relation $k_{\text{Bl}}(\omega)$ is just a linear relation for long waves. At the same time, we have

$$\frac{\omega}{c}\sqrt{\varepsilon_1}d_1 + \frac{\omega}{c}\sqrt{\varepsilon_2}d_2 = \pi \tag{7.5}$$

for the Bragg condition, and the right part of (7.4) becomes equal to $-1 - \frac{(\sqrt{\varepsilon_1}-\sqrt{\varepsilon_2})^2}{2\sqrt{\varepsilon_1\varepsilon_2}}\sin^2(\frac{\omega}{c}\sqrt{\varepsilon_1}d_1)$; this negative value is less than -1 and, therefore, k_{Bl} is imaginary, see (7.4). This implies that, firstly, wave propagation is prohibited due to the resonant reflection from an infinite 1D PC and that a photonic band gap (PBG) develops for such waves, see Fig. 7.2. Secondly, the group velocity tends to zero for modes approaching to edges of the PBG.

In spite of the similarity of wave phenomena in different areas of physics, there is a difference between electrodynamics and quantum theory of solids: the electron wave function is scalar (neglecting effects associated with spin) or two-spinor (taking into account degrees of freedom associated with spin), whereas the electric and

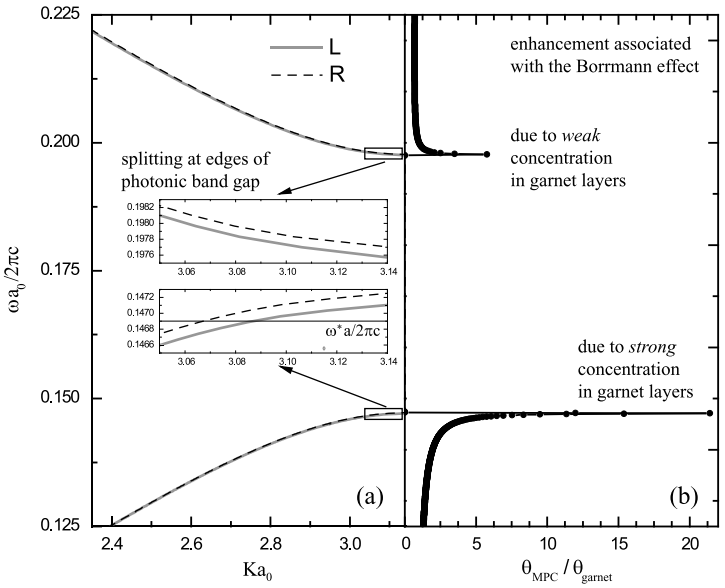

Fig. 7.2 (**a**) Photonic band structure for circularly polarized waves calculated for normal incidence of light onto a 1D MPC composed of SiO_2 layers with the dielectric constant of $\varepsilon_1 = 2.1$ and Bi:YIG layers with the diagonal component of dielectric constant of $\varepsilon_2 = 5.6$ and the off-diagonal component (gyration) of $g = 0.1$; absorption and dichroism in the layers are neglected. (**b**) Normalized Faraday rotation of a 1D MPC comprised of 20 Bi:YIG/SiO_2 bilayers–(Bi:YIG/SiO_2)^{20}; we will keep such a notation for multilayers through the chapter. Faraday rotation angle θ_{garnet} is the rotation of a homogeneous Bi:YIG film with a total thickness as that of Bi:YIG in the MPC

magnetic fields are the vector quantities. This difference becomes pronounced for magneto-optical (MO) materials that can be described by a permittivity tensor

$$\widehat{\varepsilon} = \begin{pmatrix} \varepsilon & ig & 0 \\ -ig & \varepsilon & 0 \\ 0 & 0 & \varepsilon \end{pmatrix}, \tag{7.6}$$

where g describes the MO activity, i.e. gyrotropic properties of an MO material.

Application of MO materials as components of MPCs is of a great technological interest, since manipulation of light characteristics (polarization plane and transmittance) is possible upon application of an external magnetic field. For example, modes with certain polarizations and the frequencies in the immediate proximity of a PBG edge *may satisfy either passband or band gap condition, i.e., their propagation may be either allowed or suppressed upon magnetization*. Unfortunately, most optical materials possess very small values of g. That is why to directly measure the spectral shift of PBGs is not possible. However, one may observe an alteration of PBGs when measuring rotation of the polarization plane—the Faraday effect [21].

The Faraday effect causes a rotation of the polarization plane of a wave propagating through an MO medium. This rotation is a result of splitting of the dispersions for right and left circularly polarized waves: $k_{right}(\omega) = \frac{\omega}{c}\sqrt{\varepsilon - g}$ and

$k_{\text{left}}(\omega) = \frac{\omega}{c}\sqrt{\varepsilon + g}$. Upon entering an MO material, a linearly polarized wave splits into cophased left- and right-circularly polarized waves of the same amplitude. These waves gain a relative phase shift during propagation along a traveled distance of L, and then, when emerging from the material, they rebuild a linearly polarized wave with rotated polarization plane. The angle of Faraday rotation is calculated by

$$\theta_F = \frac{1}{2}(k_{\text{left}}L - k_{\text{right}}L) = \frac{\omega}{2c}(\sqrt{\varepsilon + g} - \sqrt{\varepsilon - g})L \approx \frac{\omega g L}{2c\sqrt{\varepsilon}}. \tag{7.7}$$

Let us consider Fig. 7.2 illustrating a typical dispersion $k_{\text{Bl}}(\omega)$ for 1D MPCs. The dispersion $k_{\text{Bl}}(\omega)$ is close to a line at small frequencies, and the Faraday rotation of the MPC has the same magnitude as that of an inbuilt homogeneous MO material. However, the dispersion curves $k_{\text{left}}(\omega)$ and $k_{\text{right}}(\omega)$ more and more flatten when approaching the PBG (this illustrates decrease of the group velocity). For a wave with a certain frequency of $\omega*$, this results in the enhancement of the Faraday rotation due to a much larger difference in $|k_{\text{left}}(\omega*) - k_{\text{right}}(\omega*)|$. It should be pointed out that the band edges are distinguished not only by zero group velocities but also by a specific field distribution. It will be shown in Fig. 7.3(a) that the electric field of modes corresponding to the low-frequency edge of the PBG is mainly concentrated in the high-permittivity layers. On the contrary, the electric field concentration is greater in the low-permittivity layers for modes from the high-frequency edge of the PBG. This phenomenon can be referred to as the frequency analog of the Borrmann effect [22, 23], which is known in the X-ray spectroscopy of conventional solids [24].

In the next sections we will also discuss properties of MPCs, where the translational invariance is broken, see Figs. 7.1(b)–(e). For such MPCs, new solutions of Maxwell's equations can arise within their PBGs. These solutions will be shown to have a resonant behavior, where propagating modes are spatially localized in magneto-optical constituents of MPCs. Resonant propagation of a wave through a resonator may be represented as a *multipass regime in non-reciprocal materials*. In such a regime, the wave bounces inside resonator, i.e., travels across it many times before emerging. Thus, the effective traveled distance L from (7.7) can be much greater than the thickness of the built-in MO material. That is why *the Faraday rotation is accumulated due to non-reciprocity* of the MO material as L, governed by the Q-factor of the resonator, increases (see Chap. 1).

For 2D (and potentially for 3D) MPCs, a regime of multiple Bragg diffraction appears to play a crucial role. This regime takes place when the Bragg resonances for different families of planes of an MPC appear at the spectrally close position or simply overlap. In PBG structures, this regime corresponds to the points where two or more bands become degenerate (or nearly degenerate). It appears that the MO activity affects PBGs and optical responses of MPCs only in the close proximity to such degeneracies [17]. Due to the MO activity, components of the permittivity tensor "intermix" polarizations corresponding to the degenerate bands; note that this effect is rather marginal for modes that are far from degeneracies of a PBG [25, 26].

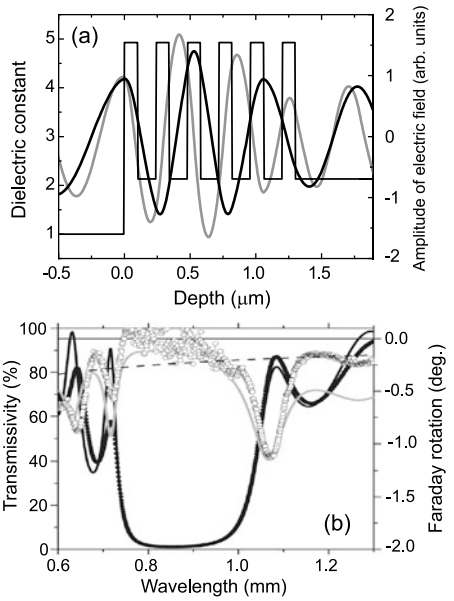

Fig. 7.3 (**a**) Spatial distribution of dielectric constants and the in-sample distribution of the electric field amplitude for wavelengths corresponding to PBG edges: *gray line* is for the short-wavelength edge and *black line*–the long-wavelength edge. (**b**) Transmission (*solid circles*) and Faraday rotation spectra (*open circles*) of the 1D MPC. *Solid curves* show the fitting of the experimental data by the four-by-four matrix approach. *Dashed line* shows the interference-subtracted spectrum of the Faraday rotation for a Bi:YIG film with the thickness equal to the total thickness of Bi:YIG in the 1D MPC shown in panel (**a**). Spectra were measured at normal incidence and for the saturating external magnetic field of 2 kOe

7.2 Optical Borrmann Effect in 1D Magnetophotonic Crystals

There is always a trade-off between the optical and magneto-optical responses for a particular MO material–called in literature the figure of merit [21], since a larger Faraday rotation is accompanied by a rise in absorption. Normally in case of MPCs under our discussion, the materials used for Bragg mirrors of MPCs have low optical losses in the visible and near infrared spectral ranges, and Bi:YIG has a significant Faraday rotation.

Let us see the electric field distribution for a 1D MPC shown in Fig. 7.1(a). The dielectric constant in a bounded MPC, which is a multilayer made of $(SiO_2/Bi{:}YIG)^5$ stack of alternating $\lambda/4$-thick SiO_2 (150 nm) and Bi:YIG (100 nm) layers is plotted in Fig. 7.3(a). For the MPC, transmission is strongly suppressed in a PBG of 730–1020 nm, see plot (b). In this spectral range, θ_F is found to decrease down to zero for light escaping from the MPC. Outside the PBG, the magnitude of θ_F oscillates and has local maxima at 640 and 720 nm that correspond to maxima in the transmission spectrum.

The maximum angle of the Faraday rotation is seen at the long-wavelength edge of the attenuation band, at 1070 nm. This is a clear manifestation of the optical

Borrmann effect in the MPC [22, 23]. The modes with wavelengths of 720 and 1070 nm are concentrated in the Bi:YIG layers. The electric field augmentation occurs most effectively for the wave with the wavelength corresponding to the long-wavelength edge of the PBG; see the maxima of the black curve in plot (a) that occur in the garnet layers. We will show in the next sections that the considered $(SiO_2/Bi{:}YIG)^{\mathbf{n}}$ multilayers provide by itself building blocks for 1D MPCs with various designs.

7.3 Light Localization or Defect Modes in Fabri–Pérot 1D MPCs

Work by Rosenberg et al. [26] states that "*Faraday rotation of the plane of polarization of light can be greatly enhanced by placing the Faraday rotating material in a resonant cavity.*" As a matter of fact, 1D MPCs with a single [8] and dual Fabri–Pérot cavity structure [9] are theoretically shown to be most efficient media to gear up the Faraday rotation of existing MO materials.

Single microcavities composed of two dielectric Bragg reflectors made of $\lambda/4$-thick materials and a $\lambda/2$-thick Bi:YIG defect layer incorporated between them, $(Ta_2O_5/SiO_2)^n/Bi{:}YIG/(SiO_2/Ta_2O_5)^n$, have been realized and evaluated in linear and non-linear optical experiments [[19], see Chap. 8]. 1D MPCs with $\mathbf{n} = 5$ is shown in Fig. 7.1(b), and an in-sample electric field distribution together with optical spectra are plotted in Fig. 7.4.

For transmission and Faraday rotation spectra, formation of sharp peaks at $\lambda = 720$ nm within an attenuation band of 600–850 nm is the result of the well-known resonant light propagation through the Fabri–Pérot microcavity, i.e. the light localization inside the Bi:YIG layer. Remarkable feature of such MPCs is that the *microcavity provides a high transmissivity and a large enhancement* of *Faraday rotation simultaneously*. Remarkable realization of all-garnet MPCs is demonstrated by Grishin et al. where the crystals were fabricated from pure bismuth iron garnet ($Bi_3Fe_5O_{12}$) and non-doped garnet layers by pulsed laser deposition or rf-magnetron sputtering: $Bi_3Fe_5O_{12}/Y_3Fe_5O_{12}$-based MPCs [13]; $Bi_3Fe_5O_{12}/Gd_3Ga_5O_{12}$-based MPCs layers [27]; $Bi_3Fe_5O_{12}/Sm_3Ga_5O_{12}$-based MPCs [28, 29]. The above-cited works showed that heteroepitaxial garnet-based MPCs exhibit excellent figures of merit in the visible and near-infrared spectral ranges.

It is worth noting that the resonant transmission of the microcavity-type 1D MPCs are controlled by the Bi:YIG defect layer; the thickness of Bi:YIG governs spectral positions and the number of localized modes exhibiting enhanced angles of Faraday rotation [19].

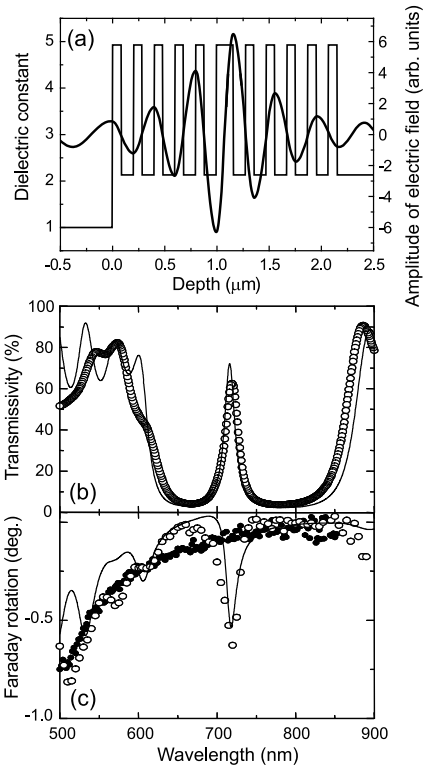

Fig. 7.4 (**a**) Spatial distribution of dielectric constants and the in-sample distribution of the electric field amplitude for a resonant wavelength. (**b**) Transmissivity and (**c**) Faraday rotation spectra of an MO microcavity, $(Ta_2O_5/SiO_2)^5$/Bi:YIG/$(SiO_2/Ta_2O_5)^5$. Spectra were measured at normal incidence and for the magnetic field of 2 kOe

7.4 Light Localization in Dual-Cavity 1D MPCs

On magnetization transmission peaks located within the PBG of the considered single-cavity MPCs split due to the difference in the refractive indices for the right and left circularly polarized light. Theoretically, this causes an unwanted effect, namely a reduction of the transmitted signal [9]. That is why magnitudes of transmissivity and the magneto-optical response of single-cavity MPCs is also a fundamental trade-off. To largely increase the responses, 1D MPCs containing two defects—dual cavities, see Fig. 7.1(c)—are analyzed and shown to exhibit a maximal possible transmissivity and Faraday rotation up to 45 degrees [9]. However, a recent experimental realization of the dual-cavity MPCs shows that even tiny structural defects have an extremely destructive effect, and the responses of the fabricated dual cavities are smaller than predicted ones [30].

Figure 7.5 illustrates an in-sample electric field distribution for a dual-cavity MPC and comparison between spectra of the dual cavity with its single-cavity counterpart [31]. Bragg mirrors (BM) for these MPCs were $\lambda/4$ stacks of $(Ta_2O_5/SiO_2)^5$, and the structures of dual and single cavities were BM/G/BM/S/BM/G/BM and BM/G/BM/, respectively; G was a $\lambda/2$-thick $Bi_{0.5}Dy_{0.7}Y_{1.8}Fe_{3.3}Al_{1.7}O_{12}$ layer and S was a $\lambda/4$-thick spacer made from SiO_2. One can see that maxima of the electric field distribution lie in the garnet layers plot (a), such a distribution should result

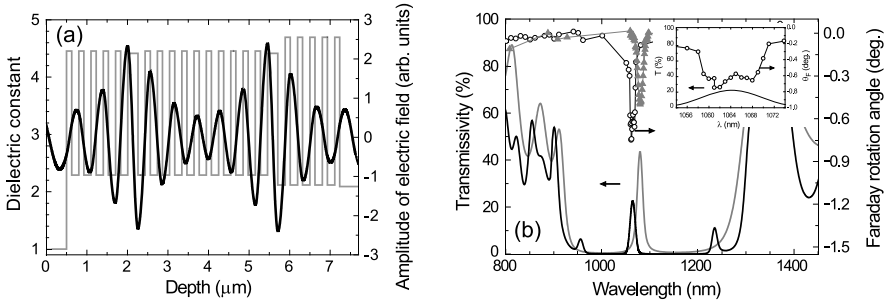

Fig. 7.5 (**a**) Dual cavity: a sketch of the spatial distribution of dielectric constants and the in-sample distribution of the electric field amplitude for a resonant wavelength. (**b**) Transmissivity and (**c**) Faraday rotation spectra of the dual (*black line*, *circles*) and single (*gray line*, *triangles*) cavities. *Inset* illustrates a double peak in the spectrum of Faraday rotation. Spectra were measured at normal incidence and for the saturating external magnetic field of 2 kOe

in large enhancement of the Faraday rotation. However, spectra in Fig. 7.5(b) show that the figure of merit of the single cavity is better than that of the dual cavity. The only signature of the "dual" behavior can be seen in the inset. Here splitting of the peak in the spectrum of Faraday rotation is an intrinsic feature of dual cavities, illustrating a resonant coupling between the garnet defect layers.

The angle of Faraday rotation of the dual cavity was smaller than the doubled angle of the single cavity, and the Q-factor of the dual cavity degraded for this experimental sample. Since the dual cavity has been fabricated by successive sputtering and two annealings, there is no identity of two single cavities composing the dual cavity. This results in detuning the resonances and degrading optical responses of the dual cavity. To conclude, our recent results show that, for realizing the concept of dual cavity, (i) fabrication accuracy and (ii) thickness of BMs must exceed those of the fabricated sample. Studies on dual cavities fabricated by adhesive bonding with improved responses can be found in Ref. [31].

7.5 Optical Tamm States in 1D MPCs

An interesting realization of 1D MPC supporting *optical surface states* has been recently demonstrated theoretically [32–37] and experimentally [38–40]. It was shown that a boundary between two 1D PCs causes a localized state to appear, and the frequency of such a state located inside the overlapping PBGs of two PCs. The eigensolution $f(z)e^{ik_{\mathrm{Bl}}z}$ inside each PC is the *Bloch wave* and consists of two factors—the exponential part $e^{ik_{\mathrm{Bl}}z}$, where k_{Bl} is the Bloch wavenumber, and a periodic function $f(z)$. For the band-gap frequencies, the electromagnetic field decreases exponentially from interfaces of a PC (since the Bloch wavenumber k_{Bl} is an imaginary quantity) and is still modulated by the $f(z)$ function. In the case of two adjoining PCs, Fig. 7.1(d), two f functions make possible to satisfy the boundary conditions between two exponentially evanescent from the boundary interface

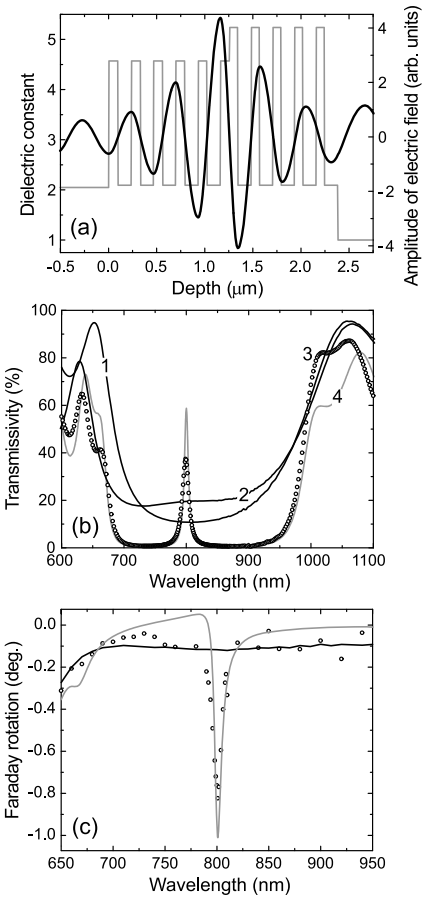

Fig. 7.6 (**a**) Spatial distribution of dielectric constants for the MPC shown in Fig. 7.1(d) and the electric field amplitude for a resonant wavelength. (**b**) Transmissivity of a nonmagnetic PC and a magnetic PC are denoted by *line 1* and *2* respectively. Transmissivity of the system of adjoining PCs (referred in the text as the MPC) is shown by *circles* (*3*); its calculated spectrum is given by *curve 4*. (**c**) Angle of Faraday rotation: a reference $(SiO_2/Bi{:}YIG)^5$ multilayer (*black solid line*), the experimental (*circles*) and calculated (*gray line*) spectra of the MPC

Bloch waves. This case results in developing a state spatially localized at the interface between two PCs. This state is intrinsically a surface one and is cognate to the Tamm state [41] known in Solid State Physics. Another mapping of Tamm's structure onto the electrodynamics would be a system comprised of a PC and a film with the negative permittivity adjoined to the PC. The existence of optical Tamm states (OTSs) has been also theoretically discussed in Refs. [42, 43]. Below we discuss OTSs in experimental MPCs.

Figure 7.1(d) shows a Tamm structure of two adjoining 1D PCs, sputtered successively on a quartz substrate. The first, non-magnetic PC was the dielectric multilayer $Ta_2O_5/(SiO_2/Ta_2O_5)^5$. Then, the magnetic $(Bi{:}YIG/SiO_2)^5$ multilayer was formed so that the resultant MPC had a structure of quartz substrate/$Ta_2O_5/(SiO_2/Ta_2O_5)^5/(Bi{:}YIG/SiO_2)^5$. Another, more simple Tamm structure was a quartz substrate/$(SiO_2/Bi{:}YIG)^5$/Au multilayer, see Fig. 7.1(e). For resonant wavelengths, the electric field pattern within the MPCs together with the dielectric constant profile is given in plots Figs. 7.6(a) and 7.7(a). For both realiza-

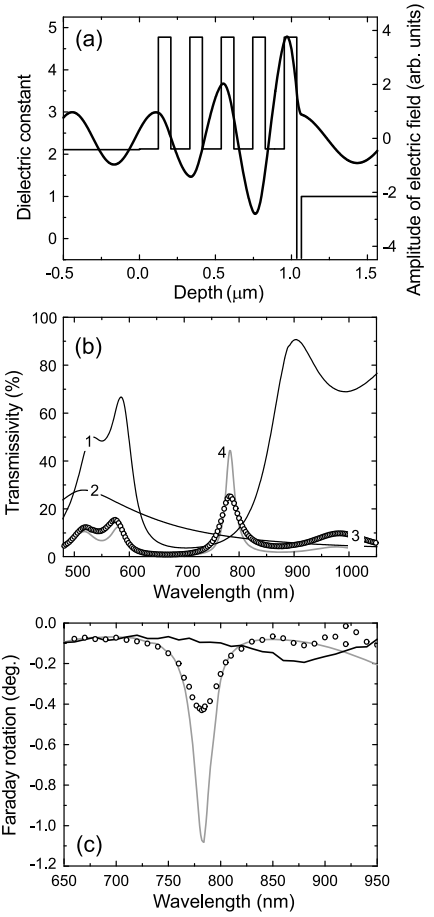

Fig. 7.7 (**a**) Spatial distribution of dielectric constants for the MPC shown in Fig. 7.1(e). (**b**) Transmissivity of the $(SiO_2/Bi{:}YIG)^5$ multilayer and the Au film alone are denoted by (*1*) and (*2*), respectively. Transmissivity of sample $(SiO_2/Bi{:}YIG)^5/Au$ is shown by *circles* (*3*); its calculated spectrum is given by *curve 4*. (**c**) Angle of Faraday rotation: the $(SiO_2/Bi{:}YIG)^5$ multilayer (*black solid line*, experiment) and the $(SiO_2/Bi{:}YIG)^5/Au$ (*circles*—experiment, *gray line*—theory)

tions, the amplitude is *remarkably high at the interface* between the magneto-optical substructure and the adjoined one, and it falls exponentially away from the interface. Such a distribution confirms the formation of the OTSs seen in transmission spectra [see plots (b), lines 3 and 4]. Also, the designs of the MPCs were such that all, for the resonant wavelength of OTS, maxima of the field pattern were spatially located inside the Bi:YIG layers.

According to work [35], if one of the adjoining PCs is magnetic, an OTS should cause a substantial enhancement of the Faraday rotation. In order to verify that the transmission peaks associated with OTSs are due to resonant coupling to Bi:YIG, MO spectra of the reference $(SiO_2/Bi{:}YIG)^5$ multilayer have been measured. The Faraday rotation of the conventional multilayer—the monotonous black solid line—follows the ordinary response from the Bi:YIG constituents, see Fig. 7.6(c). As for the Tamm structure, the Faraday rotation is enhanced at the transmission peak of 800 nm; θ_F is almost one order of magnitude larger than that of the magnetic PC. It is worth noting that, qualitatively and from the view point of the measured optical

and magneto-optical responses, this realization of MPCs is very close to the single magnetic microcavity (Sect. 7.3).

Now let us consider an OTS in MPCs with a structure of $(SiO_2/Bi{:}YIG)^5/Au$, in which the periodicity is terminated by an Au film with the negative permittivity. For this MPC, the OTS with a wavelength of 780 nm appeared inside the attenuation band of 600–850 nm. Intensity of the transmission peak was 25 %, and the corresponding enhanced Faraday rotation angle was of $-0.4°$ (see Fig. 7.7). As for the reference $(SiO_2/Bi{:}YIG)^5$ multilayer, a peak related to the Borrmann-like enhancement is seen at a wavelength of 875 nm. Note again that this Tamm structure represents the direct optical analog of the conventional crystals supporting the electron Tamm states, while the system of adjoined PCs resembles the microcavity-type MPC discussed in Sect. 7.3.

To underline peculiarities of MPCs supporting optical Tamm states, one may state that these structures can be employed for localizing light within any active material used as the constitutive layers of PCs or introduced at the interface between two PCs. OTSs might provide the additional mechanism to increase the electric field strength in photonic structures called upon to excite long-range surface plasmon–polaritons. Moreover, they can be attractive for sensing applications, since their optical responses may strongly vary with a change of dielectric conditions in the vicinity of open noble metal surfaces.

7.6 Interplay of Surface Resonances in 1D Plasmonic MPC Slab

Surface plasmon- (SPR) and localized surface plasmon resonance-affected magneto-optical responses from various structures have found a remarkable interest aimed at enhancing responses from known magneto-optical materials. Several magneto-optical composites (see Chap. 4.7 in Ref. [5] and [44–47]) and structures (see Chap. 5, [48–52]) have been reported to possess plasmon-related features in Faraday (or Kerr) rotation spectra, where enhanced polarization rotation is accompanied by light interaction with noble metal subsystems.

Here we consider overlapping resonances in spectra of an MPC terminated by a noble metal layer $[(SiO_2/Bi{:}YIG)^5/Au$ multilayer shown in Fig. 7.1(e)]—the plasmonic MPC slab, hereafter. Experimental conditions and parameters of the slab have been chosen such that the slab supported OTS originating from the periodical structure and SPR on the noble metal (Au) film's interface [53]. The Kretschmann configuration has been used to match these resonances (Fig. 7.8). Experimentally observed spectral positions of the SPR band are in agreement with that obtained from the analytical expression [54] for excitation of surface plasmons:

$$n_p \sin(\alpha) - n_{\text{eff}} = 0, \quad n_{\text{eff}} = \text{Re}\sqrt{\frac{\varepsilon_{\text{Au}}(\lambda) n^2}{\varepsilon_{\text{Au}}(\lambda) + n^2}}, \tag{7.8}$$

where n_p is the refractive index of a coupling prism ($n_p = 1.5$), α is an angle of incidence from the prism, $\varepsilon_{\text{Au}}(\lambda)$ is a dielectric permittivity of the gold layer, and

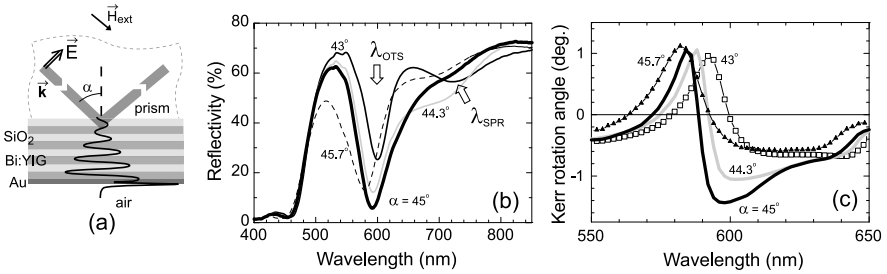

Fig. 7.8 (**a**) Experimental geometry for OTS and SPR excitation. (**b**) Reflection spectra of the plasmonic MPC slab for internal, in-prism angles of incidence, $\alpha = 43$–$45.7°$. (**c**) Kerr rotation spectra for same α as in plot (**b**)

$n = 1$ (air). The choice of the multilayer's parameters is done so as to match spectral positions of OTS and SPR in accord with the following expression:

$$\lambda(\alpha) = \lambda(0)\sqrt{1 - \left(\frac{n_p \sin\alpha}{n_{\text{eff}*}}\right)^2}, \tag{7.9}$$

where $\lambda(0)$ is a spectral position of OTS at normal incidence, α is an angle of incidence from the coupling prism, n_p is a refractive index of the prism, and $n_{\text{eff}*}$ are is the effective refractive index of multilayer.

Figure 7.8(b) presents reflection spectra of the plasmonic MPC slab where a peak associated with the OTS and the SPR band are manifested. One can see that, in the range of $\alpha = 43$–$45.7°$, the SPR band experienced a fast shift and spectrally intersected OTS. Note that, for $\alpha = 43$–$45.7°$, the OTS peak slightly shifts ($\Delta\lambda \approx$ 20 nm) in accord with (7.9).

Figure 7.8(c) demonstrates that the Kerr rotation spectra of the slab experience a large modification when the peaks associated with the OTS and SPR resonances spectrally overlap. Interestingly, the magnitude of θ_K altered with sign reversal by the crossing between OTS and SPR. For example, one can see that θ_K changed sign from $+1°$ to $-1.4°$ when scanning $\lambda = 585$–695 nm; see the spectrum for $\alpha = 45°$. Symmetrical shape of the $R(\lambda)$ curve (thick solid line, $\alpha = 45°$) is a signature indicating that the minima of the OTS and SPR resonances are spectrally close. The interplay between these overlapping resonances resulted in more and more asymmetrical shape of the $\theta_K(\lambda)$ spectra. Obviously, a power distribution 'in OTS and SPR tandem' together with phase relations between rays emerging from the slab were responsible for the observed transformation of the θ_K spectra. One may expect that, for structures with high-Q factors for OTSs, the above mentioned change of θ_K will accordingly increase.

Motivated by an idea of an artificial medium able to support resonances of different nature, the plasmonic MPC slab is considered as a new approach to engineer responses of magnetophotonic crystals and similar systems. It is rather interesting that the spectra of θ_K [Figs. 7.8(b) and (c)] have a Fano resonance-line [55] shape at the condition of $\lambda_{OTS} = \lambda_{SPR}$, where there should be an interaction of a spectrally

narrow OTS laying inside a wide SPR band. The observed modification of the polarization rotation spectrum θ_K can be thought of as a *vector-field analog of the scalar Fano resonance*.

7.7 Multiple Bragg Diffraction in Quasi Two-Dimensional MPCs

Up to the present section the chapter dealt with the realizations of one-dimensional MPCs, although fabrication of two- (2D) and three-dimensional (3D) MPCs (see Figs. 7.9 and 7.13) has been done by combining different approaches [19]. In fact, the MO responses of such experimental structures are not much competitive with that of 1D MPCs. However, theoretically predicted effects (for instance, magnetic superprism [17, 18], waveguide circulator [56, 57]) provide room for the next challenges in the development of 2D and 3D MPCs. In the search for successful MPCs with higher dimensionality, 2D MPCs [58–62] have been fabricated by autocloning [63]. For setting periodicity of MPCs, patterned substrates can be used where sputtered materials transpose symmetry of the substrates. In this section we present a discussion of the structural and optical properties of 2D MPCs fabricated on an opal film and a lithography-made pattern, Fig. 7.9(d).

Two-dimensional periodicity in the "quasi-2D" (Q-2D) MPC has been set by a structured substrate, where a 1D array of photoresist bars had a lattice constant of 400 nm and the bars had a width of 200 nm, see inset to Fig. 7.9(d). Up to seven Bi:YIG/SiO_2 bilayers have been stacked so that the symmetry of the photoresist pattern has been replicated across and along the MPC. The cleaved edge reveals the Q-2D periodicity, where scattering elements can be denoted by parallelograms, see Fig. 7.10(a). Sputtering was made simultaneously for the Q-2D MPCs and for a regular, reference 1D MPC fabricated on top of a flat quartz substrate (same type as in Sect. 7.2). The geometry of the experiment together with polarization directions for incident light and the orientation of samples is shown in Fig. 7.10(b). The linearly polarized electric field has been set by a polarizer to be of a chosen orientation: the electric field vector is across the photoresist bars for p-polarized light ($E_\perp$, $\psi = 0°$), and it is parallel to the bars for s-polarized light ($E_\parallel$, $\psi = 90°$).

Transmission spectra and spectra of the Faraday rotation at the normal incidence for the Q-2D (Bi:YIG/SiO_2)^7 multilayer, and the reference 1D MPC are shown in Fig. 7.11. One can see spectrally neighboring, overlapping bands in transmission spectra. Light with wavelengths from such an overlap will experience the so-called multiple Bragg diffraction (the effect [64] known from the X-ray spectrography). In the case of magneto-optical materials, such diffraction should introduce unusual responses from MPCs with 2D and 3D structures.

Let us consider features in spectra of the Q-2D MPC. The band in a range of 580–830 nm for 1D MPC (gray line) can be also traced in the spectra of the Q-2D MPC. Interestingly, the $T_\parallel$- and $T_\perp$-polarized spectra of the sample have a reach structure with a number of resonant peaks and showed large transmission anisotropy, Fig. 7.11(a). The prominent difference in the spectra of the sample is an additional

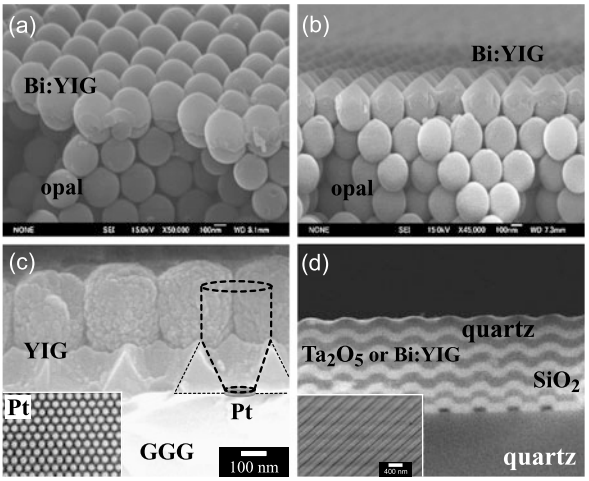

Fig. 7.9 2D MPCs fabricated by the autocloning method: (**a**) patterned Bi:YIG on an opal thin film, (**b**) same as in (**a**) after ion etching [58–60], (**c**) YIG garnet fabricated on a GGG crystalline substrate covered by a 2D platinum array–mono-and poly-crystalline YIG substructures are seen [59], and (**d**) corrugated Bi:YIG/SiO_2 multilayer with a "quasi-2D" periodicity [61, 62]

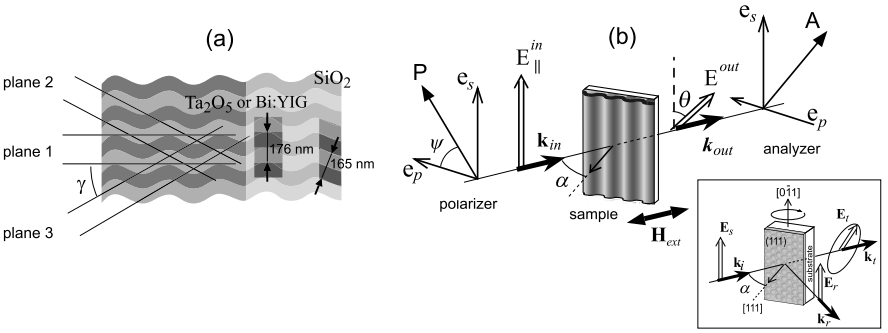

Fig. 7.10 (**a**) Model of the "quasi-2D" structure of the multilayer shown in Fig. 7.9(d): diffraction planes, interplanar spacing and scattering elements are shown. (**b**) Scheme of experiment together with orientation of the sample and the polarization plane. The *inset* shows an orientation of an opal sample under discussion in Sect. 7.8, Fig. 7.14

stop band in a range of 535–600 nm. This band with its minimum at $\lambda = 570$ nm is clearly seen in the $T_\perp$ spectrum. For $E_\parallel$-polarized light, the additional band merged with that located in the long-wavelength range. The additional band is due to diffraction from "oblique sine curve piece" (OS) periodical scattering elements of the multilayers. And "inflection sine curve piece" (IS) scattering elements are responsible for the spectral features in long wavelengths. These three sets of effective diffraction planes in the structure can be seen in Fig. 7.10(a). Thus, the set of planes 1 (or IS elements) are responsible for attenuation in the longer range. Planes 2 and 3 (or OS elements) diffract light with shorter wavelengths of $\lambda = 530$–600 nm.

Actually, when scanning the angle of incidence α, analysis of spectral features shows that the OS band splits into two bands moving apart as α raises, see Figs. 7.12(a) and (b). Decomposing the spectra into two Gaussians, shifts of minima for the splitting bands can be roughly fitted by the Bragg law, $\lambda =$

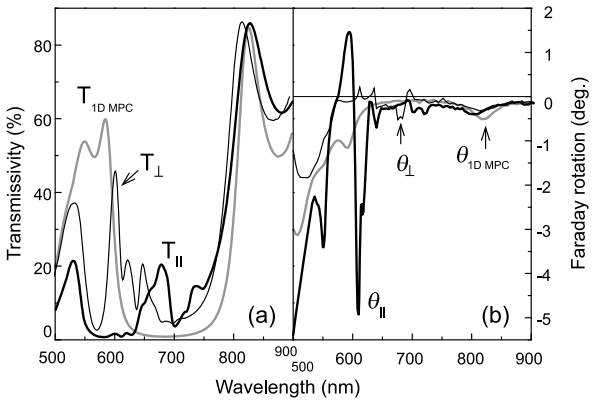

Fig. 7.11 (**a**) Polarization-resolved transmission and (**b**) Faraday rotation spectra of a Q-2D MPC at normal incidence. Spectrum of a 1D MPC with the same number of SiO_2/Bi:YIG bilayers (*gray line*) is shown for reference

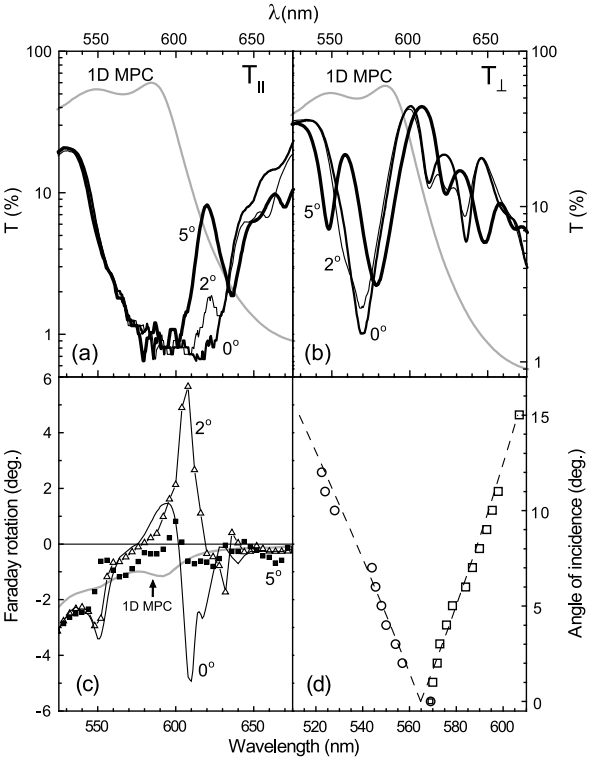

Fig. 7.12 Angle-resolved transmission spectra of the Q-2D MPC for $E_{\parallel}$- and $E_{\perp}$-polarized light; plots (**a**) and (**b**), respectively. (**c**) Angle-resolved Faraday rotation spectra for the $E_{\parallel}$ polarization. Incident angles α were 0°, 2° and 5°. *Gray lines* show spectra for the reference 1D MPC measured at normal incidence. (**d**) Angle-resolved split between the bands shown in plot (**b**); calculated Bragg wavelengths are shown by the *dashed line*

$2dn_{\mathrm{eff}}\cos(\gamma - \sin^{-1}(\sin\alpha/n_{\mathrm{eff}}))$ with due account of refraction, see Fig. 7.12(d). Here an effective refractive index (n_{eff}) of the Q-2D MPC, an angle (γ) between the Bragg diffraction plane and the sample basal plane, and also an interplanar distance (d) are the fitting parameters.

For the reference 1D MPC, the Borrmann-effect-related enhancement of Faraday rotation is seen at the band edges ($\lambda = 590$ and 825 nm); shown by a gray line in

Fig. 7.12(c) is the enhancement at the short-wavelength edge. Similarly, a significant enhancement of the rotation angle is seen in the $\theta_{\parallel}$ spectrum of the Q-2D MPC at $\lambda = 550$ nm, at the short-wavelength edge of the additional band. If compared with $\theta_{1D\ MPC}$, one order of magnitude larger rotation angle was observed for light with $\lambda = 610$ nm tunneling through the sample; transmissivity in this range is suppressed. Also, the polarization rotation rapidly changes in the range of 590–610 nm.

The observed features are attributed to the multiple Bragg diffraction, where light beams with a fixed wavelength simultaneously experience diffraction events from three diffraction planes. In this regime light should be maximally trapped inside the sample. And, as expected in accord with non-reciprocity of the Faraday effect, the polarization rotation should be accumulated. However, the $\theta_{\perp}$ spectrum illustrates that the Faraday rotation can be as well as suppressed, see Fig. 7.11(b). The processes contributing to the magneto-optical responses and the results of diffraction experiments are discussed in more detail in Ref. [61], showing a superprism effect accompanied with the demultiplexing phenomenon.

If the multiple Bragg diffraction is a key factor for altering polarization, detuning the overlap of the adjacent stop bands should bring a notable modification in the Faraday rotation spectra. We prove now this assumption. Figure 7.12(c) shows transmission and Faraday rotation spectra for normal and oblique incidence. Interestingly, a moderate change in α resulted in strong changes of spectra of Faraday rotation: $\theta_{\parallel}$ at $\alpha = 2^{\circ}$ is flipped with respect to $\theta_{\parallel}$ at $\alpha = 0$, and the rotation angle for $\alpha = 5^{\circ}$ did not exceed the rotation angle of the reference 1D MPC (gray line). Experiments showed that, at other angles of incidence except for $\alpha = 0$ and 2°, Faraday rotation spectra are similar to that measured at $\alpha = 5^{\circ}$. With due account taken of the sign of Faraday rotation, the mirror symmetry in the spectra and rotation degradation implies that the MO response is extremely sensitive to strength of each diffraction channel (one IS and two OS channels).

To conclude this section: multiple Bragg diffraction results in a significant enhancement of the MO response of Q-2D MPCs. Moreover, the enhancement is accompanied by the change of the polarization rotation direction in a narrow spectral range, where neighboring photonic stop bands overlap.

7.8 Three-Dimensional Magnetophotonic Crystals

Studies on fabrication and magneto-optical responses of 3D MPCs (Fig. 7.13) have been done mostly by use of the technology of artificial opals, where opals were 3D templates for magneto-optical materials [65–69]. Indeed, the lattice of direct opals—image (a)—with a continuous net of voids between close-packed spherical particles has been shown to be a unique, nanoscale container for various materials [image (c)] and also for inversion of the opal lattice [image (d)]. Moreover, opals have been used as building blocks of various complex structures; see image (b) and Refs. [58, 69].

To give an outlook on polarization transformation in photonic crystals, we first discuss polarized light coupling to an oriented opal sample. Opals have been shown

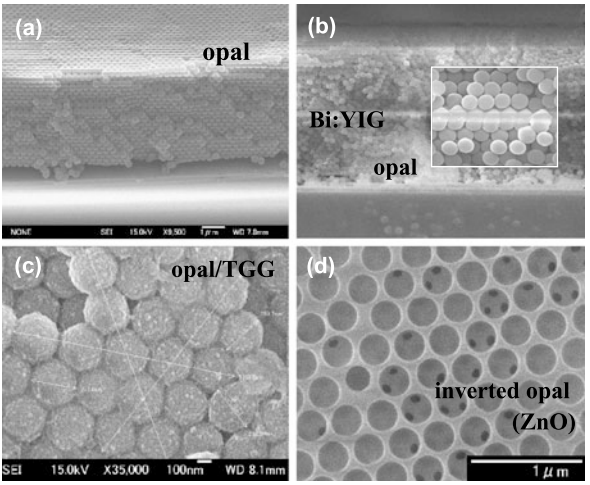

Fig. 7.13 Scanning microscope images of an opal thin film and opal-based 3D MPCs

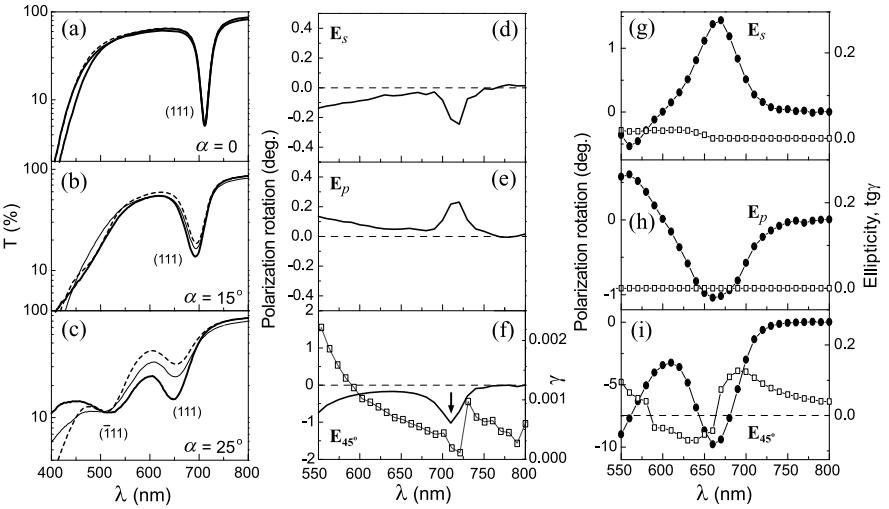

Fig. 7.14 Transmission spectra an opal sample made of SiO_2 spheres with a diameter of 315 ± 15 nm. (**a**)–(**c**) Transmittance measured at normal and oblique incidence for light with different polarizations ($\mathbf{E}_s$—*thick line*, $\mathbf{E}_p$—*dashed line* and $\mathbf{E}_{45^\circ}$—*thin line*). (**d**)–(**f**) Polarization direction alteration for $\mathbf{E}_s$, $\mathbf{E}_p$ and $\mathbf{E}_{45^\circ}$ polarizations at $\alpha = 0^\circ$. (**g**)–(**i**) same as in (**d**)–(**f**) for $\alpha = 25^\circ$

to be a unique model object for various studies on photonic crystals [5], and polarization-resolved spectra of opals are very instructive. Figure 7.14 illustrates the anisotropy of polarized light propagation together with polarization twisting in an opal sample. The sample was studied under the condition of a low dielectric contrast. These conditions were achieved by impregnating the sample—the space between spherical SiO_2 particles—with an immersion liquid. Here, for *s*, *p* and 45°

polarization directions and the angle of incidence on the (111) plane $\varphi = 0°$, 15°, 25°, one can see transmission spectra illustrating the spectral shifts of the stop bands arising from the Bragg diffraction form the {111} planes. Note that these bands have certain intensities, and detection of polarization states of attenuated waves is possible for all wavelengths from a range of the {111} stop bands.

Difference in the transmission shown in plot (a)–(c) can be coarsely understood in terms of the Fresnel theory and Brewster effect [70, 71]. Simply, apart from the Bragg diffraction, the intensity of a stop band depends on reflection coefficient at each interface in a photonic crystal. Plots (d)–(f) show that, for $\varphi = 0°$, the initial polarization directions ($\mathbf{E}_s$, $\mathbf{E}_p$ and $\mathbf{E}_{45°}$) of the incident beam are slightly altered as compared with that emerging from the sample, and the ellipticity of the transmitted wave is close to zero. However, the polarization rotation (and the ellipticity) increases as the angle of incidence is increased. The incident $\mathbf{E}_s$- and $\mathbf{E}_p$-polarized light gains an additional rotation of 1°, and the $\mathbf{E}_{45°}$-polarized light is rotated over 10° during propagation.

Why is the maximum optical rotation angle achieved for the polarization of $\mathbf{E}_{45°}$ at oblique incidence? Provided that the polarization direction for waves with linearly independent vectors $\mathbf{E}_s$ and $\mathbf{E}_p$ does not change considerably during their propagation in a crystal, it becomes obvious that considerable polarization rotation of the $\mathbf{E}_{45°}$ field appears due to the amplitude anisotropy of the orthogonal components $\mathbf{E}_{s:45°}$ and $\mathbf{E}_{p:45°}$ ($\mathbf{E}_{45°} = \mathbf{E}_{s:45°} + \mathbf{E}_{p:45°}$). This rotation is a change in the electric field orientation caused by a change in the vector sum of $\mathbf{E}_{s:45°} + \mathbf{E}_{p:45°}$ during the propagation. The phase anisotropy reveals itself in the spectra of ellipticity, showing maxima of ellipticity with the helicity of opposite sign at the (111) band edges. The validity of this model is confirmed by the fact that the ellipticity for modes corresponding to the minima of the (111) stop bands is zero; for more details see Ref. [72].

The optical properties of the opal sample discussed in Fig. 7.14 are certainly common for photonic crystals with 1D and 2D photonic crystals. In the case of MPCs, their magneto-optical activity may trigger the amplitude and phase anisotropy of light propagation. This anisotropy may contribute constructively or destructively to spectra of the Faraday rotation. In the general case, the initial linear polarization is transformed into a new state with an elliptical polarization.

Opal thin films fabricated by vertical deposition have been also used as constituent elements of MPCs, Fig. 7.13(b). Magneto-optical response of opal/Bi:YIG/opal heterostructures in the Faraday geometry at normal incidence on the (111) crystallographic plane is illustrated in Fig. 7.15; for details see Ref. [58]. Here a Faraday rotation (line 1) and transmission (line 2) spectra of the heterostructure are plotted together with a Faraday rotation spectrum of a reference single Bi:YIG film. One can see an enhancement of Faraday rotation up to $-0.30°$ for the transmission peak of 24 % at $\lambda = 567$ nm corresponding to light localization. This heterostructure is in principle analogous to 1D MPC discussed in Sect. 7.3. Unfortunately, the quality of the opal films (thickness homogeneity and limited thickness) leads to weakening and broadening of the peak associated with light localization. Also, it should be

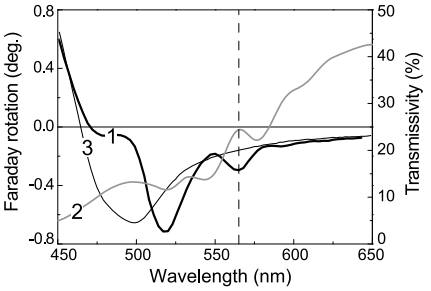

Fig. 7.15 Faraday rotation (*1*) and transmission (*2*) spectra of an opal/Bi:YIG/opal heterostructure. Spectra were measured at normal incidence. For reference, a Faraday rotation spectrum (*3*) of a Bi:YIG single film is presented. The *dashed line* shows the peaks associated with resonant propagation

noted that there was observed a dramatic variation of Faraday rotation of the heterostructure in the range of 480–520 nm. This is due to light coupling to the 2D hexagonal lattice of the patterned Bi:YIG layer shown in Fig. 7.9(a) [58, 60].

7.9 Applications of Magnetophotonic Crystals

High transmissivity and large Faraday rotation of 1D MPCs make them attractive for film-type optical isolators [10, 73] and gyrotropic waveguides (see Chap. 6) and switches [74], magnetic field [75] and refractive index sensing [76], and applications connected with modulation of light beam polarization: magneto-optical spatial light modulators (MOSLM), and a holographic data storage utilizing MOSLMs [77–79]. Interesting development for improving performance of all-garnet MPCs by erbium doping of garnets has been shown in [29, 80, 81]. These works demonstrate that the photo-luminescence of Er^{3+} atoms is intensive at room temperature and the Er^{3+}-doped MPCs provide an optical gain together with a large Faraday rotation.

Here we will confine the discussion only to a theoretical consideration and experimental data on of prototypes of reflection-type MOSLMs based on MPCs. Figures 7.16 and 7.17 show a principle of light modulation by MOSLMs [82–84] and a current-driven MOSLM chip together with a control board fabricated by FDK Company (Japan). First MOSLMs were based on liquid phase epitaxial thick garnet films with perpendicular magnetization. Their operation is done by current lines, and overheat caused by pixels' driving obstructs performances of the MOSLMs. This is why new approaches have been suggested where MPC-based MOSLMs is a promising solution [85–90].

Before discussion on MOSLMs it is worth mentioning about theoretical considerations of devices based on MPCs with 2D and 3D structures. One of such works deals with a 2D MPC-based three-port isolator/circulator [56] having a MO defect

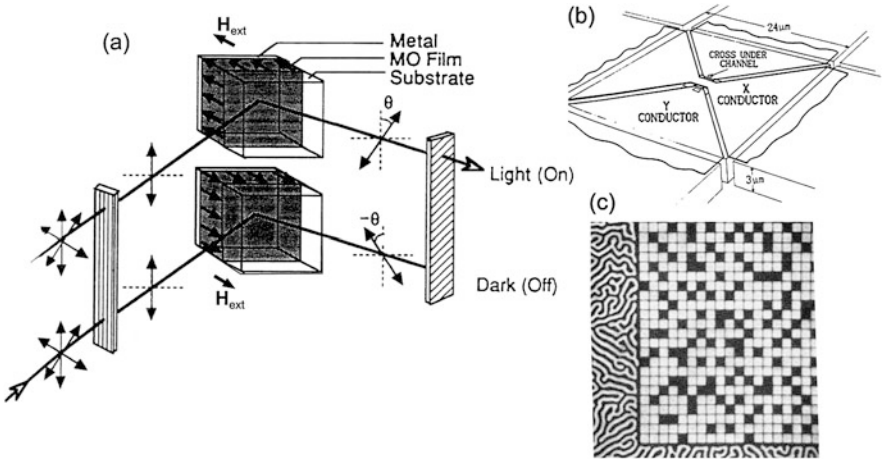

Fig. 7.16 (**a**) Magneto-optical spatial light modulator; device operation in reflection mode. (**b**) Pixel with driving, reflecting electrodes. (**c**) Micrograph of magnetic image of magnetized pixels. From Ref. [82] with modifications

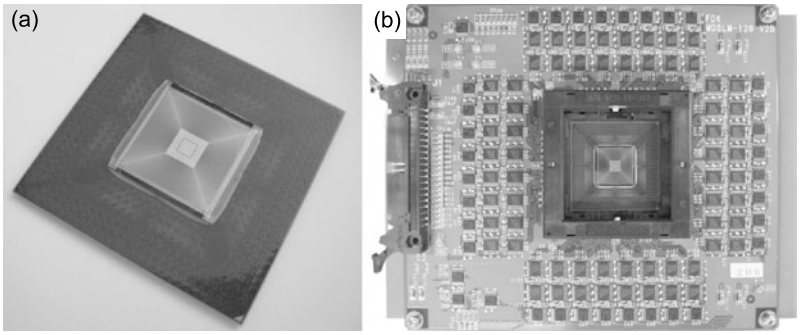

Fig. 7.17 (**a**) Magneto-optical spatial light modulator; device operation in reflection mode. (**b**) Pixel with driving, reflecting electrodes. (**c**) Micrograph of magnetic image of magnetized pixels

in the hexagonal lattice together with a complicated magnetization pattern. Isolation (circulation) in this circulator is due to an interference of counter rotating defect modes that are in-phase for one of the ports while out-of-phase for another one. These studies discuss an idealization, and an extension of the model investigation has been done in Ref. [57]. Analysis of a simplified Si/air/garnet 2D MPC circulator showed that a realistic model circulator has weaker responses.

Works devoted to a so-called magnetic superprism effect taking place in 2D MPCs have recently attracted attention [17, 18]. These works show that a large light deflection (superprism effect, known in non-magnetic 2D PCs [91, 92]) can be achieved by 2D and 3D MPC at application of the external magnetic field. Briefly, the principle of such a magnetic superprism is that the non-diagonal elements are

magnetic field dependent. Degenerated band gaps of non-magnetized crystals shift for left and right circularly polarized waves such that light flow in a particular direction in MPCs can be allowed or prohibited, where "prohibited" means strongly deflected.

Experimental 2D MPC discussed in Sect. 7.7 is noteworthy; it is a magnetic realization of the superprism exhibiting related effects together with a large alteration of the polarization plane. However, any deflection of light rays on magnetization has not been detected because of littleness of alteration of garnet permittivity and structural imperfection. A numerical analysis on magnetic superprism phenomenon by such Q-2D MPCs can be found in Ref. [93], where potentiality for light flow alteration due a scaled gyrotropy of magnetic constituents is discussed.

3D MPCs discussed in Sect. 7.8 have been in focus of experimental studies mainly discussing their synthesis and magnetic properties [14, 68, 94–96]. Fabricated representatives of 3D MPCs were mainly opal-based structures, and studies of non-magnetic opal photonic crystals dealing with their polarization-resolved spectra can be found in Refs. [70–72, 97–99].

There are various types of reusable modern SLMs with a 2D array of pixels, which have been intensively developed over the past three decades. Of these, MOSLMs have the advantages of a high switching speed, solid-state and robust device with high nonvolatility and radioactive resistance [82]. Unfortunately, however, the devices developed so far had a serious heat problem in their operations because large drive currents reaching 200 mA are needed to reverse the magnetization of a pixel.

Recent renewed interest in MOSLMs has resulted from the development of optical volumetric holographic recording [100], particularly, collinear holography [79]. Collinear holography utilizes SLM for both writing and retrieving processes, where a high speed SLM is essential for ensuring the high transfer rate. For such a purpose, MOSLM becomes very attractive due to its high operation speed. In fact, the pixel switching speed of approximately 15 ns was reported [82] in MOSLMs with LPE-grown magnetic garnet films. For such requirements, 1D MPCs are useful because they simultaneously exhibit considerably large MO response and high transmissivity for extremely thin Bi:YIG layers operated by a smaller magnetic field. To realize high-speed MOSLMs with at low power consumption, one of the possible solutions can be operation by multiferroic media [101], where the magnetization is controlled by a voltage applied to a piezoelectric subsystem of miltiferroic structures. In this respect, utilizing the concept of MPC with built-in electro-optical (EO) or piezoelectric constituents might be fruitful [89].

Theoretical analysis of responses of an electro-/magneto-optical SLM (e-MOSLM) prototype [89] shown in Fig. 7.18(a) has revealed that modulation of phase and polarization direction is possible, when controlling the EO constant of the PLZT layer and simultaneously keeping the magnetization of the Bi:YIG layer. For data under discussion in Fig. 7.18, this e-MOSLM prototype had a structure of AR coating/SGGG/$(Ta_2O_5/SiO_2)^9$/Bi:YIG/PLZT/$(SiO_2/Ta_2O_5)^{18}$. Optical constants of materials and structural parameters used for calculations can be found in Ref. [89]. Here we note only that the Bragg reflectors were the $\lambda/4$ multilayers, the

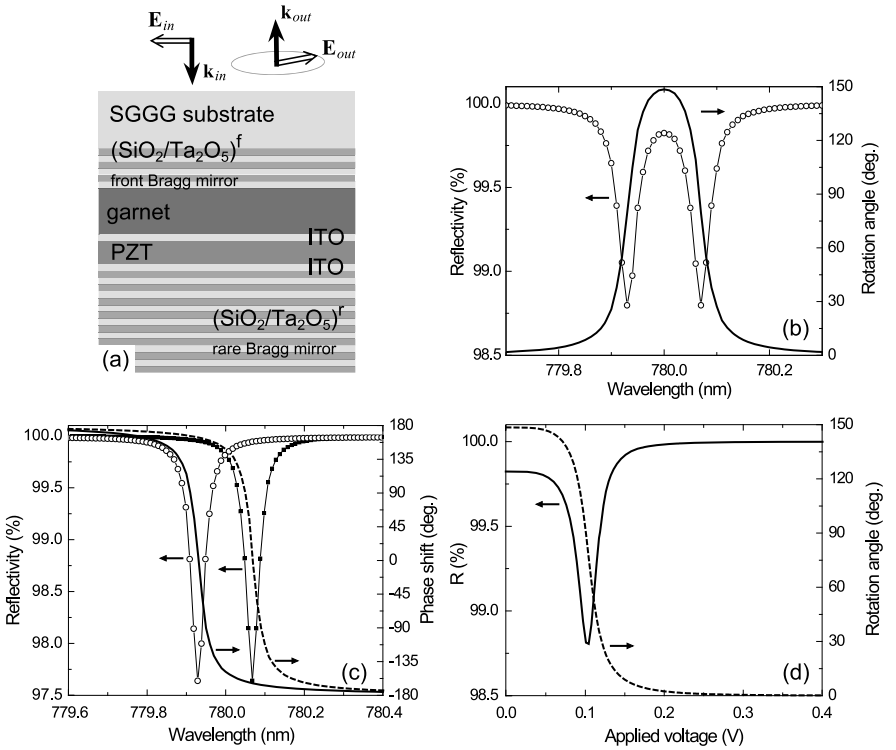

Fig. 7.18 (**a**) Prototype of e-MOSLM and geometry of analysis. (**b**) Reflection and polarization rotation spectra of the prototype. (**c**) Reflection spectra of the prototype and phase shifts accumulated during propagation for left- (*circles* and *solid line*) and right- (*squares* and *dashed line*) circularly polarized light. (**d**) Change in reflectivity and polarization direction; the magnetization of garnet is constant, and PLZT is subjected to the external electric field. Here, the rotation angle means an angle between the direction of the E-field of the emerging elliptically polarized wave and that of the incident linearly polarized wave

optical thickness of the EO layer (together with ITO electrodes) was $\lambda/2$ and that of the MO layer was 2λ.

Reflection spectrum of the prototype has a double peak in the vicinity of $\lambda = 780$ nm associated with the difference in the refractive indices for light with the eigen right- and left-circular polarizations, see Fig. 7.18(c). The maximum polarization rotation angle is seen at $\lambda = 780$ nm, which features the largest phase shift between the eigen modes rebuilding the linear polarization of light emerging from the sample. The performance of the prototype versus applied voltage is plotted in Fig. 7.18(d); the magnetization of the MO layer is assumed to be constant, and the refractive index changed is assumed to change with the voltage as in Ref. [102]. For the resonant wavelength, the polarization direction was shown to continuously decrease as the voltage increased. Importantly, when modulating the polarization direction, the intensity of reflected light is alternated insignificantly.

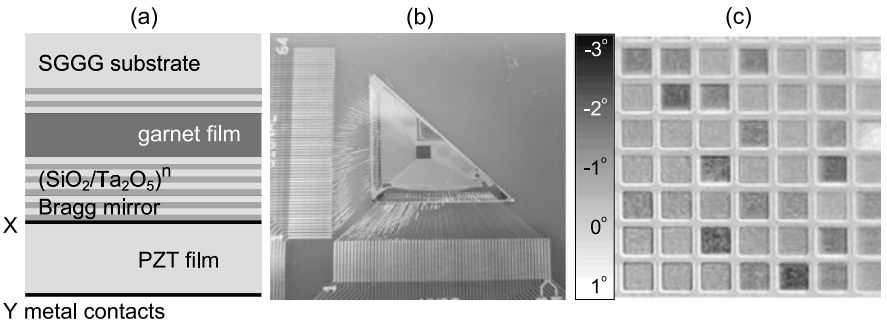

Fig. 7.19 (**a**) Structure of the working pixel of v-MOSLM, (**b**) a fabricated v-MOSLM, and (**c**) a polarization microscope image of the v-MOSLM's pixels at different running conditions

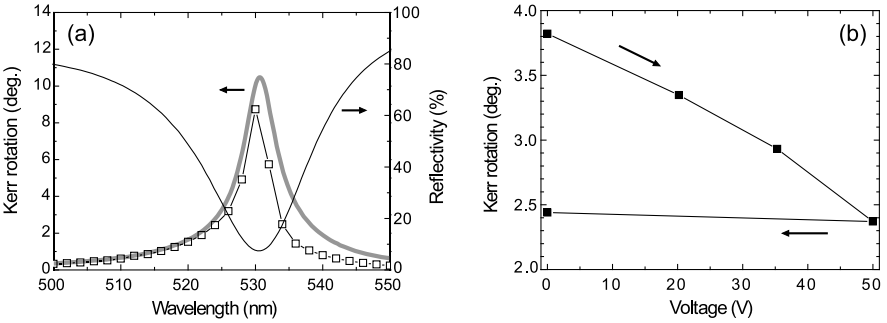

Fig. 7.20 (**a**) Optical responses of a working pixel of v-MOSLM (1D MPC prototype): reflectivity (*black line*), an experimental (*squares*) and calculated (*gray line*) angle of the Kerr rotation. (**b**) Kerr rotation versus applied voltage; *arrows* show field direction. The angle of light incidence is 7°

Another voltage-driven 1D MPC-based SLM (v-MOSLM) is shown in Fig. 7.19: (a) the structure of the working pixel, (b) a photograph of a fabricated v-MOSLM, and (c) a polarization microscope image of the v-MOSLM's pixels at different running conditions. The pixels had a multilayer structure of $(Ta_2O_5/SiO_2)^2$/BiDyAl:YIG/$(SiO_2/Ta_2O_5)^{5.5}$/PZT. Here, BiDyAl:YIG is poly-crystalline bismuth/dysprosium/aluminum-substituted yttrium iron garnet ($Bi_{1.3}Dy_{0.7}Y_{1.0}Fe_{3.1}Al_{1.9}O_{12}$). The magnetization direction of the BiDyAl:YIG layer (the polarization rotation of a pixel) is controlled continuously via inverse magnetostriction, when applying a voltage to the PZT actuator and hence a stress to BiDyAl:YIG [103].

Characteristics of the MPC shown in Fig. 7.19(a) are plotted in Fig. 7.20. Here a reflection peak together with the Kerr rotation spectrum illustrates excitation of the Fabri–Pérot resonance ($\lambda = 530$ nm) and the corresponding enhancement of the polarization rotation. Kerr rotation spectrum of the MPC has been measured at an angle of incidence of 7° in a saturating external magnetic field of 1 kOe. Performance of the MPC versus voltage (i.e. versus inverse magnetostriction) is shown in Fig. 7.20(b); the Kerr rotation for $\lambda = 530$ nm has been measured in a small bias

magnetic field of ≈600 Oe applied in the opposite direction to the magnetization direction of garnet. The angle of rotation continuously changed from 3.8° to 2.4° as the voltage increased; however, the response has not changed after switching-off voltage. This illustrates the complexity of magnetization of the BiDyAl:YIG layer in the reversing external bias field–the magnetization profile of BiDyAl:YIG films comprising small grains revealed that the magnetization reversal of each grain in the films happened independently [104].

7.10 Conclusion

Designing a microscopic distribution of fields inside the primitive cell of a PC allows tuning light interaction with PC constituents made of active materials and brings a significant change in their optical, magneto-optical, and other responses. In the chapter we have demonstrated that MPCs composed of sequences of magnetic and dielectric layers permit to enhance responses of known magneto-optical materials. *Light coupling to MPCs*, where the magneto-optical constituents are periodically arranged, built-in as a defect layers into a periodic structure, comprise structures supporting surface states or multiple Bragg diffraction, *results in a significant enhancement of the polarization rotation* and many other interesting non-reciprocal phenomena.

We have reviewed applications where magnetophotonic crystals are the key components. *Implementation of MPCs* to optical integrated devises *promises fast on-spin-relaxation*, multi-mode and multi-directional control of light flow by these miniature magnetic media.

Some additional aspects of studies on nano-magnetophotonic structures can also be found in Chap. 4.7 of Ref. [5] and Ref. [105].

Acknowledgements We greatly acknowledge all our colleagues who have analyzed, fabricated and characterized magnetophotonic crystals: Doctors A.B. Khanikaev, M.E. Dokukin, A.M. Merzlikin, K. Nishimura, R. Fujikawa, and A.V. Dorofeenko. The experiments and related publications would not be successful without activities and discussions provided by Professors H. Uchida, O.A. Aktsipetrov, A.B. Granovsky, A.A. Fedyanin, A.A. Lisyansky, A.P. Vinogradov, and K.H. Shin.

References

1. E. Yablonovitch, Phys. Rev. Lett. **58**, 2059 (1987)
2. S. John, Phys. Rev. Lett. **58**, 2486 (1987)
3. K. Sakoda, *Optical Properties of Photonic Crystals* (Springer, Berlin, 2001)
4. J.D. Joannopoulos, R. Meade, J. Winn, *Photonic Crystals* (Princeton University Press, New Jersey, 1995)
5. M.F. Limonov, R.M. De la Rue, *Optical Properties of Photonic Structures: Interplay of Order and Disorder* (SRC Press/Taylor and Francis Book, New York, 2012)
6. M. Inoue, T. Yamamoto, K. Isamoto, T. Fujii, J. Appl. Phys. **79**, 5988 (1996)

7. M. Inoue, T. Fujii, J. Appl. Phys. **81**, 5659 (1997)
8. M. Inoue, K.I. Arai, T. Fujii, M. Abe, J. Appl. Phys. **83**, 6768 (1998)
9. M.J. Steel, M. Levy, R.M. Osgood, IEEE Photonics Technol. Lett. **12**, 1171 (2000)
10. H. Kato, T. Matsushita, A. Takayama, M. Egawa, K. Nishimura, M. Inoue, J. Appl. Phys. **93**, 3906–3911 (2003)
11. I.L. Lyubchanskii, N.N. Dadoenkova, M.I. Lyubchanskii, E.A. Shapovalov, Th. Rasing, J. Phys. D, Appl. Phys. **36**, R277–R287 (2003)
12. A. Figotin, I. Vitebskiy, Phys. Rev. B **67**, 165210 (2003)
13. S. Kahl, A.M. Grishin, Appl. Phys. Lett. **84**, 1438 (2004)
14. A.V. Baryshev, T. Kodama, K. Nishimura, H. Uchida, M. Inoue, J. Appl. Phys. **95**, 7336 (2004)
15. O.A. Aktsipetrov, T.V. Dolgova, A.A. Fedyanin, R.V. Kapra, T.V. Murzina, K. Nishimura, H. Uchida, M. Inoue, Laser Phys. **14**, 685–691 (2004)
16. V.I. Belotelov, A.K. Zvezdin, J. Opt. Soc. Am. B **22**, 286–292 (2005)
17. A. Khanikaev, A. Baryshev, M. Inoue, A. Granovsky, A. Vinogradov, Phys. Rev. B **72**, 035123 (2005)
18. A.M. Merzlikin, A.P. Vinogradov, M. Inoue, A.B. Granovsky, Phys. Rev. E **72**, 046603 (2005)
19. M. Inoue, R. Fujikawa, A. Baryshev, A. Khanikaev, P.B. Lim, H. Uchida, O. Aktsipetrov, A. Fedyanin, T. Murzina, A. Granovsky, J. Phys. D, Appl. Phys. **39**, R151 (2006)
20. P.E. Wolf, G. Maret, Phys. Rev. Lett. **55**, 2696 (1985)
21. A.K. Zvezdin, V.A. Kotov, *Modern Magnetooptics and Magnetooptical Materials* (Taylor and Francis, New York, 1997)
22. A.B. Khanikaev, A.B. Baryshev, P.B. Lim, H. Uchida, M. Inoue, A.G. Zhdanov, A.A. Fedyanin, A.I. Maydykovskiy, O.A. Aktsipetrov, Phys. Rev. B **78**, 193102 (2008)
23. A.P. Vinogradov, Yu.E. Lozovik, A.M. Merzlikin, A.V. Dorofeenko, I. Vitebskiy, A. Figotin, A.B. Granovsky, A.A. Lisyansky, Phys. Rev. B **80**, 235106 (2009)
24. G. Borrmann, Phys. Z. **42**, 157 (1941)
25. A.B. Khanikaev, M. Inoue, A.B. Granovsky, J. Magn. Magn. Mater. **300**, 104 (2006)
26. R. Rosenberg, C.B. Rubinstein, D.R. Herriott, Appl. Opt. **3**, 1079–1083 (1964)
27. S.I. Khartsev, A.M. Grishin, Appl. Phys. Lett. **87**, 122504 (2005)
28. A.M. Grishin, S.I. Khartsev, H. Kawasaki, Appl. Phys. Lett. **90**, 191113 (2007)
29. S.I. Khartsev, A.M. Grishin, J. Appl. Phys. **101**, 053906 (2007)
30. T. Goto, A.V. Baryshev, K. Tobinaga, M. Inoue, J. Appl. Phys. **107**, 09A946 (2010)
31. Y. Haga, T. Goto, A.V. Baryshev, M. Inoue, J. Magn. Soc. Jpn. **36**, 54–57 (2012)
32. F. Villa, J.A. Gaspar-Armenta, Opt. Commun. **223**, 109 (2003)
33. A. Kavokin, I. Shelykh, G. Malpuech, Appl. Phys. Lett. **87**, 261105 (2005)
34. F. Villa, J.A. Gaspar-Armenta, Opt. Express **12**, 2338 (2004)
35. A.P. Vinogradov, A.V. Dorofeenko, S.G. Erokhin, M. Inoue, A.A. Lisyansky, A.M. Merzlikin, A.B. Granovsky, Phys. Rev. B **74**, 045128 (2006)
36. A.M. Merzlikin, A.P. Vinogradov, A.V. Dorofeenko, M. Inoue, M. Levy, A.B. Granovsky, Physica B **394**, 277 (2007)
37. N. Malkova, C.Z. Ning, Phys. Rev. B **76**, 045305 (2007)
38. M. Kaliteevskii, I. Iorsh, S. Brand, R.A. Abram, J.M. Chamberlain, A.V. Kavokin, I.A. Shelykh, Phys. Rev. B **76**, 165415 (2007)
39. T. Goto, A.V. Dorofeenko, A.M. Merzlikin, A.V. Baryshev, A.P. Vinogradov, M. Inoue, A.A. Lisyansky, A.B. Granovsky, Phys. Rev. Lett. **101**, 113902 (2008)
40. T. Goto, A.V. Baryshev, M. Inoue, A.V. Dorofeenko, A.M. Merzlikin, A.P. Vinogradov, A.A. Lisyansky, A.B. Granovsky, Phys. Rev. B **79**, 125103 (2009)
41. I.Y. Tamm, Phys. Z. Sowjetunion **1**, 733 (1932)
42. M.E. Sasin, R.P. Seisyan, M.A. Kaliteevski, S. Brand, R.A. Abram, J.M. Chamberlain, A.Yu. Egorov, A.P. Vasil'ev, V.S. Mikhrin, A.V. Kavokin, Appl. Phys. Lett. **92**, 251112 (2008)

43. C.R. Rosberg, D.N. Neshev, Y.V. Kartashov, R.A. Vicencio, W. Krolikowski, M.I. Molina, A. Mitchell, V.A. Vysloukh, L. Torner, Yu.S. Kivshar, Opt. Photonics News **17**, 29 (2006)
44. M. Abe, T. Suwa, J. Appl. Phys. **97**, 10M514 (2005)
45. S. Tomita, T. Kato, S. Tsunashima, S. Iwata, M. Fujii, S. Hayashi, Phys. Rev. Lett. **96**, 167402 (2006)
46. R. Fujikawa, A.V. Baryshev, J. Kim, H. Uchida, M. Inoue, J. Appl. Phys. **103**, 07D301 (2008)
47. Y. Mizutani, H. Uchida, Y. Masuda, A.V. Baryshev, M. Inoue, J. Magn. Soc. Jpn. **33**, 481 (2009)
48. H. Feil, C. Haas, Phys. Rev. Lett. **58**, 65 (1987)
49. V.E. Kochergin, A.Yu. Toporov, M. Valeiko, JETP Lett. **68**, 400 (1998)
50. V.I. Belotelov, L.L. Doskolovich, A.K. Zvezdin, Phys. Rev. Lett. **98**, 077401 (2007)
51. A.B. Khanikaev, A.V. Baryshev, A.A. Fedyanin, A.B. Granovsky, M. Inoue, Opt. Express **15**, 6612 (2007)
52. B. Sepúlveda, J.B. González-Díaz, A. García-Martín, L.M. Lechuga, G. Armelles, Phys. Rev. Lett. **104**, 147401 (2010)
53. A.V. Baryshev, K. Kawasaki, P.B. Lim, M. Inoue, Phys. Rev. B **85**, 205130 (2012)
54. M. Piliarik, J. Homola, Opt. Express **17**, 16506 (2009)
55. U. Fano, Phys. Rev. **124**, 1866 (1961)
56. Z. Wan, S. Fan, Appl. Phys. B **81**, 369 (2005)
57. K. Yayoi, K. Tobinaga, Y. Kaneko, A.V. Baryshev, M. Inoue, J. Appl. Phys. **109**, 07B750 (2011)
58. M.E. Dokukin, A.V. Baryshev, A.B. Khanikaev, M. Inoue, Opt. Express **17**, 9063 (2009)
59. S.M. Baek, M.E. Dokukin, K. Yayoi, J. Kim, H. Uchida, A.V. Baryshev, M. Inoue, J. Magn. Soc. Jpn. **33**(2), 489–492 (2009)
60. S.M. Baek, M. Dokukin, K. Yayoi, A. Baryshev, M. Inoue, J. Appl. Phys. **107**, 09A923 (2010)
61. S.M. Baek, A.V. Baryshev, M. Inoue, Appl. Phys. Lett. **98**, 101111 (2011)
62. S.M. Baek, A.V. Baryshev, M. Inoue, J. Appl. Phys. **109**, 07B701 (2011)
63. S. Kawakami, T. Kawashima, T. Sato, Appl. Phys. Lett. **74**, 463 (1999)
64. M. Renninger, Z. Phys. **106**, 141 (1937)
65. J. Galloro, M. Ginzburg, H. Miguez, S.M. Yang, N. Coombs, A. Safa-Sefat, J.E. Greedan, I. Manners, G.A. Ozin, Adv. Funct. Mater. **12**, 382–388 (2002)
66. C. Koerdt, G.L.J.A. Rikken, E.P. Petrov, Appl. Phys. Lett. **82**, 1538–1540 (2003)
67. A.V. Baryshev, T. Kodama, K. Nishimura, H. Uchida, M. Inoue, J. Appl. Phys. **95**, 7336 (2004)
68. A.V. Baryshev, T. Kodama, K. Nishimura, H. Uchida, M. Inoue, IEEE Trans. Magn. **40**, 2829 (2004)
69. R. Fujikawa, A.V. Baryshev, A.B. Khanikaev, H. Uchida, P.B. Lim, M. Inoue, IEEE Trans. Magn. **42**, 307 (2006)
70. A.V. Baryshev, A.B. Khanikaev, R. Fujikawa, H. Uchida, M. Inoue, Phys. Rev. B **76**, 014305 (2007)
71. A.V. Baryshev, A.B. Khanikaev, H. Uchida, M. Inoue, M.F. Limonov, Phys. Rev. B **73**, 033103 (2006)
72. A.V. Baryshev, M.E. Dokukin, A.M. Merzlikin, M. Inoue, J. Exp. Theor. Phys. **112**, 361–369 (2011)
73. H. Kato, T. Matsushita, A. Takayama, M. Egawa, K. Nishimura, M. Inoue, IEEE Trans. Magn. **38**, 3246–3248 (2002)
74. Z. Wu, M. Levy, V.J. Fratello, A.M. Merzlikin, Appl. Phys. Lett. **96**, 051125 (2010)
75. R. Fujikawa, K. Tanizaki, A.V. Baryshev, P.B. Lim, K.H. Shin, H. Uchida, M. Inoue, in *Proceedings of SPIE*, vol. 6369 (2006), p. 63690G
76. N.K. Dissanayake, M. Levy, A.A. Jalali, V.J. Fratello, Appl. Phys. Lett. **96**, 181105 (2010)
77. H.J. Park, J.K. Cho, K. Nishimura, M. Inoue, Jpn. J. Appl. Phys. **41**, 1813–1816 (2002)
78. M. Inoue, L. Hesselink, J. Magn. Soc. Jpn. **27**, 635–646 (2003)
79. H. Horimai, J. Li, in *Proceedings of SPIE*, vol. 5380 (2004), p. 297

80. A.M. Grishin, S.I. Khartsev, Appl. Phys. Lett. **95**, 102503 (2009)
81. A.M. Grishin, S.I. Khartsev, J. Phys., Conf. Ser. **352**, 012007 (2012)
82. J. Cho, S. Santhanam, T. Le, K. Mountfield, D.N. Lambeth, D. Stancil, W.E. Ross, J. Lucas, J. Appl. Phys. **76**, 1910 (1994)
83. J.-P. Krumme, H. Heitmann, D. Mateika, K. Witter, J. Appl. Phys. **48**, 366 (1977)
84. M.V. Loginov, V.V. Randoshkin, Yu.N. Sazhin, V.P. Klin, B.P. Nam, A.G. Solov'ev, Sov. Phys. Tech. Phys. **36**, 493 (1991)
85. J.-H. Park, H. Takagi, K. Nishimura, H. Uchida, M. Inoue, J.-H. Park, J.-K. Cho, J. Appl. Phys. **93**, 8525–8527 (2003)
86. H. Takagi, A. Tsuzuki, K. Iwasaki, Y. Suzuki, T. Imura, H. Umezawa, H. Uchida, K.H. Shin, M. Inoue, J. Magn. Soc. Jpn. **30**, 581–583 (2006)
87. K. Takahashi, H. Takagi, K.H. Shin, H. Uchida, P.B. Lim, M. Inoue, J. Appl. Phys. **101**, 09C523 (2007)
88. S. Mito, J. Kim, K.H. Chung, K. Yamada, T. Kato, H. Takagi, P.B. Lim, M. Inoue, J. Appl. Phys. **107**, 09A948 (2010)
89. T. Goto, H. Sato, H. Takagi, A.V. Baryshev, M. Inoue, J. Appl. Phys. **109**, 07B756 (2011)
90. S. Mito, H. Sakurai, H. Takagi, A.V. Baryshev, M. Inoue, J. Appl. Phys. **111**, 07A519 (2012)
91. T. Baba, M. Nakamura, IEEE J. Quantum Electron. **38**, 909 (2002)
92. H. Kosaka, T. Kawashima, A. Tomita, M. Notomi, T. Tamamura, T. Sato, S. Kawakami, Appl. Phys. Lett. **74**, 1370 (1999)
93. S. Baek, A.V. Baryshev, M. Inoue, J. Appl. Phys. **111**, 07E508 (2012)
94. T.V. Murzina, E.M. Kim, R.V. Kapra, I.V. Moshnina, O.A. Aktsipetrov, D.A. Kurdyukov, S.F. Kaplan, V.G. Golubev, M.A. Bader, G. Marowsky, Appl. Phys. Lett. **88**, 022501 (2006)
95. J. Sabataityte, I. Simkiene, G.-J. Babonas, A. Reza, M. Baran, R. Szymczak, R. Vaisnoras, L. Rasteniene, V. Golubev, D. Kurdyukov, Mater. Sci. Eng. C **27**, 985–989 (2007)
96. S.A. Grudinkin, S.F. Kaplan, N.F. Kartenko, D.A. Kurdyukov, V.G. Golubev, J. Phys. Chem. C **112**, 17855–17861 (2008)
97. J.F. Galisteo-Lopez, F. López-Tejeira, S. Rubio, C. López, J. Sánchez-Dehesa, Appl. Phys. Lett. **82**, 4068 (2003)
98. M.V. Rybin, A.V. Baryshev, M. Inoue, A.A. Kaplyanskii, V.A. Kosobukin, M.F. Limonov, A.K. Samusev, A.V. Sel'kin, Photonics Nanostruct. **4**, 146–154 (2006)
99. S.G. Romanov, Phys. Solid State **52**, 844–854 (2010)
100. H.J. Coufal, D. Psaltis, G.T. Sincerbox, *Holographic Data Storage*. Springer Series in Optical Sciences (Springer, Berlin, 2000)
101. S. Mito, J. Kim, K. Chung, H. Takagi, M. Inoue, IEICE Trans. Electron. **92-C**, 1487 (2009)
102. M. Gaidi, A. Amassian, M. Chaker, M. Kulishov, L. Martinu, Appl. Surf. Sci. **226**, 347 (2004)
103. S. Mito, H. Takagi, P.B. Lim, A.V. Baryshev, M. Inoue, J. Appl. Phys. **109**, 07E313 (2011)
104. S. Mito, J. Kim, K.H. Chung, K. Yamada, T. Kato, H. Takagi, P.B. Lim, M. Inoue, J. Appl. Phys. **107**, 09A948 (2010)
105. M. Inoue, A. Khanikaev, A. Baryshev, in *Nanoscale Magnetic Materials and Applications*, ed. by J.P. Liu, E. Fullerton, O. Gutfleisch, D.J. Sellmyer (Springer, Berlin, 2009), pp. 627–660

Chapter 8
Nonlinear Magneto-Optics in Magnetophotonic Crystals

Oleg A. Aktsipetrov, Andrey A. Fedyanin, Mitsuteru Inoue, Miguel Levy, and Tatyana V. Murzina

Abstract The chapter surveys the results on the investigation of the nonlinear magneto-optical properties of magnetophotonic crystals (MPC) and microcavities. The effects of the second- and third-harmonics generation as well as nonlinear magneto-optical Faraday and Kerr effects are reviewed. The main magnetic material used in the MPC structures, which determines the magneto-optical activity of the magnetophotonic structures, is yttrium–iron garnet (YIG), which appears as a continuous layer in 1D MPC, microcavity layer in magnetophotonic microcavities or YIG nanoparticles incorporated in artificial opal structure. We demonstrate that many-fold amplification of the nonlinear magneto-optical effects is attained within the spectral edge of the photonic band gap and within the microcavity mode as compared to linear magneto-optical analogs. Strong light localization as well as the realization of the phase matching conditions are discussed as possible mechanisms of the observed enhancement of the nonlinear magneto-optical effects.

8.1 Introduction: Nonlinear Optics and Magneto-Optics in Photonic Band-Gap Materials

Magnetic photonic band-gap materials that are spatially periodic structures composed (at least partially) of magnetic materials, are a subject of high interest due to their unique optical and magneto-optical properties absent for bulk materials of

O.A. Aktsipetrov · A.A. Fedyanin (✉) · T.V. Murzina
Faculty of Physics, M.V. Lomonosov Moscow State University, Moscow 119991, Russia
e-mail: fedyanin@nanolab.phys.msu.ru

T.V. Murzina (✉)
e-mail: murzina@mail.ru

M. Inoue
Department of Electrical and Electronic Information Engineering, Toyohashi University of Technology, Toyohashi, Aichi 441-8580, Japan

M. Levy
Physics Department, Michigan Technological University, Houghton, MI 49931, USA

M. Inoue et al. (eds.), *Magnetophotonics*, Springer Series in Materials Science 178,
DOI 10.1007/978-3-642-35509-7_8,

the same composition. These properties originate from the modification of the optical spectra of magnetophotonic crystals (MPC) that leads to the appearance of the photonic band gap and/or magnetophotonic microcavity (MMC) mode and to the corresponding strong changes in the light localization and dispersion. These effects, in turn, can modify drastically the spectral efficiency of optical and nonlinear optical processes.

In this chapter we mostly review the results of our recent studies of optical second- and third harmonics generation in garnet-based one-dimensional MPC and MMC, as well as in YIG-substituted artificial opals. In what follows we will demonstrate that such structures reveal many-fold amplification of the linear magneto-optical Faraday and Kerr effects as well as the second- and third-order nonlinear optical and magnetization-induced effects. These properties are very attractive for magnetic-field operation over the light flow in such structures, including that based on the nonlinear optical effects. In the latter case, in spite of a relative complicity of the nonlinear optical technique, enormously large values of the nonlinear magneto-optical effects (i.e. magnetization-induced rotation of the polarization plane or changes in the harmonics' phase and intensity) can be of practical interest as they combine high nonlinearity, photonic band gap (PBG) and magnetic properties of magnetophotonic crystals.

In order to increase an intrinsically weak efficiency of the nonlinear optical processes of the materials that constitute photonic crystals (PC), the following approach can be realized in case of MPC, namely, the possibility to fulfill the phase matching conditions in spatially periodic media. This phenomenon was pointed out by N. Bloembergen [1, 2]. As it is well known, for the case of second-harmonic generation (SHG) the phase matching conditions that provide the maximal efficiency of this nonlinear process can be written as $k_{2\omega} = 2k_{\omega} + \Delta_2 k$, where k_{ω} and $k_{2\omega}$ are the fundamental and SHG wave vectors and $\Delta_2 k$ is the phase mismatch that appears due to the dispersion of PC constituting materials. Similar conditions for the case of third-harmonic generation (THG) looks like $k_{3\omega} = 3k_{\omega} + \Delta_3 k$. In real anisotropic crystals the phase mismatch Δk can be compensated by the differences in the phase velocities of *o* and *e* waves of the corresponding wavelength. On the contrary, the condition $\Delta k = 0$ in a PC can be realized for the pump and harmonics waves of the same polarizations due to the modification of the PC dispersion in the spectral vicinity of the PBG edge. In that case the phase mismatch at the fundamental and harmonics wavelength can be compensated due to the appearance of the reciprocal lattice vector, $\mathbf{G}$, so that $\Delta_2 k = k_{2\omega} - 2k_{\omega} + \mathbf{G} = 0$. Such an enhancement of the nonlinear optical effects in non-magnetic PC was observed in a number of papers [3–5].

One more mechanism of the enhancement of the nonlinear optical effects is attributed to a strong spatial light localization in PBG structures—photonic crystals and photonic microcavities. In the latter case a many-fold enhancement of the local optical field resonant with the microcavity mode is attained due to the multiple interference and multipass character of light propagation within the MC layer. For the case of PC structures, an increase of the local density of states is realized because of the Bloch nature of the electromagnetic waves in PC. The mentioned above effects

of the amplification of the local optical fields in spatially periodic structures were realized in the reviewed works for the case of magnetophotonic structures so that a significant amplification of the nonlinear-optical magnetic effects were observed [33–36].

8.2 Nonlinear Magneto-Optics: Background

Nonlinear optics describes the interaction of intense light with a matter when the efficiency of the nonlinear-optical effects (harmonics generation, self-action of light, optical rectification and Kerr effect, CARS and many others) is a nonlinear function of the fundamental beam intensity. The variety of nonlinear optical phenomena is enlarged further in the case of magnetic structures, where additional symmetry operations can lead to the appearance of new effects in the nonlinear-optical response.

In centrosymmetric materials the magnetization vector does not break the inversion symmetry due to its axial nature. Thus even-order nonlinear-optical effects (like optical second harmonic generation), including nonlinear magneto-optical ones (like magnetization-induced SHG (MSGH)), require the lack of the inversion symmetry within the electric-dipole approximation. On the contrary, magnetization-induced effects in third-harmonic generation (MTHG) can be observed in materials of any symmetry. The electromagnetic fields at the double and triple frequencies of the fundamental radiation are induced by the quadratic and cubic nonlinear polarizations, $\mathbf{P}^{(2)}(2\omega)$ and $\mathbf{P}^{(3)}(3\omega)$, which are written (in the electric-dipole approximation) as follows:

$$\mathbf{P}^{(2)}(2\omega) = \chi^{(2)}(\mathbf{M}) : \mathbf{E}_\omega \mathbf{E}_\omega, \tag{8.1}$$

$$\mathbf{P}^{(3)}(3\omega) = \chi^{(3)}(\mathbf{M}) \vdots \mathbf{E}_\omega \mathbf{E}_\omega \mathbf{E}_\omega, \tag{8.2}$$

where $\mathbf{E}_\omega$ is the fundamental field amplitude, $\chi^{(2)}$ and $\chi^{(3)}$ are the quadratic and cubic electric-dipole susceptibility tensors of a magnetic material (i.e. garnets in our case) that forms the MPC and MMC structures. Hereafter the influence of the domain walls is neglected since all the presented effects in MSHG and MTHG are observed using saturating *dc*-magnetic fields providing a single-domain state of magnetic garnet films. The dependence of $\chi^{(2)}$ and $\chi^{(3)}$ tensors on the magnetization vector $\mathbf{M}$ can be written as a sum of three terms:

$$\chi^{(2)}(\mathbf{M}) = \chi^{(2,0)} + \chi^{(2,1)} \cdot \mathbf{M} + \chi^{(2,2)} : \mathbf{MM}, \tag{8.3}$$

$$\chi^{(3)}(\mathbf{M}) = \chi^{(3,0)} + \chi^{(3,1)} \cdot \mathbf{M} + \chi^{(3,2)} : \mathbf{MM}. \tag{8.4}$$

The tensors $\chi^{(2,0)}$ and $\chi^{(3,0)}$ describe the non-magnetic (crystallographic) contributions to $\chi^{(2)}$ and $\chi^{(3)}$, respectively, while the axial tensors (or pseudotensors) $\chi^{(2,1)}$ and $\chi^{(3,1)}$ induce the MSHG and MTHG contributions in $\mathbf{P}^{(2)}(2\omega)$ and $\mathbf{P}^{(3)}(3\omega)$, which are odd in the magnetization. The tensors $\chi^{(2,2)}$ and $\chi^{(3,2)}$ are responsible for the MSHG and MTHG terms that are even in $\mathbf{M}$. Non-zero tensor elements can be found when using the invariance of the susceptibility tensors under the symmetry operations valid for a particular point symmetry group of a material. Here we

necessarily have to take into account different transformation matrices for the polar and axial frames.

Yttrium–iron garnet possesses the inversion symmetry, however, thin garnet films, both epitaxial and polycrystalline, are often noncentrosymmetric. Lowering of the symmetry of initially centrosymmetric garnet lattice was concluded by observation of the magnetoelectrical effect linear in the electric field, which requires the medium with the broken inversion symmetry [11]. The lattice deformation and the variation of the lattice parameters of the polycrystalline yttrium-garnet films due to the formation of oxygen vacancies is directly obtained from X-ray diffraction analysis [12]. Numerous SHG studies in magnetic garnet films also allow breaking the YIG inversion symmetry. For example, enhancement of quadratic susceptibility of Bi-substituted YIG (Bi:YIG) films films in comparison with undoped YIG film was directly observed in reflected [13] and transmitted [14] SHG. Temperature variations of the SHG response are observed in Bi-doped garnet films grown on gadolinium-gallium garnet substrates [15, 16]. The thickness dependence of the SHG intensity from Bi:YIG films is reported in Ref. [17].

The inversion symmetry of thin Bi:YIG films is lifted since the film plane becomes mirror plane no more. Such a growth-induced film anisotropy is more likely attributed to the local distortion of the garnet cell by bismuth atoms and their ordering on nonequivalent crystallographic sites during the film growth [15]. Another source of an enhanced quadratic susceptibility of Bi:YIG films is proposed to be the lattice misfit strain in the deformed garnet layer near the substrate [12, 18] forming a polar axis along the film normal. Both mechanisms can be responsible for the inversion symmetry breaking in Bi:YIG layers in the studied MPCs and MMCs. As the garnet films used are heavily doped by bismuth atoms (one Bi atom per two Y atoms), thus large distortions in the dodecahedral rare-earth-ions sublattice of the garnet crystal cell are expected. Polar axis along the Bi:YIG film normal can be also yielded by the film sputtering on the fused quartz substrate or amorphous silicon dioxide layers and the subsequent high temperature annealing of the Bi:YIG layer with two nonequivalent, garnet–air and garnet–silicon dioxide, interfaces. Meanwhile, the description of microscopic mechanisms of the inversion symmetry breaking in Bi:YIG films remains incomplete.

We use a macroscopic description of the electric-dipole SHG sources in garnet films, which deals with appropriate symmetry elements related to the whole garnet film. Bi:YIG films are treated as layers possessing ∞m symmetry group with mirror planes perpendicular to the film plane. We will consider a Cartesian frame $\mathbf{e}_x, \mathbf{e}_y, \mathbf{e}_z$ with the xy plane perpendicular to the symmetry planes m_z so that the xy plane is the film surface and the xz plane denotes the plane of incidence. The non-zero elements of the $\chi^{(2,1)}$ and $\chi^{(3,1)}$ tensors describing the magnetization-induced quadratic and cubic polarizations, $P_i^{(2),M} = \chi_{ijkL}^{(2,1)} E_j^{\omega} E_k^{\omega} M_L$ and $P_i^{(3),M} = \chi_{ijklN}^{(3,1)} E_j^{\omega} E_k^{\omega} E_l^{\omega} M_N$, are shown in Table 8.1. For comparison, the non-zero elements of the $\chi^{(2,0)}$ and $\chi^{(3,0)}$ tensors that define the non-magnetic component of the quadratic and cubic polarizations, $P_i^{(2),NM} = \chi_{ijk}^{(2,0)} E_j^{\omega} E_k^{\omega}$ and $P_i^{(3),NM} =$

Table 8.1 Non-zero elements of $\chi^{(2,1)}_{ijkL}$, $\chi^{(3,1)}_{ijklN}$, $\chi^{(2,0)}_{ijk}$, and $\chi^{(3,0)}_{ijkl}$ tensors for the ∞m symmetry group divided into the magnetization vector components (columns) and polarization combinations of the fundamental and harmonic waves (rows). M_X, M_Y and M_Z relate to the longitudinal, transversal and polar nonlinear magneto-optical Kerr effect (NOMOKE) configurations. $\times 1$ denotes the columns containing non-magnetic SHG and THG contributions. m indicates the mixed polarization of the fundamental radiation, which is 45°-rotated relative to the s and p-polarizations. Last two rows contain the non-zero tensor elements, which contribute in polarization combinations with m-polarization only

	THG				SHG			
	$\times M_X$	$\times M_Y$	$\times M_Z$	$\times 1$	$\times M_X$	$\times M_Y$	$\times M_Z$	$\times 1$
$s \to s$	0	0	0	χ_{yyyy}	χ_{yyyX}	0	0	0
$s \to p$	χ_{zyyyX}	0	χ_{xyyyZ}	0	0	χ_{xyyY}	0	χ_{zyy}
$p \to s$	χ_{yxxzX}, χ_{yzzzX}	0	χ_{yxzzZ}, χ_{yxxxZ}	0	χ_{yxxX}, χ_{yzzX}	0	χ_{yxzZ}	0
$p \to p$	0	χ_{zxzzY}, χ_{xxxzY}, χ_{zxxxY}, χ_{xzzzY}	0	χ_{zzzz}, χ_{xxxx}, χ_{zxxz}, χ_{xxzz}	0	χ_{xxxY}, χ_{xzzY}, χ_{zxzY}	0	χ_{zzz}, χ_{xzx}, χ_{zxx}
$m \to s$	χ_{yyyzX}	χ_{yxyzY}	χ_{yxyyZ}	χ_{yxxy}, χ_{yyzz}	0	χ_{yxyY}	0	χ_{yzy}
$m \to p$	χ_{zxxyX}, χ_{xyzzX}, χ_{xxyzX}	χ_{zxyyY}, χ_{xyyzY}	χ_{xyzzZ}, χ_{xxxyZ}	χ_{xxyy}, χ_{zyyz}	χ_{zyzX}, χ_{xyxX}	0	χ_{xyzZ}	0

$\chi^{(3,0)}_{ijkl} E^{\omega}_j E^{\omega}_k E^{\omega}_l$, are presented as well. The tensor elements are divided into different columns in accordance with the magnetization direction and combinations of polarization of the fundamental and harmonics' waves.

In transparent materials, the elements $\chi^{(2,0)}$ and $\chi^{(3,0)}$ tensor elements are real values, while $\chi^{(2,1)}$ and $\chi^{(3,1)}$ tensor components are imaginary. Interference between non-magnetic and magnetization-induced components of the second harmonic (SH) and third harmonic (TH) fields which leads to the observation of odd in the magnetization effects in the SHG and THG intensity, requires absorption. This is the case of Bi:YIG films, which reveal the absorption band above 500–550 nm depending on the Bi content [19]. Bi:YIG films transparency in the red and IR regions allows the high contrast multiple interference of the fundamental radiation resulting in pronounced photonic band gap effects and fundamental field localization at the microcavity mode.

One more but equivalent approach for the description of nonlinear magneto-optical effects is based on another form of phenomenological description of the magnetization-induced nonlinear-optical susceptibility tensor. The general expression for the nonlinear polarization is as written in (8.1), while the second- and third-order susceptibility tensors are divided into odd and even in **M** parts,

$$\chi^{(2)}(\mathbf{M}) = \chi^{(2)\text{even}}(\mathbf{M}) \pm \chi^{(2)\text{odd}}(\pm\mathbf{M}), \tag{8.5}$$

$$\chi^{(3)}(\mathbf{M}) = \chi^{(3)\text{even}}(\mathbf{M}) \pm \chi^{(3)\text{odd}}(\pm\mathbf{M}), \tag{8.6}$$

where even in **M** susceptibility components include both the crystallographic and even (quadratic) in magnetization effects. Such a description was first developed in

Ref. [7] for the surfaces of a cubic crystal of different crystallographic orientations. Such formulas do not require to justify the expansion of the nonlinear polarization in powers of **M** and to estimate the corresponding small parameter.

It should be noted that non-zero tensor elements summarized in Table 8.1 or in more detail in Ref. [7] reveal the symmetry of magnetization-induced nonlinear-optical response of the surface of an isotropic or cubic medium, which can be applied to the case of iron-garnet layers. At the same time, in case of MPC or MMC the propagation effects of the fundamental and SHG waves within the YIG layers determine the SHG efficiency and should be considered when analyzing the values of the magnetization-induced SHG effects.

It stems from Table 8.1 that depending on the geometry of the application of the dc-magnetic field, magnetization-induced rotation of the SHG polarization plane (polar and longitudinal NOMOKE), or intensity and phase (transversal NOMOKE) changes of the harmonics' waves can be observed, similarly to the linear magneto-optics. At the same time, there is a difference in the values of the linear- and nonlinear magneto-optical effects (NOMOKE). In the latter case the intensity and polarization effects for typical ferromagnetic metals or dielectrics exceed magneto-optical analogs by one-two orders of magnitude, which was shown both theoretically and experimentally [6–10].

The wave equation for the fundamental, second and third harmonics can be written as

$$\mathbf{E}(j\omega) + \frac{\varepsilon(j\omega)}{c^2}\frac{d^2}{dt^2}\mathbf{E}^j(j\omega) = -\frac{1}{\varepsilon_0 c^2}\frac{d^2}{dt^2}\mathbf{P}^{(2,3)}\delta_{(2,3)j} \tag{8.7}$$

where $j = 1, 2, 3$, $\varepsilon(j\omega)$ is the dielectric function at the corresponding frequency, and second- and third-order nonlinear polarizations are the source terms. In the linear case (8.7) is homogeneous, and left- and right-circularly polarized waves are its eigen solutions. Magneto-optical effects are governed in that case by the non-diagonal components of $\varepsilon(\omega)$, or by the complex refractive indices for the circular waves $n_\pm$. For the harmonics' generation not only the $n_\pm$ at the SHG and THG wavelengths rule out the magnetic field induced effects, but $\chi^{(2,3)\mathrm{odd}}(\mathbf{M})$ as well, which are present in the right-hand part of (8.7) and that are comparable in value with the even in magnetization terms, $\chi^{(2,3)\mathrm{even}}$. This additional magnetic-field induced material susceptibility is mostly responsible for large values of NOMOKE.

In what follows we will mostly describe the transversal NOMOKE, i.e. magnetic-field induced changes in the SHG(THG) intensity. As a measure of this effect the SHG(THG) magnetic contrast is introduced as

$$\rho_{2\omega,3\omega} = \frac{I_{2\omega,3\omega}(+) - I_{2\omega,3\omega}(-)}{I_{2\omega,3\omega}(+) + I_{2\omega,3\omega}(-)}, \tag{8.8}$$

where the signs + and − denote the direction of the transversal *dc*-magnetic field. Taking into account that the susceptibility terms $\chi^{(2,3)\mathrm{even}}$ and $\chi^{(2,3)\mathrm{odd}}(\mathbf{M})$ are the sources of the corresponding SHG(THG) fields $\mathbf{E}(2\omega, 3\omega)$, the total field at the second- and third-harmonics wavelengths is expressed by the vector sum

$$I(2\omega, 3\omega) = \left|\mathbf{E}^{\mathrm{even}}(2\omega, 3\omega) \pm \mathbf{E}^{\mathrm{odd}}(2\omega, 3\omega)\right|^2, \tag{8.9}$$

Thus in the assumption of a small value of odd in **M** component of the SHG (THG) fields one can obtain the expression for the magnetic contrast

$$\varrho_{2\omega,3\omega} \approx 2\frac{E^{\text{odd}}(2\omega,3\omega)}{E^{\text{even}}(2\omega,3\omega)}\cos\varphi, \tag{8.10}$$

where φ is the phase shift between E^{odd} and E^{even}. Thus both the relative value $E^{\text{odd}}(2\omega,3\omega)/E^{\text{even}}(2\omega,3\omega)$ as well as φ determine the magnetic contrast that is measured experimentally. The latter quantity can be estimated experimentally from the SHG(THG) interferometry measurements.

8.3 Samples and Set-Ups

Magnetophotonic microcavities are formed from two dielectric Bragg reflectors and a ferrimagnetic cavity spacer. Reflectors consist of five pairs of alternating quarter-wavelength-thick SiO_2 and Ta_2O_5 layers. The cavity spacer is a Bi-substituted yttrium–iron-garnet layer, $Bi_{1.0}Y_2Fe_5O_x$. The spacer optical thickness is a half of wavelength. MMCs are grown on a glass substrate by the RF sputtering of corresponding targets in Ar^+ atmosphere with the sputtering pressure of 6 mTorr. Before fabrication of the top Bragg reflector, the sample is annealed in air at 700 °C for 20 minutes for the residual oxidation and crystallization of the Bi:YIG spacer. The MMC samples have $\lambda_{\text{MC}} \simeq 900$ nm and $\lambda_{\text{MC}} \simeq 1115$ nm that correspond to the Bi:YIG spacer thickness of approximately 195 nm and 245 nm, respectively. Hereafter λ_{MC} denotes the spectral position of the microcavity mode at normal incidence and determine the optical thickness of layers in MMC. For magnetophotonic crystals λ_{MC} is replaced by λ_{PC} which is related to the PBG center of the MPC at normal incidence.

The fabrication procedure [20] of 1D magnetophotonic crystals consists of successive rf-sputtering of SiO_2 and Bi:YIG from the corresponding targets in Ar^+ atmosphere with the residual pressure of 6 mTorr onto a 2.5 mm thick fused quartz substrate. The latter was initially optically polished with residual roughness below 5 nm to increase the interface quality of the MPC layers. Substrate temperature is kept at 140 °C at all sputtering stages to avoid the temperature-induced drift of the sputtering rate. After evaporation of each successive garnet layer, the MPC is removed from the sputtering machine and annealed in air at 700 °C for 20 minutes. The oxygen access during annealing is necessary for oxidation and crystallization of initially amorphous garnet films that are responsible for the ferrimagnetic state of MPC constituting garnet films.

Cleavage of MMCs and MPCs is studied using field-emission scanning electron microscope (FESEM). The FESEM images are shown in Fig. 8.1. Abrupt interfaces between magnetic garnet and dielectric layers as well as a reproducible layer thickness in all repeats can be seen. The layer-by-layer thickness deviation is estimated to be below 2 percents. The SiO_2 layers of the thickness of $d_1 \simeq (134 \pm 5)$ nm alternate the Bi:YIG layers of $d_2 \simeq (87 \pm 3)$ nm thick. The layers' thickness is kept constant

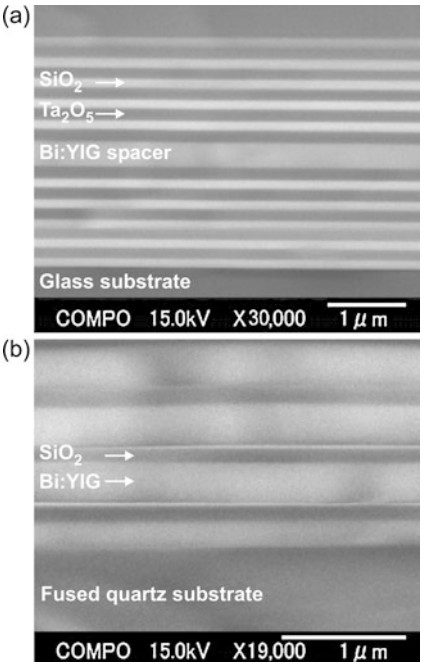

Fig. 8.1 The FESEM images of the MMC (*upper panel*) and MPC (*lower panel*) cleavages

along the sample with the lateral corrugation in thickness being below 5 nm/μm. The atomic-force microscope (AFM) image of surface of the uppermost garnet layer of MPC showed that Bi:YIG layers are formed from columnar microcrystals with the lateral size ranging from 1 to 2 μm. The surface roughness is estimated to be approximately 2 nm everywhere at the garnet microcrystallite surface but at the boundaries where it is increased up to 5 nm.

Small gradual increase of the upper garnet layers thickness in MPCs is apparently associated with different shrinkage of garnet films during annealing and changes in sputtering rate due to the change of substrate temperature during sputtering. Hysteresis loops measured in vibrating sample magnetometer are shown in Fig. 8.2 and demonstrate that the coercivity of MPCs and MMCs is approximately 30 Oe for the longitudinal magnetic field. Saturating field which is slightly above 100 Oe indicates that the easy-magnetization axis is aligned along the Bi:YIG surfaces as expected for thin ferromagnetic films.

Spectroscopy of microcavities and one-dimensional photonic crystals implies the tuning the wave-vector component k_z parallel to the periodicity direction. Two configurations of the nonlinear spectroscopy are used in the study. In the first one, the fundamental radiation wavelength λ_ω is tuned at the fixed angle of incidence θ and is named below as spectroscopy in the frequency domain. The output of a nanosecond OPO laser system tunable from 720 nm to 1000 nm is used as the fundamental radiation. The laser energy is approximately 10 mJ per pulse, pulse width is below 2 ns and the laser spot area is below 0.5 mm^2.

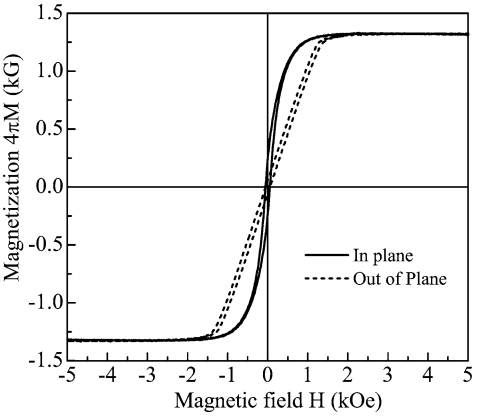

Fig. 8.2 Magnetization curve of a 1D-MPC

The case of the fixed fundamental radiation and tuning angle of incidence is named angular spectroscopy, or spectroscopy in the wave-vector domain. In that case, the output of a nanosecond YAG laser at the wavelength of 1064 nm is used. The energy of the fundamental beam is below 10 mJ per pulse, pulse width is approximately 15 ns and the laser spot area is about 1.0 mm^2. The radiation at the SH or TH wavelength is selected by an appropriate set of filters and detected by a photomultiplier tube. The SH intensity spectrum acquired in the frequency domain is normalized over the spectral sensitivity of the detection system and the tuning OPO curve using a SH intensity reference channel operating with a wedged z-cut quartz plate and with the detection system identical to the one in the sample channel.

The saturating *dc*-magnetic field of the strength up to 2 kOe providing the single-domain state is applied to the samples for the longitudinal and transversal NOMOKE, or along the normal to the samples for the polar NOMOKE using permanent FeNdB magnets. The schematic view of the experimental laser set-up along with the SHG interferometry scheme are shown in Fig. 8.3.

8.4 Optical and Magneto-Optical Spectra of Magnetophotonic Crystals and Microcavities

8.4.1 Faraday Effect Enhancement Induced by Multiple Interference

Figure 8.4 shows the transmission spectrum of MMC with $\lambda_{MC} \simeq 900$ nm. Low transmission is observed in the spectral region from 750 to 1000 nm, where the transmittance is decreased down to 10^{-3}. This corresponds to the photonic band gap of the structure. The PBG spectral width and the value of attenuation in the PBG are determined by the number of repeats and the refractive index difference in the SiO_2/Ta_2O_5 Bragg reflectors. A peak in the transmittance spectrum observed at

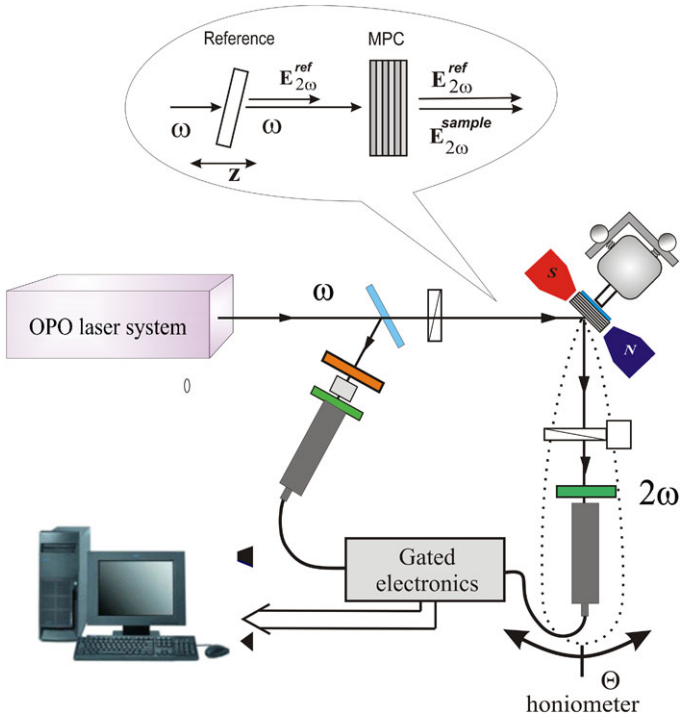

Fig. 8.3 Scheme of the experimental set-up for the SHG spectroscopy in magnetophotonic structures. Callout in the figure: the scheme of the SHG interferometry

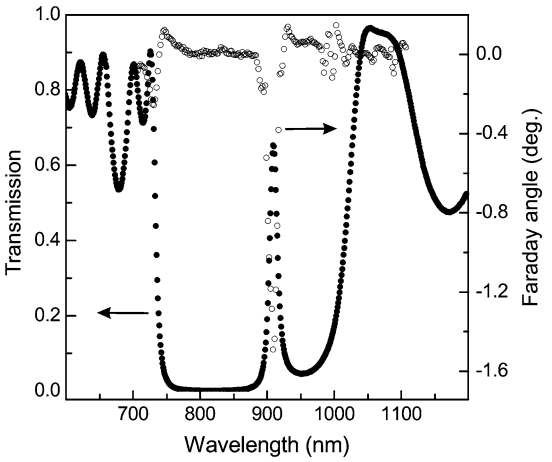

Fig. 8.4 Spectra of transmittance (*filled circles*, *left scale*) and the Faraday rotation angle (*open circles*, *right scale*) of the MMC with $\lambda_{MC} \simeq 900$ nm measured at normal incidence

910 nm is attributed to the microcavity mode. The quality factor of MMC is $Q_\omega = \lambda_0/\Delta\lambda_0 \simeq 75$ where λ_0 is the resonant wavelength and $\Delta\lambda_0$ is the full width at half-magnitude. The spectrum of the Faraday rotation angle θ_F measured in crossed

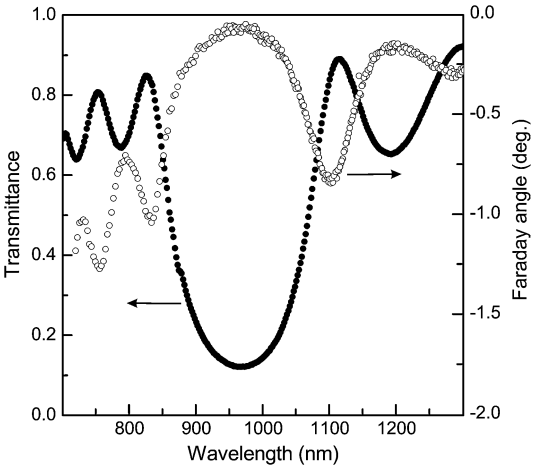

Fig. 8.5 Spectra of transmittance (*filled circles*, *left scale*) and the Faraday rotation angle (*open circles*, *right scale*) of the MPC measured at normal incidence

Glan-prizm polarizer and analyzer is also shown in Fig. 8.4. The θ_F spectrum has a peak at the MMC mode, where θ_F is enhanced up to $-1.5°$. It corresponds to an effective value of $-7.7°/\mu m$, which is approximately 50 times larger than the Faraday rotation angle for a single Bi:YIG film of the same thickness deposited directly on the substrate and measured at this wavelength.

Optical transmission spectrum of MPC is shown in Fig. 8.5. The spectral region from 850 to 1100 nm with a small transmittance indicates the existence of photonic band gap. The smallest transmittance value is reached at $\lambda_\omega \simeq 965$ nm and is approximately 0.10. Outside the PBG, optical spectrum demonstrates the interference fringes, where transmittance is increased up to 0.9. θ_F is enhanced up to $-0.8°$ at the long-wavelength edge of PBG at 1100 nm. It corresponds to an effective value of $-0.75°/\mu m$, which is approximately 8 times larger than the Faraday rotation angle for the single Bi:YIG film at this wavelength. For the wavelengths tuned inside the PBG, Faraday rotation is strongly suppressed. The spectral position of the peaks of θ_F at 750 nm and 830 nm correlate with the transmission spectrum maxima and ride on the monotonous θ_F increase with the wavelength decrease associated with the Faraday rotation spectrum of Bi:YIG.

The four-by-four matrix technique is utilized for the Faraday effect calculation. The optical field inside each layer is given as a sum of four normal modes: right and left circular polarized waves for both propagation directions. Then a set of four-by-four matrices is calculated: each matrix corresponds to each layer of the structure and determines the values of optical field on the layer boundaries. Multiplying all the matrices one can obtain the matrix characterizing reflectance and transmittance of the whole structure. Among the reflection and transmittance, Faraday angle and spatial optical field distribution in the structure are calculated. The same approach can be also applied for calculating the transversal Kerr effect spectra in 1D-MPCs [21].

For the calculation, the considered model of MMC consists of two Bragg reflectors and a magnetic Bi:YIG MC layer squeezed between them. Each Bragg reflector has five pairs of alternating $\lambda/4$-thick magnetic Bi:YIG and non-magnetic SiO_2 lay-

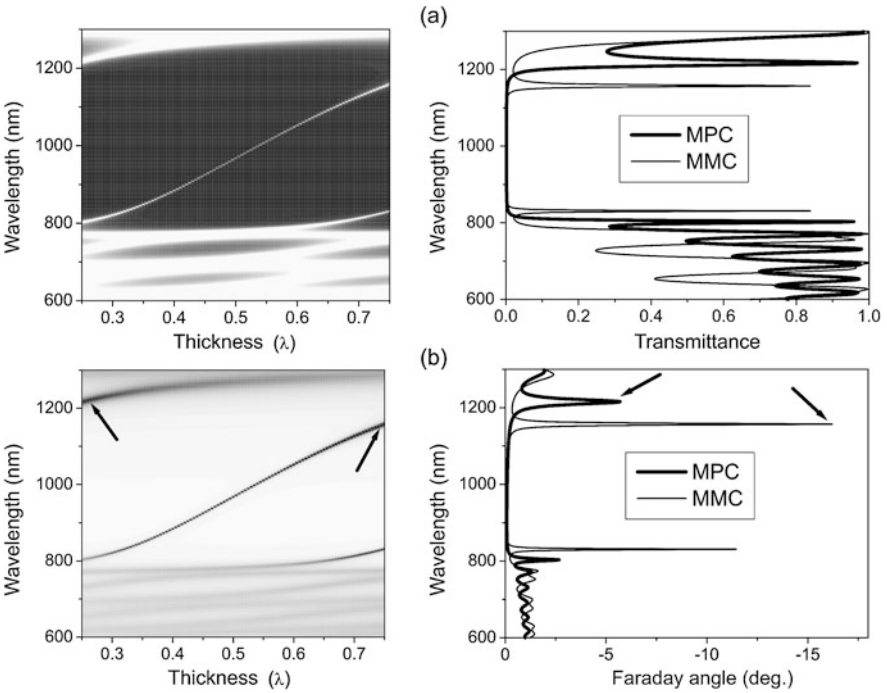

Fig. 8.6 Set of optical (**a**) and magneto-optical (**b**) spectra vs. thickness of the MMC cavity spacer. Transmittance and Faraday angle are shown by gray scale on the patterned plot. *Right plots* show the optical (**a**) and magneto-optical (**b**) spectra for MPC and $3\lambda/4$-MMC structures

ers. The refractive indices are supposed to be $n_{\mathrm{Bi:YIG}} = 2.6$ and $n_{\mathrm{SiO_2}} = 1.45$. The gyration vector is assumed to be $g_{\mathrm{Bi:YIG}} = 0.0054$ which is close to the experimental values. Optical thickness of the cavity spacer, Λ, is varied from $\lambda/4$ to $3\lambda/4$. The $\lambda/2$-thick cavity spacer corresponds to the MMC with the microcavity mode centered at the wavelength λ that coincides with the PBG center. The $\lambda/4$-thick spacer corresponds to the MPC with no microcavity mode. For $\Lambda = 3\lambda/4$, the microcavity mode is almost degenerated into a long-wavelength PBG edge, such a structure is called $3\lambda/4$-MMC. The transmittance (a) and Faraday angle (b) spectral dependences as functions of the spacer thickness are shown in Fig. 8.6 in the patterned plot. Right plots in Fig. 8.6 represent optical (a) and magneto-optical (b) spectra for MPC and $3\lambda/4$-MMC, labeled MPC and MMC, respectively.

White areas in the patterned plot in Fig. 8.6(a) correspond to the transmittance maxima. Black area in the patterned plot in Fig. 8.6(a) for the wavelengths from 800 to 1200 nm corresponds to the PBG, white curve across the PBG shows the thickness dependence of the microcavity mode, white areas at the PBG edges reveal the transmittance maxima. White area in the patterned plot in Fig. 8.6(b) shows a strong suppression of the Faraday effect at the wavelengths corresponding to the PBG. It can be seen that the Faraday angle θ_{F} is enhanced drastically at the microcavity mode. For $\Lambda = \lambda/4$ and $\Lambda = 3\lambda/4$, θ_{F} is enhanced at the PBG edges, especially at

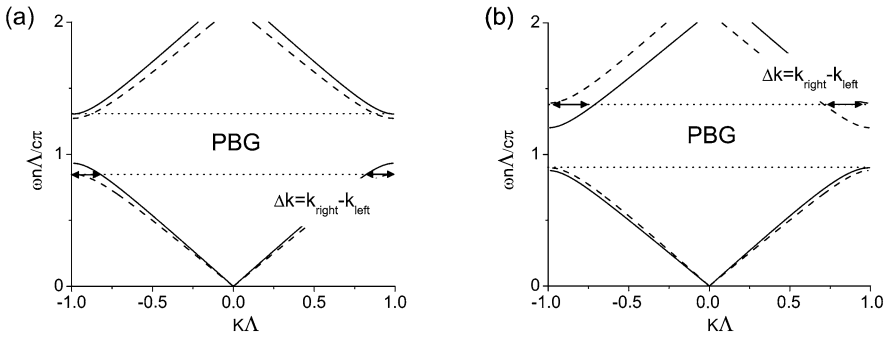

Fig. 8.7 (**a**) Band structures of 1D MPC for $\omega(\mathbf{k}_L)$ (*solid line*) and $\omega(\mathbf{k}_R)$ (*dashed line*) calculated for normal incidence at the 1D MPC consisted of layers of non-magnetic material with dielectric constant of $\varepsilon_1 = 2.1$ and magnetic one with diagonal component of dielectric constant of $\varepsilon_2 = 5.6$. (**b**) The same for $\varepsilon_1 = 5.6$ and $\varepsilon_2 = 2.1$

the long-wavelength one at 1200 and 1150 nm, respectively, as is indicated in the figure by black arrows.

The spectral positions of the Faraday rotation maxima are correlated with the transmittance maxima. The calculations show the absence of the ellipticity of the transmitted light polarization at the maximum of θ_F. It means that MPC and $3\lambda/4$-MMC give an opportunity to rotate efficiently the polarization plane without distortion and weakening the transmitted light. The θ_F enhancement in the $3\lambda/4$-MMC is nearly 3 times higher than the same in the MPC and reaches the values up to $-16°$ at the wavelength of 1150 nm corresponding to the long-wavelength PBG-edge.

8.4.2 Nonlinear Verdet Law in Magnetophotonic Crystals

The Faraday effect originates from different phase velocities for the right- and left-circular polarized waves traveling inside a magnetic medium. Taking into consideration the band structure of a photonic crystal, this approach can be extended on the Faraday effect in multilayered photonic structures. Figure 8.7 shows the dispersion relations $\omega(\mathbf{k}_L)$ and $\omega(\mathbf{k}_R)$ calculated for the left- and right-circularly polarized (RCP and LCP) optical waves propagating in MPC formed from a stack of magnetic and non-magnetic quarter-wavelength-thick layers. The main differences of dispersion properties for the normal modes and consequently for Faraday rotation are achieved at the photonic-band-gap edges. In the case of magnetic layers with higher refractive index, which corresponds to the experimental materials, Faraday effect is predicted at the long-wavelength PBG edge (Fig. 8.7(a)). In the opposite case (magnetic layers possess lower refractive index) short wavelength PBG edge exhibits an enhancement of the Faraday effect (Fig. 8.7(b)) [23].

It is worth mentioning that the difference in the dispersion properties and phase velocities of LCP and RCP waves in photonic crystals is accompanied by flattening

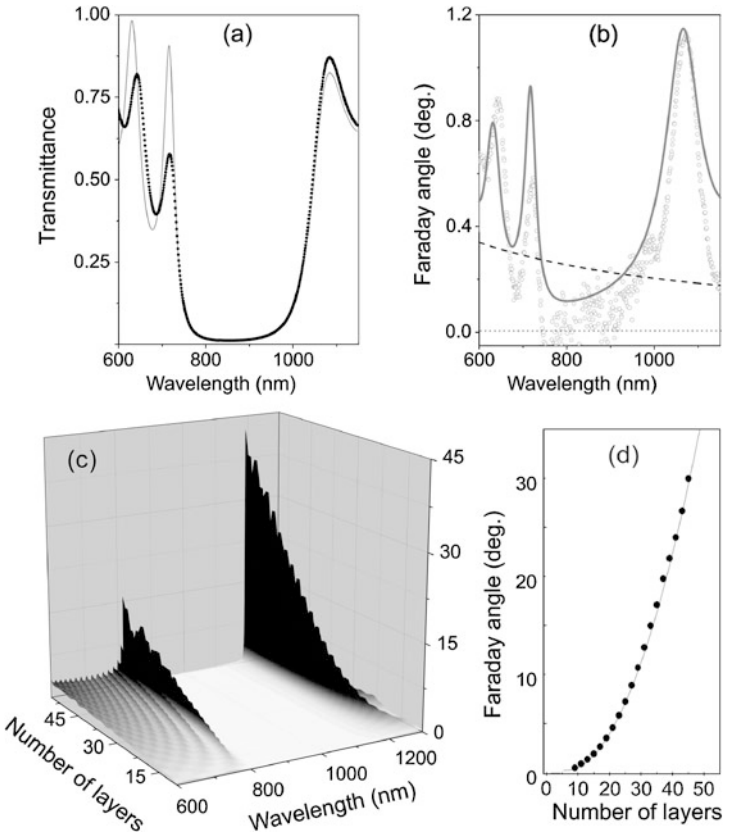

Fig. 8.8 (**a**) The transmission spectrum of 1D MPC upon normal incidence (*filled circles*) and its numerical approximation (*gray curve*). (**b**) Faraday rotation angle spectrum (*open circles*) and its numerical approximation (*gray curve*), dashed curve is the interference-subtracted spectrum of Faraday angle in homogeneous Bi:YIG slab of the same thickness. (**c**) Set of θ_F spectral dependencies vs. number of layers of MPC (3D plot) (numerical results). (**d**) Maximum θ_F vs. number of layers of MPC: calculated data and nonlinear fit

of the dispersion curves, resulting in the decrease of the group velocity of a wave packet traveling through the photonic crystal. It is equal to the localization of the electromagnetic field in different layers of MPC. A strong point lies in the fact that the difference in the phase velocities at different PBG edges is correlated with the optical field localization in magnetic and non-magnetic layers, correspondingly [22, 23].

Optical and magneto-optical spectra of 1D MPC are shown in Figs. 8.8(a) and (b). The spectral region from 725 to 1025 nm (where the transmission is strongly suppressed) corresponds to the photonic band gap of MPC. The Faraday rotation angle is also decreasing in this spectral region. Outside the PBG the transmission of the MPC increases and shows interference fringes. The Faraday rotation angle θ_F also oscillates with the spectrum having a local maxima at 640 and 720 nm, which cor-

relates well with the local transmission maxima. In can be seen that the largest enhancement of θ_F is observed near 1070 nm that coincides with the long-wavelength PBG edge.

The spectrum of the Faraday angle for a uniform slab of Bi:YIG with the thickness of 520 nm corresponding to the total Bi:YIG thickness in MPC is calculated using the known spectra of the diagonal and off-diagonal components of the complex dielectric function tensor of Bi:YIG with the same Bi concentration [19]. The θ_F enhancement coefficient at the long-wavelength PBG edge reaches the value of 6.5 in comparison with a homogeneous Bi:YIG slab, while θ_F increase at the short-wavelength PBG edge appears to be 1.9 and 2.7 at the certain interference fringes.

Both experimental spectra are fitted simultaneously using the four-by-four matrix technique with the spectral dependence of the refractive indices and absorption coefficients taken into account [19]. Particular applications of the 4×4 matrix formalism for 1D MPC are discussed in detail in Refs. [24, 25]. Briefly, transmission and polarization transformation of linearly polarized waves upon the propagation through 1D MPC is governed by a set of transfer matrices $\mathbf{M}_{ij}$ and Φ_j, accounting the boundary conditions for the complex amplitudes of the left- and right-circular polarized waves at the interface between ith and jth layers and their propagation through particular jth layer, respectively. Therefore, the field $\mathbf{E}_{N+1}$ outgoing from the 1D photonic crystal consisted of N layers is expressed for every wavelength λ as a result of tensorial multiplication of the incoming field $\mathbf{E}_0$ on series of transfer matrices:

$$\mathbf{E}_{N+1} = \mathbf{M}_{N+1,N}\Phi_N \cdots \mathbf{M}_{2,1}\Phi_1\mathbf{M}_{1,0}\mathbf{E}_0. \tag{8.11}$$

Vector-columns $\mathbf{E}_{N+1}$ and $\mathbf{E}_0$ are formed by a set of complex amplitudes $\mathbf{E}$ of normal modes, i.e. right- and left-circular polarized waves (indices r and l, respectively):

$$\mathbf{E}_0 = (1, r_r, 1, r_l)^T, \qquad \mathbf{E}_{N+1} = (t_r, 0, t_l, 0)^T, \tag{8.12}$$

where $r_{r,l}$ and $t_{r,l}$ are the amplitudes of the transmission and reflection coefficients for the two circular polarizations, which can be obtained by solution of a corresponding set of four algebraic equations. Optical properties of MPC are fully derived from $r_{r,l}$ and $t_{r,l}$; for example, the Faraday rotation angle is given by

$$\theta_F = \mathrm{Im}\left[\arctan\left(\frac{t_r - t_l}{t_r + t_l}\right)\right], \tag{8.13}$$

while the real part of this expression characterizes the ellipticity η of transmitted light. In this way, reflection and transmission coefficients are given by

$$R = \left(|r_r + r_l|^2 + |r_r - r_l|^2\right)/4, \tag{8.14}$$

$$T = \left(|t_r + t_l|^2 + |t_r - t_l|^2\right)/4. \tag{8.15}$$

The enhancement is predicted and experimentally observed at the wavelength tuned at the long-wavelength PBG edge at 1060 nm. The Faraday effect is 6.5 times enhanced in comparison with single Bi:YIG layer with the thickness equal to the total thickness of the magnetic material in MPC. Experimental results are

in good agreement with theoretical calculations. The correlation of θ_F and transmittance maxima opens up prospects for practical application of MPC in various magneto-optical devices as it gives an opportunity to rotate polarization plane without neither distortion nor weakening transmitted light. The calculations also show that ellipticity of the transmitted light η achieves a minimum at the maximum of θ_F.

An increase of the number of layers in MPC, N, leads to a better field localization in MPC combined with the total magnetic material thickness increase. Such combination is expected to result into specific thickness dependence $\theta_F(N)$. Figure 8.8(c) shows a 3D-plot of thickness and spectral dependence $\theta_F(\lambda, N)$. Faraday angle maxima are achieved at both PBG edges. However, for considered experimental situation as magnetic layers have larger refractive index, θ_F enhancement at the long-wavelength PBG edge is significantly larger than that at the short-wavelength edge and shows a *nonlinear* dependence $\theta_F(N)$ of maximum values achieved at the wavelength tuned at the PBG edge (Fig. 8.8(d)). It can be interpreted as Verdet rule violation. As has been mentioned above for the uniform media $\theta_F(D) \sim D$, where D is magnetic material thickness. However, in the case of multilayered structure this rule is broken, MPC exhibits *nonlinear* $\theta_F(D) \sim D^2$ dependence. In conclusion combination of spatial optical field distribution with difference in phase velocities of RCP in LCP is shown to be responsible for nonlinear dependence of $\theta_F(D) \sim D^2$.

Spectral dependences of spatial optical field distribution in the sample for the $\lambda/4$-MPC (a) and the $3\lambda/4$-MMC (b) are given in Fig. 8.9. In the case of the $\lambda/4$-MPC, the field is localized in all magnetic layers at the long-wavelength PBG edge at approximately 1200 nm and the field amplitude in the central layer is 2.7 times higher than that of the incident light. The $3\lambda/4$-MMC provides the better field localization in all magnetic layers in comparison with the $\lambda/4$-MPC, the field amplitude in the microcavity spacer at the wavelength of 1150 nm is almost two times higher than that in the $\lambda/4$-MPC sample. The field localization in magnetic layers indicates the constructive interference resulted in the Faraday effect enhancement and vividly explains the Θ_F enhancement at the PBG edge of $\lambda/4$-MPC and $3\lambda/4$-MMC.

The increase of number of layers in MPC leads to the enhancement of Faraday rotation at the PBG edge by the combined effect of field localization and the increase of magnetic material thickness. The enhancement up to $\theta_F = 45°$ is expected in $3\lambda/4$-MMC consisting of about 20 pairs of layers. Therefore, Faraday rotation angle in the finite MPCs appears to be a nonlinear function of the total thickness of magnetic material in the stack that can be interpreted as the nonlinear Verdet law. Relation between the enhancement of the Faraday rotation and localization of optical field in magnetic layers is treated as a Borrmann-type effect. This relation shows that the Faraday rotation can be considered as a measure of the density of photonic states trapped within Bi:YIG layers [22, 23].

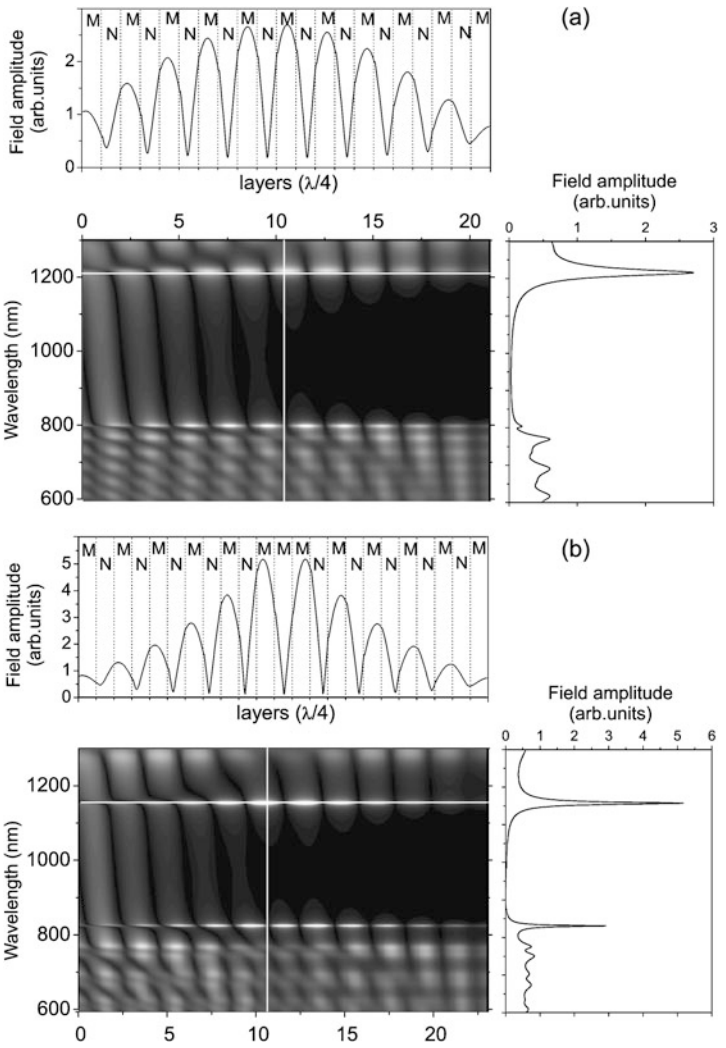

Fig. 8.9 Spectral dependence of spatial optical field distribution in $\lambda/4$-MPC (**a**) and $3\lambda/4$-MMC (**b**). Field amplitude is shown by gray scale on the patterned plot. White color corresponds to the maxima of the field amplitude. *Upper* and *right plots* at each panel represent spatial field distribution at the PBG edge and its spectrum in the central layer taken at cross sections marked by *white lines*. Magnetic layers are labeled M and non-magnetic layers N

8.5 MSHG and MTHG in Magnetophotonic Microcavities and Magnetophotonic Crystals

In this section, the results of the nonlinear magneto-optical Kerr effect in magnetic microcavities formed from dielectric Bragg reflectors and a magnetic garnet spacer are discussed [26, 28–30, 35, 36]. Magnetization-induced variation of the

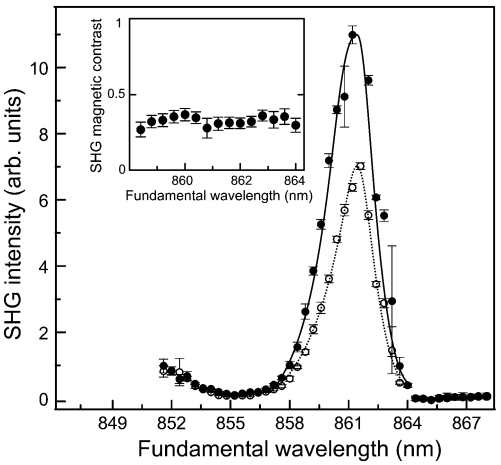

Fig. 8.10 Transversal NOMOKE in SHG measured in the *p*-in, *p*-out polarization combination for opposite directions of magnetic field, solid, and open circles, respectively. *Inset*: the spectrum of the SHG magnetic contrast in the vicinity of the microcavity mode

SH intensity, rotation of the SH wave polarization, and the shift of the relative SH phase are observed at the wavelength (angular) resonance of the fundamental radiation with the microcavity mode. The symmetry properties of quadratic susceptibility (pseudo)tensors allow the clear separation of the magneto-optical effects. Namely, magnetization-induced changes in the SH intensity and relative phase are observed in the transversal configuration, while the SH wave polarization rotation is obtained in the longitudinal and polar configurations. Then, the mechanisms of magnetization-induced variations in SH intensity in MPCs consisted of the stack of Bi:YIG layers are discussed in terms of local field enhancement phase-matching fulfillment [36]. Finally, the MTHG studies in magnetophotonic microcavities are reviewed [36].

8.5.1 Transversal NOMOKE in MSHG: Intensity and Phase Effects

Intensity effects in MSHG are demonstrated in Fig. 8.10 where the spectral dependence of the SH intensity measured in the MMC with $\lambda_{MC} \simeq 900$ nm is shown [26, 36]. Dc-magnetic field is applied in the transversal configuration, i.e. $\mathbf{M} = (0, M_Y, 0)$.

The SH intensity is enhanced as the fundamental wave is tuned across the microcavity mode. The ratio of the intensities for the opposite directions of the magnetic field is almost two. Spectral dependence of the magnetic contrast in the SH intensity, $\rho = (I_+ - I_-)/(I_+ + I_-)$, where $+$ and $-$ denote the directions of the field, is shown in the inset of Fig. 8.10. ρ reached values of 0.3 and appears to be independent of spectrum. The inverting the magnetic-field direction varies only the SH intensity and no spectral shifts of SHG resonances are observed.

Another experimental configuration is angular spectroscopy. Figure 8.11 shows the SH intensity as a function of the angle of incidence measured in the MMC with

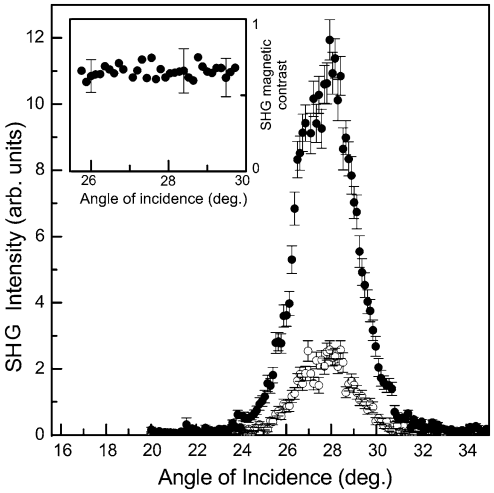

Fig. 8.11 Transversal NOMOKE in SHG measured in the p-in, p-out polarization combination for opposite directions of magnetic field, solid, and open circles, respectively. *Inset*: the angular spectrum of the SHG magnetic contrast in the vicinity of the microcavity mode

$\lambda_{\mathrm{MC}} \simeq 1115$ nm in the transversal NOMOKE configuration. The inverting the magnetic field direction varies $I_{2\omega}$ approximately by a factor of four. The angular spectrum of the SHG magnetic contrast shown in the inset of Fig. 8.11 is independent of the angle of incidence and achieves values of 0.65.

Magnetization-induced changes of the relative phase of the SH wave are observed using SHG interferometry [27]. The SHG interference patterns are obtained by translating the SHG reference sample along the direction of the laser beam propagation, so that the distance l between the reference and the MMC sample is varied. The SHG reference sample is a 30 nm-thick indium tin oxide film deposited on fused quartz plate. The total SH intensity, $I_{2\omega}(l, \mathbf{M})$, is produced by the coherent sum of the SH waves from the reference, $\mathbf{E}^r_{2\omega}$, and the MMC sample, $\mathbf{E}_{2\omega}(\mathbf{M})$:

$$I_{2\omega}(l, \mathbf{M}) = \frac{c}{8\pi}\left|\mathbf{E}^r_{2\omega}(l) + \mathbf{E}_{2\omega}(\mathbf{M})\right|^2$$
$$= I^r_{2\omega} + I_{2\omega}(\mathbf{M}) + 2\alpha\sqrt{I^r_{2\omega} I_{2\omega}(\mathbf{M})}\cos\left(2\pi kl + \Phi_{\mathrm{rs}}(\mathbf{M})\right), \quad (8.16)$$

where $k = 2\Delta n/\lambda_\omega$ with $\Delta n = n_{2\omega} - n_\omega$ describing air dispersion, Φ_{rs} is the phase difference between the reference and sample SH waves, and $\alpha < 1$ is the phenomenological parameter accounting for both spatial and temporal coherence of the laser pulses. Changing the magnetic field direction to the opposite one shifts the SHG interference patterns by almost a half of a period. This indicates the shift of the relative SH phase at approximately 180°. The angular dependence of the SH phase shifts measured at the vicinity of the mode is shown in Fig. 8.12. The phase shifts are slightly smaller than 180° and almost constant in θ.

The SH intensity variations which are odd in the magnetization are observed only in the transversal NOMOKE configuration. In the p-in, p-out polarization combination, the non-magnetic (crystallographic) SH field E^{NM} is induced by χ_{zzz}, χ_{zxx}, and χ_{xxz} elements of the $\chi^{(2,0)}$ tensor. The magnetization-induced SH field

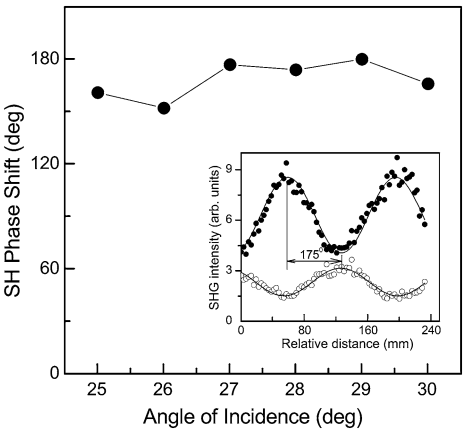

Fig. 8.12 Phase effects in MSHG: The magnetization-induced shift of the relative SH phase measured in the transversal NOMOKE configuration in the angular vicinity of the microcavity mode. *Inset*: row SHG interference patterns for opposite directions of magnetic field measured at $\theta = 28°$

$E^{\mathrm{M}} \exp(i\varphi_M)$ is generated by χ_{xzzY}, χ_{zxzY}, and χ_{xxxY} elements of the $\chi^{(2,1)}$ tensor and is shifted in phase by φ_M with respect to the E^{NM} field. Interference of the non-magnetic and magnetization-induced SH fields leads to the cross-term $\pm 2E^{\mathrm{NM}}E^{\mathrm{M}} \cos\varphi_M$ in the SH intensity. This term changes the sign upon the reversing the magnetic-field direction and results in the SH intensity variations, which are linear in **M**. The relative value of these variations depends on the phase shift φ_M. The constant value of ρ in the vicinity of the microcavity mode indicates that the SH fields E^{NM} and E^{M} are enhanced similarly due to the fundamental field localization. For the 1064-nm fundamental wavelength φ_M takes the values close to 0° or to 180° for opposite directions of **M**. This is seen in phase measurements, where the magnetization-induced shift of the relative SH phase is close to 180°. For small refraction angle θ_ω in the Bi:YIG layer and $\varphi_M \simeq 0$, the ratio between E^{NM} and E^{M} can be estimated as

$$E^{\mathrm{NM}}/E^{\mathrm{M}} \simeq \chi_{xxxY} M_Y/(2\chi_{zxx} \tan\theta_\omega). \tag{8.17}$$

It gives the ratio of $\chi_{xxxY} M_Y/\chi_{zxx} \simeq 0.15$ for $\rho \simeq 0.65$.

8.5.2 *Longitudinal and Polar NOMOKE in MSHG: Polarization Effects*

Figure 8.13 shows dependences of the SH intensity on the orientation angle Θ of the analyzer axis measured for opposite directions of magnetic field applied in the longitudinal NOMOKE configuration [28, 30]. The fundamental radiation is *s*-polarized and its wavelength is 868 nm, which corresponds to the microcavity mode. The SH wave is linearly polarized. The longitudinal NOMOKE manifests itself in the magnetization-induced rotation of the SH wave polarization. The angle of polarization rotation is $\Delta\Theta = 38°$ for the angle of incidence of 30° and almost $\Delta\Theta = 48°$ as the angle of incidence is 15°.

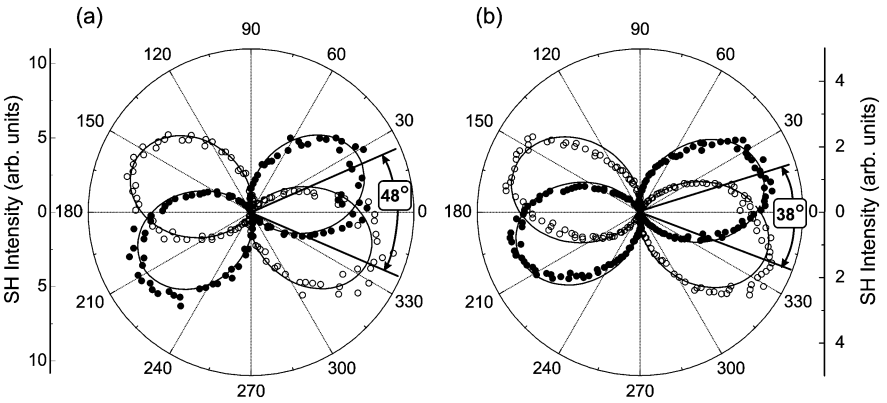

Fig. 8.13 SH wave polarization diagrams measured for opposite directions of magnetic field applied in the longitudinal configuration to the MMC with $\lambda_{MC} \simeq 900$ nm. The angle of incidence is 15° (**a**) or 30° (**b**). The zeroth value of the analyzer angle corresponds to the p-polarized SH wave. *Curves* are the fit to intensity of the linearly polarized wave

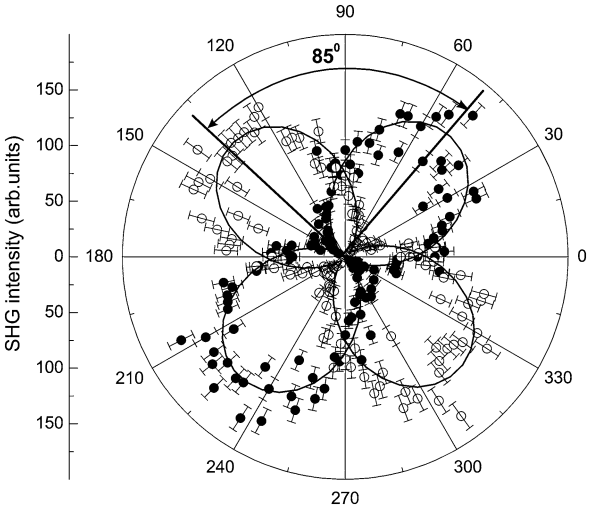

Fig. 8.14 SH wave polarization diagrams measured in MMC with $\lambda_{MC} \simeq 1115$ nm for the opposite directions of the magnetic field applied in the longitudinal configuration. The angle of incidence is 28°. The zeroth value of the analyzer angle corresponds to the p-polarized SH wave. *Curves* are the fit to intensity of the linearly polarized wave

The magnetization-induced rotation of the SH wave polarization plane is increased as the fundamental radiation is tuned to the long-wavelength region. Figure 8.14 shows the SH wave polarization diagrams measured for the s-polarized fundamental radiation with $\lambda_\omega = 1064$ nm. The magnetization-induced rotation of the polarization plane up to $\Delta\Theta = 85°$ is observed, while for the p-polarized fundamental radiation the $\Delta\Theta$ value is approximately 60°.

In the longitudinal NOMOKE configuration, the non-magnetic and magnetization-induced SH fields are polarized orthogonally, E^{NM} being p-polarized and E^{M}—s-polarized, respectively. The magnetization-induced effects appear in rota-

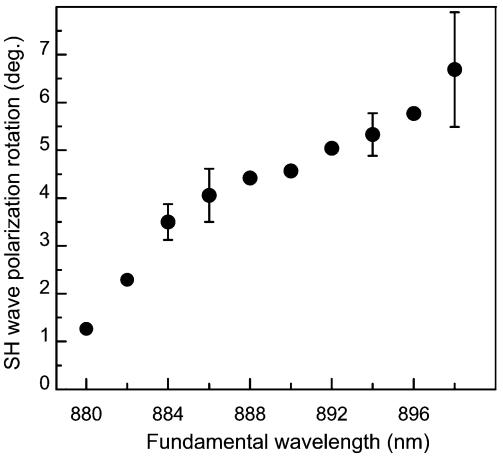

Fig. 8.15 Polarization effects in MSHG: The spectrum of the SH wave polarization rotation in MMC with $\lambda_{MC} \simeq 900$ nm upon the inverting the magnetic field direction in the polar NOMOKE configuration

tion of the polarization plane of the total SH light. The SH intensity depends on the analyzer angle Θ as

$$I_{2\omega}(\Theta) \propto \left| E_p^{\mathrm{NM}} \cos\Theta + E_s^{\mathrm{M}} \exp(i\phi_M) \sin\Theta \right|^2, \tag{8.18}$$

where the phase shift ϕ_M describes the SH field ellipticity and the subscripts s and p indicate the polarization of the corresponding SH fields. The SH wave is considered as linearly polarized with $\phi_M \simeq 0$. The rotation angle of the SH field polarization upon the inverting the magnetic field direction is estimated as $\Delta\Theta \simeq 2\arctan(E_s^{\mathrm{M}}/E_p^{\mathrm{NM}})$ and depends on the ratio of corresponding elements of the $\chi^{(2,0)}$ and $\chi^{(2,1)}$ tensors [28]. For longitudinal NOMOKE configuration and the s-polarized fundamental radiation

$$\Delta\Theta \simeq 2\arctan\left(\chi_{yyyX} M_X / (\chi_{zyy} \sin\theta_\omega)\right). \tag{8.19}$$

For $\Delta\Theta_{2\omega} = 48°$ and $\theta = 15°$, it gives the ratio of $\chi_{yyyX} M_X / \chi_{zyy} \simeq 0.1$ at $\lambda_\omega = 870$ nm, which is close to the value of the $\chi_{xxxY} M_Y / \chi_{zxx}$ ratio estimated from the transversal NOMOKE measurements. For $\Delta\Theta_{2\omega} = 85°$, $\theta = 28°$, it gives the ratio of $\chi_{yyyX} M_X / \chi_{zyy} \simeq 0.15$ at $\lambda_\omega = 1064$ nm.

The spectrum of the polar NOMOKE is shown in Fig. 8.15. Tuning the fundamental wavelength through the microcavity mode leads to a gradual increase of $\Delta\Theta$, from 1° to 7°. In the polar NOMOKE configuration, E_s^{M} is yielded by three sources. First, it is generation of the s-polarized magnetization-induced SH field described by the χ_{yxzZ} element, $E_{s,1}^{\mathrm{M}} = F_y^{2\omega} F_x^{\omega} F_z^{\omega} \chi_{yxzZ} M_Z I_\omega^2$ with F_i^{Ω} is the Green-function correction for corresponding component of the SH or fundamental wave amplitudes [31] and I_ω is the fundamental wave intensity. Second, it is the generation of the s-polarized SH field via the χ_{yzy} element of the crystallographic quadratic susceptibility, $E_{s,2}^{\mathrm{M}} = F_y^{2\omega} F_z^{\omega} F_y^{\omega} \chi_{yzy} I_\omega^2 \sin(\Theta_\omega/2)$, where Θ_ω is the linear (Faraday) rotation angle of the fundamental wave. The Faraday rotation of the fundamental radiation is greatly enhanced at the resonance with the microcavity mode due to multiple reflection in the Bi:YIG spacer [32] that is the directly attributed to the

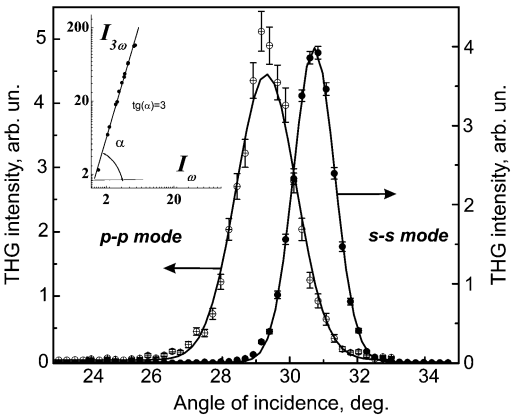

Fig. 8.16 Angular spectra of the THG intensity for different polarization combinations of the pump and THG modes

nonreciprocity of the light propagation in the magnetic materials. Faraday rotation of initially p-polarized fundamental wave is equivalent to the appearance of the s-polarized component of the fundamental radiation that allows generation of the s-polarized SH wave in the m-in, s-out polarization combination. The last source of the s-polarized SH wave is the Faraday rotation of the p-polarized SH wave, $E_{s,3}^{\mathrm{M}} = E_p^{\mathrm{NM}} \sin(\Theta_{2\omega}/2)$, where $\Theta_{2\omega}$ is the Faraday rotation angle of the SH wave. For small angles of incidence, the contribution of the χ_{zzz} susceptibility element is small and $E_p^{\mathrm{NM}} = (F_z^{2\omega}(F_x^{\omega})^2 \chi_{zxx} + F_x^{2\omega} F_z^{\omega} F_x^{\omega} \chi_{xzx}) I_{\omega}^2$. For the correct calculation of the total SH wave polarization rotation, $\tan \Delta\Theta = 2(E_{s,1}^{\mathrm{M}} + E_{s,2}^{\mathrm{M}} + E_{s,3}^{\mathrm{M}})/E_p^{\mathrm{NM}}$, one should know the relation between χ_{yzy}, χ_{zxx} and χ_{xzx} elements. However, for the estimation, suppose them to be equal one to each other. For small refractive angles θ_{ω}, Green-function corrections $F_z^{2\omega}$, $F_z^{\omega} \to 0$ and $F_x^{2\omega}$, F_x^{ω}, F_y^{ω}, $F_y^{2\omega} \to 1$, $\tan \Delta\Theta \simeq \Delta\Theta$, $\sin \Theta_{2\omega} \simeq \Theta_{2\omega}$ and $\sin \Theta_{\omega} \simeq \Theta_{\omega}$. The $\Delta\Theta$ value can be estimated within these assumptions as [35]

$$\Delta\Theta \simeq \chi_{yxzZ} M_Z / \chi_{zxx} + \Theta_{\omega}/2 + \Theta_{2\omega}. \tag{8.20}$$

The first term in (8.20) is wavelength-independent since the elements of the $\chi^{(2,0)}$ and $\chi^{(2,1)}$ tensors are constant within narrow spectral region of the MC mode. The term $\Theta_{2\omega}$ is also independent from λ_{ω} due to large absorption at the SH wavelength. The second term in (8.20), $\Theta_{\omega}(\lambda_{\omega})$ reaches the maximum for oblique angles of incidence when s- and p-modes are overlapped. Note that the rotation of the SH field polarization plane via *non-magnetic* quadratic susceptibility is related strongly to the symmetry of the magnetic spacer since it requires the non-zero χ_{yzy} element.

8.5.3 MTHG in Magnetophotonic Microcavities

Optical third harmonic generation in MMC was first studied in the absence of the external magnetic field in near-resonant conditions for the excitation of the microcavity mode. Figure 8.16 shows the angular spectra of the THG intensity for different polarization combinations of the pump and THG modes. In accordance with

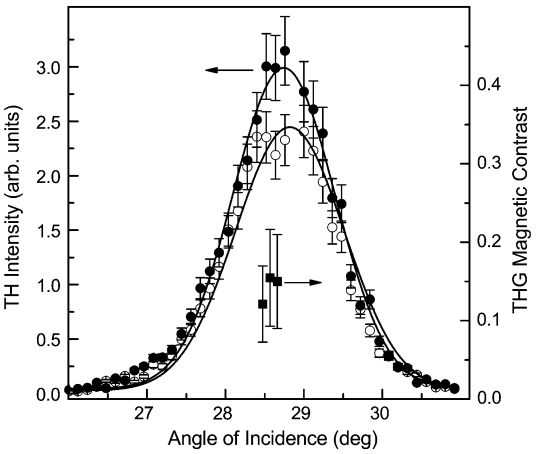

Fig. 8.17 Intensity effects in MTHG: Angular spectra of transversal NOMOKE in THG measured in MMC with $\lambda_{MC} \simeq 1115$ nm for opposite directions of magnetic field, *solid*, and *open circles*, respectively. *Squares* shows the THG magnetic contrast in the angular vicinity of the microcavity mode

the symmetry analysis summarized in Table 8.1, only s-in, s-out and p-in, p-out geometries are allowed for the THG in an isotropic medium that was proven experimentally. The magnetization-induced effects in the intensity of the third-harmonic generation are studied for the transversal NOMOKE configuration. The symmetry analysis shows that for this geometry of the magnetic field application the elements of the cubic susceptibility tensor $\chi^{(3,1)}$, which are odd in the magnetization, lead to the appearance of additional contributions to the p-polarized THG signal. The experiments performed for the p-in, p-out polarization combination for the transversal NOMOKE do not reveal magnetization-induced variations of the THG intensity within the experimental accuracy, on the contrary to a much larger magnetic contrast in the SHG intensity.

In order to reveal a small magnetization-induced effect in the THG intensity, the following experimental scheme is chosen. The p-polarized THG intensity is measured, while the polarization plane of the fundamental radiation is chosen to form an angle of about 5–10 degrees out from the s-polarization. For this polarization combination, almost the entire magnetic component of the THG intensity generated by the χ_{zyyx} component is recorded, which interfered with a strongly suppressed non-magnetic p-in, p-out THG signal. Figure 8.17 shows the THG spectra measured in the wave-vector domain for the oppositely directed magnetic field for the transversal NOMOKE configuration. Similar to the magnetization-induced SHG, the THG magnetic contrast is determined by the expression $\rho_{3\omega} = (I_+^{3\omega} - I_-^{3\omega})/(I_+^{3\omega} + I_-^{3\omega})$, where $I_+^{3\omega}$ and $I_-^{3\omega}$ are the THG intensities for the oppositely directed magnetic fields. The measured value of the magnetic contrast in the THG intensity is found to be about 0.1 for the angles of incidence corresponding to the resonance with the microcavity mode.

The observed THG magnetic contrast is due to the third-order susceptibility $\chi^{(3,1)}$ components' interference with the non-magnetic ones due to the internal homodyne effect. This results in the revelation of a weak magnetic THG contribution on the background of a much stronger non-magnetic THG. In this case, an esti-

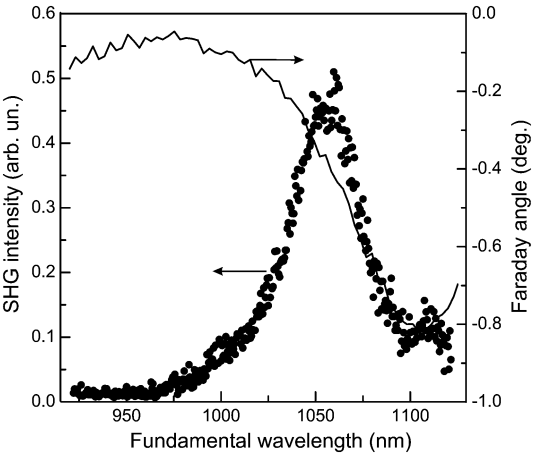

Fig. 8.18 *Filled circles*. Intensity spectrum of the SH wave reflected from MPC in the p-in, s-out polarization combination in longitudinal configuration of the dc-magnetic field application. *Line*: the Faraday rotation spectrum at normal incidence

mation can be made for the χ_{zyyyX} element as $\chi_{zyyyX} \sim 10^{-3}\chi_{\text{eff}}^{(3)}$, where $\chi_{\text{eff}}^{(3)}$ is the effective non-magnetic cubic susceptibility responsible for the generation of the p-polarized TH field with s- or mixed-polarized fundamental radiation.

8.5.4 Phase-Matched MSHG in Magnetophotonic Crystals

Figure 8.18 shows the spectrum of the SH intensity measured in MPC for the p-in, s-out polarization combination in the longitudinal NOMOKE configuration. Spectrum demonstrates the resonant enhancement at $\lambda_\omega \simeq 1055$ nm. The spectral position of the peak correlates with the long-wavelength PBG edge, which is blue-shifted from 1110 nm for oblique angles of incidence. In the p-in, s-out polarization combination, the non-magnetic (crystallographic) SH field $E_{2\omega}^{\text{NM}}$ induced by the $\chi^{(2,0)}$ tensor is equal to zero. Thus in the longitudinal NOMOKE configuration as $\mathbf{M} = (M_X, 0, 0)$, the SH intensity is entirely associated with the magnetization-induced SH field $E_{2\omega}^{\text{M}}$ induced by the χ_{yxxX} and χ_{yzzX} elements of the $\chi^{(2,1)}$ tensor. The MSHG enhancement in MPC is interpreted as a result of the phase matching conditions achieved as the fundamental wavelength is tuned across the PBG edge. This stems from the comparison of the amplitudes of the SHG resonances at PBG edges. The intensity enhancement at the long-wavelength PBG edge of MPC is at least five times larger than that at the short-wavelength edge. Spatial localization of the optical field is similar at both PBG edges and the SHG enhancement yielded by this mechanism is expected to be the same order of magnitude. Inversion of the magnetic field direction does not change the value of the SH intensity, which indicates that $E_{2\omega}^{\text{NM}} = 0$.

This is in contrast to the p-in,p-out polarization combination. In the transversal NOMOKE configuration the non-magnetic SH field $E_{2\omega}^{\text{NM}}$ interferes with the magnetization-induced SH field $E_{2\omega}^{\text{M}} \exp(i\varphi_M)$. The intensity cross-term

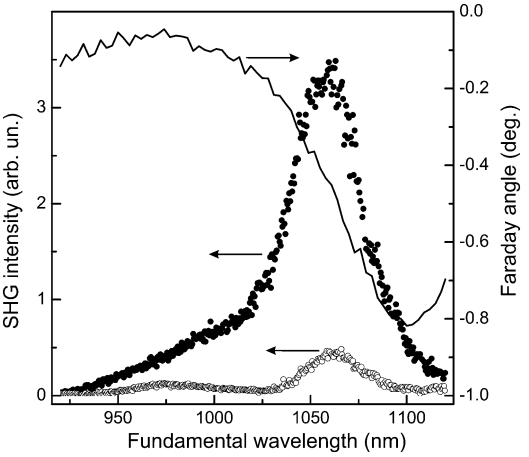

Fig. 8.19 The SHG spectra of MPC in the p-in, p-out polarization combination and in transversal magnetic-field configuration measured for opposite directions of the dc-magnetic field; *open* and *filled circles*, respectively. *Line*: the Faraday rotation spectrum at normal incidence

$\pm 2E_{2\omega}^{\mathrm{NM}} E_{2\omega}^{\mathrm{M}} \cos\varphi_M$ changes the sign upon changing the magnetic field direction and manifests the internal homodyne effect in MSHG. This term leads to variations of the SH intensity, which are linear in $\mathbf{M}$ and depends on the relative phase φ_M between $E_{2\omega}^{\mathrm{NM}}$ and $E_{2\omega}^{\mathrm{M}}$. Figure 8.19 shows the SHG spectra measured for opposite directions of magnetic field in the transversal NOMOKE configuration. The SHG intensity is many-fold enhanced in the spectral vicinity of 1050 nm corresponding to the phase-matched conditions for SHG at the long-wavelength PBG edge of MPC. Changing the magnetic field direction varies the SH intensity approximately by a factor of seven at $\lambda_\omega \simeq 1055$ nm that indicates the noticeable interference between the $E_{2\omega}^{\mathrm{NM}}$ and $E_{2\omega}^{\mathrm{M}}$ fields. At $\lambda_\omega \simeq 1025$ nm the SH intensity for one of the magnetic field direction is close to zero. It means that the contrast of the magnetization-induced variations in the SH intensity is close to unit, which the upper limit for SHG magnetic contrast.

8.5.5 Nonlinear Magneto-Optical Kerr Effect in Three-Dimensional Magnetophotonic Crystals

As has been discussed above MPC and MPMC are attractive structures for potential applications. One of the perspective approaches for the composition of MPC is the infiltration of a magnetic material into porous PC template, thus the structure periodicity is governed by the non-magnetic porous PC and the magneto-optical properties are supplied by the infiltrated magnetic material.

Synthetic opals composed of spheres of silica oxide are unique self-assembling materials that form a strongly periodic 3D structure. Depending on the size of the constituting spheres they can reveal the PBG in the visible and near infra-red spectral regions. The structure of the opals supposes the existence of hexagonal system of pores with the volume fraction of no less than 26 % (in case of close packed

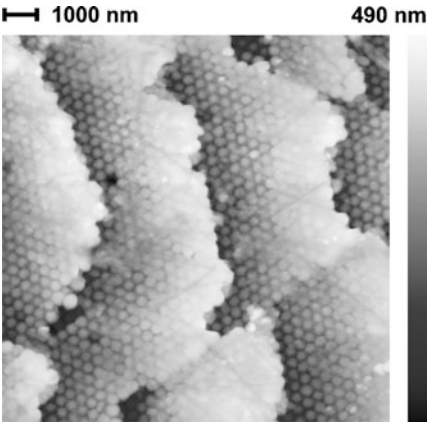

Fig. 8.20 SEM image of the experimental opal sample

silica oxide spheres). As concerning 3D MPCs, there are several papers related to studies of their magnetic and structural properties, including the observation of an enlarged Faraday rotation [10, 11]. Here we describe the results on the composition and investigation of the nonlinear magneto-optical Kerr effect (NOMOKE) in 3D MPC based on artificial opals infiltrated by yttrium–iron garnet (YIG). Here we will mainly describe the results from [37].

8.5.5.1 Sample Composition and Characterization

Templates of artificial opals were composed of monodisperse amorphous close-packed SiO_2 spheres with the diameter of about 330 nm. The bare opals have been grown by use of the technological route described in [39]. The samples studied in the nonlinear-optical experiments were the plates of about $(4 \times 4 \times 0.5)$ mm in size cut parallel to the (111) opal crystalline plane (Fig. 8.20). Opal templates possessed polydomain structure, the size of a single domain with highly ordered SiO_2 spheres ranged from 30 to 100 μm.

Two technological approaches were used for the infiltration of opals templates by yttrium–iron garnet. The first batch of samples was soaked by the colloidal solution of yttrium–iron hydroxides taken in stoichiometric proportion, the size of the colloidal particles being about 5 nm. The filling factor of pores was 25–30 % vol. In order to form YIG nanocrystals inside the pores the subsequent annealing at 1300 K was performed. X-ray diffraction analysis has shown the appearance of the strongest YIG peak from [420] set of planes. Such a relatively poor XRD spectrum can evidently be caused by the formation of silicate due to the reaction of yttrium oxide with SiO_2, so that only a small amount of crystalline YIG was formed.

An attempt to prevent the chemical reactions between the yttrium oxide and the silica matrix was made for the second set of samples, where a thin platinum layer covering the inner surface of the opal matrix was deposited prior to the infiltration by YIG. A thin layer of platinum (2–3 nm) is deposited on silica surface using the

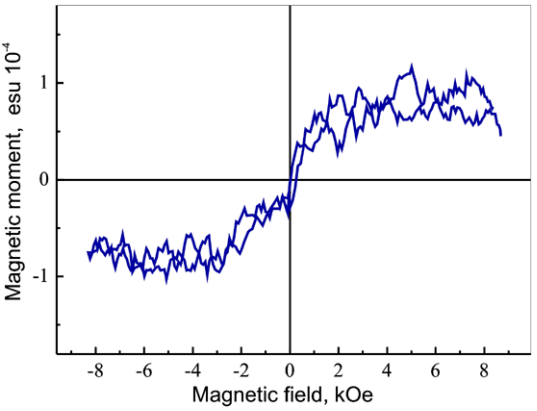

Fig. 8.21 Magnetization curve for opal-Pt-YIG composite PC

method described in [17, 18]. The gravimetric measurements have shown that the filling factor of pores by Pt is about 5 % vol. After the deposition of a thin Pt layer the samples were infiltrated by an aqueous solution of yttrium and iron acetates followed by the thermal annealing in a similar way as described above for bare opals. The filling factor of pores with YIG was about 30 % vol. In the case of this set of samples the XRD analysis revealed the existence of the following crystalline phases: Pt, yttrium–iron garnet $Y_3Fe_5O_{12}$ with the lattice parameter $a = 12.25(7)$ Å, as well as some impurities [γ-Fe_2O_3, yttrium silicates and crystalline forms of SiO_2 (cristobalite and tridymite)]. Before starting the optical measurements, the rest volume of pores in the opal-YIG and opal-Pt-YIG samples was infiltrated with glycerol to decrease diffuse scattering. Magnetization measurements for Pt-covered YIG-infiltrated opals (Fig. 8.21) have shown that within the experimental accuracy there is no hysteresis in the magnetization curve, while for the magnetic fields over approximately 2 kOe the magnetization is close to the saturation. Such features are typical for super-paramagnetic systems composed of nanocrystallites of magnetic materials such as YIG crystallized within opals' nanopores.

Optical characterization of YIG-infiltrated opals was first performed by linear reflectance spectroscopy. The reflectance spectra measured for different angles of incidence of the fundamental beam with the wavelength range from 500 to 1100 nm are shown in Fig. 8.22. The reflectivity maxima correspond to the PBG and demonstrate a blue-shift with the increase of the angle of incidence, which is typical for opals [40, 41]. The inset in Fig. 8.22 shows a linear dependence of the central PBG wavelength on $\sin^2(\theta)$ that stays in good agreement with the Bragg diffraction condition $\lambda = 2d_{111}\sqrt{\epsilon_{\text{eff}} - \sin^2\theta}$, where d_{111} is the crystal lattice parameter along the crystallographic direction [111] and ϵ_{eff} is the effective dielectric constant of the composite opal.

When studying the nonlinear optical spectroscopy in composite opals with YIG, the output of a nanosecond OPO laser system in the spectral range from 700 to 1100 nm with a pulse duration of about 4 ns and a peak intensity of 1 MW/cm^2 is used as the fundamental radiation. A Fresnel rhomb (placed in front of the sample)

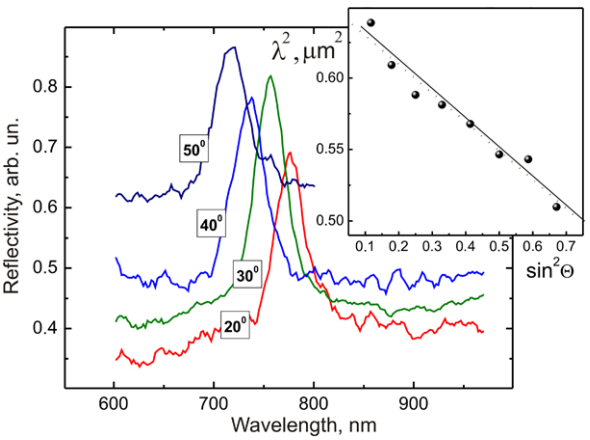

Fig. 8.22 Reflectivity spectra of opal-Pt-YIG composite PC for various angles of incidence of the fundamental beam. *Inset*: dependence of the square of the PBG central wavelength λ^2 on $\sin^2(\theta)$

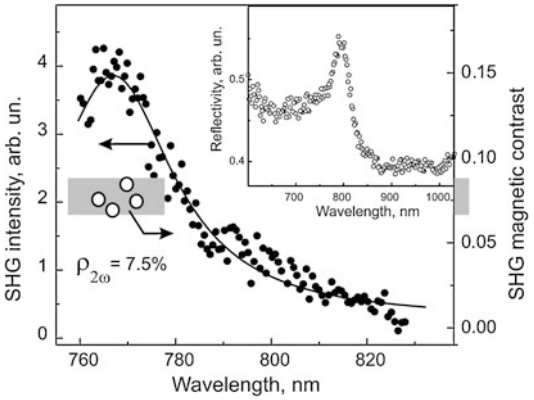

Fig. 8.23 Main panel: SHG intensity (*left scale*) and the NOMOKE (*right scale*) spectra in opal-YIG sample measured for $\theta = 20°$. *Insets*: reflectivity spectra of the same sample and for $\theta = 20°$

and Glan–Taylor polarizer (placed in the reflected from the sample beam) select the p-polarizations of both the fundamental and SHG waves. The SHG signal in the direction of the specular reflection is detected by a PMT and a boxcar integrator. The magnetic field of 2 kOe is applied to the sample in the geometry of the transversal magneto-optical Kerr effect, i.e. in the plane of the sample and perpendicular to the plane of incidence, as is shown schematically on the inset in Fig. 8.23. As has been described in the previous sections, this experimental geometry can lead only to the magnetization-induced changes the intensity of the reflected SHG.

Figure 8.23 shows the linear reflectivity spectra measured for $\theta = 20°$ for opal-YIG composite (without the Pt coverage) that reveals a spectral maximum centered at $\lambda \approx 790$ nm. SHG intensity spectrum of the same sample attained also for $\theta = 20°$ in the spectral vicinity of the PBG is shown in the main panel of Fig. 8.23. The spectral peak of the SHG intensity is centered around 770 nm, which corresponds to the PBG edge similarly to observed for Si-infiltrated opals [38]. Such behavior can be attributed to the fulfillment of the phase-matching conditions for the second harmonic generation, similarly to observed in 1D MPC and associated with a modified

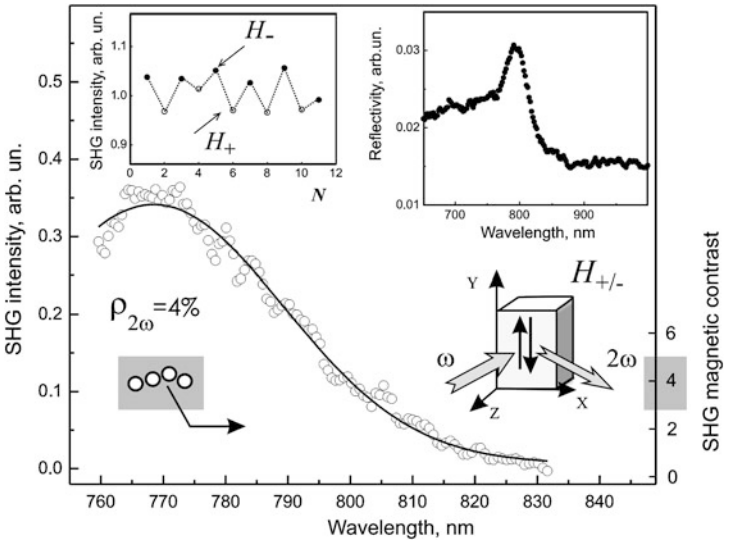

Fig. 8.24 Main panel: SHG intensity (*left scale*) and the NOMOKE (*right scale*) spectra in opal-Pt-YIG sample measured for $\theta = 20°$. *Inset*: reflectivity spectra of the same sample and for $\theta = 20°$

dispersion law of opal-based PC in this spectral region, which can be treated as nonlinear diffraction in 3D PC.

To reveal the magnetic state of opal-YIG composites, the transversal NOMOKE is studied for the two types of sample and the SHG contrast was measured for fixed wavelengths of the fundamental beam. The SHG intensity was first measured for one of the directions of the magnetic field for about 5000 laser pulses and gave the value $I_{2\omega}(H+)$, then the direction of H was reversed and the value $I_{2\omega}(H-)$ was measured. This procedure was repeated for dozens of times for each wavelength of the pump beam close to the spectral maximum of the SHG intensity. An example of the measured SHG intensities for the subsequent experiments is shown in Fig. 8.23, where N indicates the number of switching of the magnetic field. The values of the SHG intensity $I_{2\omega}(H+)$ and $I_{2\omega}(H-)$, averaged over the whole set of measurements, were taken to determine the SHG magnetic contrast.

The NOMOKE contrast for opal-YIG composites is shown in Fig. 8.23 (right scale for the main panel), the attained value is $\rho_{2\omega} = 4$ %. For comparison, in linear magneto-optical transversal Kerr effect for thin YIG films the analogous value is about 0.1 % or less.

Figure 8.24 shows the results of linear-optical (inset) and nonlinear-optical (main panel) spectroscopy of opal-Pt-YIG sample measured for $\theta = 20°$. The reflectivity maximum for the opal-Pt-YIG composite is twice as high as that for the opal-YIG composite under the same experimental conditions (insets in Figs. 8.23 and 8.24). This is probably related to a better quality of the SiO_2-Pt-YIG interfaces as compared with the SiO_2-YIG sample, as platinum prevents chemical reactions between yttrium oxide and the silica opal matrix. The main panel in Fig. 8.24 shows the SHG

spectrum, which reveals a sharp peak centered around 767 nm, which corresponds to the spectral position of the short-wavelength wing of the reflectivity spectrum. The mechanism of the SHG enhancement in the opal-Pt-YIG sample is expected to be the same as in the opal-YIG sample and is attributed to the realization of the phase-matching conditions for the SHG process at the PBG edge, while the increase of the SHG peak intensity is about one order of magnitude larger.

The SHG magnetic contrast in opal-Pt-YIG samples is about 7.5 % for the wavelengths close to the SHG spectral maximum. This value was obtained in the same way as for the SHG magnetic contrast for the opal-YIG composites and is shown in Fig. 8.24 for several wavelengths (the data refer to the right scale of the panel). Larger $\rho_{2\omega}$ values attained for opal-Pt-YIG composites as compared with Pt-free opal-YIG samples are probably caused by larger concentration of crystalline YIG inside the opal-Pt matrix due to the protective role of the Pt internal layers preventing strong chemical interaction of YIG precursors and the SiO_2 spheres. As the result, this leads to higher magnetization-induced nonlinear-optical effects in the sample.

Summing up, the SHG and NOMOKE spectroscopy are studied in 3D magnetophotonic crystals based on artificial opals infiltrated by yttrium–iron garnet. The existence of the crystalline magneto-optical YIG inside the 3D opal matrix is proven by XRD studies. The SHG magnetic contrast of 7.5 % is observed for the spectral edge of the photonic band gap of the composed magnetophotonic crystals.

8.6 Conclusions and Prospectives

In this chapter we have discussed the modern trends in nonlinear optics of novel photonic-band-gap systems based on conjugation of gyrotropic materials with broken time-reversal symmetry with photonic crystals approach yielding new possibilities to control the nonlinear generation and propagation of light that is flexible under external control impacts, such as a dc magnetic field. Nonlinear-optical analog of magneto-optical Kerr effect revealing itself in magnetization-induced changes of second- or third-harmonic intensity, polarization or relative phase is experimentally demonstrated in transversal, longitudinal and polar configuration of magnetic field application. One of the further developments of nonlinear magneto-optics in magnetophotonic crystals might be the search of similar effects in magnetoplasmonic crystals [42–44] and magnetoplasmonic nanostructures [45, 46] involving collective excitations of electron plasma. This might stimulate the integration of these new materials in modern telecommunication systems.

Acknowledgements We would like to thank our colleagues T.V. Dolgova, A.G. Zhdanov, R.V. Kapra, D.A. Kurdyukov, N.S. Perov, V.G. Golubev for their participation in this work. We greatly acknowledge the fruitful discussions with A.B. Granovsky, A. Khanikaev, A. Baryshev. This work was partially supported by the Russian Foundation for Basic Research (RFBR).

References

1. J.A. Armstrong, N. Bloembergen, J. Ducuing, P.S. Pershan, Phys. Rev. **127**, 1918 (1962)
2. N. Bloembergen, J. Sievers, Appl. Phys. Lett. **17**, 483 (1970)
3. S. Nakagawa, N. Yamada, N. Mikoshiba, D.E. Mars, Appl. Phys. Lett. **66**, 2159 (1995)
4. A.V. Balakin, V.A. Bushuev, N.I. Koroteev, B.I. Mantsyzov, I.A. Ozheredov, A.P. Shkurinov, D. Boucher, P. Masselin, Opt. Lett. **24**, 793 (1999)
5. M. Centini, G. D'Aguanno, M. Scalora, C. Sibilia, M. Bertolotti, M.J. Bloemer, C.M. Bowden, Phys. Rev. E **64**, 046606 (2001)
6. U. Pustogowa, W. Hubner, K.H. Bennemann, Phys. Rev. B **49**, 10031 (1994)
7. R.-P. Pan, H.D. Wei, Y.R. Shen, Phys. Rev. B **39** (1989)
8. J. Reif, J.C. Zink, C.-M. Schneider, J. Kirschner, Phys. Rev. Lett. **67**, 2878 (1991)
9. K. Bennemann, J. Magn. Magn. Mater. **200**, 697 (1999)
10. T.V. Murzina, E.M. Kim, R.V. Kapra, O.A. Aktsipetrov, A.F. Kravets, M. Inoue, S.V. Kuznetsova, M.V. Ivanchenko, V.G. Lifshits, Phys. Rev. B **73**, 140404(R) (2006)
11. B.B. Krichevtsov, V.V. Pavlov, R.V. Pisarev, JETP Lett. **49**, 535 (1989)
12. E. Popova, N. Keller, F. Gendron, M. Guyot, M.-C. Brianso, Y. Dumond, M. Tessier, J. Appl. Phys. **90**, 1422 (2001)
13. G. Petrocelli, S. Martellucci, M. Richetta, Appl. Phys. Lett. **63**, 3402 (1993)
14. V.N. Gridnev, V.V. Pavlov, R.V. Pisarev, A. Kirilyuk, Th. Rasing, Phys. Rev. B **63**, 184407 (2001)
15. R.V. Pisarev, B.B. Krichevtsov, V.N. Gridnev, V.P. Klin, D. Frohlich, C. Pahlke-Lerche, J. Phys. Condens. Matter **5**, 8621 (1993)
16. V.V. Pavlov, R.V. Pisarev, A. Kirilyuk, Th. Rasing, Phys. Rev. Lett. **78**, 2004 (1997)
17. O.A. Aktsipetrov, O.V. Braginskii, D.A. Esikov, Sov. J. Quantum Electron. **20**, 259 (1990)
18. I.L. Lyubchanskii, N.N. Dadoenkova, M.I. Lyubchanskii, Th. Rasing, J.-W. Jeong, S.-C. Shin, Appl. Phys. Lett. **76**, 2000 (2000)
19. S. Wittekoek, T.J.A. Popma, J.M. Robertson, P.F. Bongers, Phys. Rev. B **12**, 2777 (1975)
20. A.A. Fedyanin, O.A. Aktsipetrov, D. Kobayashi, K. Nishimura, H. Uchida, M. Inoue, J. Magn. Magn. Mater. **282**, 256 (2004)
21. S. Erokhin, Yu. Boriskina, A. Vinogradov, M. Inoue, D. Kobayashi, A. Fedyanin, M. Kochneva, E. Gan'shina, A. Granovsky, J. Magn. Magn. Mater. **300**, e257 (2006)
22. A.G. Zhdanov, A.A. Fedyanin, O.A. Aktsipetrov, D. Kobayashi, H. Uchida, M. Inoue, J. Magn. Magn. Mater. **300**, e253 (2006)
23. A.B. Khanikaev, A.V. Baryshev, M. Inoue, A.B. Granovsky, A.P. Vinogradov, Phys. Rev. B **72**, 035123 (2005)
24. H. Kato, T. Matsushita, A. Takayama, M. Egawa, K. Nishimura, M. Inoue, J. Appl. Phys. **93**, 3906 (2003)
25. A.K. Zvezdin, V.I. Belotelov, J. Opt. Soc. Am. B **22**, 228 (2005)
26. O.A. Aktsipetrov, E.M. Kim, R.V. Kapra, T.V. Murzina, A.F. Kravets, M. Inoue, S.V. Kuznetsova, M.V. Ivanchenko, V.G. Lifshits, Phys. Rev. B **73**, 140404 (2006)
27. K. Kemnitz, K. Bhattacharyya, J.M. Hicks, G.R. Pinto, K.B. Eisenthal, T.F. Heinz, Chem. Phys. Lett. **131**, 285 (1986)
28. T.V. Dolgova, A.A. Fedyanin, O.A. Aktsipetrov, K. Nishimura, H. Uchida, M. Inoue, J. Appl. Phys. **95**, 7330 (2004)
29. A.A. Fedyanin, T. Yoshida, K. Nishimura, G. Marowsky, M. Inoue, O.A. Aktsipetrov, J. Magn. Magn. Mater. **258–259**, 96 (2003)
30. O.A. Aktsipetrov, T.V. Dolgova, A.A. Fedyanin, R.V. Kapra, T.V. Murzina, K. Nishimura, H. Uchida, M. Inoue, Laser Phys. **14**, 685 (2004)
31. P. Guyot-Sionnest, Y.R. Shen, Phys. Rev. B **33**, 8254 (1986)
32. M. Inoue, K. Arai, T. Fujii, M. Abe, J. Appl. Phys. **85**, 5768 (1999)
33. M. Inoue, R. Fujikawa, A. Baryshev, A. Khanikaev, P.B. Lim, H. Uchida, O. Aktsipetrov, A. Fedyanin, T. Murzina, A. Granovsky, J. Phys. D, Appl. Phys. **39**, R151 (2006)

34. T.V. Murzina, I.E. Razdolski, O.A. Aktsipetrov, A.M. Grishin, S.I. Khartsev, J. Magn. Magn. Mater. **321**, 836 (2009)
35. A.A. Fedyanin, K. Nishimura, G. Marowsky, M. Inoue, O.A. Aktsipetrov, JETP Lett. **76**, 609 (2002)
36. O.A. Aktsipetrov, T.V. Dolgova, A.A. Fedyanin, T.V. Murzina, M. Inoue, K. Nishimura, H. Uchida, J. Opt. Soc. Am. B **22**, 176 (2005)
37. T.V. Murzina, E.M. Kim, R.V. Kapra, I.V. Moshnina, O.A. Aktsipetrov, D.A. Kurdyukov, S.F. Kaplan, V.G. Golubev, M.A. Bader, G. Marowsky, Appl. Phys. Lett. **88**, 022501 (2006)
38. A.A. Fedyanin, O.A. Aktsipetrov, D.A. Kurdyukov, V.G. Golubev, M. Inoue, Appl. Phys. Lett. **87**, 151111 (2005)
39. W. Stober, A. Fink, E. Bohn, J. Colloid Interface Sci. **26**, 62 (1968)
40. Y. Xia, B. Byron, Y. Yin, Y. Lu, Adv. Mater. **12**, 693 (2000)
41. C. Lopez, Adv. Mater. **15**, 1679 (2003)
42. A.A. Grunin, A.G. Zhdanov, A.A. Ezhov, E.A. Ganshina, A.A. Fedyanin, Appl. Phys. Lett. **97**, 261908 (2010)
43. A.A. Grunin, N.A. Sapoletova, K.S. Napolskii, A.A. Eliseev, A.A. Fedyanin, J. Appl. Phys. **111**, 07A948 (2012)
44. A.V. Chetvertukhin, A.V. Baryshev, H. Uchida, M. Inoue, A.A. Fedyanin, J. Appl. Phys. **111**, 07A946 (2012)
45. I.A. Kolmychek, T.V. Murzina, J. Wouters, T. Verbiest, O.A. Aktsipetrov, J. Opt. Soc. Am. B **29**(1), 138 (2012)
46. T.V. Murzina, I.A. Kolmychek, A.A. Nikulin, E.A. Gan'shina, O.A. Aktsipetrov, JETP Lett. **90**, 504 (2009)

Index

M. Inoue et al. (eds.), *Magnetophotonics*, Springer Series in Materials Science 178,
DOI 10.1007/978-3-642-35509-7,